SECONDARY ORGANIC AEROSOL IN THE PRISTINE AMAZONIAN ATMOSPHERE: CHEMICAL PROPERTIES, FORMATION PATHWAYS, AND INTERACTIONS WITH CLOUDS

Dissertation
zur Erlangung des Grades
„Doktor der Naturwissenschaften“
am Fachbereich Physik, Mathematik und Informatik
der Johannes Gutenberg-Universität
in Mainz

CHRISTIANE SCHULZ

geboren in Bad Saarow

Mainz, den 11. Februar 2019

1. Berichterstatter: PD Dr. Johannes Schneider
2. Berichterstatter: Prof. Dr. Peter Hoor
Tag der mündlichen Prüfung: 17. April 2019

...
I am the daughter of Earth and Water,
and the nursling of the Sky;
I pass through the pores of the ocean and shores;
I change, but I cannot die.

For after the rain when with never a stain
the pavilion of Heaven is bare,
and the winds and sunbeams with their convex gleams
build up the blue dome of air.
...
And out of the caverns of rain,
...
I arise and unbuild it again.

Percy B. Shelley
The Cloud
1820

ZUSAMMENFASSUNG

Das Amazonasgebiet stellt eines der größten Ökosysteme mit vornehmlich natürlichen Bedingungen dar. In diesem Kontext wurden flugzeuggetragene Messungen in verschiedenen Höhen bis zu 14 km durchgeführt, die unter anderem einen tieferen Einblick in die Aerosolzusammensetzung in der Atmosphäre über dem Amazonasgebiet erlauben. Ziel dieser Arbeit ist die quantitative Analyse der chemischen Zusammensetzung sowohl von Aerosolpartikeln, die außerhalb von Wolken gemessen wurden, als auch von Wolkenpartikelresiduen. Diese Messungen wurden in-situ mit einem Aerosolmassenspektrometer durchgeführt, das Aerosolpartikel in einem Größenbereich von 40 bis 800 nm analysiert. Neben der chemischen Zusammensetzung liegt der Fokus dieser Arbeit auf sekundär gebildeten organischem Aerosol (SOA) und verschiedenen Entstehungsprozessen von SOA, die in der Atmosphäre über dem Amazonasgebiet auftreten.

Das Aerosol außerhalb von Wolken besteht in allen vermessenen Höhen hauptsächlich aus organischem Material. Die höchsten Massenkonzentrationen wurden in der unteren Troposphäre (0.1 - 4.5 km) gemessen, in größeren Höhen nehmen die Konzentrationen ab. Allerdings zeigen sowohl die Organik- als auch die Nitratmassenkonzentrationen eine Zunahme in der oberen Troposphäre (8 - 14 km). Die Oxidationsstufe der organischen Aerosole in der unteren Troposphäre ist deutlich höher als die der organischen Aerosole, die in der oberen Troposphäre gemessen wurden. Diese Ergebnisse können durch SOA-Bildung in der oberen Troposphäre erklärt werden. Die Aerosolgrößenverteilung unterstützt diese These ebenfalls.

Die Analysen ergaben, dass aus Isopren-Epoxydiol gebildetes SOA (IEPOX-SOA) einen wesentlichen Anteil an der Organik darstellt. In der unteren Troposphäre lag der Beitrag bei 10 %, in der oberen Troposphäre bei etwa 20 %. Insgesamt weisen die Resultate auf ein allgegenwärtiges Auftreten von IEPOX-SOA in allen Höhen hin. Das lässt sich durch das Vorhandensein von Isopren erklären, das als Vorläufergas dieser Verbindung wirkt und von der Vegetation emittiert wird. Der Entstehungsprozess von IEPOX-SOA wird durch saure Bedingungen begünstigt, da das gasförmige Isopren-Epoxydiol (IEPOX) vornehmlich auf sauren Aerosoloberflächen kondensiert. Insbesondere in der oberen Troposphäre scheinen diese Bedingungen vorhanden zu sein. Die erhöhten Nitratkonzentrationen deuten darauf hin, dass sich bei der Entstehung von IEPOX-SOA auch Organonitrate bilden können.

Zusammenfassend lässt sich sagen, dass die Bildung von SOA ein wichtiger Prozess in der Atmosphäre des Amazonasgebietes ist, der die Eigenschaften von Aerosolen sowohl in der unteren als auch in der oberen Troposphäre

maßgeblich beeinflusst.
Neben den Messungen von Aerosolen außerhalb von Wolken war es in diesem Projekt zum ersten Mal möglich, quantitative Messungen der chemischen Zusammensetzung von Wolkenpartikelresiduen (engl. cloud particle residuals, CPR) bis zu einer Höhe von 14 km durchzuführen. Dafür wurde das Aerosolmassenspektrometer mit einem speziellen Flugzeugeinlasssystem gekoppelt (HALO-CVI), das es ermöglicht, flüssige Wolkentröpfchen und Eiskristalle von Luft und Aerosolpartikeln zu separieren, und damit eine Analyse der CPR zulässt. Diese Messungen konnten sowohl in flüssigen Wolken als auch in Eiswolken durchgeführt werden. Die CPR, die in flüssigen Wolken gemessen wurden, bestanden zu 70 % aus Organik. Die restlichen 30 % waren inorganische Substanzen, wobei Sulfat hier dominierte. Im Gegensatz dazu bestanden die Eisresiduen fast ausschließlich aus Organik. Die Analyse der organischen Massenspektren ergab, dass die CPR in Flüssigwasserwolken aus oxidierter, wahrscheinlich sekundärer Organik bestanden. Die CPR in Eiswolken wiesen hingegen eine Struktur auf, die auf primär emittierte kohlenwasserstoffähnliche Organik (engl. hydrocarbon-like organic aerosol, HOA) hindeutet. Es scheint, als seien die HOA-beinhaltenden CPR als Eiskeime aktiviert worden, während hingegen die CPR, die aus oxidierter Organik, Sulfat und Nitrat bestehen, in der unteren Troposphäre als Wolkenkondensationskeime aktiviert und ausgewaschen wurden. Die Prozesse des Gefrierens in den vermessenen Eiswolken scheinen sich von homogenem hin zu heterogenem Gefrieren zu verschieben. Das heterogene Gefrieren wird durch die HOA-enthaltenden Partikel induziert, die vertikal in große Höhen transportiert wurden. Die Wechselwirkungen zwischen Aerosolen und Wolken werden dadurch beeinflusst.
Die hier vorliegende Arbeit liefert neue Erkenntnisse hinsichtlich der Bildung sekundärer organischer Aerosole in der Atmosphäre des Amazonasgebietes unter Berücksichtigung von IEPOX-SOA und Organonitraten. Außerdem wurden neue Ergebnisse zur chemischen Zusammensetzung von Wolkenpartikelresiduen in der tropischen oberen Troposphäre gewonnen.

ABSTRACT

The Amazon basin serves as one of the largest ecosystems, providing remote and mostly natural conditions. In this context, airborne measurements were conducted in the scope of a field campaign above the Amazon rainforest at altitudes up to 14 km. Quantitative chemical composition measurements of out-of-cloud aerosol particles as well as of cloud particle residuals (CPR) in the size range of 40-800 nm were analysed in this thesis. The in-situ data were obtained using a compact time-of-flight aerosol mass spectrometer (C-ToF-AMS). Besides the chemical composition of submicron aerosol, the focus is on secondary organic aerosol (SOA) and different formation pathways of SOA occurring in the Amazonian atmosphere.

The out-of-cloud aerosol consisted at all altitudes predominantly of organics. The highest aerosol mass concentrations were found in the lower troposphere (0.1 - 4.5 km, LT) decreasing at higher altitudes. However, organic and nitrate mass concentrations showed enhanced values in the upper troposphere (8 - 14 km, UT). The organic aerosol was highly oxidized in the LT, whereas a lower oxidation state was found for the organics measured in the UT. These findings are explained by SOA formation in the UT and supported by aerosol size distribution measurements.

One significant contributor to the organic aerosol composition in the LT (10 %) as well as in the UT (20 %) was identified as isoprene-epoxydiol secondary organic aerosol (IEPOX-SOA). A ubiquitous occurrence of IEPOX-SOA was found at all altitudes and can be explained with the abundance of isoprene, the precursor gas of this compound emitted by vegetation. The formation pathway of IEPOX-SOA depends on the aerosol acidity as the condensation of gaseous isoprene epoxydiols (IEPOX) is favoured on acidic surfaces. Indeed, the aerosol particles observed in the UT were acidic. The increased values of nitrate suggested that the acidic conditions can be provided not only by sulfate but also by nitrate resulting in the formation of organic nitrates.

Taken together, the formation of SOA is an important process in the Amazonian atmosphere affecting the aerosol properties at low and high altitudes. For the first time, airborne measurements of a C-ToF-AMS coupled with the aircraft inlet system HALO counterflow virtual impactor (HALO-CVI) were conducted during the same field campaign at altitudes up to 14 km, allowing the investigation of CPR especially in the UT. The measurements included liquid and ice clouds. The CPR sampled in liquid clouds consisted mainly of organics (70 %), whereas the inorganics were dominated by sulfate. In contrast, organics contributed up to 95 % to the ice cloud residuals. Whereas the

CPR of liquid clouds consisted of oxidized, most likely secondary organic matter, the ice residuals consisted of primarily emitted hydrocarbon-like organic aerosol (HOA). It seems that the HOA-containing CPR in the UT acted as ice nucleating particles (INP), while the CPR consisting of oxygenated organic aerosol (OOA), sulfate and nitrate were activated in the LT as cloud condensation nuclei (CCN) and removed by wet deposition. The freezing process in the observed ice clouds appears to be dominated by heterogeneous freezing induced by vertically transported HOA-containing particles and thus affecting aerosol-cloud-interactions.

This study offers valuable insights into formation processes of SOA in the pristine Amazonian atmosphere regarding IEPOX-SOA and organic nitrates, as well as provides new findings of the composition of CPR in the tropical upper troposphere.

CONTENTS

Part I

THESIS

1

INTRODUCTION

1.1 MOTIVATION

Aerosol with its different properties affect the Earth's climate permanently. Especially in today's changing conditions due to increasing anthropogenic influence on the atmospheric composition it is crucial to understand processes that would proceed in a pre-industrial atmosphere. Such conditions are rare to find on Earth, but the Amazon rainforest is partly still in its natural state and offers a green laboratory to investigate the undisturbed atmosphere.

Aerosol, suspended solid or liquid particulate matter in air, can either be emitted directly (primary aerosol) or formed in the atmosphere (secondary aerosol) via chemical processing of precursor gases. Different size ranges (a few nm to several µm) and different compositions of aerosol particles show that various sources and processes influence their properties. Primary aerosol particles are e.g., mineral dust, sea salt or black carbon (BC), whereas secondary aerosol consists of non-sea-salt sulfate, nitrate or ammonium. Organic aerosol originates from both primary (primary organic aerosol (POA)) and secondary (secondary organic aerosol (SOA)) sources and are influenced by anthropogenic and natural emissions (Boucher et al., 2013a).

Composition measurements of aerosol particles smaller than 10 µm show the various prevalence of seven major components for different regions in the world (see Fig. 1). Here, the aerosol is divided into sulfate, organic carbon, nitrate, ammonium, elemental carbon, mineral and sea salt. In several rural and urban regions around the world organic aerosol plays a major role due to its high contribution to the aerosol composition (see Fig. 1). For particles smaller than 1 µm a substantial fraction consists also of organic material (e.g., Kanakidou et al., 2005; Murphy et al., 2006; Zhang et al., 2007b; Jimenez et al., 2009; Hallquist et al., 2009; Shrivastava et al., 2017). From model studies it is suggested that under certain conditions the main fraction of the sub-micron organic aerosol origins from secondary organic aerosol (SOA). For the Amazon basin in South America up to 90 % of the aerosol mass for sub-micron particles can be attributed to organic material (e.g. Artaxo et al., 1990; Andreae and Crutzen, 1997; Martin et al., 2010; Artaxo et al., 2013; Martin et al., 2016). On the surface SOA can explain up to 20 % of the organic fraction in the Amazon basin (see Fig. 2), whereas in the upper troposphere (UT) above the Amazon basin almost 90 % of organic aerosol (OA) can be attributed to SOA (Kanakidou et al., 2005).

Secondary aerosol in general is formed via chemical processing of atmospheric

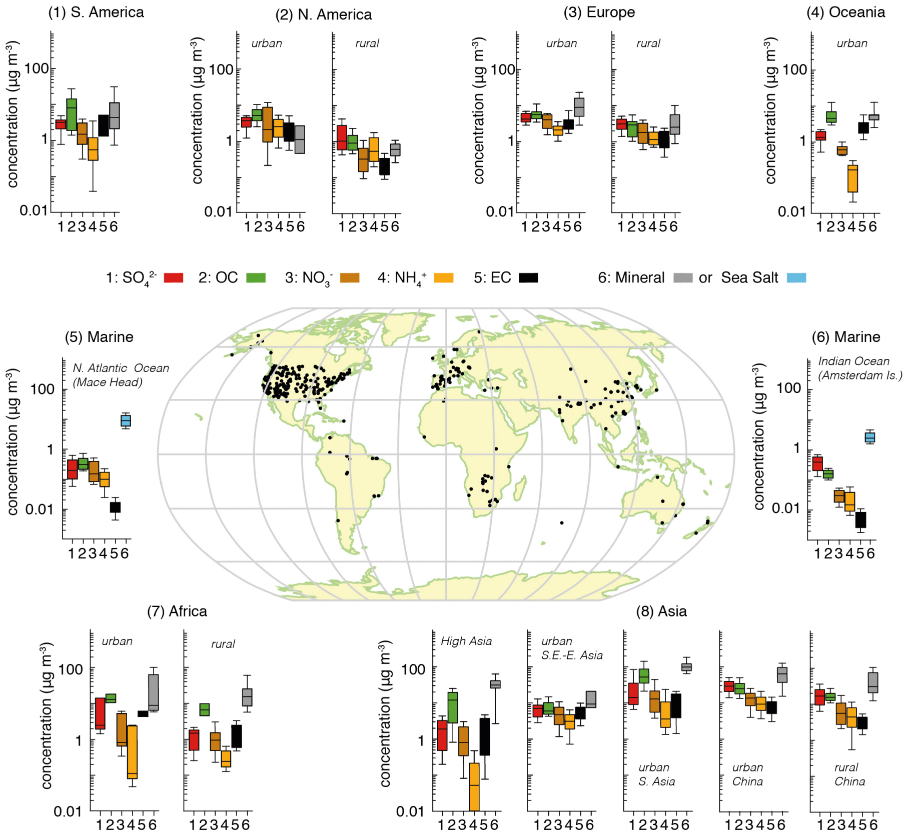

Figure 1: Mass concentrations of aerosol particles smaller than 10 µm for seven major components, measured at different sites around the world. This figure is taken from Boucher et al. (2013b).

precursor gases. Therefore, the volatility of these compounds is important. Due to the oxidation with hydroxide (OH), ozone (O_3) and other oxidants such as nitrate radicals (NO_3) the volatility decreases and the solubility of the gases increases (e.g., Jimenez et al., 2009; Drewnick, 2012; Shrivastava et al., 2017). The processes leading to secondary aerosol are various, e.g., new particle formation (NPF), condensation, coagulation or chemical reaction in the aqueous phase (e.g., Boucher et al., 2013a; Shrivastava et al., 2017).

NPF describes the nucleation of stable molecular clusters out of low-volatility vapours and the subsequent rapid growth of these clusters to nanometer-sized aerosol particles. The more dominant process of the conversion of low-volatility vapours to aerosol particles is the condensation onto pre-existing particles (Boucher et al., 2013a). Directly linked thereto is the particle growth.

Besides NPF and condensation, aerosol particles can experience coagulation. Thereby, particles collide with other aerosol particles and stick to them. This is especially important in the sub-micrometer range and has an influence on the internal mixing state of aerosol particles.

Aqueous phase reactions can occur in clouds producing SOA, often from wa-

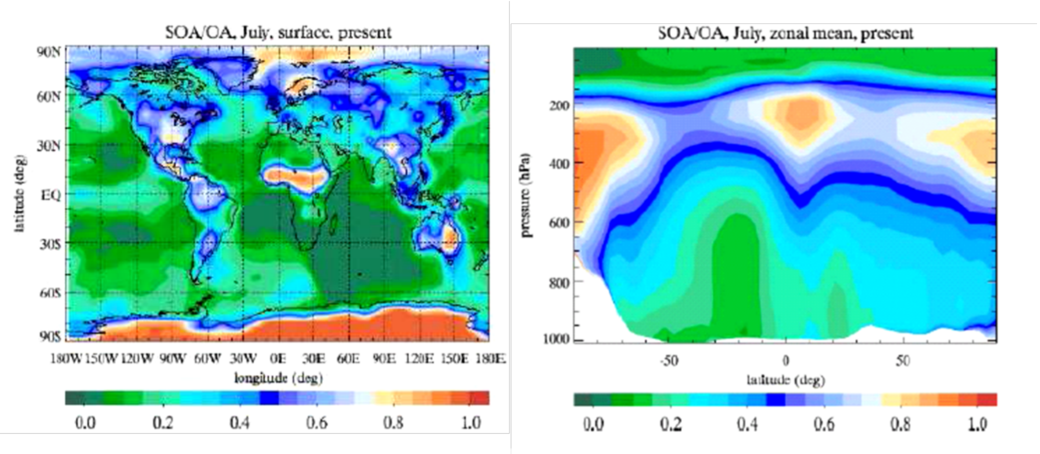

Figure 2: Ratio of SOA to OA computed by a global chemistry transport model for July for the surface (left panel) and zonal mean distribution (right panel) (Tsigaridis and Kanakidou, 2003; Kanakidou et al., 2005).

ter soluble compounds dissolved in the aqueous phase and further oxidation (e.g., Ervens et al., 2011; Shrivastava et al., 2017). The different processes showing the importance of SOA are summarized in Fig. 3.
Several processes make aerosol particles and especially SOA to an important factor regarding the impact on climate. Aerosol in general can influence the climate with two effects, aerosol-radiative and aerosol-cloud interactions (Boucher et al., 2013a). The first one, aerosol-radiative interactions, describes the aerosol's properties of scattering and absorbing sunlight resulting in cooling or warming the climate, respectively. The second one, aerosol-cloud interactions, summarizes the ability of aerosol particles to act as cloud condensation nuclei (CCN) and ice nucleating particles (INP), such that cloud droplets or ice particles can form, and cloud properties are affected (see Fig. 3). As SOA represent a high contribution to sub-micrometer aerosol particles, properties and the effects of SOA are of strong interest in current research.

1.2 SECONDARY ORGANIC AEROSOL IN THE AMAZON REGION (partly adapted from Schulz et al. (2018))

The Amazon region provides one of the most pristine continental area that allows to study pre-industrial atmospheric conditions and processes (Artaxo et al., 2013). The Amazon acts as a large source of volatile organic compounds (VOCs) that are emitted by the vegetation, and SOA is the major contributor to the aerosol composition (e.g., Zhang et al., 2007b; Hallquist et al., 2009; Jimenez et al., 2009; Martin et al., 2010; Shrivastava et al., 2017). One important VOC is isoprene (C_5H_8, 2-methyl-1,3-butadiene), the most abundant non-methane VOC, with a global emission rate of ~500 $\mathrm{Tg\,y^{-1}}$

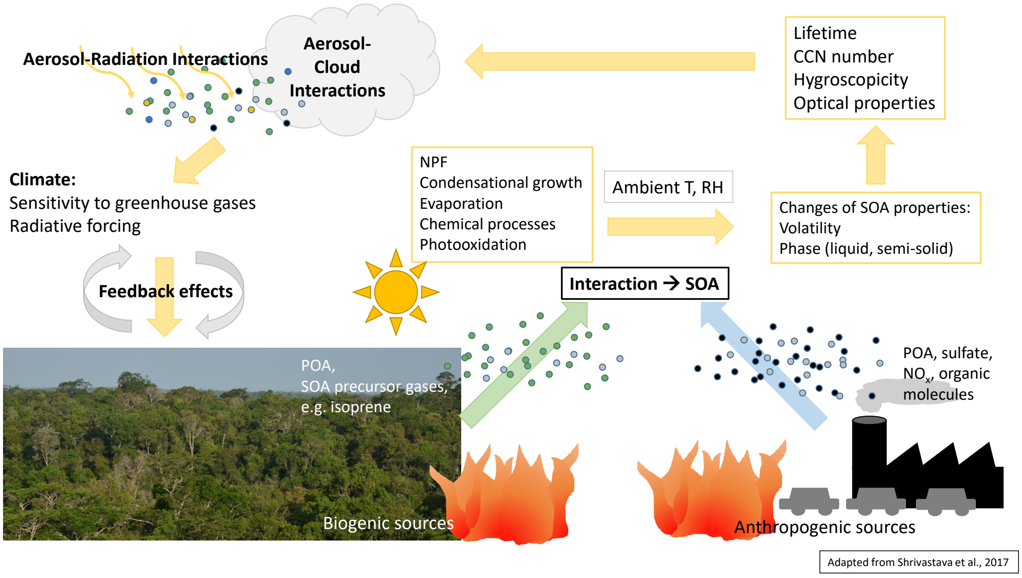

Figure 3: Overview of sources, pathways and processes influencing SOA properties and further affecting climate relevant processes (adapted from Shrivastava et al. (2017)).

(Guenther et al., 2012). Isoprene is a short-lived atmospheric gas, which is oxidized in the atmosphere by reactions with OH, O_3 or NO_3. OH-initiated oxidation leads to isoprene peroxide radicals (ISOPOO). Depending on the concentrations of nitrogen oxide radicals (NO_x) and hydrogen oxide radicals (HO_x), ISOPOO can react further through different pathways. An overview of the reaction pathways is given in Fig. 4 and explained in the following.

For HO_x dominant conditions, meaning conditions with low amounts (< 1 ppb) of nitric oxide (NO) (Wennberg, 2013), ISOPOO will mainly react with hydroperoxyl radicals (HO_2) to the intermediate oligomer isoprene hydroxy hydroperoxides (ISOPOOH). Further oxidation of ISOPOOH may lead to isoprene epoxydiols (IEPOX), which then can partition into the particle phase by condensation or reactive uptake and thus, SOA derived from IEPOX (isoprene-epoxydiol secondary organic aerosol (IEPOX-SOA)) can be formed (e.g., Claeys et al., 2004; Carlton et al., 2009; Paulot et al., 2009; Surratt et al., 2010; Lin et al., 2012; Budisulistiorini et al., 2013; Worton et al., 2013; St. Clair et al., 2016; Liu et al., 2016b). Laboratory studies demonstrate that around 50 % of isoprene-derived particulate matter is associated with IEPOX production and uptake through the HO_2 pathway and in the presence of acidic aerosol particles (Liu et al., 2015). The existence of aerosol as seed particles seems to be necessary (Surratt et al., 2010; Lin et al., 2012), but also the acidity of aerosol can influence the formation yield of IEPOX-SOA. Laboratory and field studies found a correlation between IEPOX-SOA and sulfate, which is related to the acidity of aerosol (Surratt et al., 2007; Bud-

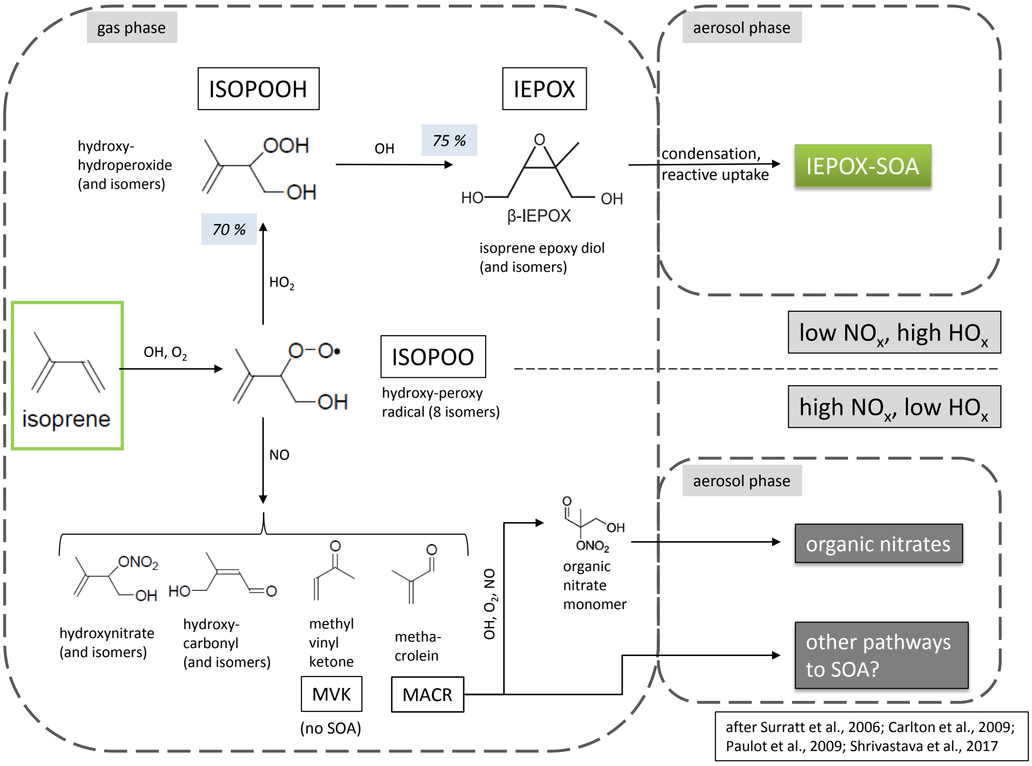

Figure 4: Possible chemical reaction ways of isoprene.

isulistiorini et al., 2013). Although the IEPOX pathway is considered as the dominant one, further laboratory studies show that also other gas-phase reactions of ISOPOOH with multifunctional hydroperoxides contribute to the formation of isoprene-derived SOA (e.g., Krechmer et al., 2015; Liu et al., 2016b; Riva et al., 2016).

A different oxidation pathway occurs at increased NO concentrations (>1 ppb) in NO dominant conditions (Wennberg, 2013). Reaction pathways for ISOPOO change towards reactions with NO instead of HO_2, leading to hydroxynitrates and/or hydroxyalkoxy radicals, which decompose further to methacrolein (MACR) and methyl vinyl ketone (MVK). Whereas MACR is a precursor for isoprene-derived SOA, MVK has almost no SOA contribution (Surratt et al., 2006; Liu et al., 2016a).

In the central Amazon region, both HO_2 and NO dominated conditions were observed dependent on the time and location of measurements (Kuhn et al., 2010; Andreae et al., 2015; Martin et al., 2016). Thus, isoprene can undergo different gas-phase reactions depending on several conditions, leading either to IEPOX-SOA or to other types of isoprene-derived SOA. Some of these conditions are anthropogenically influenced and disturb the natural balance resulting in partly severe consequences on Earth's climate.

Besides isoprene as an important source for SOA, also the chemical processing of other VOCs and the following conversion into particles contribute to the chemical composition of SOA in the Amazon region (e.g., Kroll and Seinfeld, 2008; Martin et al., 2010). SOA from biomass burning (BB) provide a substantial fraction of aerosol composition especially during the dry season (e.g Andreae and Andreae, 1988; Martin et al., 2010; Artaxo et al., 2013; Allan et al., 2014; Martin et al., 2016). The BB impact can derive from forest or agricultural fires in the Amazon basin, but also long-range transported air mass from BB sites in Africa affects aerosol properties in the Amazon (Capes et al., 2008; Chen et al., 2009).

Another recent research topic is the presence of organic nitrates and sulfates. Oxidation of VOCs with the highly reactive NO_3 can lead to different nitrogen-containing oxidation products that can partition to the aerosol-phase (e.g., Kroll and Seinfeld, 2008; Shrivastava et al., 2017). The nitrate radical oxidation of VOCs can contribute up to 20 % of the global VOC oxidation and is supposed to increase the aerosol mass significantly (Boyd et al., 2015). Polluted urban regions are often dominated by inorganic nitrates (Farmer et al., 2010). However, in rural forested areas a dominance of particulate organic nitrates formed from oxidation of monoterpenes was reported (Fry et al., 2013). A recent study from the Amazon showed with measurements at ground level that up to 87 % of the total nitrate can be attributed to organic nitrate (de Sá et al., 2018). Field measurements have shown that the major aerosol-phase product of monoterpene oxidation with nitrate radical is likely a hydroperoxy nitrate ($C_{10}H_{17}NO_5$) whereas the analogous isoprene oxidation product has a contribution of less than 1 % of the total organic nitrate and occurs more in gas phase (Ayres et al., 2015).

Organic sulfates also contribute to SOA. Sulfur-containing compounds from natural and anthropogenic sources can take part in the production of organic sulfates together with VOCs like isoprene (Paulot et al., 2009; Froyd et al., 2010b; Shrivastava et al., 2017).

Most of these findings were found out during ground or aircraft measurements in the (planetary) boundary layer (BL). Very few measurements at altitudes higher than the BL were reported. In the tropical free troposphere up to the tropopause region sulfate-containing SOA is present, for altitudes between 5 and 10 km also isoprene-derived organic sulfates were identified (Froyd et al., 2009, 2010b). In general, the tropical troposphere contains besides primary aerosol also a mixture of different secondary aerosol, such as from BB emissions, and SOA derived from regional (isoprene and other VOCs) and transported source gases (e.g., Froyd et al., 2009; Martin et al., 2010; Allan et al., 2014; Andreae et al., 2018).

The presence of SOA in the tropical upper troposphere can have different effects. For example, it can be entrained into the tropical transition layer (TTL) from where further slow, radiatively-driven lifting could transport them into the lower stratosphere (Fueglistaler et al., 2009). There, and in the TTL region of enhanced NPF near the tropopause, the SOA could become part of the global tropical layer of elevated sub-micron particle abundances (Bormann et al., 2010; Weigel et al., 2011). It has also been suggested that aerosol formation in the upper troposphere can provide a source for CCN for lower altitudes in the Amazon region (Wang et al., 2016a; Andreae et al., 2018).

1.3 THE ROLE OF CLOUDS FOR SECONDARY ORGANIC AEROSOL

Due to cloud processing (e.g., scavenging, condensation and/or evaporation of the water phase) and aqueous phase chemistry in clouds the number concentration, chemical composition, size and mixing state of the residual particles can change compared to the state before the aerosol was in a cloud (e.g., Boucher et al., 2013a; Shrivastava et al., 2017). Aerosol particles can be cloud-active and act as a CCN or INP. In the presence of sufficient water supersaturation CCNs are activated and grow to droplet size, influencing clouds properties (Seinfeld and Pandis, 2006; Rosenfeld et al., 2008; Rosenfeld et al., 2014). The availability to act as a CCN is described by the Köhler theory, which combines the Raoult and the Kelvin effect (Köhler, 1936; Farmer et al., 2015). Both effects determine the vapour pressure over an aqueous solution droplet. The Kelvin effect tends to increase the vapour pressure, whereas the Rauolt effect, also described as solute effect, tends to decrease the vapour pressure (Seinfeld and Pandis, 2006). With increasing relative humidity values aerosol particles take up water. If the critical supersaturation and diameter is reached, the aerosol particle will be activated as CCN. This process is dependent on particle size and composition. However, particle size is thought to play the more important role (Dusek et al., 2006). Larger particles need less supersaturation to be activated compared to smaller ones (Boucher et al., 2013a). Whereas particles bigger than 200 nm often consist of sufficient soluble substances to be activated under atmospheric conditions, particles below 40 nm are often too small for being activated (Shrivastava et al., 2017). Particles with a diameter between 40 and 200 nm need to experience growing mechanism, e.g. condensation, to act as CCN. Low-volatile organic compounds are of great importance for growing small particles to CCN-active sizes (e.g., Riipinen et al., 2012; Mei et al., 2013; Levin et al., 2014).

During the lifetime of a CCN of about one week, it experiences up to 10 cloud activation and evaporation cycles before it is removed, most likely by precipitation (Seinfeld and Pandis, 2006).

Although clouds are a net sink for aerosol due to wet deposition (precipitation) and scavenging in general, some clouds also can produce aerosol (Andreae et al., 2018). Dissipating clouds lead to the oxidation of water-soluble organics to produce SOA precursors (e.g., Zhang et al., 2004; Carlton et al., 2007; Lim et al., 2010; Liu et al., 2012). Laboratory studies showed that especially carbonyl compounds lead to carboxylic acids as oxidation products in aqueous-phase reactions, which then can result in SOA formation (Carlton et al., 2007; Ervens et al., 2011). Also isoprene and NO_x photooxidation can generate SOA during cloud evaporation or cloud condensation processes (Brégonzio-Rozier et al., 2016). Changing the liquid water content of cloud droplets or aqueous aerosol may lead to different partitioning of organic oxidation compounds to the gas and particle phase (Daumit et al., 2014). This could also be important when looking at clouds at different altitudes representing liquid, ice or mixed-phased clouds with varying liquid water content. Results of some field studies suggest high aqueous SOA production, whereas other field campaigns show little deviation in the organic amount between cloud residual particles and interstitial (non-activated) aerosol (e.g., Sorooshian et al., 2010; Shrivastava et al., 2013; Sullivan et al., 2016). Some mountaintop field studies found highest mass concentrations of organics and nitrate in cloud particle residuals (Drewnick et al., 2007; Schneider et al., 2017). In another field study mainly organic acids and oxygenated species were identified in cloud particle residuals compared to out-of-cloud aerosol (Sorooshian et al., 2010, 2013). In general, cloud water oxidation of water soluble organic compounds is a feasible pathway of SOA formation.

Besides the formation of SOA also the condensation of organic compounds can influence the ability of an aerosol particle to act as a CCN or an INP. The addition of soluble organic compounds is supposed to increase the CCN properties (Henning et al., 2014; Asa-Awuku et al., 2015). Whereas SOA-coated dust particles show a reduced INP-ability, glassy SOA at low temperatures is supposed to act as effective INP (Möhler et al., 2008; Berkemeier et al., 2014).

An overview of the different mechanisms of aerosol-cloud interactions is given in Fig. 5.

1.4 KNOWLEDGE GAPS

It is now well established that aerosol and clouds have an impact on climate and also interact with each other (e.g., Boucher et al., 2013a). However, some mechanisms regarding SOA are still not fully understood, e.g., formation and growth of SOA in and out of clouds, transportation pathways of aerosol leading to different climate impacts on different places on Earth, the SOA-forming potential of BB plumes or the influence of low temperatures (atmospherically relevant at higher altitudes in the troposphere) on the volatility of SOA precursor gases (e.g., Kanakidou et al., 2005; Carlton et al., 2009; Riipinen et al., 2012; Boucher et al., 2013a; Pandis et al., 2013; Wang et al., 2016a; Shiraiwa et al., 2017; Shrivastava et al., 2017; Andreae et al., 2018).

The knowledge of the pre-industrial atmosphere is crucial in order to char-

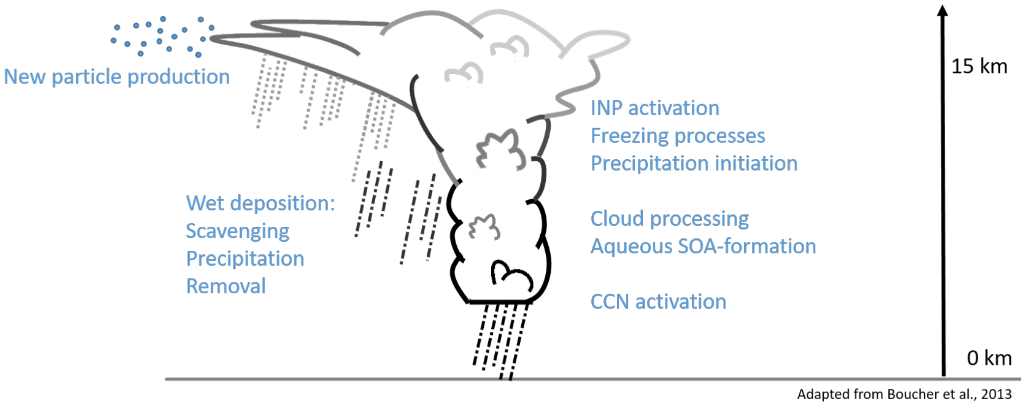

Figure 5: Scheme of primary processes affecting aerosol-cloud interactions. This figure is adapted from Boucher et al. (2013a).

acterize climate change. One of the last places on Earth to study the natural atmosphere is the Amazon as it represents a source of biogenic VOCs, which are fundamental for SOA, and is a place of high oxidation potential due to high solar radiation. Nevertheless, influences of urban plumes and biomass burning, caused both naturally and anthropogenically, change the Amazonian atmosphere. Recent campaigns focus on different aspects of the characteristics of the Amazonian atmosphere, e.g. VOC emissions, aerosol formation pathways and sources, the impact of long-range transport, anthropogenic influences, and cloud processes. However, the occurring processes and interactions of VOC, aerosol particles and clouds are complex and need further research.

1.5 STRUCTURE OF THE THESIS

The major objective of this thesis is the investigation of SOA in the Amazon region. For this, data were obtained using an aerosol mass spectrometer during the aircraft measurement campaign Aerosol, Cloud, Precipitation, and Radiation Interactions and Dynamics of Convective Cloud Systems - Cloud Processes of the Main Precipitation Systems in Brazil: A Contribution to Cloud Resolving Modeling and to the GPM (Global Precipitation Measurement) (ACRIDICON-CHUVA) and analysed. The current chapter introduces the topic. Chapter 2 includes the explanation of the aerosol mass spectrometer, results from laboratory measurements for a newly designed inlet system, as well as the explanation of software related tools, i.e. the data evaluation methods and the determination of the detection limit (DL). Furthermore, complementary data that are used for the evaluation are presented and explained shortly. Chapter 3 describes the aircraft campaign ACRIDICON-CHUVA, the meteorological conditions during the measurement time, and the measurement platform High Altitude and LOng range research aircraft (HALO). Results of the data analysis are presented in Chap. 4 with foci on SOA and cloud particle residual measurements. The last chapter of this thesis summarizes the results, draws conclusions and gives an outlook for further investigations.

2

METHODS

Instrumental as well as software deployed methods will be presented in this chapter. The instrument description will be held short due to the wide prevalence of the instrument and a large number of publications related to it. One focus is put on the newly developed inlet system for airborne measurements. In the software related section different tracer ions that are used for identifying aerosol types and four different methods to determine the detection limits (DLs) are presented. Parts of this chapter are already published in Schulz et al. (2018) and labelled when used here.

2.1 INSTRUMENTAL METHODS

2.1.1 *Compact time-of-flight aerosol mass spectrometer - measurement principle*

The compact time-of-flight aerosol mass spectrometer (C-ToF-AMS) provides quantitative information on the mass concentration (unit mass resolution) and the chemical composition of sub-micron non-refractory aerosol particles with a diameter between 40 nm and 800 nm (e.g., Drewnick et al., 2005; Canagaratna et al., 2007; Schmale et al., 2010). In the following the measurement principle will be described briefly. Further explanations can be found e.g. in Drewnick et al. (2005) and in Canagaratna et al. (2007). A scheme of the C-ToF-AMS is shown in Fig. 6.

Aerosol particles enter the C-ToF-AMS via the constant pressure inlet (CPI), which is described in detail in Sect. 2.1.2. The CPI is located upstream of an aerodynamic lens system (Liu et al., 1995a,b) that accelerates and focuses the aerosol particles into a narrow beam. Exiting the aerodynamic lens the particles enter the vacuum chamber and are accelerated according to their size, shape and density. The vacuum chamber is pumped differentially with a total of five turbo molecular pumps that are connected in a cascade system and distributed between the vacuum chamber (three pumps), the ionization region (one pump) and the mass spectrometer (one pump). With this pumping system the pressure in the ionization region is less than $3 \cdot 10^{-6}$ hPa. In the ionization region the aerosol particles are flash-vaporized on the vaporizer, i.e. a hot surface ($T = 600$ °C). The resulting gas molecules are ionized by electron impact. The temperature of the vaporizer limits the detection to non-refractory aerosol particles. Quantitative measurements of organics, nitrate, sulfate, ammonium and the non-refractory chloride are obtained,

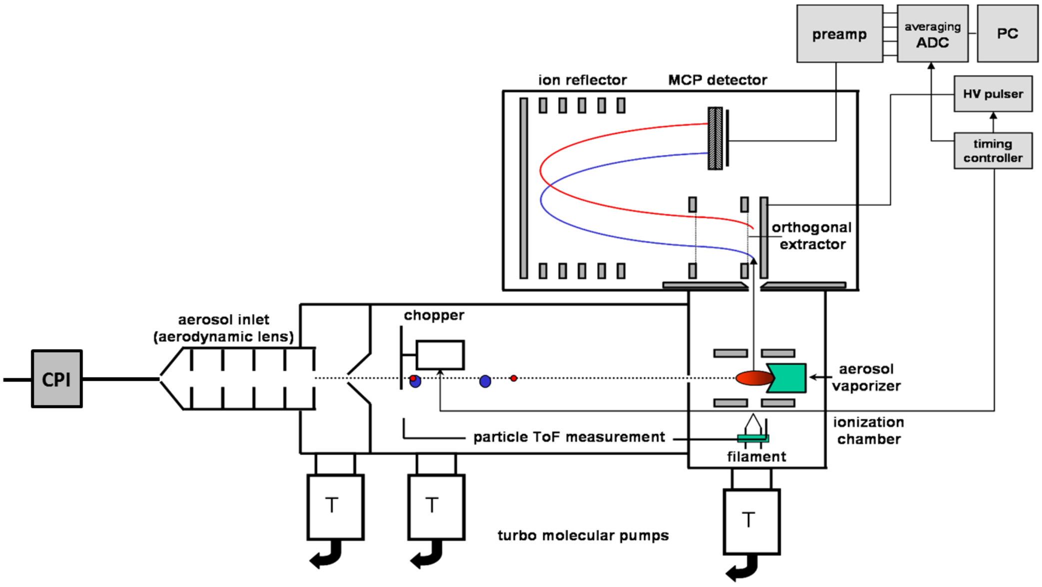

Figure 6: Scheme of the C-ToF-AMS, adapted from Drewnick et al. (2005). The constant pressure inlet (CPI) is the constant pressure inlet. Note that not all pumps are shown in this scheme.

whereas mineral dust, black carbon, sodium chloride and metals cannot be vaporized under the described conditions and are therefore not available for detection. The electrons that are responsible for the ionization are emitted continuously by a tungsten filament with an emission current of 2 mA. Via a lens system with different high voltages the ions generated from the vaporized aerosol particles are finally guided into the time-of-flight mass spectrometer (Tofwerk, Switzerland). An orthogonal extractor turns the flight path of the ions to a c-shape and a separation of the ions depending on their mass to charge ratio (m/z) occurs. A micro-channel plate (MCP) detects the ions and gives an analogue signal as an output. The conversion to a digital signal is done by a high speed acquisition card (ADC) and the data are stored by the AMS data acquisition software ToF DAQ (DeCarlo et al., 2006; Sueper and collaborators, 2018).

Measurements with a C-ToF-AMS are difference measurements between the incoming air with aerosol particles and the background in the vacuum system. The difference between the incoming air with particles and the background provides the actual signal of the particles. Therefore, background measurements must occur at time intervals shortly before or after measurements of the air with particles. This is achieved by a chopper, a metal plate located in the vacuum chamber that can be moved in and out of the particle beam by a servo motor. The chopper can be operated in three different measurement modi: open, closed, and chopped.

In the open mode the chopper is moved out of the particle beam, thus the incoming air with aerosol particles is measured and an “open” signal is provided.

For the closed mode the chopper is completely moved into the particle beam. The incoming aerosol particles hit the chopper, do not reach the vaporization/ionization region and will not be detected. In this mode the background signal (“closed”) is derived.

In the chopped mode a part of the chopper is used where two small slits enable the division of the particle beam into distinct packages. The chopper is rotating with a speed of 120 Hz. This mode is used for particle size measurements. The distance between the chopper and the ionization region is known (395 mm) and the time that aerosol particles need to overcome this distance is measured. Therefore, aerosol size information is obtained when measuring in this mode since the particle vacuum aerodynamic diameter (d_{va}) is related to the velocity of the particles.

The final difference signal is calculated by the subtraction of the “closed” from the “open” signal and is converted to an ion signal using the regularly performed single ion calibration (Hings, 2006). The conversion from the ion signal to a mass concentration is received by applying Eq. (1) (Canagaratna et al., 2007):

$$C_s = \sum_i I_{s,i} \cdot \frac{MW_{NO_3}}{IE_{NO_3} \cdot RIE_s \cdot CE} \cdot \frac{AB_{Corr} \cdot 10^{12}}{Q \cdot N_A} \text{ in } \mu\text{gm}^{-3}. \tag{1}$$

In this equation $\sum_i I_{s,i}$ describes the sum of all ion fragments of the species s per second, MW_{NO_3} the molecular mass of ammonium nitrate ($62\,\text{g}\,\text{mol}^{-1}$), IE_{NO_3} the ionization efficiency of nitrate, RIE_s the relative ionization efficiency of the species s, CE the collection efficiency, AB_{Corr} the air beam correction factor, 10^{12} a dimensionless unit conversion factor, Q the air volume sampling rate into the C-ToF-AMS (typically $\sim 1.4\,\text{cm}^3\ \text{s}^{-1}$), and N_A the Avogadro constant.

The air beam signal (AB) corresponds to the signal at $m/z\,28$ that is dominated by N_2^+ from the air. The concentration of nitrogen in air is assumed to be constant and can be used as an internal standard. Changes of the flow into the C-ToF-AMS or a reduced performance of the MCPs can lead to a decreasing signal at $m/z\,28$. Thus, a corrected air beam (AB_{Corr}) factor is used for the conversion (Allan et al., 2003). The ionization efficiency (IE) is defined as the ratio of detected ions to the parent molecules available in the ionization region. The collection efficiency (CE) is defined here as the ratio of particles entering the C-ToF-AMS and being evaporated at the vaporizer. Several effects can lower the CE. To quantify the CE, Huffman et al. (2005) introduced Eq. (2).

$$CE(d_{va}) = TE_L(d_{va}) \cdot TE_S(d_{va}) \cdot CE_B(d_{va}) \tag{2}$$

Here, TE_L describes the particle transmission efficiency through the aerodynamic lens, TE_S is the particle shape related efficiency due to a less efficient focusing of the aerodynamic lens for non-spherical particles and CE_B describes bouncing effects of primarily solid particles on the vaporizer, which reduces the fraction of vaporized particles (Huffman et al., 2005; Canagaratna et al., 2007; Liu et al., 2007). It has been shown that a CE factor of 0.5 represents ambient aerosol sampling quite well (Middlebrook et al., 2012). For laboratory measurements with ammonium nitrate particles the CE factor changes as TE_S and CE_B are equal to 1. CE is then equal to TE_L. A dependency of TE_L on the critical orifice upstream of the aerodynamic lens and on the lens system itself is known. For ground measurements the critical orifice usually has a fixed diameter. However, for aircraft operation the critical orifice was replaced by a squeezable O-ring (constant pressure inlet (CPI)) with changeable inner diameters. The dependency of the transmission efficiency on the CPI is investigated in Sect. 2.1.2.

2.1.2 *Constant pressure inlet for aircraft sampling*

For ground measurements usually a fixed critical orifice of a certain diameter (typically 100 µm for 1000 hPa) is located in front of the aerodynamic lens providing a constant volumetric flow into the C-ToF-AMS. The mass flow can be assumed constant as well, when considering that the pressure and temperature conditions are the same. However, during airborne measurements the ambient pressure will change from 1000 hPa (ground conditions) to roughly 120 hPa (15 km altitude) and thus, the mass flow will change with air density resulting in different aerodynamic lens pressures. This would lead to changing aerodynamic lens transmission efficiency (TE_L) depending on the particle diameter. Previous results show that for lower aerodynamic lens pressures the TE_L shifts to smaller particle diameters (Liu et al., 2007). Furthermore, varying the pressure in the aerodynamic lens during the same measurement period (here e.g. one flight) cause different particle velocities and accelerations within the lens and when exiting it via the nozzle (last stage of the aerodynamic lens). All this would lead to a different TE_L of the particles through the lens, a non-reproducible particle sizing and higher uncertainties in the measurements. In order to minimize these uncertainties, a custom-built inlet system was developed and replaced the fixed orifice in front of the aerodynamic lens.

One possible approach for aircraft-based measurements with a C-ToF-AMS is described in Bahreini et al. (2008) and has been used in several field campaigns (e.g., Schmale et al., 2010, 2011; Shilling et al., 2013; Brito et al., 2018). It consists of a small chamber with a critical orifice, and an additional pumping system via a bypass. This pressure controlled inlet is mounted in front of the critical orifice of the instrument. The dimensions are selected such that particle losses are minimized. Incoming air expands in the chamber and the pressure inside this chamber is controlled by variable pumping. The

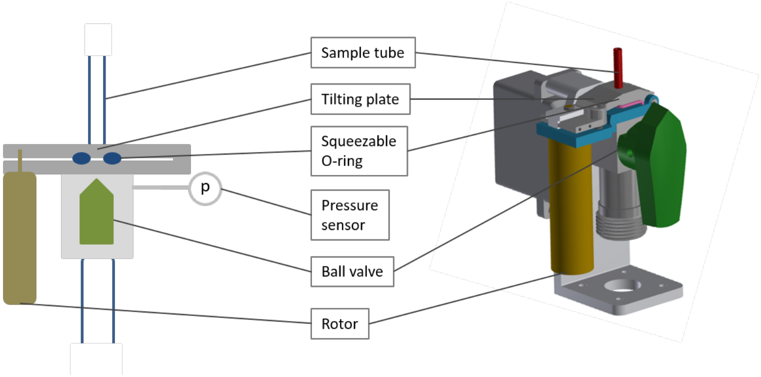

Figure 7: Scheme and technical drawing of the CPI (designed by the Instrumental Development and Electronics Department of the Max Planck Institute for Chemistry (MPIC)). Further details can be found in Molleker et al. (2019).

particle concentration becomes uniform and the sampling flow is extracted to the inlet system of the C-ToF-AMS. This system has the advantage that particle losses are negligible in the size range between 100 and 700 nm d_{va} (Bahreini et al., 2008). However, it needs an extra pump and controlling system, the dimensions are not handy for the aircraft installation and the altitude range that can be covered with this approach is only up to 6.5 km (Bahreini et al., 2008).

In contrast to the approach by Bahreini et al. (2008) the custom-made (at the Max Planck Institute for Chemistry (MPIC)) constant pressure inlet (CPI) has a compact design and consists of two plates with a flexible O-ring as the orifice in between. It is connected to a rotor (see Fig. 7). The rotor moves the plates towards or away from each other depending on the pressure in the aerodynamic lens that is measured. This results in either squeezing or relaxing the O-ring, thereby changing the orifice size and leading to a change of the volumetric flow rate into the C-ToF-AMS such that the pressure in the aerodynamic lens remains constant when the ambient pressure changes. A constant mass flow into the instrument is achieved ensuring a stable behaviour of the lens. The O-ring used for the measurements has an inner diameter of 0.8 mm when it is relaxed and consists of Viton/FKM 80. This material is characterized by a high resistance to temperature changes, chemical influences and aging processes (ERIKS GmbH, 2015). A picture of the CPI mounted in the C-ToF-AMS can be seen in Fig. 8.

Pictures of the relaxed and partly squeezed O-ring were made with the help of a microscope and a digital camera, and are shown in Fig. 9. The relaxed O-ring has a circular shape similar to the fixed orifice (see Fig. 9, panel a). However, as soon as the O-ring is squeezed, the shape is changing in a non-circular way (see Fig. 9, panel b). The change of the O-ring hole size is intended in order to provide a constant mass flow into the C-ToF-AMS at higher ambient pressures. The non-circular change of the shape is not opti-

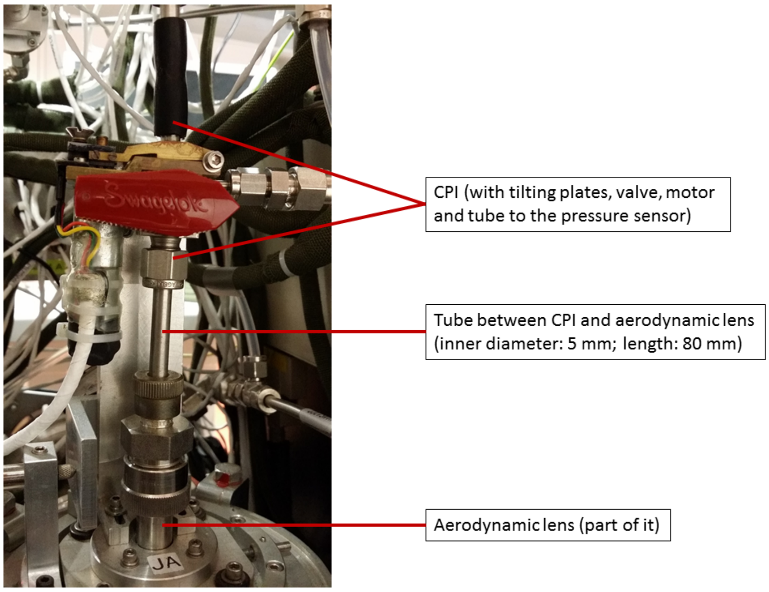

Figure 8: Picture of the CPI and the following tube to the aerodynamic lens.

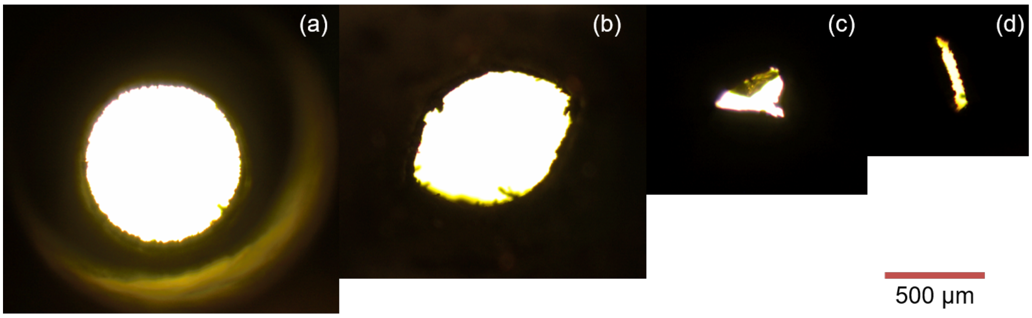

Figure 9: Pictures of the relaxed (a) and partly squeezed (b - d) O-ring taken with a camera via a microscope. The scale is given by the red line and valid for all four pictures.

mal as some losses due to impaction or turbulences could occur. Depending on the level of the squeezing the hole in the O-ring looks e.g. like a triangle (Fig. 9, panel c) or like a small slit (see Fig. 9, panel d). During taking this pictures it was not possible to adjust the level of squeezing according to different ambient pressures. Thus, it cannot be said to which extent the O-ring is squeezed at ambient pressure. In a different measurement setup colleagues at the MPIC managed to monitor the behaviour of the O-ring for different ambient pressures. For a pressure of 1000 hPa that are representative for ground measurements and the highest level of squeezing no light passed the O-ring on a straight way (personal communication: S. Molleker and O. Appel, MPIC, 2018).

When light cannot pass the O-ring at the maximal squeezing, the question arises how the particles will behave in such a system. As a consequence of a gas flow that converges or changes directions, the gas streamlines will be curvilinear and suspended particles also experience a curvilinear motion (Hinds, 1999). This can be described with the dimensionless Stokes number (Stk). The Stokes number is given in Eq. (3) and defines the ratio of the time τ it takes a particle to adjust to the time L_c/v_{gas} available for adjustment. When $Stk \gg 1$ the particles continue moving in a straight line when the gas turns. When $Stk \ll 1$ the particles will follow the gas stream (Hinds, 1999).

$$Stk = \frac{\tau \cdot v_{gas}}{L_c} \tag{3}$$

In Eq. (3) τ is the relaxation time of the particles, v_{gas} the velocity of the undisturbed gas (air) and L_c the characteristic length. The equations for calculating the gas velocity v_{gas} and the relaxation time τ are (Hinds, 1999):

$$v_{gas} = \frac{f}{A} \tag{4}$$

$$\tau = \frac{\rho \cdot d_p^2 \cdot C_c}{18 \cdot \eta} \tag{5}$$

$$C_c = 1 + \frac{2.52 \cdot \lambda}{d_p} \tag{6}$$

with f as the flow, and A as the cross section area of the tube. In Eq. (5), ρ is the particle density ($1.72\,\mathrm{g\,cm^{-3}}$ for ammonium nitrate), d_p the particle diameter, C_c the Cunningham correction factor (see Eq. 6), and η the gas viscosity ($1.82 \cdot 10^{-5}\,\mathrm{Pa\,s}$). The Cunningham correction factor C_C takes into account that the relative velocity of the gas on the surface of a particle is not equal to zero (Hinds, 1999). This correction needs to be applied for particles with a diameter less than 1 µm at standard conditions. In Eq. (6), λ is the mean free path (0.066 µm for air at 1000 hPa and 20 °C). For further explanation on the mean free path see e.g. Atkins et al. (2018).

As an example, the Stokes number of ammonium nitrate particles *upstream* of the O-ring at 1000 hPa is calculated. This calculation shows if obstacles like an O-ring would stop the particles when entering it. The particles are in equilibrium with the gas in the tube, that means:

$$v_{particle} = v_{gas} \tag{7}$$

For an assumed particle diameter of $d_p = 800\,\mathrm{nm}$ is $\tau = 4 \cdot 10^{-6}\,\mathrm{s}$. With a flow of $f = 1.4\,\mathrm{cm^3\,s^{-1}}$ and an inner tube diameter of 5 mm (6.25 mm outer diameter (1/4 inch)) is $v_{gas} = 0.07\,\mathrm{m\,s^{-1}}$.

The characteristic length L_c is set to 100 µm as this would be the diameter of a fixed orifice and representative for a pressure of $p_{lens} = 2.5\,\mathrm{mbar}$ in the aerodynamic lens. Finally, a Stokes number of $Stk = 0.0028$ is derived for this exemplary calculation. The resulting number is much smaller than 1 and means that even bigger particles with a diameter of 800 nm will follow the gas stream into the O-ring without impaction.

For an ambient pressure of 1000 hPa, the O-ring is most squeezed. The squeezing does not provide a circular shape and thus, the walls of the O-ring do not provide a plain surface. As a consequence the particles will experience shifts in their movement direction resulting in curvilinear motion in the O-ring.

Calculating the Stokes number *inside* of the O-ring remains difficult, because the characteristic length L_c is defined differently at different positions in the O-ring. Therefore, only an estimation for the upper limit can be made:

The gas velocity v_{gas} *inside* of the O-ring can be calculated using Eq. (4) with a flow of $f = 1.4\,\mathrm{cm^3\,s^{-1}}$ (the same as in the tube *upstream* of the O-ring) and a diameter of 100 µm resulting in $v_{gas} = 178.34\,\mathrm{m\,s^{-1}}$.

The distance that particles with a diameter of $d_p = 800\,\mathrm{nm}$ need to adjust to this velocity can be derived by multiplying τ and v_{gas}, which results in 710 µm, assuming the same τ ($4 \cdot 10^{-6}\,\mathrm{s}$) as in the calculation *upstream* of the O-ring. After 710 µm even bigger particles with a diameter of 800 nm are adjusted to v_{gas}, thus it can be further assumed that $v_{particle}$ is equal to v_{gas} *inside* of the O-ring.

Choosing the critical length L_c correctly is difficult as *inside* of the O-ring several curves or folds can be expected. For this calculation an equivalent critical length of 100 µm is assumed. All together, $Stk = 7$ is achieved *inside* of the O-ring, which is greater than 1 and implies that particle losses due to impaction occurs very likely in the O-ring.

The same calculation for a fixed orifice leads to $Stk = 7$, as the parameters are the same. However, in a fixed orifice no edges or folds appear in the flow stream, therefore particle losses are not expected in a fixed orifice. The assumption of a constant τ is not fully correct as the mean free path λ changes with different pressures. As the pressure *inside* the O-ring is not known, only a qualitative estimation can be made. The pressure drops down *inside* the O-ring compared to the pressure *upstream*. With decreasing pressure, λ is increasing (Atkins et al., 2018). Due to the direct proportionality of τ and λ via the Cunningham correction (see Eq. 6), τ also becomes larger and so does Stk. This supports the estimation of particle losses *inside* of the O-ring due to impaction.

Laboratory measurements were conducted to investigate this further and to determine the transmission efficiency of the squeezable O-ring. As explained in Sect. 2.1.1 the collection efficiency (CE) for ammonium nitrate particles is equal to the aerodynamic lens transmission efficiency (TE_L), which is dependent on the critical orifice upstream of the aerodynamic lens and on the lens system itself. As only the critical orifice is changed from a 100 µm fixed orifice to the squeezable orifice for the conducted measurements, the difference in the TE_L of the O-ring to the fixed orifice can be derived.

The set-up used for the measurements is given as a scheme in Fig. 10. Ammonium nitrate particles are generated with an atomizer. The polydisperse

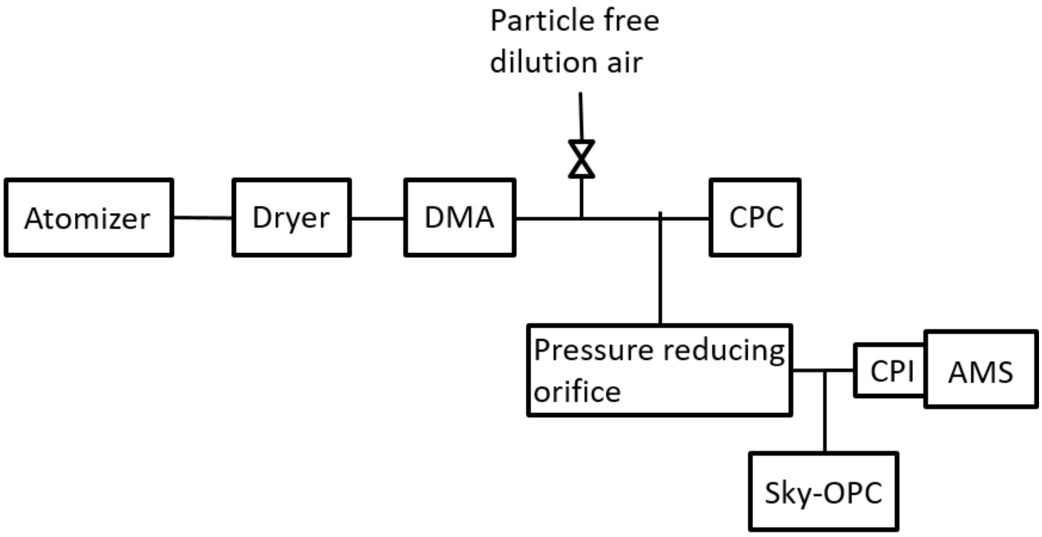

Figure 10: Set-up for measurements of the CPI characterization.

aerosol is dried with silica gel and size selected by a differential mobility diameter (DMA, TSI 3080). After passing the DMA the aerosol is monodisperse with a mobility diameter d_{mob} and the flow is divided to a condensation particle counter (CPC) (TSI 3010), a Sky optical particle counter (OPC) (GRIMM Sky-OPC 1.129) and the C-ToF-AMS. For the measurement principles of DMA, CPC and OPC the reader is referred to the literature, e.g. Kulkarni et al. (2011). Particle free air was added through a filter to provide enough flow for the different instruments. Between the actual measurements with ammonium nitrate for different ambient pressures, measurements with pure water were conducted to determine the background. Filter measurements have been done in order to test the set-up for leakages. To simulate changing ambient pressure in front of the CPI another orifice ("pressure reducing orifice" in Fig. 10) was implemented in the tubing. The used orifices to reduce the pressure had different inner diameters ranging from 0.65 mm to 0.2 mm providing a pressure range from 950 hPa to 230 hPa. This corresponds to altitudes between 0.5 km and 12 km. As a reference measurements with a fixed orifice with a diameter of 100 µm were conducted. The CPC is not applicable for measurements at lower pressure, thus an OPC was used. This limits the lower measurable particle diameter to 250 nm.

Measurements with a fixed orifice

From the measurements with the fixed orifice two resulting curves can be calculated. On the one hand, the TE_L of the C-ToF-AMS relative to the CPC for the fixed orifice and on the other hand, a comparison between the CPC and the OPC can be made. The necessary calculations including the conversion from number to mass concentration and the estimation of the un-

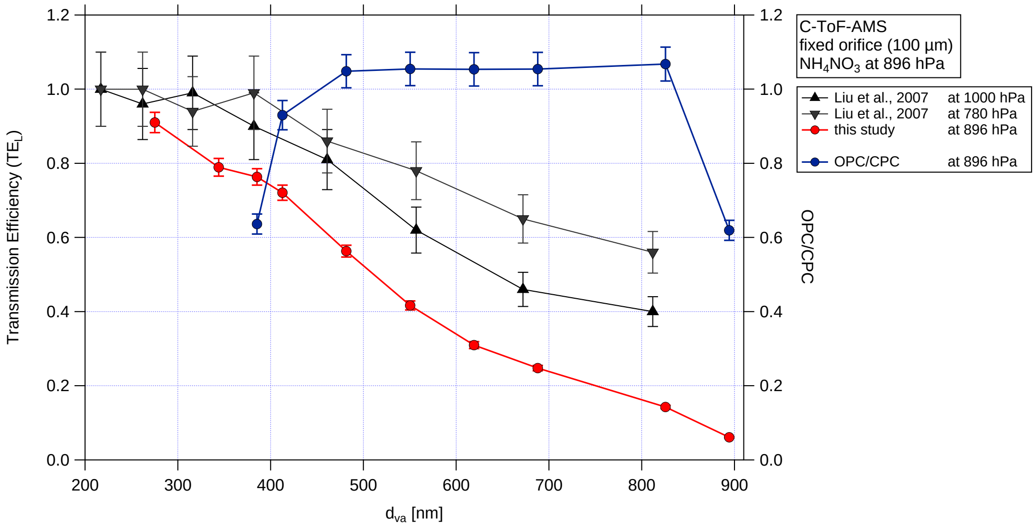

Figure 11: Transmission efficiency (TE_L) for a 100 µm fixed orifice obtained from measurements of the C-ToF-AMS to the CPC at 896 hPa (red). As a reference the calculated transmission efficiency of Liu et al. (2007) at 1000 hPa (black) and 780 hPa (dark grey) are shown. Furthermore, the ratio OPC/CPC is depicted (blue) in order to justify the use of the CPC as the reference instrument for the transmission efficiency determination.

certainties are described in Sect. A.1.

Figure 11 shows the measured TE_L of the C-ToF-AMS relative to the CPC (AMS/CPC), two transmission efficiency curves as a reference reported by Liu et al. (2007) and the comparison between the OPC and the CPC (OPC/CPC) against particle vacuum aerodynamic diameter (d_{va}). For converting the mobility diameter d_{mob} to the vacuum aerodynamic diameter d_{va}, see Sect. A.2. The comparison between the OPC and the CPC shows good agreement. For diameters between 400 nm and 800 nm the ratio is close to unity, showing that the pressure reducing orifice in the sampling line does not cause significant losses in this size range. The decreasing ratio for smaller diameters than 400 nm are due to the reduced detection at smaller particle sizes of the OPC (Grimm Aerosol Technik, 2008). The decrease for diameters larger than 800 nm could result from losses in the sampling line from the pressure reducing orifice. The size range of the OPC is reduced compared to the CPC. However, as both instruments show good agreement for the comparison measurements, the CPC is used as the reference instrument for transmission efficiency determination of the C-ToF-AMS as smaller particle diameters can be measured as well.

The aerodynamic lens transmission efficiency (TE_L) of a similar aerodynamic lens used in the C-ToF-AMS was investigated by Liu et al. (2007). The difference between the aerodynamic lens used here and the described lens is another stage ending with a smaller nozzle. This leads to a better focusing of particles with diameters less than 100 nm. As this laboratory measurements focused on particles with a diameter larger than 200 nm due to the set-up, this difference is not relevant here. The two reference curves represents the TE_L at different ambient pressures, 1000 hPa and 780 hPa, respectively (see Fig. 11). For particles with a diameter smaller than $d_{va} = 400$ nm the TE_L is above 90 %. For larger diameters TE_L is decreasing. However, the TE_L at 780 hPa is still enhanced compared to TE_L at 1000 hPa. This implies, that at higher ambient pressures (and also higher lens pressures) bigger particles are transmitted with a lower efficiency (Liu et al., 2007).

The measured TE_L for the C-ToF-AMS (AMS/CPC, red curve in Fig. 11) shows overall smaller values than the curves reported by Liu et al. (2007). As the measurements were conducted with a fixed orifice, a similar curve as the ones described by Liu et al. (2007) can be expected. The reduced ambient pressure of approx. 900 hPa would lead to a slightly enhanced TE_L compared to TE_L at 1000 hPa. Several reasons explaining the difference can be assumed. First, the pressure reducing orifice in front of the C-ToF-AMS can be responsible for the losses, especially of the bigger particles. The comparison of the CPC and the OPC showed, as already mentioned above, good agreement though. Therefore, this can be ruled out as a reason for the difference. Second, the set-up of the tubing behind the critical orifice is slightly different to the set-up described by Liu et al. (2007), where the critical orifice is connected to a valve and directly afterwards mounted to the aerodynamic lens. In the C-ToF-AMS used for this measurements a tube of 5 mm inner diameter (1/4 inch tube) and 80 mm length is between the critical orifice and the beginning of the aerodynamic lens (see Fig. 8). Furthermore, a valve is mounted directly behind the critical orifice. This set-up may lead to particle losses due to impaction, especially for bigger particles (see Fig. 4 in Liu et al. (2007)). The third reason for the difference in the TE_L could be the holding of the orifice, which is different to the one used by Liu et al. (2007) and may also lead to particle impaction. A fourth reason could be the different lens pressures in the aerodynamic lens used for this measurements and the one reported in Liu et al. (2007). The aerodynamic lens that was used here has an additional nozzle and, thus, the lens pressure is higher. Following the results shown in Liu et al. (2007), it was also confirmed that bigger particles are transmitted with a lower efficiency at higher lens pressures. However, it would be expected that a higher pressure leads to a smaller Cunningham correction factor, which also reduces the Stokes number (Hinds, 1999). Thus, the particle losses due to impaction would diminish. This is not fully understood. Taken all together, the discrepancy between the TE_L curves cannot be fully explained.

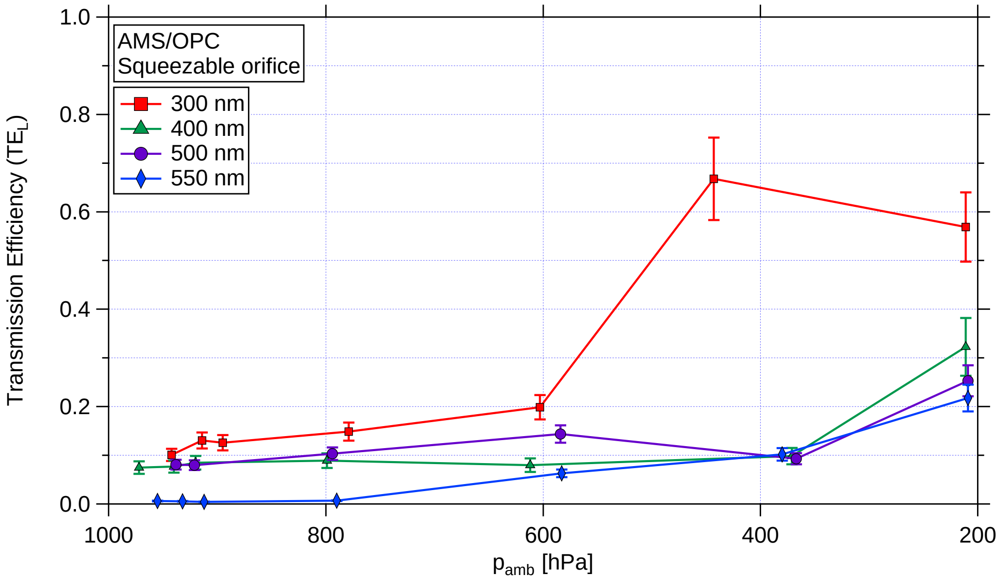

Figure 12: Transmission efficiency for the C-ToF-AMS with the squeezable orifice with respect to the OPC for different diameters and different ambient pressures.

Measurements with a squeezable orifice

Measurements with the squeezable orifice were conducted for five different ambient pressures (approximately 980 hPa, 800 hPa, 600 hPa, 400 hPa and 200 hPa). Four different sizes for d_{mob} (300 nm, 400 nm, 500 nm, and 550 nm) are used. Figure 12 depicts the TE_L for the C-ToF-AMS with the squeezable orifice with respect to the OPC for the different diameters. For all measured diameters the TE_L of the particles increases with decreasing pressure. For highest ambient pressures particles of all measured diameters show the lowest TE_L. This is due to the maximal squeezing of the O-ring at highest ambient pressure resulting in an increased Stokes number at least for bigger particles and thus, impaction of the particles in the O-ring occurs. As the ambient pressure decreases, the O-ring is less squeezed and allows a better transmission and thus, a higher TE_L. This explains the increase in the TE_L for all particle diameters for lower ambient pressures. The OPC has a reduced detection for particle diameters smaller than 400 nm (see Fig. 11). Therefore, the TE_L shown for 300 nm particles can just be taken qualitatively. The increasing TE_L at lower pressures can be attributed to a better CPI performance with an improved transmission of particles through the less squeezed O-ring. However, as there is no complete comparison between the fixed and the squeezable orifice for a larger range of particle diameters, a quantitative correction for the particle losses for different ambient pressures remains difficult. Ground-based or close to ground measurements are affected the most, but for aircraft measurements particle losses will decrease or even vanish with increasing altitude. The reduced ambient pressures that occur during aircraft measurements lead to lesser squeezing of the O-ring, especially at high altitudes. For small particles, which could not be tested with this measurement set-up, the transmission losses might be negligible. This was confirmed by comparison measurements during the ACRIDICON-CHUVA campaign between the C-ToF-AMS and a high resolution time-of-flight aerosol mass spectrometer (HR-ToF-AMS) on board of the American research aircraft G-1 using the approach described in Bahreini et al. (2008). Above 2500 m altitude both instruments show similar results (see Fig. 27 in Sect. 4.1.2.1, and Mei et al. (2019)). A general correction would still be difficult due to the non-reproducibility of the squeezing (see Köllner (2019)) and the O-ring material fatigue. An improvement of the system is ongoing work at the MPIC. The O-rings are now produced in-house and show improved properties. Especially the inner diameter of the O-ring was reduced to 0.5 mm such that the squeezing at ground ambient pressures could result in less or only few particle losses (Molleker et al., 2019).

2.2 DATA EVALUATION METHODS

Calibration procedures of the C-ToF-AMS can be found in e.g. Jayne et al. (2000), Allan et al. (2003), Hings (2006), and Kimmel (2011) and won't be explained here. For all the data presented in this study the general calibrations were performed. Before each measurement flight a single ion (SI) calibration was carried out. The flow calibration is explained in more detail in Sect. A.3.1. Several ionization efficiency (IE) calibrations were conducted with the so called brute-force single particle (BFSP) method. The applied values for IE and relative ionization efficiency (RIE) are listed in Tab. A.3.2. The data analysis was performed with IGOR Pro 6.37 (Wave Metrics) using the software SQUIRREL 1.57. Within SQUIRREL the usual m/z calibration, baseline correction and fragmentation table adjustments (Allan et al., 2004) were conducted. Further adjustments in the fragmentation table were made following Fry et al. (2018). These changes are related to influences from the organic signals on nitrate signals, and are explained in more detail in Sect. 2.2.2.

The default value of the CE implemented in the analysis software of 0.5 was used (Matthew et al., 2008; Middlebrook et al., 2012). This default value is supposed to be valid for ambient measurements. The main fraction of the measured aerosol consists of organic matter (see Ch. 4), which has no clear effect of changing the CE. Furthermore, large amounts of nitrate that would lead to a higher CE (Middlebrook et al., 2012) were not observed during the campaigns.

The time stamps of the C-ToF-AMS data are corrected for delays in the tubing between the inlet mounted on top of the fuselage of the aircraft and the C-ToF-AMS.

In the following different tracer ions that are used in the analysis to identify distinct aerosol types are presented. Furthermore, different methods to estimate the presence and amount of organic nitrates are described. The determination of the detection limits (DLs) is demonstrated by four different methods.

2.2.1 *Tracer ion analysis*

Different sources of aerosol particles can result in different mass spectra. Especially the organic part of the mass spectra can contain specific information that can be attributed to distinct sources or origins of the aerosol. One possibility to obtain a detailed analysis of the organic mass spectra is achieved by evaluating distinct tracer ions that are unique for some types of organic aerosol, e.g. for biomass burning (BB), fossil fuel combustion (FF) or secondary organic aerosol (SOA) formation from different precursor gases. In this section some of these tracer ions are introduced.

2.2.1.1 *Photochemical aging* (partly adapted from Schulz et al. (2018))

Organic aerosol can be grouped into hydrocarbon-like organic aerosol (HOA) and oxygenated organic aerosol (OOA), whereby the latter is further classified into low-volatile OOA (LV-OOA) and semi-volatile OOA (SV-OOA), recently also referred to as more oxidized OOA (MO-OOA) and less oxidized OOA (LO-OOA), respectively (e.g., Alfarra et al., 2004; Zhang et al., 2005a; Canagaratna et al., 2007; Zhang et al., 2007b; Jimenez et al., 2009; Sorooshian et al., 2010; Ng et al., 2011b; Zhang et al., 2011; Xu et al., 2015a; Ortega et al., 2016). HOA is often found in urban areas and associated with combustion exhaust and has a clearly different signal than OOA (Zhang et al., 2005a). A more detailed description of HOA is given in Sect. 2.2.1.2. OOA is ubiquitous in the atmosphere and related to oxidized organic aerosol in rural and urban areas. The mass spectrum of OOA is dominated by smaller fragments and contains only little signal above $m/z\,55$ (15 %, Zhang et al. (2005a)). The most prominent peak is at $m/z\,44$ (mostly CO_2^+, see Fig. 13). It correlates well with secondary species like O_3, sulfate and/or nitrate, and is a surrogate for SOA (Ng et al., 2011b). LV-OOA is more oxidized than SV-OOA. Whereas OOA and LV-OOA are very similar to each other the mass spectrum of SV-OOA shows a slight difference (see Fig. 13). It is suggested that areas where only OOA is identified are dominated by aged regional OOA without significant fresh SOA contributions (Ng et al., 2011b). The averaged standard mass spectra of OOA, LV-OOA and SV-OOA are presented in Fig. 13.
The oxidation state of the organic aerosol indicates the degree of photochemical aging. It can be determined using the correlation between the ratio of the

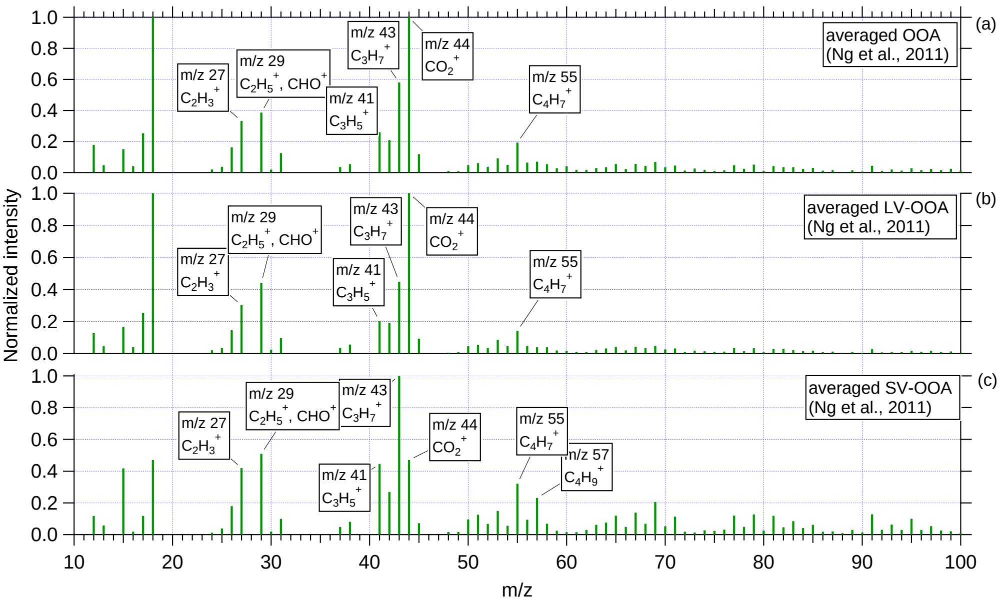

Figure 13: Normalized mass spectra of OOA (a), LV-OOA (b) and SV-OOA (c). These spectra are averaged over several data sets (Ng et al., 2011b). The individual tracer ions are labelled, respectively.

signal at $m/z\,44$ to the total organic signal, f_{44}, and the ratio of the signal at $m/z\,43$ (mostly $C_2H_3O^+$) to the total organic signal, f_{43} (Ng et al., 2010). Figure 14, panel (a) shows the exemplary scatter plot of f_{44} and f_{43}. The two dashed lines depict the range of measurements that were obtained on ground. The arrow indicates where the data points are located in this graph depending on their photooxidation state. The ratios f_{43} and f_{44} change during photochemical aging of organic aerosol, leading to higher f_{44} and lower f_{43} values for LV-OOA than SV-OOA. With increasing photochemical aging, organic aerosol of different origins become more similar in terms of chemistry (Jimenez et al., 2009).

2.2.1.2 *Biomass burning and fossil fuel combustion*

Combustion processes such as traffic, heating, power generation, but also natural and anthropogenic biomass burning (BB) forms both gaseous and particulate emissions. These combustion derived particles can contain organic, elemental and/or black carbon (BC), unburned fuel components, but also components that form during the combustion process and condense on the particles like polycyclic aromatic hydrocarbons (PAH), or can contain inorganic material like potassium or sulfur species (e.g., Rogge et al., 1998; Canagaratna et al., 2004; Schneider et al., 2005; Decesari et al., 2006).
Key tracer ions for BB organic aerosol in the C-ToF-AMS are enhanced signals at $m/z\,60$ ($C_2H_4O_2^+$) and $m/z\,73$ ($C_3H_5O_2^+$) (Schneider et al., 2006; Alfarra et al., 2007). These ions mainly arise from levoglucosan, an organic

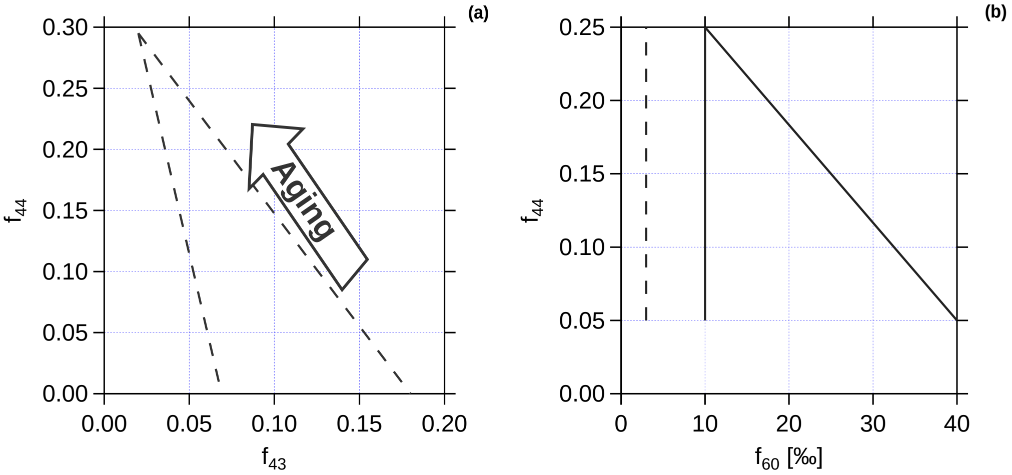

Figure 14: Example of an f_{44} vs. f_{43} (a) and f_{44} vs. f_{60} (b) scatter plot to obtain information on the photochemical aging and the biomass burning signature of organic aerosol.

molecule that forms during the pyrolysis of cellulose, which is emitted by BB sources (Simoneit et al., 1999; Schauer et al., 2001). Besides levoglucosan similar species as mannosan, galactosan and other molecules contribute to the signal at $m/z\,60$, but all of them count for a levoglucosan-like tracer for BB (Aiken et al., 2009; Lee et al., 2010; Cubison et al., 2011). A normalized spectrum of levoglucosan and a normalized averaged BB organic aerosol spectrum are depicted in Fig. 15, panel (a). The levoglucosan spectrum was achieved from laboratory measurements with levoglucosan that was dissolved in water and nebulized before analysed with a quadrupole aerosol mass spectrometer (Q-AMS) (Schneider et al., 2006). The BB spectrum was averaged from 25 data sets across Europe (Crippa et al., 2014). The tracer ions to identify BB influence are labelled.

In order to quantify the amount of BB influence on the organic aerosol the ratio f_{60} is defined as the signal at $m/z\,60$ divided by the total organic signal. A threshold value of f_{60} to define BB influenced air masses was found to be $3 \pm 0.6\,‰$ (DeCarlo et al., 2008; Docherty et al., 2008; Aiken et al., 2009). However, the tracer ion is not inert and degrades with photochemical processing due to addition of SOA and evaporation of or reaction with primary organic aerosol (POA) species (Huffman et al., 2009; Cubison et al., 2011). Furthermore, levoglucosan can be oxidized by OH resulting in chemical degradation (Hennigan et al., 2010). The scatter plot shown in Fig. 14, panel (b) illustrates the influence of photooxidation on f_{60} and was first published by Cubison et al. (2011). The threshold is shown with a vertical dashed line and organic aerosol particles influenced by BB show up in the triangle shaped area. Previous studies from laboratory measurements have reported a lifetime of f_{60} of 15 h to 10 days. However, f_{60} whilst not inert is

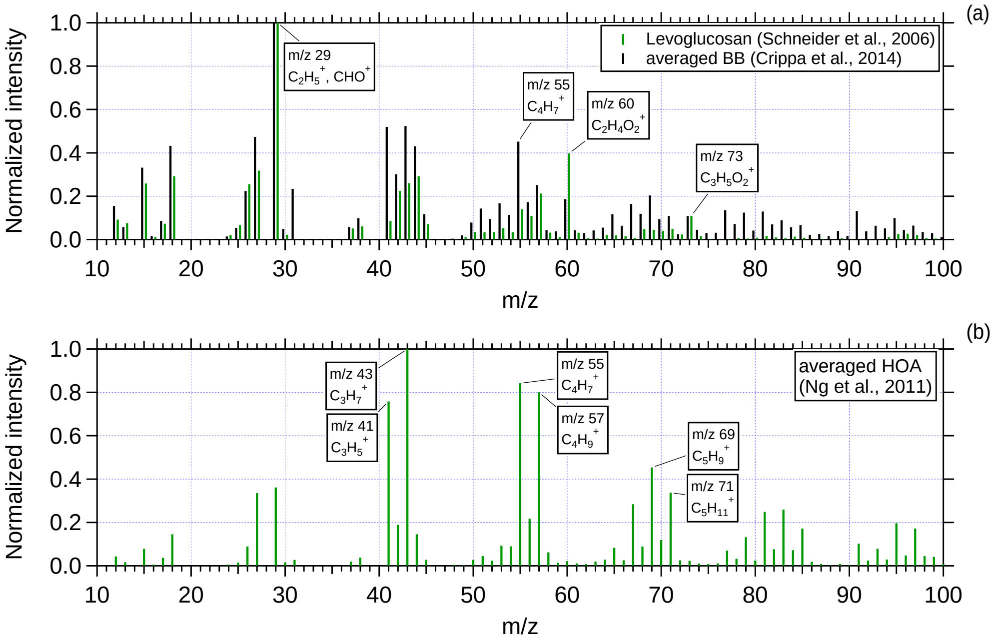

Figure 15: Panel (a): Normalized mass spectrum of levoglucosan as a tracer for biomass burning (BB) organic aerosol and a normalized averaged BB organic aerosol spectrum (Schneider et al., 2006; Crippa et al., 2014). Panel (b): Normalized mass spectrum of HOA as a representative for fossil fuel combustion (FF) organic aerosol (Ng et al., 2011b). The individual tracer ions are labelled, respectively.

still seen as a characteristic tracer to identify BB influence on organic aerosol composition (Cubison et al., 2011).

Mass spectra from fossil fuel combustion (FF) emissions are mainly characterised by ions of hydrocarbon molecules such as alkane, alkene, cyclic alkane hydrocarbons and also aromatic species (e.g., Alfarra et al., 2004; Schneider et al., 2005; Zhang et al., 2005a,c; Schneider et al., 2006; Alfarra et al., 2007; Canagaratna et al., 2007; Zhang et al., 2007b; Ulbrich et al., 2009; Ng et al., 2011b; Crippa et al., 2013). Alkane hydrocarbons fragment to a series of ions of $C_nH_{2n+1}^+$ (e.g. m/z 29, 43, 57, 71, 85, 99), alkene hydrocarbons (and also alkyl groups) show fragments at ions of $C_nH_{2n-1}^+$ (e.g. m/z 27, 41, 55, 69, 83, 97), whereas cyclic alkane hydrocarbons peaks at ions of $C_nH_{2n-3}^+$ (e.g. m/z 67, 81, 95, 107) and aromatic species show enhanced signals e.g. at m/z 77, 91, 105, 119. Typical fragment patterns of these “doubled peaks” often appear due to the difference of two hydrogen atoms. This spectrum represents a typical HOA spectrum with a pronounced ion distribution of 27 % of $C_nH_{2n+1}^+$ and 28 % of $C_nH_{2n-1}^+$ (Ng et al., 2011b) (see Fig. 15, panel b). In contrast to the mass spectrum of OOA that consists mostly of smaller fragments, 60% of the HOA signal is above m/z 55 (see Fg. 15, panel b) (Ng et al., 2011b).

As already mentioned in Sect. 2.2.1.1, the signal at $m/z\,43$ and $m/z\,44$ can be used to determine the photochemical aging of organic aerosol. In a hypothetical pure HOA spectrum $m/z\,44$ (and thus f_{44}) would be zero. In typical ambient HOA spectra the f_{44} values are very low (Ng et al., 2011b). Due to photochemical processing HOA becomes chemically more similar to OOA with an increasing distinct peak at $m/z\,44$ (Jimenez et al., 2009). Previous studies show that HOA correlates well with gas-phase combustion tracers such as carbon monoxide (CO) and NO_x (e.g., Zhang et al., 2005c; Aiken et al., 2009; Ulbrich et al., 2009).

2.2.1.3 *Isoprene epoxydiol secondary organic aerosol* (adapted from Schulz et al. (2018))

The tracer ion at $m/z\,82$ ($C_5H_6O^+$) is attributed to methylfuran and was identified to be related to IEPOX-SOA (Robinson et al., 2011). Due to thermal vaporization and subsequent electron impact ionization in the C-ToF-AMS, isoprene photooxidation products in the aerosol are decomposed and lead to an increased signal at $m/z\,82$ (Robinson et al., 2011; Lin et al., 2012). A strong correlation is found with the ion at $m/z\,53$, which corresponds to $C_4H_5^+$ (Robinson et al., 2011; Lin et al., 2012). Calculating the ratio of the signal at $m/z\,82$ to the whole organic signal leads to the fraction f_{82} (e.g., Budisulistiorini et al., 2013; Allan et al., 2014; Hu et al., 2015). This fraction is identified as a tracer only for IEPOX-SOA, not for other isoprene-derived SOA from different reaction pathways (e.g., Robinson et al., 2011; Allan et al., 2014; Hu et al., 2015). A study by Hu et al. (2015) found background values of $f_{C_5H_6O^+}$ (ratio of $C_5H_6O^+$ to the total organic signal) for different regions worldwide. For urban and BB influenced regions an averaged background value of $1.7 \pm 0.1\,‰$ is found. Areas strongly impacted by monoterpene emissions show higher averaged background values of $3.1 \pm 0.6\,‰$. For ambient organic aerosol particles that are influenced by enhanced isoprene emissions and no extensive NO emissions with presence of HO_2, a value of $6.5 \pm 2.2\,‰$ has been reported (Hu et al., 2015). This enhanced value indicates a strong IEPOX-SOA influence. All the mentioned values are derived from HR-ToF-AMS data. A C-ToF-AMS with unit mass resolution might show some interferences from other ions at $m/z\,82$, but nevertheless the tracer f_{82} is also seen as useful for identifying IEPOX-SOA (Hu et al., 2015).

Figure 16 shows the normalized, measured mass spectrum for a period with high f_{82} during flight AC13 of the ACRIDICON-CHUVA campaign (see Sect. 3.1) conducted on September 19, 2014 at an altitude of 12.6 km. The averaging time for this spectrum was one minute (15:54-15:55 UTC). The two peaks for determining IEPOX-SOA, $m/z\,82$ and $m/z\,53$, are labelled and clearly visible in the spectrum. For $m/z\,82$ and $m/z\,53$ the same *RIE*

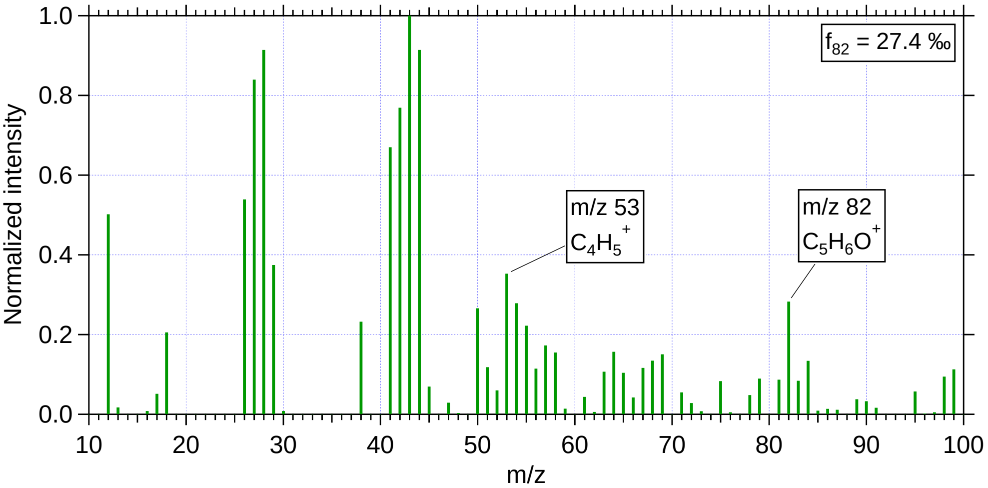

Figure 16: Normalized mass spectrum of IEPOX-SOA at an altitude of 12.6 km acquired during flight AC13 on September 19, 2014. Averaging time for this spectrum was one minute (15:54 - 15:55 UTC). The two distinct IEPOX-SOA tracers $m/z\,82$ and $m/z\,53$ are labelled. The calculated f_{82} from this mass spectrum is 27.4 ‰.

as for organics is applied (Allan et al., 2014). The calculated f_{82} from this spectrum is 27.4 ‰.

A method for the estimation of the mass concentration of IEPOX-SOA has been reported by Hu et al. (2015), see Eq. (8). For this calculation the mass concentration at $m/z\,82$ ($C_{m/z82}$), total organic mass concentration (C_{Org}), a reference f_{82} value for IEPOX-SOA ($f_{82}^{\mathrm{IEPOXSOA}}$), and a background value (f_{82}^{Bg}) are taken into account. The reference value for $f_{82}^{\mathrm{IEPOXSOA}}$ is set to 22 ‰ (Hu et al., 2015). The background value f_{82}^{Bg} can be determined with an empirical equation and depends on the influence of urban, biomass burning or strong monoterpene emissions (Hu et al., 2015). For the data set presented in this study strong monoterpene emissions are assumed and Eq. (9) is used to determine f_{82}^{Bg} according to Hu et al. (2015).

$$C_{\mathrm{IEPOX\text{–}SOA}} = \frac{C_{m/z82} - C_{\mathrm{Org}} \cdot f_{82}^{\mathrm{Bg}}}{f_{82}^{\mathrm{IEPOXSOA}} - f_{82}^{\mathrm{Bg}}} \tag{8}$$

$$f_{82}^{\mathrm{Bg}} = 0.0077 - 0.019 \cdot f_{44} \tag{9}$$

In Eq. (8), $C_{m/z82}$, and C_{Org} designate mass concentrations in units of µg m^{-3}.

2.2.2 *Estimation of organic nitrates* (partly adapted from Schulz et al. (2018))

The oxidation of VOCs with the highly reactive nitrate radical NO_3 can lead to different nitrogen-containing oxidation products (organic nitrates) that

can partition to the aerosol-phase (e.g., Kroll and Seinfeld, 2008; Shrivastava et al., 2017). The nitrate radical oxidation of VOCs can contribute up to 20 % of the global VOC oxidation and is supposed to increase the aerosol mass significantly (Boyd et al., 2015). Polluted urban regions are often dominated by inorganic nitrates (Farmer et al., 2010). However, in rural forested areas a dominance of particulate organic nitrates formed from the oxidation of monoterpenes was described (Fry et al., 2013). The oxidation of isoprene in NO dominant conditions can also lead to particulate organic nitrates (see Fig. 4 and Ng et al. (2017)). A recent ground-based study from the Amazon basin shows that up to 87 % of the total nitrate can be attributed to organic nitrate (de Sá et al., 2018).
Several studies describe that qualitative measurements and quantification of organic nitrates are of major interest (e.g., Fry et al., 2009; Bruns et al., 2010; Farmer et al., 2010; Ayres et al., 2015; Kiendler-Scharr et al., 2016; Liu et al., 2017; Schneider et al., 2017). Organic nitrates are decomposed during the evaporation and/or ionization processes in the C-ToF-AMS and therefore, divided into an organic and a nitrate signal (Farmer et al., 2010). The following use of nitrate content of organic nitrates ($RONO_2$) refers to the nitrate content of organic nitrates, as the organic content cannot be estimated with the described methods. In the following four methods to detect the presence of organic nitrates from C-ToF-AMS mass spectra are introduced.

- A first estimation of organic nitrates can be derived from the ratio of the nitrate-related ions at m/z 30 (NO^+) and m/z 46 (NO_2^+). The signal at m/z 30 is mostly from NO^+, but also the organic ion CH_2O^+ can contribute with a small amount (Allan et al., 2014). Such interferences at m/z 30 with CH_2O^+ are corrected in the evaluation software by the fragmentation table (Allan et al., 2004), but it is not possible to distinguish unambiguously between the NO^+ and the CH_2O^+ ions with a C-ToF-AMS. The signal at m/z 46 is usually dominated by NO_2^+ ions (Jimenez et al., 2003; Allan et al., 2004).
  As organic interferences on the mass spectral signals at m/z 30 (interference from CH_2O^+) and m/z 46 (interference from $CH_2O_2^+$) can occur in environments with high biogenic contribution and/or small nitrate concentrations, a correction according to Fry et al. (2018) was applied. The correction of both signals at m/z 30 and 46 is achieved by using correlated organic signals at m/z 29, 42, 43, and/or 45 derived by high resolution measurements. The organic signals at m/z 29 (CHO^+) and m/z 45 (CHO_2^+) are closest to those affected by the interference and used for the correction here. Equations 10 and 11 give the individual correction for the nitrate signal at m/z 30 and 46, respectively. The correction for NO^+ includes the total signal at m/z 30, the default fragmentation correction from the air signal (Allan et al., 2004), and a

correction coefficient that depends on the m/z used for the correction (A_i). As for $m/z\,30$ the correlated organic signal at $m/z\,29$ is used here, the organic signal at $m/z\,29$ (Org29) needs to be taken into account as well as the contribution of the isotopes of organic CO. For the correction of the nitrate fraction at $m/z\,46$ a term that includes a correlation coefficient B_i and the organic signal at $m/z\,45$ is subtracted from the signal at $m/z\,46$. The correction coefficient A_i is in this case 0.215, B_i is 0.127 (see Fry et al. (2018), Supplement). In the organic signal at $m/z\,28$, 29, 30 and 45 the RIE for organics (RIE_{Org}) is already applied and needs to be reversed for the correction of the nitrate signal.

Nitrate fraction at m/z 30 :

$$\begin{aligned}\mathrm{NO}^+ &= m/z\,30 - 0.0000136 \cdot m/z\,28 \\ &\quad - A_i \cdot (\mathrm{Org29} - 0.011 \cdot \mathrm{Org28}) \cdot RIE_{\mathrm{Org}} \\ &\quad - \mathrm{Org30} \cdot RIE_{\mathrm{Org}} \qquad (10)\end{aligned}$$

Nitrate fraction at m/z 46 :

$$\mathrm{NO}_2^+ = m/z\,46 - B_i \cdot \mathrm{Org45} \cdot RIE_{\mathrm{Org}} \qquad (11)$$

The total nitrate signal is then calculated by adding both fractions. The ratio of NO^+ to NO_2^+ is different for inorganic ammonium nitrate and organic nitrate. The ratio for inorganic nitrate is known from the IE calibration with pure ammonium nitrate. For the C-ToF-AMS used for this thesis its value lies between 1.49 and 1.56 with a mean and standard deviation value of 1.52 ± 0.03 and is derived from calibration measurements during the measurement campaign. For organic nitrates the literature presents a range of ratios of NO^+ to NO_2^+ that are higher than the ratio for inorganic nitrates, and lie between 5 and 12.5 (e.g., Fry et al., 2009; Rollins et al., 2009; Fry et al., 2011; Bruns et al., 2010; Farmer et al., 2010; Boyd et al., 2015).

- Second, a range of possible mass concentrations of particulate organic nitrate ($\mathrm{pRONO_2}$) can be determined by using C-ToF-AMS data. This range is defined with an upper and lower limit. The amount of inorganic nitrate is calculated from the neutralization with ammonium and the following subtraction from the measured nitrate.
  For the upper limit full neutralization of sulfate by ammonium is assumed and only the remaining excess ammonium is allowed to be available for the neutralization of nitrate (see Eq. 12). Resulting negative values in the first step (neutralization of sulfate) mean that not enough ammonium for full neutralization of sulfate was available and thus, these values were set to zero. In this case, nitrate could be present

as organic nitrate such that the upper limit for organic nitrate equals total measured nitrate.
For the lower limit full neutralization of nitrate is assumed by the available amount of ammonium (see Eq. 13). Resulting negative values were taken as due to statistical variation. The remaining nitrate is the lowest possible amount of organic nitrate, assuming that particulate nitric acid is not present.

$$\text{Upper Limit :}$$
$$\text{pRONO}_2^{\text{up}} = C_{\text{NO3}} - \left[\left(C_{\text{NH4}} - \frac{36}{96} \times C_{\text{SO4}}\right) \times \frac{62}{18}\right] \tag{12}$$
$$\text{Lower Limit :}$$
$$\text{pRONO}_2^{\text{low}} = C_{\text{NO3}} - \left[C_{\text{NH4}} \times \frac{62}{18}\right] \tag{13}$$

In Eq. (12) and Eq. (13) $\text{pRONO}_2^{\text{up}}$, $\text{pRONO}_2^{\text{low}}$, C_{NO3}, C_{NH4}, and C_{SO4} designate mass concentrations.

- The third possibility to estimate the mass concentration of RONO_2 comes from recent studies (Farmer et al., 2010; Kiendler-Scharr et al., 2016) (see Eq. 14). Besides the measured ratio of the mass concentrations for NO^+ to NO_2^+ (R_{ambient}), the ratio of NO^+ to NO_2^+ derived from calibrations with ammonium nitrate (R_{cal}), and a fixed value for the ratio from organic nitrates (R_{RONO_2}) are used. In this analysis a value of 10 for R_{RONO_2} was taken as described in Kiendler-Scharr et al. (2016). For a detection limit, Bruns et al. (2010) took $0.1\,\mu\text{g}\,\text{m}^{-3}$ for a conservative data evaluation of pRONO_2^{Farmer}.

$$\text{pRONO}_2^{Farmer} = C_{\text{NO3}} \times \left[\frac{(1 + R_{\text{RONO}_2}) \times (R_{\text{ambient}} - R_{\text{cal}})}{(1 + R_{\text{ambient}}) \times (R_{\text{RONO}_2} - R_{\text{cal}})}\right] \tag{14}$$

- The fourth estimation method is described by Fry et al. (2013) and links the ratios determined for inorganic and organic nitrate. The ratios of NO^+ to NO_2^+ calculated for inorganic and organic nitrate are instrument specific, but a proportional co-variation is observed. Thus, a ‘ratio of the ratios’, χ, is proposed and a value for χ of 2.25 ± 0.35 is reported.

$$\chi = \frac{R_{\text{RONO}_2}}{R_{\text{cal}}} \tag{15}$$

With this χ and the above mentioned calibration value R_{cal}, a value for R_{RONO_2} is calculated using Eq. (15). The next step puts the derived ratio for organic nitrates into Eq. (14) to determine pRONO_2^{Fry}.

It should be emphasized again, that only the mass concentration of the nitrate content of organic nitrate is determined by all of the described methods.

2.2.3 *Detection limits*

Quantitative measurements require an analysis of the detection limit (DL) to make a substantial statement about the data validity. The DL can be described as the minimum detectable absolute amount of each measured species. For low concentrations of the species it can get difficult to distinguish between an actual signal with a low intensity and the background signal (Drewnick et al., 2009). To classify a signal as significant, a DL of

$$\mathrm{DL} = \mu_b + 3 \cdot \sigma_b \tag{16}$$

is used. Here μ_b is the arithmetic mean and σ_b the standard deviation of a blank measurement (Drewnick et al., 2009). With the use of 3σ 99.7% of the normal distributed noise is suppressed.

The background signal in the C-ToF-AMS is defined by the closed measurement mode (see Sect. 2.1.1). In the following four different methods to obtain DL values will be discussed. The first two are described in detail in Drewnick et al. (2009), the third one is a self-developed method and the last one is described in detail in Reitz (2011).

2.2.3.1 *Detection limits derived from blank measurements using a filter*

The most common method to derive DLs is to use the measured mass concentration (difference signal) with a particle filter in front of the C-ToF-AMS (e.g., Bahreini et al., 2003; Zhang et al., 2005c; DeCarlo et al., 2006). Thus, only particle free air gets into the instrument and provides a blank measurement according to the definition in Sect. 2.2.3. Calculating the standard deviation σ_{Filter} from the encountered mass concentrations leads to a species-specific DL ($\mathrm{DL}_{\mathrm{Filter}}$) (see Eq. 17).

$$\mathrm{DL}_{\mathrm{Filter}} = 3 \cdot \sigma_{\mathrm{Filter}} \tag{17}$$

The obtained $\mathrm{DL}_{\mathrm{Filter}}$ are regarded to be reliable (Drewnick et al., 2009), but nevertheless this method has some disadvantages. First, taking filter measurements needs typically several tens of minutes. Interruptions during the measurement time result in missing data. In the case of aircraft measurements the measurement time is limited to the flight time, typically just some hours. Furthermore, $\mathrm{DL}_{\mathrm{Filter}}$ is dependent on actual measurement conditions during the filter and the measurement period. When these conditions change remarkably, the $\mathrm{DL}_{\mathrm{Filter}}$ might not be representative for the whole measurement period.

2.2.3.2 *Detection limits derived from the C-ToF-AMS background signal*

As described in Sect. 2.1.1 every measurement point contains information on the "open" and "closed" signal. The latter provides the background signal that can be used to conduct a continuous measurement of the DL according to Eq. (18).

$$\mathrm{DL_{BG}} = 3 \cdot \sqrt{2} \cdot \sigma_{\mathrm{BG}} \tag{18}$$

In Eq. (18) σ_{BG} describes the standard deviation of the background signal. Since the background of the "open" and the "closed" signal can reasonably assumed to be the same, the calculated difference signal has a noise of $\sqrt{2}$ times the noise of the "closed" signal. This method is widely used for C-ToF-AMS measurements (e.g., Drewnick et al., 2009; Schmale et al., 2011; Allan et al., 2014; Brito et al., 2018), but implies some disadvantages for aircraft measurements. Typically, the vacuum in the C-ToF-AMS is not preserved because power consumption is not allowed over night resulting in an enhanced background signal compared to signals after long pumping periods. Due to limited pumping time before take-off the background signal is decreasing while flying and measuring (see Fig. 17, panel a). The resulting trend of the background signal increases σ_{BG} since this method cannot distinguish between a trend and the noise. Thus, the calculated $\mathrm{DL_{BG}}$ is substantially overestimated. For ground based measurements, where the background signal has no trend, this method is applicable.

2.2.3.3 *Detection limits derived from a detrended time-dependent method*

As the main disadvantages of the former two described methods are changing background signals during aircraft measurements, a continuous method to determine the DL for each measurement point is preferred. This method consists of two steps. The first one is the detrending of the long-term signal by subtracting an exponential fit of the background signal. The second step is the consideration of the time-dependency by using a moving averaging algorithm. The background signal is highest at the beginning of the measurement period due to limiting pumping time (see Fig. 17, panel a). The decreasing trend of the background signal is eliminated with the first step of this method, whereas the actual noise is still present (see Fig. 17, panel (a)). $\mathrm{DL_{DetrendTime}}$ is determined by calculating a time dependent detection limit via a moving window and using the three sigma standard deviation (similar to Eq. 18). The moving window is defined by three values before and after a data point from the "closed" signal to calculate a moving standard deviation. The values of the calculated $\mathrm{DL_{DetrendTime}}$ vary during one flight due to the averaging window. An advantage is the continuous determination of the detection limit. However, as can be seen in Fig. 17, panel (a), not all trends can be excluded with this method. Even in the small window of seven points (= three values before and after a data point) the remaining trends lead to a significant overestimation of $\mathrm{DL}_{\mathrm{DetrendTime}}$. Thus, another method is tested.

2.2.3.4 *Detection limits derived from a cubic spline algorithm* (partly adapted from Schulz et al. (2018))

In order to further improve the DL a cubic spline function is used. This method was developed at the MPIC and is introduced and explained in more detail in Reitz (2011). For every data point of the background signal a third order polynomial (cubic) function is calculated through the four neighbouring points (two before and two behind) while omitting the actual point. Applying this method, all trends from the background signal are excluded and just the short-term noise remains. This denotes the advantage of this method compared to the above-mentioned ones. A quantity R is introduced that characterizes the statistical spread of the noise. It is defined by the squares of the deviation between the omitted centre point and the cubic function along a moving window. To relate this R to the desired $\sigma_{\mathrm{CubicSpline}}$ a proportionality factor of $\sqrt{\frac{18}{35}}$ is needed (Reitz, 2011). The exact derivation of the proportionality factor will not be explained here, but qualitatively it accounts by the fact that not only the points are affected by noise but also the cubic function itself. Thus, R is larger than $\sigma_{\mathrm{CubicSpline}}$. This calculation also provides a continuous $\sigma_{\mathrm{CubicSpline}}$ from which the $\mathrm{DL}_{\mathrm{CubicScpline}}$ can be derived using Eq. (17).

2.2.3.5 *Comparison of the different methods*

A comparison of the above-mentioned different methods to determine the DLs is illustrated in Fig. 17, panel (b). The organic mass concentrations during the flight on September 9, 2014 of the ACRIDICON-CHUVA campaign were taken as an example. The filter method is presented as $\mathrm{DL}_{\mathrm{Filter}}$. The filter measurements were taken at the end of the flight. The value of $\mathrm{DL}_{\mathrm{Filter}}$ is the lowest one for this example, but will result in an underestimation of the $\mathrm{DL}_{\mathrm{Filter}}$ for the earlier parts of the flight. The highest value is derived from the background method, $\mathrm{DL}_{\mathrm{BG}}$. The trend in the “closed” signal leads to significantly enhanced differences to the mean value as the short-term noise would cause and thus, σ_{BG} is overestimated. The long-term trend of the decreasing background signal is considered in the detrended time-dependent method and results in a much lower value for the DL than for $\mathrm{DL}_{\mathrm{BG}}$. However, some trends in the background signal cannot be excluded with this method (see Fig. 17, panel a). The cubic spline method results in similar values as $\mathrm{DL}_{\mathrm{Filter}}$, but has an individual DL value for each data point. This provides the most representative calculation of the DLs as the background is taken into account, the long-term trend is excluded, and thus, just the short-term noise accounts for the DL.

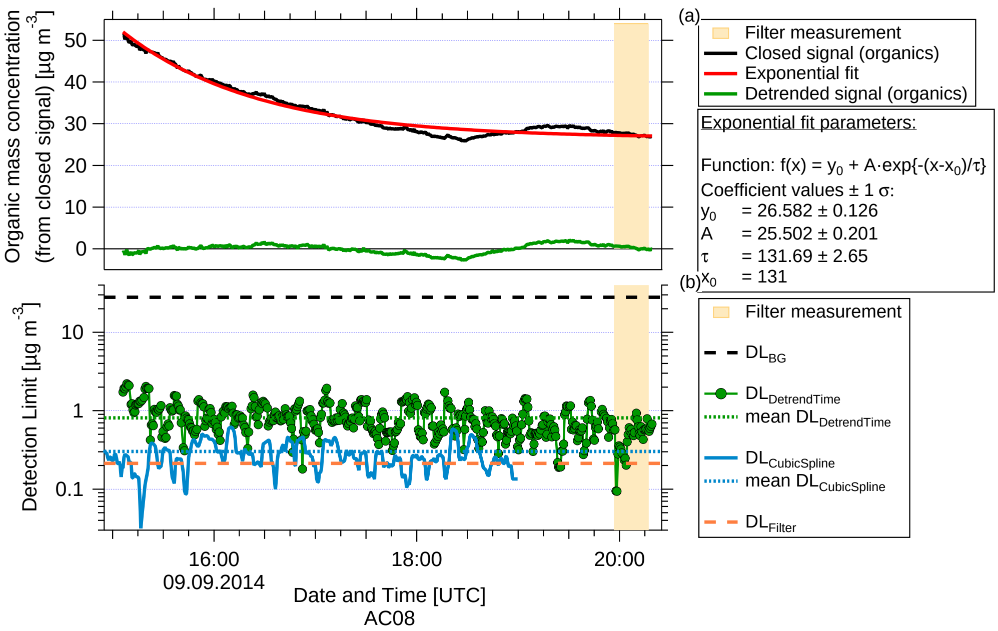

Figure 17: Panel (a): Background signal of the organic mass concentration for flight AC08 conducted on September 9, 2014 during the ACRIDICON-CHUVA campaign. The massive change in the background signal (black) is visible. The exponential fit (red) is used to detrend the background signal, which results in the detrended background for organics (green). Panel (b): Overview of the organic DLs derived with different methods for the same flight. A constant high mean value is determined using the background method ($\mathrm{DL}_{\mathrm{BG}}$). Lower DLs are obtained with the detrending time-dependent, the filter and the cubic spline method ($\mathrm{DL}_{\mathrm{DetrendTime}}$, $\mathrm{DL}_{\mathrm{Filter}}$, and $\mathrm{DL}_{\mathrm{CubicSpline}}$). The period of the filter measurement is highlighted in orange in both panels.

An overview of the DLs for all species for the flight AC08 conducted on September 9, 2014 during the ACRIDICON-CHUVA campaign is given in Tab. 1. The time resolution is 30 s. $\mathrm{DL}_{\mathrm{Filter}}$, $\mathrm{DL}_{\mathrm{DetrendTime}}$ and $\mathrm{DL}_{\mathrm{CubicSpline}}$ are similar for nitrate and chloride. For sulfate, $\mathrm{DL}_{\mathrm{DetrendTime}}$ and $\mathrm{DL}_{\mathrm{CubicSpline}}$ give similar values, whereas $\mathrm{DL}_{\mathrm{Filter}}$ is lower than both of them. $\mathrm{DL}_{\mathrm{BG}}$ is much higher than the DLs derived with the other methods for all species. For organics and ammonium the lowest DLs are derived with the filter method. However, the cubic spline algorithm represents the measurement circumstances best as it is a continuous calculation method excluding long-term trends and just regarding the noise that is responsible for the detection limit (DL).

Note, that for organics and ammonium an additional uncertainty to the derived DL needs to be considered. As there are cross-references in the fragmentation table between the gas signal and the ammonium or organics signal, corrections were applied (Allan et al., 2004). These corrections account for $m/z\,16$ ($^{16}\mathrm{O}^{+}$) for ammonium and $m/z\,44$ (CO_2^{+}) for organics, respectively,

Table 1: Examples for derived averaged DLs for all species in µg m^{-3} for flight AC08 conducted on September 9, 2014 during the ACRIDICON-CHUVA campaign. The time resolution is 30 s.

AC08 DL (µg m^{-3})	$\mathrm{DL}_{\mathrm{Filter}}$	$\mathrm{DL}_{\mathrm{BG}}$	$\mathrm{DL}_{\mathrm{DetrendTime}}$	$\mathrm{DL}_{\mathrm{CubicSpline}}$
organics	0.212	27.966	0.812	0.300
nitrate	0.040	0.725	0.042	0.041
sulfate	0.059	0.920	0.095	0.092
ammonium	0.171	3.895	0.485	0.221
chloride	0.086	0.324	0.090	0.105

and are derived usually with filter measurements and correlation plots. Deviations between different flights are determinable with this method, but deviations during one flight cannot be quantified. Thus, an upper limit of this additional uncertainty is determined and lies in the range of a few ng m^{-3}. As this uncertainty cannot be quantified exactly for every data point, this order of magnitude needs to be in mind when evaluating the data as significantly above the DL.

2.2.3.6 *Derived detection limits for the ACRIDICON-CHUVA campaign*

The detection limits (DLs) derived with the cubic spline algorithm are shown in Fig. 18. The vertical profiles show the mean mass concentrations with the standard deviation of organics (green), nitrate (blue), sulfate (red), ammonium (yellow), and chloride (pink) and the DL for each species, respectively. The values of the DLs are derived by averaging each flight and altitude bin, and divided by the amount of data points per bin. Finally, the median is calculated for all flights and shown here with their interquartile ranges. Note, that the axes for the mass concentrations are logarithmic except for chloride in order to show the smaller values of the DL in comparison with the derived mass concentrations. All averaged mass concentrations lie above the DL except ammonium at altitudes above 5 km and chloride. Thus, the chloride mass concentration is not considered in the following analysis. It lies not only below the DL, but also below 0 (see Fig. 18, panel e). The negative values for chloride possibly result from gas-phase interferences that are not corrected properly in the fragmentation table. This effect is not fully understood.

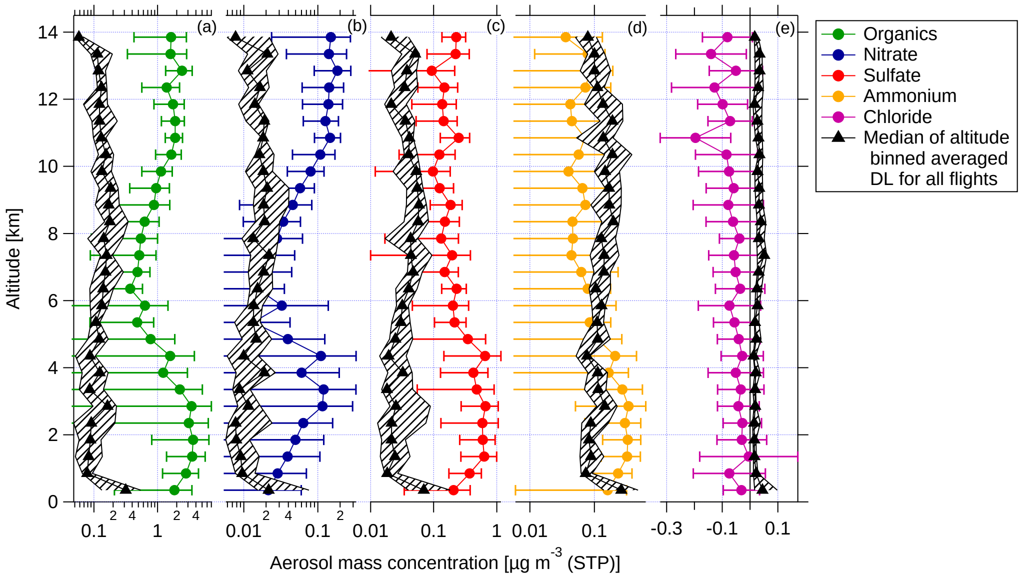

Figure 18: Vertical profile of the mean mass concentrations (coloured dots, bars represent standard deviation) and the median per altitude bin and flight averaged detection limits (black triangles, striped areas represent interquartile ranges) for all flights of the ACRIDICON-CHUVA campaign.

2.3 COMPLEMENTARY DATA

In the following short descriptions of complementary data are given. These data support the data evaluation of the ACRIDICON-CHUVA campaign in Ch. 4. Further details can be found in Wendisch et al. (2016). Most parts of this section are already published in an adapted form in Schulz et al. (2018). An overview of the used parameters is given in Tab. 2.

2.3.1 *Basic meteorological data* (adapted from Schulz et al. (2018))

Basic meteorological data were obtained from the BAsic HALO Measurement And Sensor system (BAHAMAS) at 1 s time resolution (DLR, 2018b). BAHAMAS was operated by DLR Flight Experiments (DLR-FX). This measurement system acquires data from air flow and thermodynamic sensors as well as from the aircraft avionics and a high precision inertial reference system to derive basic meteorological parameters like pressure, temperature and the 3-D wind vector as well as aircraft position and altitude. Water vapour mixing ratio and further derived humidity parameters are measured by SHARC (Sophisticated Hygrometer for Atmospheric ResearCh) based on direct absorption measurement by a tunable diode laser system. Typical absolute accuracy of the basic meteorological data is 0.5 K for temperature, 0.3 hPa for pressure, 0.4 - 0.6 $\mathrm{m\,s^{-1}}$ for wind and 5 % ± 1 ppmv for water vapour volume mixing ratio.

Table 2: Overview of parameters of different instruments, their units, measurement range, and accuracy/precision of the complementary data.

Instrument	Used parameter	Unit	Measurement range	Accuracy (A), Precision (P)
BAHAMAS	p	hPa		A: 0.3 hPa
	T	K		A: 0.5 K
	v (wind speed)	$m\,s^{-1}$		A: 0.4 - 0.6 $m\,s^{-1}$
	location	°Lat, °Lon		
	GPS altitude	m		
SHARC	RH_w	%	0 - 100 %	5 %
AMETYST	N_d	cm^{-3}	5 - 1000 nm	
SP2	rBC	$ng\,m^{-3}$	mass: 0.5 fg - 80.3 fg 65 - 510 nm	A: 10 %
AENEAS	NO, NO_y	ppb	5 ppt - 60 ppb	A: 7 % / 15 %, P: 5 % / 10 %
AMTEX	CO, O_3	ppb		A: 5 % / 10 %, P: 2 ppb / 6 ppb
NIXE-CAPS	Cloud mask			
UHSAS-A	Particle size distribution	cm^{-3}	90 - 600 nm	A: 11 %

2.3.2 *Aerosol number concentrations* (adapted from Schulz et al. (2018))

Aerosol particle number concentrations were measured using the aerosol measurement system (AMETYST). AMETYST was operated by DLR Institute of Atmospheric Physics (DLR-IPA) and includes four butanol-based condensation particle counters (modified model 5.410 by Grimm Aerosol Technik, Ainring, Germany) with flow rates of 0.6 and 0.3 $\mathrm{l\,min^{-1}}$, configured with different nominal lower cut-off diameters at 4 nm and 10 nm (set via the temperature difference between saturator and condenser). AMETYST samples behind the HALO aerosol submicrometer inlet (HASI) mounted on top of the fuselage that provides near-isokinetic sampling of aerosol particles up to diameters of 2 - 3 µm. During this campaign, sampling line losses and inlet transmission limited the lower size cut-off to about 20 nm in the upper troposphere. As cloud hydrometeors are found to cause artefacts in the detected number concentrations, cloud passages have been removed from the data set. For details see Wendisch et al. (2016) and Andreae et al. (2018).

For particles in the size range between 90 and 600 nm data from an ultra-high sensitivity aerosol spectrometer airborne (UHSAS-A) that was installed as an underwing probe were analysed. The measurement system is based on the detection of scattered light from laser illuminated aerosol particles. For the ACRIDICON-CHUVA flights used here (AC07 - AC10 and AC15 - AC20), the mentioned size range was divided into 66 logarithmic size bins. Data for the other four flights (AC11 - AC14) are recorded in a different size binning and not used here. Cloud passages and intervals with sample flow deviations were removed. The UHSAS-A was calibrated using spherical polysterene latex particles. The accuracy of the size determination was found to be 11 % (Mahnke, 2018).

2.3.3 *Black carbon measurements* (adapted from Schulz et al. (2018))

The refractory black carbon (rBC) particles were measured with a single particle soot photometer (SP2) (Droplet Measurement Techniques, Longmont, CO, USA). The instrument was operated by the Multiphase Chemistry Department (MPC) of the MPIC. It uses a laser-induced incandescence technique to quantify the mass of rBC in individual aerosol particles (Stephens et al., 2003; Schwarz et al., 2006; Dahlkötter et al., 2014). Calibrations of the incandescent signal were conducted before, during and after the campaign using size-selected fullerene soot particles. The scattering signal was calibrated using either spherical polystyrene latex size standards or ammonium sulfate particles of different diameters selected by a differential mobility analyser. The accuracy of the SP2 is 5 % for the rBC number, and 10 % for the rBC mass concentration according to (Laborde et al., 2012).

2.3.4 *NO and NO_y measurements* (adapted from Schulz et al. (2018))

The atmospheric nitrogen oxides measuring system (AENEAS) instrument measures NO and total reactive nitrogen (NO_y). The measurements were performed by DLR-IPA and conducted by a dual-channel chemiluminescence detector (CLD-SR, Eco Physics). Ambient air is sampled via a standard HALO trace gas inlet with a Teflon tube. For the NO_y channel, the chemiluminescence detector is combined with a custom-built gold converter that reduces all oxidized reactive nitrogen species to NO (Ziereis et al., 2000). NO from ambient air reacts with O_3 produced from an ozone generator in a chamber resulting in excited NO_2. The emitted luminescence signal is detected. The detector channel is equipped with a pre-reaction chamber for determining cross-reactions of other compounds in ambient air reacting with O_3. The time resolution is 1 s. The precision and accuracy of the measurements depend on the ambient concentrations, with typical values of 5 % and 7 % (NO) and 10 % and 15 % (NO_y), respectively.

2.3.5 *CO and O_3 measurements*

The atmospheric tracer experiment (AMTEX) instrument measures CO and O_3 and was operated by DLR-IPA. CO was measured with vacuum-UV fluorescence and has a precision of 2 ppb and a accuracy of 5 % (Gerbig et al., 1999). Measurements of O_3 were conducted with UV absorption (Baehr et al., 2003). The precision is 6 ppb and the accuracy is 10 %. The time resolution for both instruments is 1 Hz.

2.3.6 *Cloud particle number concentrations* (adapted from Schulz et al. (2018))

In order to distinguish between measurements inside and outside of clouds data from the instrument Novel Ice eXpEriment - Cloud, Aerosol and Precipitation Spectrometer (NIXE-CAPS) were used to develop a cloud mask. The NIXE-CAPS was operated by Forschungszentrum Jülich (FZ Jülich) and is mounted beneath a wing of an aircraft for in-situ measurements. It consists of two instruments, the Cloud and Aerosol Spectrometer and the Precipitation Imaging Probe. The measurement principle of the Cloud and Aerosol Spectrometer is based on the detection of forward scattered laser light from particles or small cloud droplets in the size range between 0.6 and 50 µm. It is possible to distinguish between spherical and aspherical particles and droplets by measuring the change of polarization of the scattered laser light (Meyer, 2013; Baumgardner et al., 2014; Weigel et al., 2016). The measurement principle of the Precipitation Imaging Probe is based on two dimensional images of cloud droplets and ice crystals in the size range between 15 and

950 µm (Knollenberg, 1970; Meyer, 2013). The cloud mask was provided by FZ Jülich. Further details on the instrument can be found in Meyer (2013).

2.3.7 *Meteorological reanalysis data*

Backward trajectories help to investigate the origin of air masses that arrive in the Amazon region during the campaign period. The atmospheric transport model FLEXPART was used to calculate the backward trajectories (Stohl et al., 2002, 2005). FLEXPART is a Lagrangian particle dispersion model that calculates trajectories of a large number of small air parcels (particles). This is possible in a forward and backward motion while transport and diffusion of the tracers occur. The FLEXPART backward trajectories used in the analysis here were calculated using Global Forecast System (GFS) data with a 0.5 degree grid resolution. The model calculations were performed by the Ludwig Maximilian University Munich.

3

MEASUREMENT CAMPAIGN ACRIDICON-CHUVA

3.1 OVERVIEW AND AIMS OF THE CAMPAIGN

The aircraft measurement campaign Aerosol, Cloud, Precipitation, and Radiation Interactions and Dynamics of Convective Cloud Systems - Cloud Processes of the Main Precipitation Systems in Brazil: A Contribution to Cloud Resolving Modeling and to the GPM (Global Precipitation Measurement) (ACRIDICON-CHUVA) aimed at the investigation of convective cloud systems to better understand and to quantify aerosol-cloud-interactions and radiative effects of convective clouds. This campaign was performed with the High Altitude and LOng range research aircraft (HALO), which is operated by the Deutsches Zentrum für Luft- und Raumfahrt (DLR). HALO was based in Manaus, Brazil, a city of two million inhabitants and located in the central Amazon basin. The isolated urban area allows the investigation of several aspect, e.g. the undisturbed natural atmosphere above the Amazon rainforest. Another aspect is the impact of local pollution on this undisturbed atmosphere in terms of e.g. aerosol composition changes or cloud evolution. Comprehensive measurements of several parameters in different regions up to 1300 km around Manaus were possible with HALO. Especially the regions north (rural area) and south (deforested area) of Manaus were investigated within 14 flights (see Fig. 19).

The campaign was conducted in September and October 2014 during the dry season that is characterized with an enhanced impact of biomass burning (BB) on the tropospheric composition (Andreae et al., 2018). Altitudes up to 14.4 km were reached and allowed for the investigation of air masses and clouds in different heights. The aircraft was equipped with instruments for measuring basic meteorological parameters, radiation, several trace gases, cloud and aerosol properties, such as size, number and mass concentration, and chemical composition. Thus, several objectives and scientific questions were targeted:

- cloud processing of aerosol particles and trace gases with probing the inflow and outflow of deep convective clouds
- cloud formation over forested and deforested areas
- vertical evolution and life cycle of deep convective clouds (cloud profiling)
- vertical transport and mixing via tracer experiments

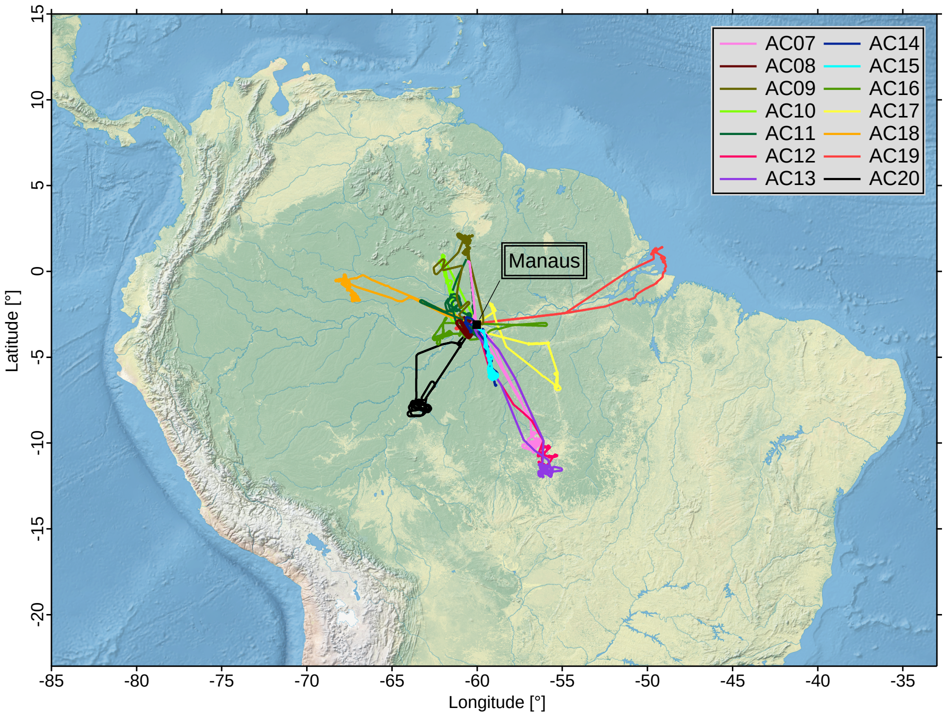

Figure 19: Overview of the scientific flights during the ACRIDICON-CHUVA campaign.

- satellite and radar validation for radiative measurements

Some of these objectives can be partially answered with the analysis of the C-ToF-AMS data and are addressed in Chap. 4. An overview of the flights conducted during the ACRIDICON-CHUVA campaign is given in Tab. 3. Further information on the campaign, the overall instrumentation and additional explanation of the scientific objectives can be found in Wendisch et al. (2016). Results from ACRIDICON-CHUVA can be found in a joint special issue of the journals *Atmospheric Chemistry and Physics* (*ACP*) and *Atmospheric Measurement Techniques* (*AMT*) under the following link https://www.atmos-chem-phys.net/special_issue852.html.

3.2 METEOROLOGICAL CONDITIONS DURING ACRIDICON-CHUVA (partly adapted from Schulz et al. (2018))

The city of Manaus is located in the centre of the Amazon basin at 3° S and 60° W. The intertropical convergence zone (ITCZ), a belt of converging trade winds with seasonally dependent location, was shifted northwards between 4 and 12° N during the time of the ACRIDICON-CHUVA campaign (Andreae et al., 2018). The seasons in the Amazon basin are divided into a dry and a wet season with transition periods in between. For the year 2014 the wet season last from January to March and the dry season from

Table 3: Overview of all flights with date, duration, the maximum altitude that was reached and meteorological situation. Furthermore, information on the flight strategy and comments to the C-ToF-AMS measurements are given (Schulz et al., 2018). The flights AC01 - AC06 were certification, test and ferry flights, and not discussed here.

Flight No.	Date in 2014	Duration	Altitude [km]	Meteorological characteristics	Flight strategy and C-ToF-AMS comments
AC07	06.09.	7 h 35 min	13.9	Convection	Cloud profiling; no zero filter measurements
AC08	09.09.	5 h 30 min	13.8	Convection	Cloud profiling
AC09	11.09.	6 h 10 min	12.6	Convection	Cloud profiling; no zero filter measurements
AC10	12.09.	7 h 25 min	14.4	Convection, cirrus	Cirrus sampling; CVI measurements only
AC11	16.09.	7 h 25 min	12.9	Convection	In- & outflow measurements, cloud profiling
AC12	18.09.	6 h 15 min	13.8	Convection	Polluted cloud profiling
AC13	19.09.	6 h 30 min	12.9	Convection	Polluted cloud profiling
AC14	21.09.	7 h 15 min	15.2	Convection	No zero filter measurements
AC15	23.09.	7 h 20 min	13.8	Convection	Outflow measurements, cloud profiling
AC16	25.09.	6 h 50 min	13.2	Convection	In- & outflow measurements
AC17	27.09.	6 h 40 min	8.1	Convection	Cloud contrast measurements: clouds above forested and deforested areas
AC18	28.09.	6 h 50 min	14.4	Convection	Clean cloud profiling
AC19	30.09.	7 h 15 min	13.8	Convection, pyro-cumulus	Marine and biomass burning influence
AC20	01.10.	7 h 05 min	14.4	Convection	Cloud profiling

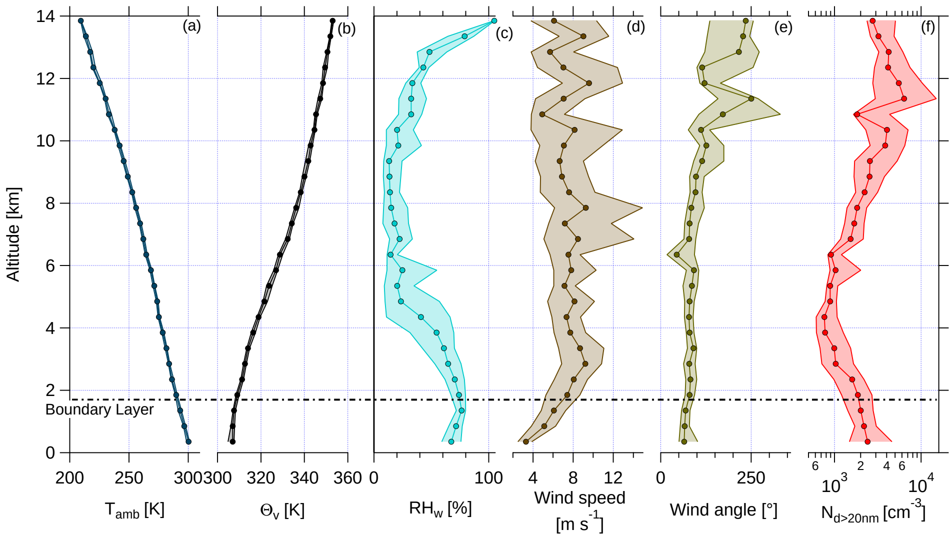

Figure 20: Vertical profiles of (a) ambient temperature (T_{amb}), (b) virtual potential temperature (Θ_{v}), (c) relative humidity with respect to water ($\mathrm{RH_w}$), (d) horizontal wind speed, (e) wind angle, and (f) aerosol number concentration for particle diameters larger than 20 nm ($N_{\mathrm{d>20nm}}$) for all flights during the ACRIDICON-CHUVA campaign. Here, medians (connected dots) with interquartile ranges (shaded area) are shown for each plot. The horizontal dashed line shows the mean height of the top of the BL.

August to October (Machado et al., 2018). The northward shift of the ITCZ creates thermodynamic conditions that are typical for the dry season in the Amazon basin. These are characterized by synoptic-scale subsidence, a dry (planetary) boundary layer (BL) with enhanced temperatures at the top of it and a relatively dry middle troposphere (MT) (Andreae et al., 2018).

The dry season in the Amazon basin in general is characterized by less shallow convection, cloud cover and rainfall than the wet season (Collow et al., 2016; Andreae et al., 2018; Machado et al., 2018). Although the total rain fall is less in the dry season than in the wet season, the rainfall rate is larger during the dry season (Machado et al., 2018). During the measurement campaign a contrast of the weather conditions was observed. In the northeast of the Amazon basin the conditions were drier than in the southwest of the basin where wetter conditions occurred (Saha et al., 2014; Andreae et al., 2018).

The BL height was determined with the help of data measured on board of HALO, i.e. ambient temperature (T_{amb}), virtual potential temperature (Θ_{v}), and relative humidity with respect to water ($\mathrm{RH_w}$) (see Fig. 20). Also wind information like horizontal speed and direction were used (see Fig. 20, panels d and e). As the flights lasted for several hours the daily evolution of the BL was noticeable in the data. The maximum heights of the BL varied between 1.2 km and 2.3 km, depending on the flight time. The highest BL heights

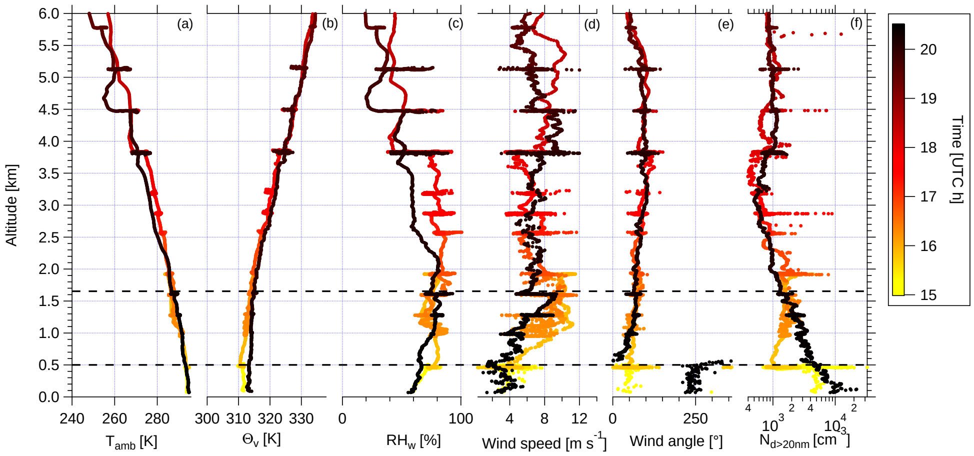

Figure 21: Vertical profiles up to 6 km of (a) ambient temperature (T_{amb}), (b) virtual potential temperature (Θ_{v}), (c) relative humidity with respect to water (RH_{w}), (d) horizontal wind speed, (e) wind angle, and (f) aerosol number concentration for particle diameters larger than 20 nm ($N_{\mathrm{d}>20\mathrm{nm}}$) for flight AC08 during the ACRIDICON-CHUVA campaign. The two dashed lines indicate the different BL heights depending on the day time.

were measured later in the afternoon. Averaged over the whole measurement period, a mean height of the BL was found to be at 1.7 ± 0.2 km (Fig. 20, horizontal dashed line; see also Fig. 21). Note, that the BL height shown in Fig. 20 is not so obvious due to smoothing effects while averaging over all flights. An example of the six parameters from one flight (AC08, conducted on September 9, 2014) used for the determination of the BL height is shown in Fig. 21. The different heights of the BL due to different day times are shown with the two dashed lines. The observed BL height is consistent with previous studies in the Amazonian dry season (e.g., Fisch et al., 2004; Andreae et al., 2018).

Figure 20 shows also the vertical profile of the median relative humidity with respect to water (RH_{w}). RH_{w} decreases above the BL showing a minimum with constant median values between 5 and 9 km. This represents the dry MT that is typical for the dry season in the Amazon basin. At higher altitudes, RH_{w} increases again with altitude. The wind speed varies between the BL with lower values and increased values at higher altitudes. The wind direction is fairly consistent at different altitudes, but changes significantly at altitudes above 10 km.

The meteorological situation during the campaign was quite similar for all days. Convection was dominating the daily weather and affected every flight (see Tab. 3). The invariance of the meteorological situation is also visible in the temperature profile (see Fig. 20, panels a and b) that barely shows any deviation.

The virtual potential temperature (Θ_{v}) shows a stratification above the BL up to 8 km and above this altitude a slightly steeper gradient. The temperatures around Manaus were relatively high, especially at the top of the BL (Wendisch et al., 2016).

This leads to elevated values for the convective inhibition (CIN), representing a higher tropospheric stability (Collow et al., 2016). The thermodynamic parameter CIN is defined as the required energy of an air parcel to reach the level of free convection (LFC) and subsequently to develop convection (Riemann-Campe et al., 2009). It illustrates a stable layer between the surface and the LFC, that needs to be overcome by an air parcel to reach an unstable layer for further convection. The higher the CIN, the higher is the stability of this layer and less convection occurs.

A compensating effect of CIN is convective available potential energy ($CAPE$). This parameter describes the potential buoyancy that an air parcel has after reaching the LFC, and the instability of the troposphere (Holton, 2004). The higher the $CAPE$, the stronger is the convection, but only if the air parcel overcomes the CIN.

CIN and $CAPE$ vary in the Amazon basin throughout the seasons. Both of them show a maximum at the end of the dry season and in the transition time between the dry and the wet season (e.g., Machado et al., 2004; Collow et al., 2016; Giangrande et al., 2017; Machado et al., 2018). During the measurement period in September 2014 the mean $CAPE$ was $1536\,\mathrm{J\,kg^{-1}}$ and the mean CIN was $37\,\mathrm{J\,kg^{-1}}$ (Andreae et al., 2018). Both of these parameters are important when looking at convective processes, the updraft of warm air masses.

Convection occurs regularly on a daily basis in the Amazon basin, although it is the dry season. Under the circumstances of enhanced values for CIN and $CAPE$, and less available water vapour due to the relatively dry MT (see Fig. 20, panel c) there are less convective cells. But if convection develops, it is more organized and proceeds with pronounced vertical extent (deep convection) (Machado et al., 2018). The deep convection influences altitudes from the cloud bottom up to the cloud top that is often at high altitudes (above 10 km).

Above the BL is the convective cloud layer, which reached altitudes of about 4 - 5 km during the campaign (Andreae et al., 2018). The thermal tropopause was at an altitude of 16.9 ± 0.6 km (mean and standard deviation) (Andreae et al., 2018). Maximum flight altitudes of HALO were between 12.6 and 14.4 km. Thus, all the measurements during ACRIDICON-CHUVA were performed in the troposphere.

The measured altitude range between the surface and the highest reachable altitudes of 14.4 km was distributed into three regions based on the total aerosol mass concentration (see Fig. 29 and Sect. 4.1.2.2) and on the parameters described above. The lower troposphere (LT) ranges from 0.1 to 4.5 km and includes the BL. The MT covers altitudes between 4.5 and 8 km, and the upper troposphere (UT) includes altitudes between 8 and 14 km.

The backward trajectories presented in Andreae et al. (2018) show that most air masses between 7 and 14 km had remained over the Amazon basin for the previous three days, and were most likely affected by deep convection and deep convective outflow (Andreae et al., 2018).

In the dry season the air masses above the Amazon basin are influenced by different sources. Besides the rain forest as a remote source for VOC, also pollution affects the chemical composition of the troposphere. Pollution in the Amazon can arise from regional and remote sources (e.g., Andreae and Andreae, 1988; Artaxo et al., 2013; Pöhlker et al., 2018b; Andreae et al., 2018). Regional sources are deforestation and pasture maintenance burning, both happening more frequently in the southern part of the basin (Andreae et al., 2012). Remote sources are long-range transported air masses from Africa. These air masses occasionally transport volcanic sulfur emissions and POA into the basin. During the transport oxidation occurs, leading to the formation of OOA, SOA and secondary inorganic aerosol. The influence of African air masses on the atmospheric composition above the Amazon basin was also identified during the ACRIDICON-CHUVA campaign (Saturno et al., 2018).

3.3 MEASUREMENT PLATFORM HALO

The aircraft HALO is a German research aircraft operated by the DLR. This aircraft is a Gulfstream G550 type (see Fig. 22, panel a). Its major advantages are the high altitudes (15.5 km) that are reachable and the long distance (12000 km) that can be flown (DLR, 2018a). During the ACRIDICON-CHUVA campaign altitudes up to almost 15 km were reached. In the tropics this altitude is still in the troposphere (see above). However, in other regions of the world this altitude range is sufficient enough to reach at least the tropopause. The possible flight time is large and can be up to 10 hours. The speed of HALO during the ACRIDICON-CHUVA campaign was approximately 200 $\mathrm{m\,s^{-1}}$.

The instrumentation on board was diverse due to the different objectives of the ACRIDICON-CHUVA campaign (see Tab. 2 and Wendisch et al. (2016)). Several aerosol instruments were mounted inside HALO, e.g. the AMETYST for measuring aerosol number concentration, the SP2 for rBC measurements, the HALO-CVI-Rack to investigate cloud droplets and ice crystals, and the C-ToF-AMS for chemical composition measurements (see Tab. 2 and Wendisch et al. (2016)). These instruments were connected to different inlet systems providing near-isokinetic conditions for sampling ambient aerosol particles. The HALO aerosol submicrometer inlet (HASI) was used for out-of-cloud aerosol measurements. For measurements of cloud particle residuals the aerosol instruments were switched to the HALO counterflow virtual impactor (HALO-CVI). Both inlets will be introduced shortly in the following

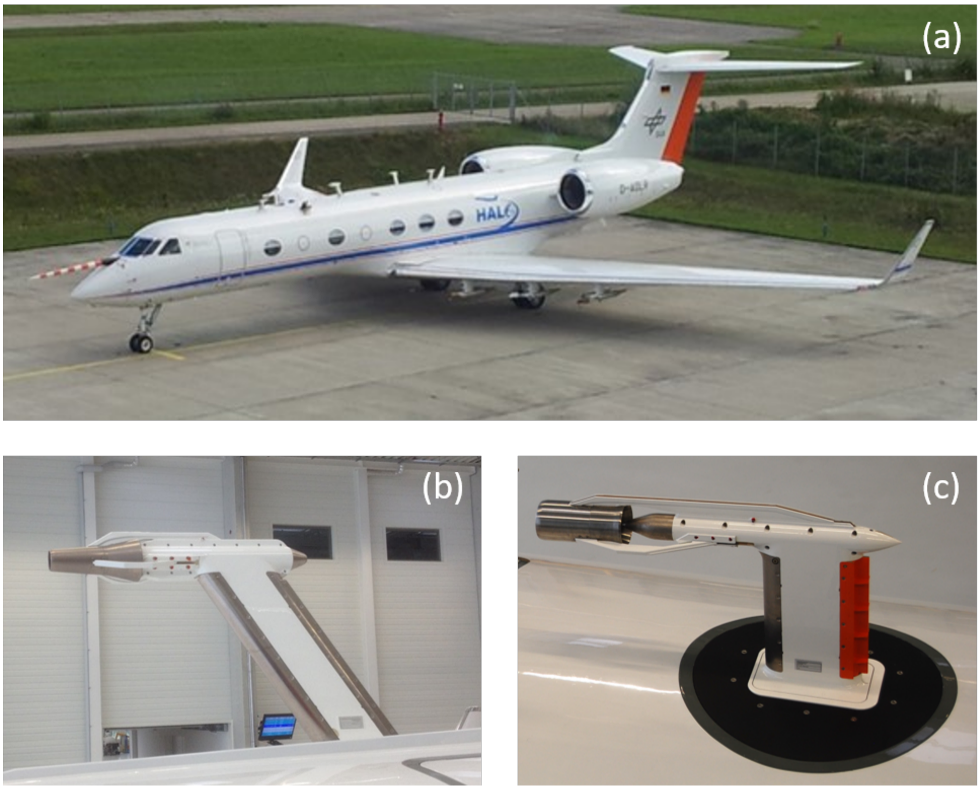

Figure 22: Pictures of (a) the German research aircraft HALO, and of the (b) HASI and (c) HALO counterflow virtual impactor (HALO-CVI) mounted on top of the fuselage of HALO. Pictures in (b) and (c) are courtesy of J. Schneider and S. Mertes, respectively.

with specifications and a particle loss calculation of the tubing between the inlets and the C-ToF-AMS.

3.3.1 *HALO Aerosol Submicrometer Inlet - HASI*

The HALO aircraft has a special inlet system for sub-micrometer aerosol measurements, HASI (see Fig. 22, panel b). This inlet was designed by DLR in collaboration with enviscope GmbH (Frankfurt, Germany) and provides up to 30 l min^{-1} sample air flow, which can be divided via four sample lines to different aerosol instruments inside the aircraft (Minikin et al., 2017; Andreae et al., 2018). HASI is located on top of the fuselage and outside of the aircraft boundary layer. Thus, the aerosol particle sampling should not be affected by the aircraft itself. Incoming air is aligned in the inlet using a front shroud and decelerated. Four sample tubes are located inside of the HASI to provide connected instruments with the sampling air. The overall airflow in each tube is regulated to achieve isokinetic sampling conditions according to the actual aircraft speed. This was not fully automated for the time of the ACRIDICON-CHUVA campaign, but adjusted manually. The upper cut-off is calculated to be between 2 and 3 µm (Minikin et al., 2017) and does not interfere with the upper cut-off of the C-ToF-AMS inlet. Large cloud droplets and ice crystals should not enter the sampling lines directly and thus, not affect the aerosol measurements. However, artefacts in liquid clouds cannot be excluded (Andreae et al., 2018). Therefore, all HASI measurements conducted with the C-ToF-AMS are filtered with respect to cloud passages and represent only out-of-cloud aerosol measurements. The C-ToF-AMS was connected to HASI together with the SP2 partly sharing a tube. Thus, the flow in the connecting tube was increased allowing a shorter residence time of the aerosol particles before reaching the C-ToF-AMS.

3.3.2 *HALO Counterflow Virtual Impactor - HALO-CVI*

The HALO counterflow virtual impactor (HALO-CVI) was used for sampling cloud droplets and ice crystals inside clouds (see Fig. 22, panel c). The HALO-CVI is based on the sampling principle described the first time in Ogren et al. (1985) and designed by the Leibniz Institute for Tropospheric Research (TROPOS) to collect and process cloud particles between 5 and 40 µm at typical HALO flight conditions (Wendisch et al., 2016). It consists of two concentric tubes with particle free and dry air streaming between both tubes towards the tip of the HALO-CVI. The inner tube consists at the tip of porous material so that the particle free and dry air flows through it into the sampling line. The main part of this dry and particle free air is sucked back through the sampling line as carrier air to the instruments inside the cabin, whereas a minor fraction flows out of the tip providing a so called counterflow to segregate gases and interstitial particles from the cloud droplets and ice particles. The droplets and/or ice particles that are large enough to overcome the counterflow enter the carrier air, where the condensed water is driven into the gas phase releasing their cloud particle residuals (CPR). The flow in the HALO-CVI is regulated automatically.

The HALO-CVI, like all other HALO inlets, had to be installed at the upper fuselage of the HALO cabin. Thus smaller and larger cloud particles are enriched and depleted, respectively, as shown by Afchine et al. (2018). As a consequence the HALO-CVI sampling is not affected by large cloud particle shattering, but on the other hand the sampling efficiency is size dependent with respect to ambient conditions, which can only be roughly corrected for the different HALO flight conditions (Afchine et al., 2018). Thus, mainly fractions of the CPR chemical composition can be evaluated whereas the specification of absolute concentrations are less precise, depending on the HALO flight and the cloud microphysical conditions.

A particle enrichment occurs during the separation process. This enrichment improves the detection limit of the aerosol sensors, but needs to be accounted for in the data analysis. The enrichment factor (EF) is defined as the ratio between the air flow in front of the HALO-CVI to the sample flow inside the HALO-CVI. The C-ToF-AMS was connected to the HALO-CVI during cloud measurements enabling chemical composition analysis of CPR.

3.3.3 *Particle loss calculation*

Particle losses occur in the tubing between the inlets and the C-ToF-AMS due to long sampling lines and curvatures. The sampling line between the HASI and the C-ToF-AMS was 3.06 m, between the HALO-CVI and the C-ToF-AMS 3.38 m long. Losses in the sampling line were calculated with the particle loss calculator (PLC). The PLC was developed at the MPIC and determines the transmission efficiency (or the particle loss) through the tubing (von der Weiden et al., 2009). This tool provides calculations that includes several loss processes as diffusion, sedimentation, turbulent inertial deposition, inertial deposition in bends and contractions, and considers general sampling conditions like (non)-isokinetic and (non)-isoaxial sampling. However, for shrouded inlets the tool is not applicable (von der Weiden et al., 2009). As the HASI and the HALO-CVI have a shrouded inlet, both inlets are not considered in the following calculation. Thus, just the tubing between the inlets and the C-ToF-AMS are included. An overview of the used parameters can be found in Tab. 8 and 9 in Sect. B.1. The resulting transmission efficiencies are shown in Fig. 23.

For the tubing between the HASI and the C-ToF-AMS the transmission efficiency is calculated for two different pressures. The ambient conditions on ground are set to a pressure of 1013 hPa and a temperature of 30&,°C. Particles with a particle diameter (d_p) between 100 and 1000 nm have a transmission efficiency of 90 % or more, whereas for particles with a d_p between 50 and 100 nm a transmission efficiency of 80 % or more is derived (see Fig. 23, dark blue curve). The cutoff diameter at 50 % efficiency (d_{50}) is 20 nm. Changing the conditions that are valid for higher altitudes (pressure of 200 hPa, temperature of -65 °C), the transmission efficiency is reduced (see Fig. 23, light blue curve). Particles with a d_p between 90 and 1000 nm have a transmission efficiency of 80 % or more. For particles between 200 and 600 nm the transmission efficiency is above 90 %. The d_{50} is 35 nm.

A similar behaviour for the transmission efficiency is observed for the tubing between the HALO-CVI and C-ToF-AMS (see Fig. 23, dark red curve). The curve for ground conditions (red curve) is slighty shifted towards bigger particle diameters compared to the tubing between the HASI and C-ToF-AMS, but still the same diameter range (100 - 1000 nm) is transmitted with 90 % or more. For low pressure conditions the overall transmission efficiency is reduced and slightly shifted to bigger particle diameters. However, particles with a d_p between 100 and 1000 nm are transmitted with 80 % or more. The d_{50} ranges between 25 nm for ground conditions and 40 nm for conditions at

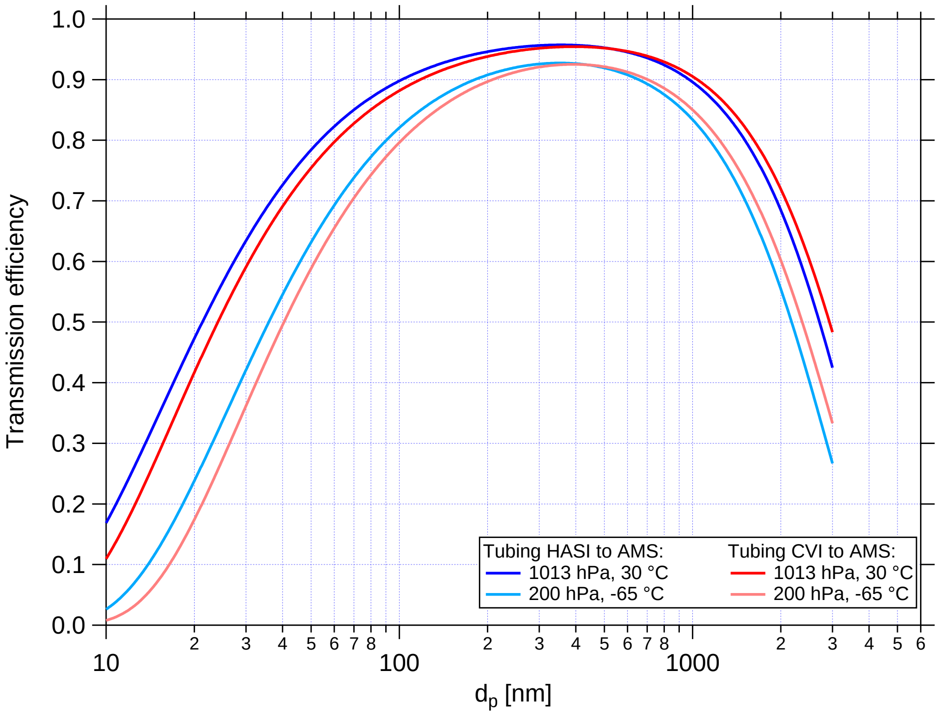

Figure 23: Transmission efficiency for different particle sizes for the tubing between the HASI (blue) and the HALO-CVI (red) to the C-ToF-AMS, respectively.

higher altitudes.
Smaller particles will not reach the C-ToF-AMS due to the long sampling line where diffusion losses occur, and particles larger than 1000 nm begin to experience sedimentation losses and impaction in the bends. Since the sampling line losses are small in the size range between 100 and 900 nm (majority of the measurement range of the C-ToF-AMS) a correction is not necessary. For particles with a d_p smaller than 100 nm a correction would be preferable. Unfortunately, size-resolved data are not available in a sufficient data quality, so a correction for sampling line losses for particles smaller than 100 nm and for the reduced transmission efficiency at low pressures is not feasible.

4

RESULTS FROM THE ACRIDICON-CHUVA CAMPAIGN

In the following the results of the data analysis from the ACRIDICON-CHUVA campaign are presented. Regarding to the objectives of the campaign mentioned in Sect. 3.1 the specified questions will be answered:

- What characterizes the out-of-cloud aerosol above the Amazon rainforest?
- Is there a difference in the aerosol composition over forested and deforested areas?
- Are there any effects of long-range transported aerosol on the characteristics of the Amazon aerosol properties in the dry season?
- What is the influence of biomass burning on the composition of out-of-cloud aerosol and cloud residual particles?
- What characterizes the cloud particle residuals (CPR) above the Amazon rainforest?
- Is there a difference between the chemical composition of out-of-cloud aerosol and CPR?
- What cloud processes of aerosol particles acting as CCN or INP occur in deep convective clouds?

The first part of this chapter gives an overview of out-of-cloud aerosol characteristics. The second part gives insights into the analysis of cloud particle residuals (CPR).

In general, all cloud passages were removed for the out-of-cloud aerosol data set. These cloud passages are identified with data from the NIXE-CAPS (see Sect. 2.3.6). Also, data during take-off and landing (all data at altitudes below 100 m) were removed in order to minimize the influence of the airport. The data are calculated for standard pressure and temperature (STP) conditions, whereas STP for the C-ToF-AMS data means $T = 300\,\mathrm{K}$ and $p = 995\,\mathrm{hPa}$ as these are the conditions during calibration measurements on ground. All vertical profiles shown in the following give median and interquartile ranges of the different parameters unless otherwise noted. The median and interquartile range values are calculated for altitude bins of 500 m. Data sampled at altitudes above 14 km are also not considered due to the low amount of available data points and missing statistics. Data from 13

flights (out of 14 flights) are analysed for the out-of-cloud aerosol, whereas for the cloud particle residual analysis data from all flights are considered. An overview of the uncertainty calculations is given in Sect. C.4.
Some of the figures shown and part of the text written in this chapter are adapted from Schulz et al. (2018) and referred to appropriately.

4.1 OUT-OF-CLOUD AEROSOL PROPERTIES

In the following the characteristics of the out-of-cloud aerosol is analysed. Therefore, different parameters are evaluated. Especially the difference or similarities between the LT and UT are discussed. The characteristics of the MT are mentioned just briefly as the data density is too low.

4.1.1 *Aerosol number properties* (partly adapted from Schulz et al. (2018))

The vertical profile of the aerosol number concentrations for particles larger than 20 nm (already shown in Fig. 20, panel f, see also Fig. 24, panel a) is characterized with decreasing concentrations in the LT, and increasing values for the MT and UT. The median number concentrations in the LT range between ~2000 to 2500 cm^{-3} in the BL and lower values (~800 cm^{-3}) at 4 km altitude. The range is especially in the lower altitude bins wider as influences from BB pollution affect the number concentration. In the MT median number concentrations increase to ~2000 cm^{-3}, similar to values in the lower LT. The UT is characterized with further increase in aerosol number concentrations. The median values are ~6500 cm^{-3} and show higher concentrations than in the LT.
Information on the particle size distributions is derived from UHSAS-A data (see Sect. 2.3.2 and Fig. 24, panel b and 25). The vertical profile of the median with interquartile ranges and the mode of the altitude binned size distributions is shown in Fig. 24, panel (b). In the LT median diameters are between 140 and 150 nm, the modal diameter is between 100 and 135 nm. Both, the modal and median diameter are shifted towards smaller values in the MT and UT with a value of 90 nm for the modal and 110 nm for the median diameter. It should be noted here, that the lowest cut-off of the considered size range of the UHSAS-A is at 90 nm. Accordingly, the displayed mode and median diameters are confined by this lower limit and should only be interpreted in this context.
The colour code in the vertical profile in Fig. 24, panel (b) refers to the size distributions for the three different altitude regions shown in Fig. 25. In the LT the median size distribution (blue) has its maximum at 130 nm and covers a diameter range up to 360 nm. The size distributions for the MT and UT are shifted towards smaller diameters and only the tail of the distribution is visible in the measured size range. The width of the distribution, espe-

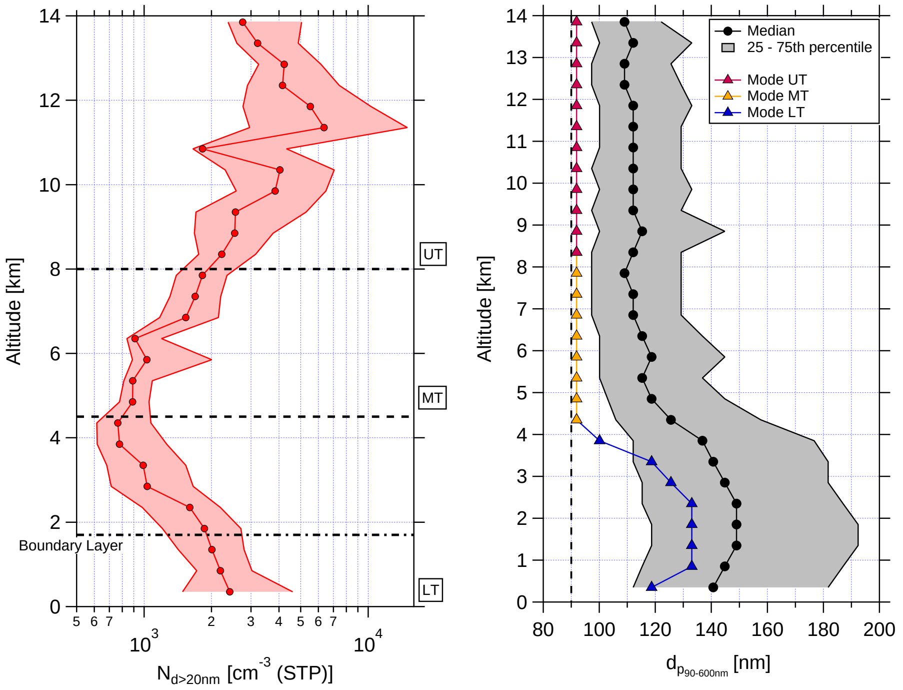
(a) (b)

Figure 24: Panel (a): Vertical profile of the median and interquartile ranges of the aerosol number concentration with diameters larger than 20 nm, measured with the AMETYST (see Sect. 2.3.2). Panel (b): Vertical profile of mode (triangles) and median (black dots) diameters of the binned size distributions measured by the UHSAS-A (see Sect. 2.3.2). The grey shaded area gives the interquartile range. The vertical dashed line indicates the lower cut-off of the considered size range of the UHSAS-A. The statistics shown in (b) are calculated from all valid UHSAS-A data from 10 flights (AC07 - AC10, AC15 - AC20). Both figures are adapted from Schulz et al. (2018).

cially for the UT, seems to be reduced. The highest concentrations of small particles (with diameters of 90 nm) are found in the UT. This observation fits into the number concentration increase of particles with diameters larger than 20 nm measured with the AMETYST (see Fig. 24, panel a).

4.1.1.1 *Comparison with literature*

Several field studies characterized the aerosol number properties during the dry and the wet season. The ACRIDICON-CHUVA campaign was conducted during the dry season. Therefore, a comparison with recent studies is limited only to those who also presented data of the dry season. As a general remark it should be noted that aerosol number concentrations differ between the dry and wet season. The aerosol number concentrations measured on ground is

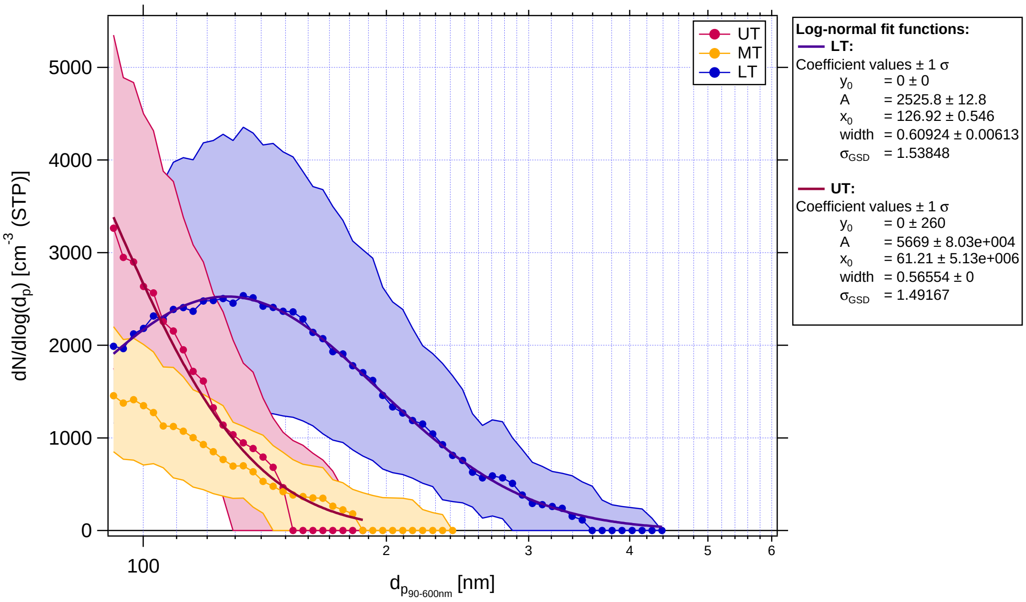

Figure 25: Median and interquartile size distributions of particles between 90 and 600 nm in the UT (pink), in the MT (yellow) and in the LT (blue). The statistics are calculated from all valid UHSAS-A data from 10 flights (AC07 - AC10, AC15 - AC20). Data are calculated for STP conditions. This figure is adapted from Schulz et al. (2018).

overall low during the wet season. However, the dry season is represented by number concentrations four times higher than measured during the wet season (Artaxo et al., 2013).

Artaxo et al. (2013) reported aerosol number concentrations from a remote forested measurement site north of Manaus (TT34) of ~2200 cm^{-3}. The size distribution was dominated by the accumulation mode (particle diameters between 100 and 1000 nm) with a mean geometric diameter of 130 nm.

The South American Biomass Burning Analysis (SAMBBA) campaign in 2012 focused on Amazonian aerosol characterization with ground and airborne measurements. At the ground site near Porto Velho (southwest of Manaus) an aerosol number concentration of ~1000 cm^{-3} was measured (Brito et al., 2014). The size distribution was dominated by the Aitken (there defined as particle diameters between 30 and 120 nm) and accumulation mode (there defined as particle diameters between 70 and 280 nm). Airborne measurements of the aerosol size distribution showed a bimodal distribution with maxima at 200 and 400 nm (Marenco et al., 2016; Malavelle et al., 2019).

The Amazon tall tower observatory (ATTO) provides continuous measurements of aerosol concentration and size distribution since March 2012 (Andreae et al., 2015). ATTO is located near Manaus in a remote and forested area. The aerosol number concentration range between 500 to 2000 cm^{-3} in the dry season. A dominance of Aitken and accumulation mode particles was also observed here. The maximum of the distribution was found at ~140 nm (Andreae et al., 2015).

The aerosol number concentrations and size distributions for the LT measured during the ACRIDICON-CHUVA campaign confirm the findings reported in previous studies. The BL shows aerosol number concentrations of ~2000 to 2500 cm^{-3} with interquartile ranges between ~1000 and 4000 cm^{-3}. The wider range of the number concentration results from regional influences, e.g. biomass burning in the southern part of the Amazon that leads to enhanced values (Andreae et al., 2018). The size distribution of the LT also confirms previous findings, although only the accumulation mode was measured with the UHSAS-A. However, the maximum of the distribution of ~130 nm is very similar to the maxima of the size distributions reported in Artaxo et al. (2013) and Andreae et al. (2015).

4.1.1.2 *Summary*

In summary, the characteristics of the aerosol in the LT and UT are different in terms of number properties. In the UT an increase in the number concentration for aerosol particles larger than 20 nm and smaller than 90 nm is observed. The size distributions for particles between 90 and 600 nm are shifted to smaller diameters with increasing altitudes. Thus, the aerosol particles in the LT and UT can have different sources. Previous results from ground measurements in the Amazon were confirmed.

4.1.2 *Aerosol composition* (partly adapted from Schulz et al. (2018))

4.1.2.1 *Comparison of AMS and UHSAS*

Originating from the size-resolved number concentrations of the UHSAS-A mass concentrations can be obtained. The necessary equations for this calculation can be found in Sect. C.1. Thus, a comparison of the total mass measured by C-ToF-AMS and SP2 ($C_{\mathrm{AMS}}+C_{\mathrm{rBC}}$) and the UHSAS-A mass is possible and shown in Fig. 26. Ideally, the total mass is the same as the mass derived from the UHSAS-A data. If discrepancies appear, they are often compensated with changing the CE in the C-ToF-AMS data processing. Here, the CE is set to the default value of 0.5 (see Sect. 2.2).

The different patterns of the data are visible in Fig. 26 and classified by three linear fit functions. Data points sampled below 2.5 km (lower LT) are described with the blue fit function. Overall these data are quite below the 1:1 line. This means, that the total mass is underestimating the actual aerosol mass concentration. The fit function shows that the difference between total mass and UHSAS-A mass can be explained by a factor of ~2. The main reason is the use of the CPI in the inlet system of the C-ToF-AMS. The CPI causes particle losses at lower altitudes (high ambient pressures) due to

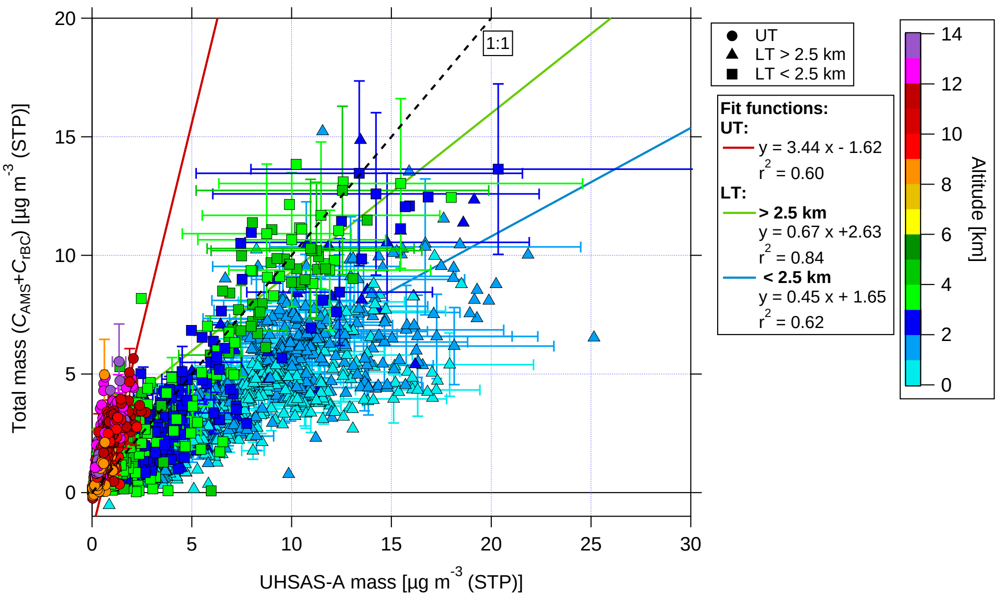

Figure 26: Scatter plot of total mass (C_{AMS}+C_{rBC}) against the mass concentrations derived from the UHSAS-A, coloured with altitude. The solid lines present the fit functions at different altitude regions. The uncertainties of both parameters are considered for the calculation of the linear fit curve coefficients (see Sect. C.4). The dashed line shows the 1:1 line. For clarity reasons only some of the uncertainty bars are shown.

particle impaction inside of the CPI (see Sect. 2.1.2).

The green fit function describes data that are sampled between 2.5 and 4.5 km, representing the upper LT. Compared to the blue fit function, which represent the lower LT, it is much closer to the 1:1 line. This implies that the influence of the CPI is decreasing with increasing altitude. This conclusion is also supported from a comparison study with data from a HR-ToF-AMS on board of the American research aircraft G-1 and the C-ToF-AMS data. The measurement flights of the G-1 were completed in the scope of the Green Ocean Amazon Experiment (GoAmazon14/5) campaign, which partly took place during the same time and place as the ACRIDICON-CHUVA campaign. Flights with parallel flight tracks of the two aircraft were performed allowing a comparison of the two data sets. The HR-ToF-AMS was compared with a UHSAS-A on board of the G-1 and showed good agreement at all altitudes (Mei et al., 2019). However, the aerosol volume concentration measured by the UHSAS-A is slightly lower than the one measured with the HR-ToF-AMS at altitudes above 2.5 km (see Fig. 27, panel b). Data of the HR-ToF-AMS and C-ToF-AMS show similar results above 2.5 km (see Fig. 27, panel a and Mei et al. (2019)) indicating that the impaction losses of the CPI is reduced already at this altitude. The difference between the total and the UHSAS-A mass in the LT above 2.5 km could be caused by the shift of the aerosol size distribution towards smaller particle diameters resulting in an underestima-

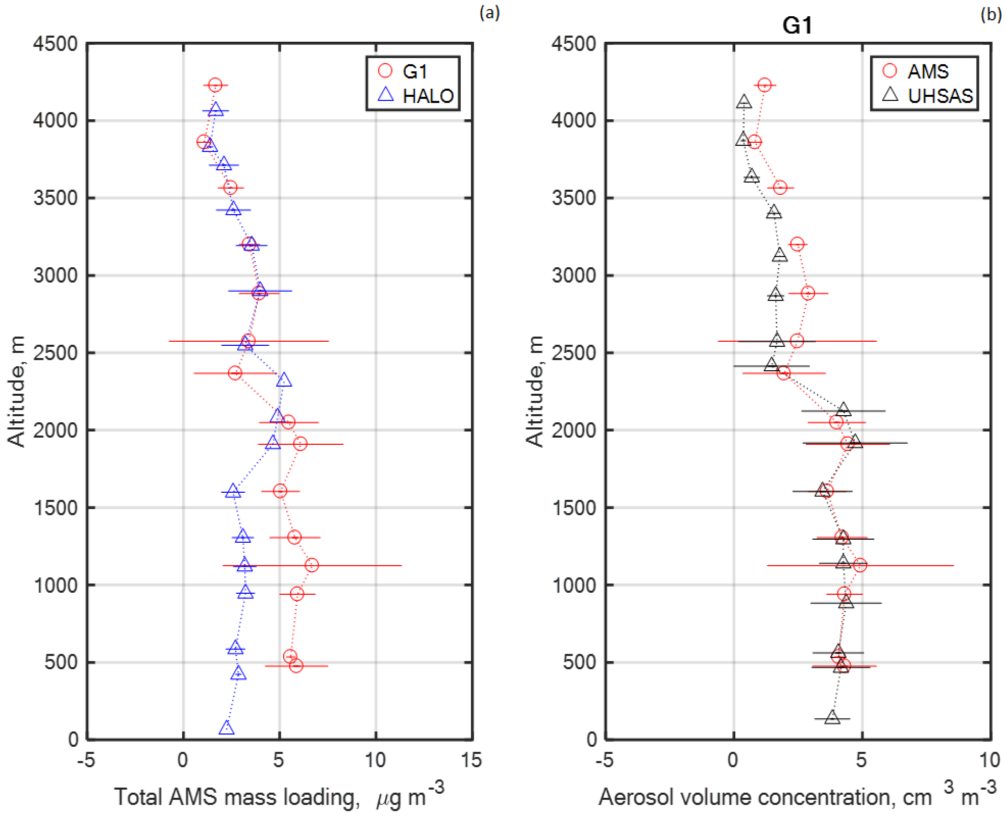

Figure 27: Panel (a): Comparison of total AMS mass measured on board the G-1 and HALO. Panel (b): Comparison of volume concentration measured with HR-ToF-AMS and UHSAS-A on board the G-1. This figure is adapted from Mei et al. (2019).

tion of the UHSAS-A mass concentrations. The maximum altitude that was reachable for the G-1 was 6 km. Thus, it is not possible to compare the two data sets for higher altitudes.

The red fit function represents data from the UT. The data for the MT are removed for clarity reasons. The fit function for the UT shows that the total mass is overestimated by a factor of ~3.4.

One possible reason for the mass discrepancy could be the *CE* value of 0.5 that was chosen for this dataset (see Sect. 2.2). This value is valid when measuring ambient aerosol (Middlebrook et al., 2012). However, some circumstances can change (more precise: increase) the *CE*, e.g. a large fraction of nitrate, high relative humidity (RH) or the phase state of the aerosol. Although the relative fraction of nitrate is increased in the UT compared to the LT or MT, it still comprises a minor part in the aerosol composition such that the condition of high nitrate is not given (see Fig. 30 in Sect. 4.1.2.2). The influence of the RH can be seen as negligible as the aerosol is dried in the tubing between the HASI and the C-ToF-AMS. Thus, a *CE* of 0.5 is

Table 4: Overview of parameters from the fit function of the UHSAS-A number size distribution (σ).

Parameter	LT	UT
d_p^0	126.9 nm	61.2 nm
σ_{GSD}	1.53848	1.49167
CMD	152.8 nm	71.8 nm
MMD	266.6 nm	116.0 nm
$d_{\overline{m}}$	201.9 nm	91.3 nm

justified. Some previous studies in the Amazon region used a CE of 1. This was explained with the phase state of the organic-dominated aerosol that is most likely liquid on ground (Chen et al., 2009; Allan et al., 2014). However, Shiraiwa et al. (2017) showed that organics are solid in the Amazon above 5 km. Thus, the argument of liquid particles that are sampled more efficiently is not given any more for most of the data. In fact, all the mentioned circumstances would lead to a higher CE than 0.5 and consequently to less aerosol mass derived from the C-ToF-AMS. But as they can be excluded, the default value of 0.5 is applied.

The main reason for the mass discrepancy is most likely the limited size range of the UHSAS-A, although particles smaller than 90 nm do not contribute dominantly to the aerosol mass. However, the size distributions show a vast shift to smaller particle diameters (see Fig. 24, panel b and Fig. 25). This shift can explain the discrepancy in the mass concentrations between the total mass and the UHSAS-A mass. This argument is supported by the log-normal fit function of the size-resolved number concentration shown in Fig. 25.

The fit function allocates information on the width σ_{GSD} and d_p^0 (diameter of the amplitude) of the distribution. With these parameters it is possible to derive different diameters, e.g. count median diameter (CMD), mass median diameter (MMD) or diameter of average mass ($d_{\overline{m}}$). The definitions and equations for calculating each of these diameters can be found in Sect. C.1. The fit function for the LT reproduces the data very well (see Fig. 25, blue curve). In contrast to this, the fit function of the UT distribution can only be aligned to the tail of the distribution (see Fig. 25, pink curve). This makes it difficult to find parameters such as σ_{GSD} that describe the distribution appropriately. As a result, the received numbers for the diameters can have large errors, especially for the UT distribution.

The different parameters are given in Tab. 4. The mass median diameter (MMD) is the diameter of interest when facing the comparison of the

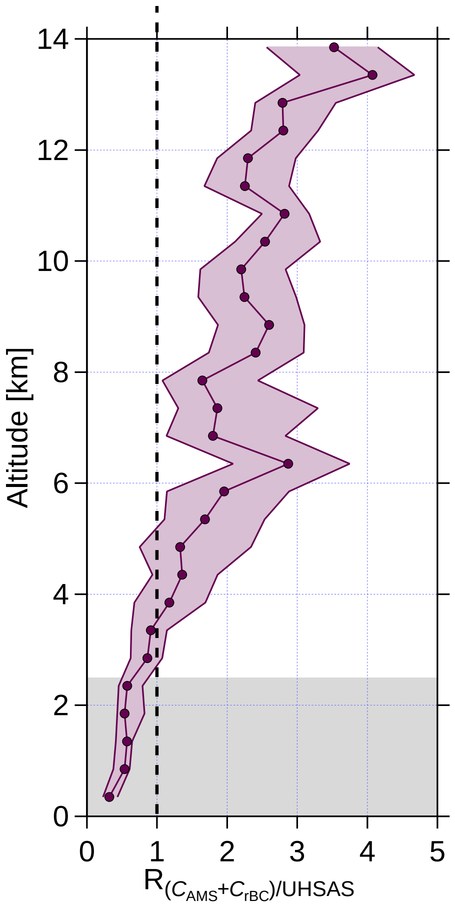

Figure 28: Vertical profile of median mass ratio of (C_{AMS}+C_{rBC}) and UHSAS-A with interquartile ranges. The vertical dashed line shows where full agreement would be (at 1). The grey shaded area covers data sampled below 2.5 km, which are underestimated due to impaction losses of the CPI in the C-ToF-AMS inlet system (see Sect. 2.1.2).

total mass and the UHSAS-A mass. It describes the diameter at which half of the mass is below (at smaller diameters) and above (at larger diameters). The MMD for the LT is much higher than for the UT. Additionally, the MMD for the UT is close to the lower cut-off of the UHSAS-A of 90 nm, where the highest number concentrations were measured within the size range. This shows, as previously mentioned, the shift of the distribution to much smaller particle diameters in the UT and also explains the difference in the comparison of total mass measured by C-ToF-AMS as well as SP2, and the mass derived from the UHSAS-A.

The vertically resolved median mass ratio between the total and UHSAS-A mass is depicted in Fig. 28. With increasing altitudes an increase in the mass ratio is visible. At altitudes below 2.5 km the total mass is underestimating the UHSAS-A mass. The reason for this is most likely the particle losses in the inlet system of the C-ToF-AMS, as already explained above. At alti-

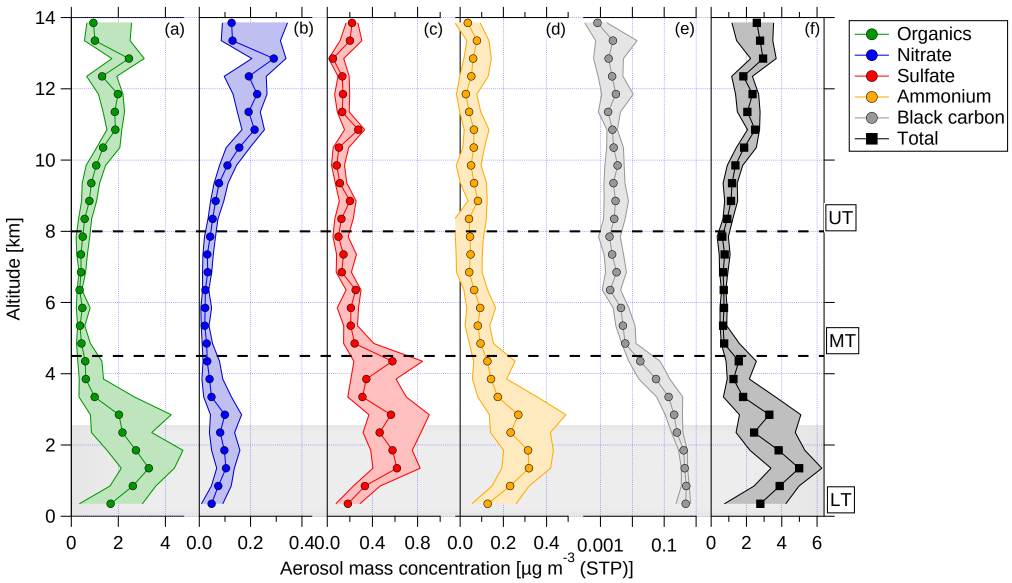

Figure 29: Vertical profiles of (a) organics (green), (b) nitrate (blue), (c) sulfate (red), (d) ammonium (yellow), (e) black carbon (grey), and (f) total aerosol (black) median mass concentration and interquartile ranges. The horizontal dashed lines indicate the division into LT, MT, and UT. Note, that the axis of (e) is logarithmic. The grey shaded area covers data sampled below 2.5 km, which are underestimated due to impaction losses of the CPI in the C-ToF-AMS inlet system (see Sect. 2.1.2). This figure is adapted from Schulz et al. (2018).

tudes around 4 km good agreement is observed, whereas for higher altitudes the mass ratio is further increasing. The main reason for the discrepancy is the limited measurement range of the UHSAS-A.

4.1.2.2 *Aerosol mass concentrations*

The vertical profiles of median mass concentrations of organics, nitrate, sulfate, ammonium, black carbon, and the total median mass concentration are shown in Fig. 29.

The highest total median mass concentrations are observed in the LT with 5 µg m^{-3} (STP). The main fraction consists of organics, minor fractions consist of sulfate, rBC, and ammonium (see Fig. 30). The nitrate mass concentration is rather low and contributes only as a small fraction to the total mass concentration in the LT. Note, that values below 2.5 km are underestimated due to impaction losses of the CPI in the inlet system of the C-ToF-AMS (see grey shaded area in Fig. 29 and Sect. 2.1.2). Thus, the total amount of the mass concentration can be higher.

The MT is characterized with a sharp decrease of the aerosol mass that remains constant at ~1 µg m^{-3} (STP) over the altitude range between 4.5 and 8 km. The main fraction is still organic matter, whereas the sulfate fraction

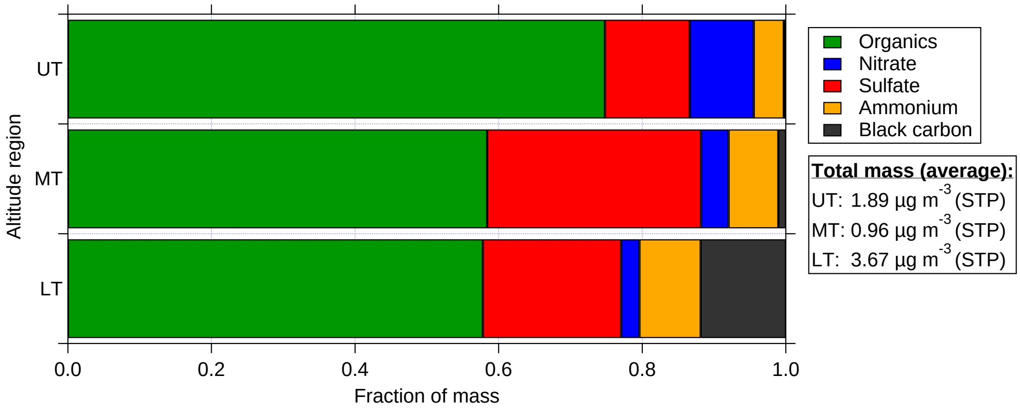

Figure 30: Fractions of the species divided in the different altitude regions lower troposphere (LT), middle troposphere (MT), and upper troposphere (UT). The averaged mass concentrations for the different altitude regions are given on the right.

increases and the rBC fraction is reduced to a negligible amount. The higher contribution of sulfate to the aerosol composition in the MT is attributed to long-range transport of volcanically influenced air masses from Africa (Andreae et al., 2018; Saturno et al., 2018). Sulfate aerosol was formed during the transportation and comprises to a large fraction of the composition in the MT. Interestingly, the fraction of rBC is decreased remarkably in the MT compared to the LT. The sharp decrease of rBC median mass concentrations indicates scavenging in clouds, meaning that rBC and also other aerosol particles are efficiently removed during convective vertical transport (Andreae et al., 2018).

Interestingly, the total median mass concentration is enhanced in the UT with values up to $3\,\mu\mathrm{g\,m^{-3}}$ (STP). The main fraction is, again, organic matter, similar to the LT and MT. The sulfate is decreased compared to the LT and MT. Ammonium and rBC comprises only to a small amount to the aerosol composition. Just between 13 and 14 km, sulfate median values show a slight increase again as can be seen in Fig. 29, panel (c). However, nitrate is increasing, especially at altitudes above 10 km, showing the highest measured median mass concentrations in the UT and contributing significantly to the total aerosol mass compared to the LT and MT (see Fig. 30). Although the nitrate median values decrease between 13 and 14 km, the interquartile range still indicates that enhanced mass concentrations were encountered. The enhancement of organics and nitrate at such high altitudes leads to the question of the source of these aerosol particles and will be addressed in Sect. 4.1.3.2 and 4.1.3.3.

4.1.2.3 *Acidity*

The mass concentration data of the C-ToF-AMS allow acidity calculations. The inorganic fraction is considered in these calculations. Ammonium serves as neutraliser for sulfate and nitrate (see Eq. 28 in Sect. C.3). Chloride is not considered here, as the concentrations are always below the DL (see Sect. 2.2.3.6). The result of this calculation provides information on the fact whether the aerosol is neutralized or acidic (Zhang et al., 2007a). In regions with organics dominating the aerosol chemical composition it is also possible that neutralization processes occur through organic alkaline substances. However, this process is not considered here.

The vertical profile of median measured and for neutralization needed ammonium is shown in Fig. 31 together with the median per altitude bin averaged DL for ammonium. The measured ammonium lies above the DL in the LT. Furthermore, it is comparable to the amount of ammonium that is needed for neutralization. Thus, it can be concluded, that the aerosol is mainly neutralized in the LT. The amount of ammonium decreases in the MT and UT compared to the mass concentrations derived in the LT. The derived DL is larger than the measured ammonium. The ammonium that is needed for neutralization lies also below the DL, only for the very upper part of the UT (higher than 13 km) the values are above the DL. As a result, it can be concluded that with increasing altitude the aerosol tends to be acidic. Especially in the very upper part of the UT the data are above the DL and allow a quantitative statement. It should be noted here again, that the values below 2.5 km are underestimated. This is given with the grey shaded area in Fig. 31, respectively.

The scatter plot of measured and for neutralization needed ammonium supports this (see Fig. 32). The data are averaged over five minutes, above the DL and coloured with altitude. The regression line for the data from the LT is slightly above the 1:1 line. This indicates that the aerosol was neutralized in the LT. In contrast to this seems the aerosol in the UT acidic. The measured ammonium is lower than the needed ammonium for full neutralization. There are two fit functions shown for the UT in Fig. 32. Whereas one has no constraints (solid red line), the dotted red line has a fixed intercept of zero as could be expected. However, the correlation of the data is lower for the constrained fit function ($\mathrm{r}^2 = 0.15$) as for the unconstrained ($\mathrm{r}^2 = 0.45$). From both fit functions it can be concluded that between 36 and 66 % of the aerosol particles in the UT were neutralized regarding the inorganic species. Thus, the aerosol particles in the UT are acidic. However, it should be noted here, that the correlation of the data is lower in the UT ($r^2 = 0.45$) than in the LT ($r^2 = 0.80$).

Interestingly, some data points measured at altitudes between 4 and 5 km show a completely different behaviour. The measured ammonium hardly exceeds $0.2\,\mu\mathrm{g\,m^{-3}}$, but the ammonium needed for neutralization would lead

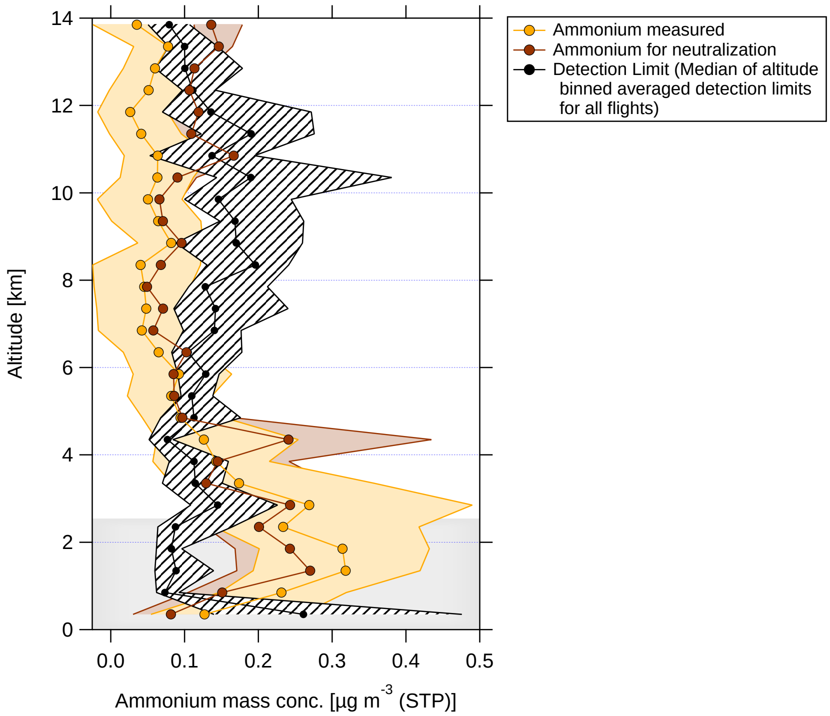

Figure 31: Vertical profiles of the median ammonium mass concentration (yellow), median for neutralization needed ammonium mass concentration (red) and the median per altitude bin averaged detection limits of ammonium (black) for all flights of the ACRIDICON-CHUVA campaign. The grey shaded area covers data sampled below 2.5 km, which are underestimated due to impaction losses of the CPI in the C-ToF-AMS inlet system (see Sect. 2.1.2). This figure is adapted from Schulz et al. (2018, Supplement).

to much higher values. These data points originate from flights sections of flights AC14 and AC17 conducted on September 21 and 27, 2014. Different air masses were sampled during both flights. Aerosol particles sampled at altitudes between 4 and 5 km were strongly acidic (see Fig. 32, green diamonds). The sulfate mass concentration increased rapidly during these flight sections. The linear fit functions are shown in green. The solid green line presents the unconstrained fit function, whereas the dotted green line is constrained regarding the intercept, that is fixed to zero. The correlation coefficients are very low, and also the derived values for the slopes show that the aerosol particles of these specific flights sections are strongly acidic. The origin of the sampled air mass was found to be from Africa (Saturno et al., 2018). In case of this example, the increased sulfate mass concentrations were correlated with a volcanic eruption in central Africa. As a result the aerosol is much more acidic, despite of the long range transport time scale of ~ 15 days (Saturno et al., 2018). This case study is further analysed in Sect. 4.1.4.2.

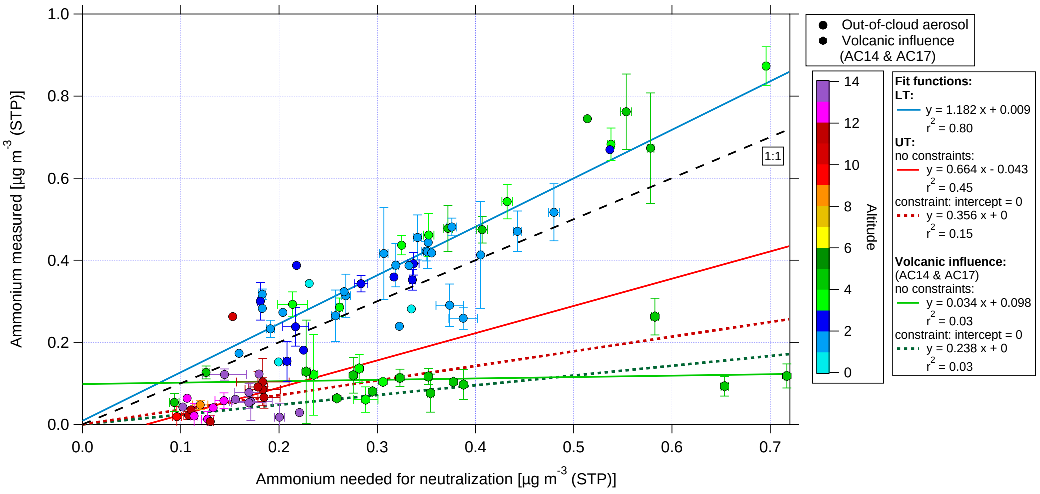

Figure 32: Scatter plot of measured and for neutralization needed ammonium. Data are averaged over five minutes, filtered according to the DL, and coloured with altitude. The dashed black line shows the 1:1 line. The diamonds indicate flight sections during AC14 and AC17 with strongly acidic aerosol at altitudes between 4 and 6 km. The solid coloured lines are the linear fit functions for the LT (blue), the UT (red), and the flight sections with strongly acidic aerosol (green), respectively. Also shown are two additional fit functions for the UT and the specific flight sections with strongly acidic aerosol assuming an intercept of zero (dotted lines in red and green, respectively). The uncertainties of both parameters are considered for the calculation of the linear fit coefficients (see Sect. C.4). For clarity reasons only some of the uncertainty bars are shown.

4.1.2.4 *Comparison with literature*

Measurements at different sites in the Amazon (e.g. ATTO as an example for remote forested areas close to Manaus, and Porto Velho as an example for areas that are affected by BB and deforestation in the south-western part) show the prevalent contribution of organic matter to the submicron non-refractory particle composition (e.g. Artaxo et al., 2013; Brito et al., 2014; Andreae et al., 2015). These findings are very similar to the observations made during the ACRIDICON-CHUVA campaign.

The main objectives of the SAMBBA campaign was the study of BB influence, but some flights were completed to investigate biogenic characteristics. The aerosol particles in the BL consisted predominantly of organics, followed by rBC and sulfate. According to the acidity calculations explained in Sect. C.3, the aerosol was found to be acidic in the flights around Manaus and north of Porto Velho, and neutralized in the flights to the south of Porto Velho (Allan et al., 2014). It was concluded that also organics can be involved in neutralization processes, but these are not included in the calculation as already mentioned.

Chen et al. (2015) reported that the organics accounted for 80 % of the submicron non-refractory aerosol and that the aerosol was acidic. It should be noted that these measurements were done during the wet season.

Shilling et al. (2018) investigates the aerosol chemical composition during the wet and dry season in the scope of the GoAmazon2014/5 campaign. The measurement period during the dry season was completed in parallel to the ACRIDICON-CHUVA campaign. The median mass concentrations measured on board of the G-1 at altitudes between 0.5 and 6 km were around 5 µg m^{-3} and thus slightly higher than the derived values from HALO ranging between 2.5 and 4 µg m^{-3} (see Fig. 27, panel a). The differences can be explained by the inlet losses in the CPI of the C-ToF-AMS on board of HALO (see Sect. 2.1.2). In a recent paper the data sets from both aircraft are compared (Mei et al., 2019).

4.1.2.5 *Summary*

The comparison between C-ToF-AMS and UHSAS-A was hindered by the different size ranges of both instruments. The shift of the size distribution to smaller particle diameters showed that mainly small particles ($d_p < 90$ nm) were present. These particles were measured with the C-ToF-AMS, but lie outside of the size range of the UHSAS-A. Thus, the observed differences in the comparison of the total mass (C_{AMS}+C_{rBC}) can be explained.

In general, the aerosol mass properties are different in the LT and UT. Organic matter is dominating the chemical composition at all altitudes with fractions of around 70 %. rBC contributes to the composition in the LT, but is negligible for higher altitudes. This indicates scavenging of aerosol particles during vertical transport of air masses. This is also supported by less aerosol mass in the MT compared to the LT. The contribution of nitrate increases significantly in the UT, indicating a different source compared to the LT.

For the acidity calculations only the inorganic fraction was considered. In the LT the aerosol was found to be mainly neutralized, whereas in the UT the aerosol is more acidic.

The measured aerosol mass concentrations and the observed dominant organic fraction during the ACRIDICON-CHUVA campaign confirm previous results from different field campaigns in the Amazon. In the following, the organic aerosol fraction is discussed in more detail.

4.1.3 *Secondary organic aerosol*

4.1.3.1 *Oxidation state of the organic aerosol* (partly adapted from Schulz et al. (2018))

The oxidation state gives further information on the properties of organic aerosol. The correlation between f_{43} and f_{44} was calculated for all out-of-

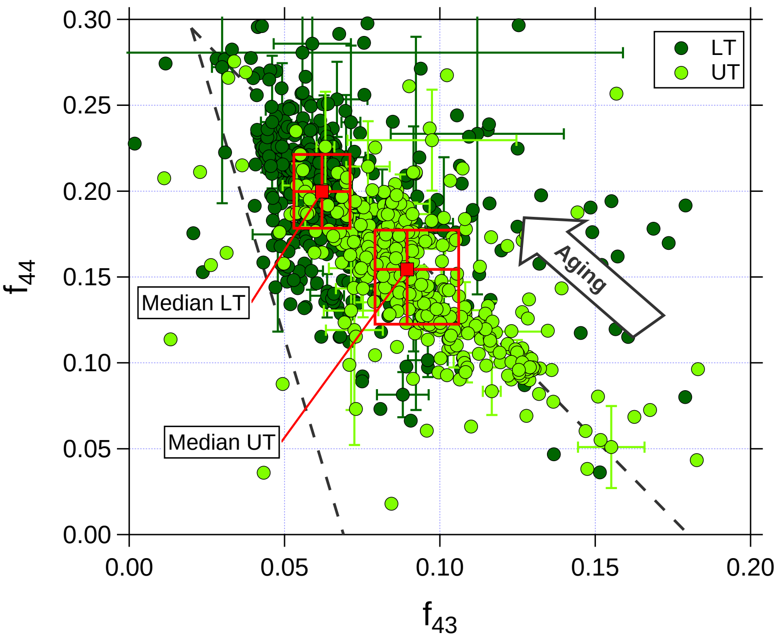

Figure 33: Scatter plot of f_{44} against f_{43} for the LT (dark green) and UT (light green) for data averaged over two minutes. Dashed lines indicate the triangular area according to the criteria introduced by Ng et al. (2010). Squared coloured markers and boxes show the median values and interquartile ranges for the LT and UT, respectively. For clarity reasons only some of the uncertainty bars are shown. This figure is adapted from Schulz et al. (2018).

cloud aerosol data from ACRIDICON-CHUVA (see Sect. 2.2.1.1). Figure 33 presents these data for the two different altitude regimes LT and UT averaged over two minutes. The two different colours indicate the altitude dependency. The dark green markers represent data sampled in the LT, whereas the light green markers show data from the UT. Although there is an overlapping region of both, a difference between LT and UT is observed. Most of the data sampled in the LT are located towards the upper left corner of the triangle, meaning that they are more oxidized. In comparison to this, data from the UT show different properties. Lower f_{44} and at the same time increased f_{43} values show a lower oxidation level of the organic aerosol. Also presented in Fig. 33 are the median values with the interquartile ranges for LT and UT, respectively. The median value for the UT has higher f_{43} and lower f_{44} values than the UT. That means organic aerosol measured in the UT is significantly less photooxidized than in the LT. Thus, the organic aerosol particles in LT and UT are different from each other. Some of the LT organic aerosol may be transported to higher altitudes, but most of the organic aerosol measured in the UT must have a different source that is not located in the BL or in the LT. The possibility that substantial amounts of aerosol are transported from the BL into the UT has been ruled out by the study of Andreae et al. (2018), based on the absence of detectable amounts of rBC in the UT (also

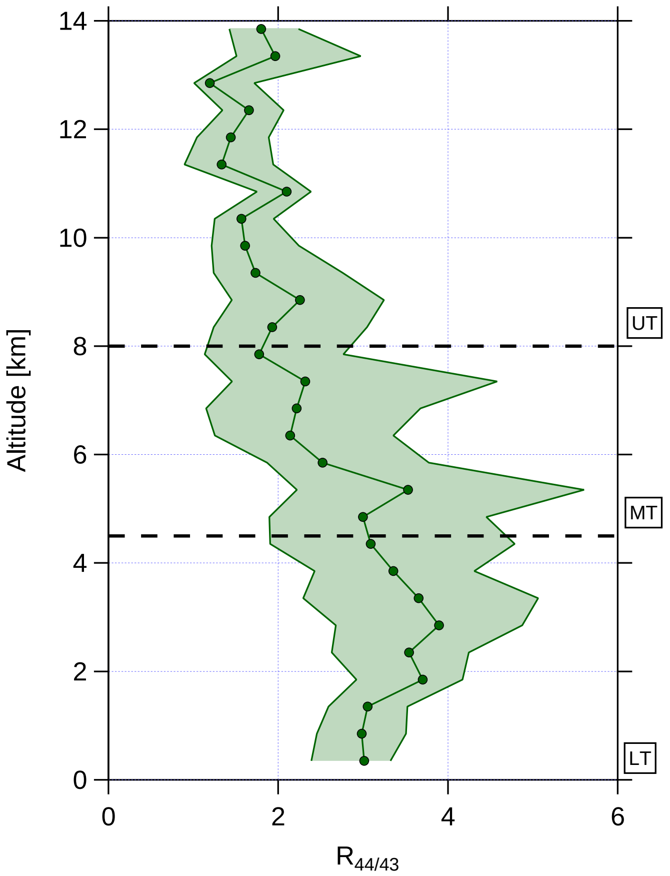

Figure 34: Vertical profile of median and interquartile ranges of $R_{44/43}$. The horizontal dashed lines indicate divisions into LT, MT and UT. This figure is adapted from Schulz et al. (2018).

see Fig. 29), and other differences in the properties of aerosol in the LT and UT.

Figure 34 illustrates the changes of $R_{44/43}$ with altitude. In the BL $R_{44/43}$ is constant, demonstrating that this layer is well mixed. With increasing altitudes this ratio decreases significantly to much lower values than in the LT. The lowest median values are observed in the UT.

This raises the question about the source of the observed organics in the UT. There are three different possibilities. First, horizontal long-range transport and a subsequent mixing of these air masses with convectively lofted air could occur. Second, particles from the near or distant BL might be transported aloft. A third possibility would be in-situ secondary organic aerosol formation (SOA) in the UT.

A horizontal long-range transport of air masses can be excluded due to the less photochemically aged organics in the UT. The organic aerosol particles in the UT show a lower $R_{44/43}$ ratio meaning that they did not experience much photooxidation, as it would be expected from aerosol influenced by

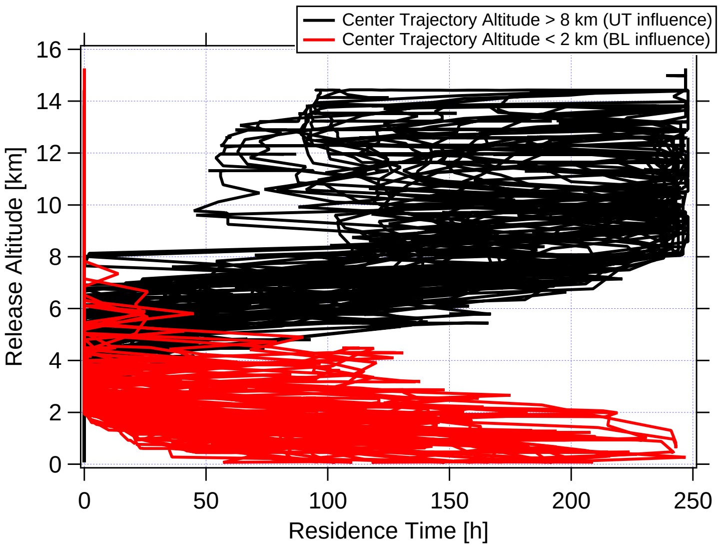

Figure 35: Release altitude of the FLEXPART trajectories against the residence time, i.e. the time that the trajectories spend in the BL (red) and in the UT (black). This figure is adapted from Schulz et al. (2018, Supplement).

long-range transport.

The second possibility, representing the fast convective vertical transport of particles from the BL, can also be ruled out as already mentioned above. The aerosol number concentrations differ considerably (see Fig. 24, panel a) between the LT and UT with strongly increased values in the UT. Furthermore, the sulfate and rBC aerosol mass concentrations show the highest values in the LT and decrease at higher altitudes (see Fig. 29, panel c and e). In case of a fast convective vertical transport of BL particles, the sulfate and rBC aerosol mass concentrations would show similar values in the LT and UT. The decrease at altitudes above 4.5 km indicates that the aerosol particles have been efficiently removed (e.g. scavenging) during vertical transport (Andreae et al., 2018).

Air mass trajectories were calculated using the FLEXPART model. The trajectories are calculated along the flight tracks starting every minute and calculated backwards for 10 days providing hourly information on the location of each trajectory. The FLEXPART model is not able to resolve convective transport (see Fig. 35) for the ACRIDICON-CHUVA campaign. Nevertheless, the origin of the trajectories that are released in the LT differs from the origin of the trajectories released in the UT (see Fig. 36). The trajectories released in the LT have their origin also in the LT, and show almost no interaction with air masses from higher altitudes (see Fig. 36, panel a). Most of the trajectories come from the Atlantic Ocean and the southern part of South America. In contrast to this, the trajectories released above 8 km have their origin mainly above the Pacific Ocean and circulate at high altitudes above South America (see Fig. 36, panel b). Just a minor part of the tra-

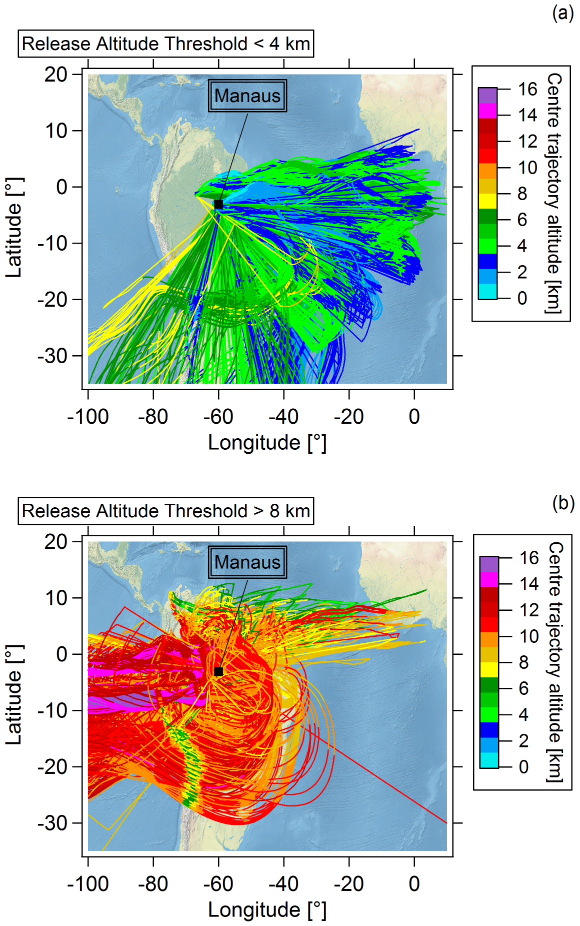

Figure 36: Maps with FLEXPART trajectories that are released in the (a) LT and (b) UT. The colour code refers to the altitude of the center trajectories. This figure is adapted from Schulz et al. (2018, Supplement).

jectories origins from the eastern direction, coming from the Atlantic Ocean and/or Africa. Interactions with air masses at lower altitudes are rare, most prominent is the lifting at the Andes mountains.

This leads to the conclusion that the third possibility, in-situ SOA formation with subsequent growth of the aerosol particles to large enough sizes that they can be detected by the C-ToF-AMS, is the dominant process in the UT. Another indication supporting this is the size information of aerosol particles with diameters between 90 and 600 nm. The size distribution is shifted to smaller diameters in the UT compared to the LT as already shown in Sect. 4.1.1. The highest concentrations of small particles in the specific size range are found in the UT (see Fig. 25).

The findings suggest the occurrence of SOA formation, especially in the UT. One formation pathway of SOA will be investigated in Sect. 4.1.3.2.

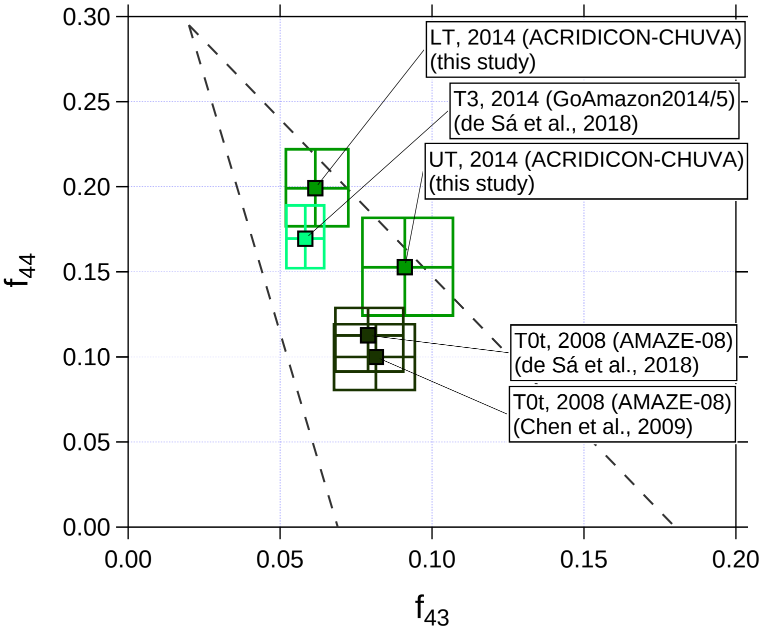

Figure 37: Scatter plot of f_{44} against f_{43} showing a comparison between different field campaigns performed in the Amazon region (Chen et al., 2009; de Sá et al., 2018). Dashed lines indicate the triangular area according to the criteria introduced by Ng et al. (2010). This figure is adapted from Schulz et al. (2018).

Comparison with literature

Previous field measurements that have been performed in the Amazon allow a comparison of the oxidation state from the data set of the ACRIDICON-CHUVA campaign with measurements taken at the ground at two different stations (T3 and T0t). Station T3 is an open field ca. 70 km west of Manaus and has frequent pollution influence from this city, whereas T0t is in a near-pristine rainforest ca. 60 km northwest of Manaus. Thus, they provide anthropogenically influenced or natural measurement conditions, respectively. For further information on the research stations see Martin et al. (2010) and Martin et al. (2016).
The data were collected during the AMAZE-08 and the GoAmazon2014/5 campaigns during the wet season (Feb/Mar 2008 and Feb/Mar 2014, respectively), and represent ground measurements (Chen et al., 2009; Schneider et al., 2011; de Sá et al., 2018). Figure 37 illustrates the median and interquartile ranges for the different data sets. Median values from the GoAmazon2014/5 campaign are similar to the median values derived from the ACRIDICON-CHUVA campaign sampled in the LT, showing that the organic aerosol is oxidized. In comparison, the AMAZE-08 campaign data differ, showing that the organic aerosol during AMAZE-08 was less oxidized. The data of the UT from the ACRIDICON-CHUVA campaign differ from both these data sets, indicating again a different source for the organic aerosol

in the UT than in the LT. Shilling et al. (2018) reported from airborne data of the GoAmazon14/5 campaign that the organics are more oxidized during the dry season compared to the wet season. However, it should be mentioned here that there is a significant variability of $m/z\,44$ (and f_{44}) among different AMS instruments (Crenn et al., 2015; Fröhlich et al., 2015; Pieber et al., 2016) such that a direct quantitative comparison between the different data sets shown in Fig. 37 is difficult.

Summary

The oxidation state of organic aerosol particles differs between different altitudes. In the LT median values of $R_{44/43}$ are higher than in the UT. This means that the organic aerosol is less oxidized with increasing altitude and shows the lowest ratios of f_{43} and f_{44} in the UT. However, also in the LT less oxidized organic aerosol can be found. Overall, lower ratios of f_{43} and f_{44} seem to be not the typical case in the LT. Compared to previous field campaigns, the oxidation state of the organic aerosol in the LT sampled during the ACRIDICON-CHUVA campaign is similar to ground measurements. Photooxidation of organic aerosol progresses with increasing residence time in the atmosphere. Thus, the organic aerosol in the UT need to have a different source than in the LT. The vertical profiles of the sulfate and rBC mass concentrations also indicate scavenging during vertical lifting, such that particles from the BL mostly do not reach the UT. This indicates that SOA formation occurs in the UT. The aerosol particle size is another hint that SOA formation takes place in the UT. The highest concentrations of the smallest particles in the size range between 90 and 600 nm are found in the UT (see Sect. 4.1.1).

4.1.3.2 *Observations of isoprene-epoxydiol-derived secondary organic aerosol (IEPOX-SOA)* (partly adapted from Schulz et al. (2018))

The previous section shows that SOA formation in the UT is responsible for less oxidized organic aerosol in the UT. Isoprene is an abundant VOC, especially in the Amazon basin. SOA from oxidation products of isoprene can contribute to the organic aerosol composition.

In the following, the out-of-cloud aerosol data are analysed with the question whether IEPOX-SOA is a general contributor to the organic aerosol in the Amazon basin.

As already explained above (see Sect. 2.2.1.3), f_{82} serves as a marker for IEPOX-SOA. A geographical overview of the measurements of f_{82} for the out-of-cloud aerosol during ACRIDICON-CHUVA is given in Fig. 38. Panel (a) shows the altitude against the longitude, and panel (b) shows the altitude against the latitude. Thus, the spatial dimensions of the flight tracks are depicted. The data points are coloured with f_{82}. Values that are similar to the

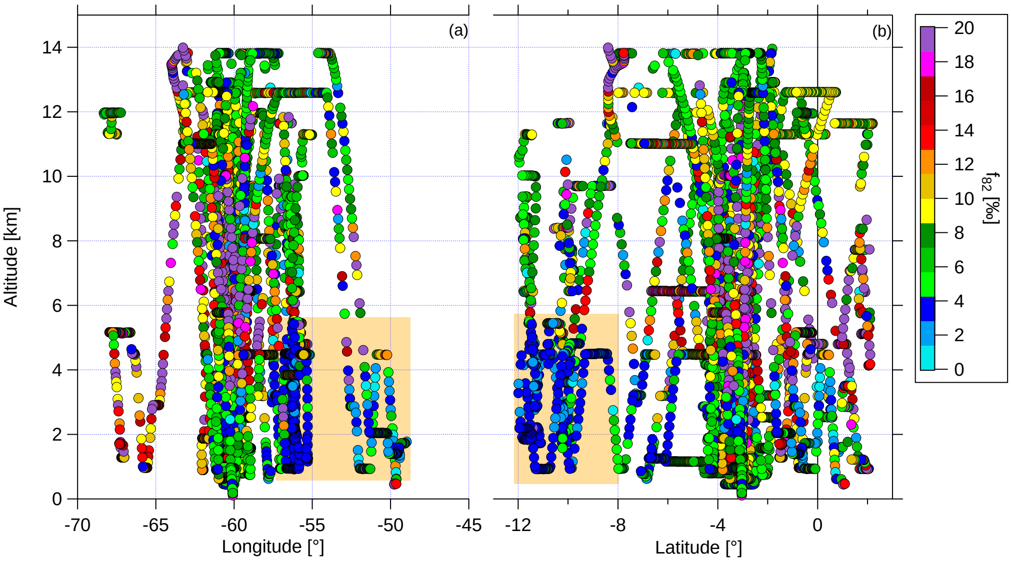

Figure 38: Flight tracks mapped with altitude against (a) longitude and (b) latitude, coloured with f_{82}. The orange shaded area depicts the region of the lowest f_{82} values that were observed during ACRIDICON-CHUVA.

background value for monoterpene regions (see Sect. 2.2.1.3) are shown in dark blue, whereas enhanced values are shown in green, yellow, red or pink. The background value of f_{82} is calculated using Eq. (9) and ranges between 4 and 5 ‰ (see Fig. 39, panel a). This value is slightly higher than the reported background value of 3 ‰ by Hu et al. (2015). Interestingly, in both panels (a) and (b) of Fig. 38 the orange shaded area highlights the lowest observed values for f_{82}. This area is located at -56 - -50° Lon and -12 - -8° Lat at altitudes between 0 and 5 km.

The reason for this can be seen in the map shown in Fig. 46. The southern part of the Amazon basin is characterized with deforested, often pastured areas. Thus, the remote rainforest gave way for agriculturally used land. The rainforest is the major emitter of VOCs as isoprene, the precursor gas of IEPOX-SOA. The changed land surface means that the composition of the local atmosphere is changed, as well. IEPOX-SOA cannot be formed above deforested areas without the precursor gas. A case study of this feature is presented later (see Sect. 4.1.4.1). This can also be observed when looking at all out-of-cloud aerosol data. Thus, the anthropogenically caused change of the land surface implies a regional modification of the locally formed aerosol composition above those surfaces.

A general increase of f_{82} is observed in the air above Manaus (-60° Lon, -3° Lat) at altitudes between 4 and 10 km. In the surrounding a mixture of organic aerosol with more enhanced and similar to background values are observed. Interestingly, values far above the background value are measured in the UT. In general, there seems to be a general abundance of IEPOX-SOA

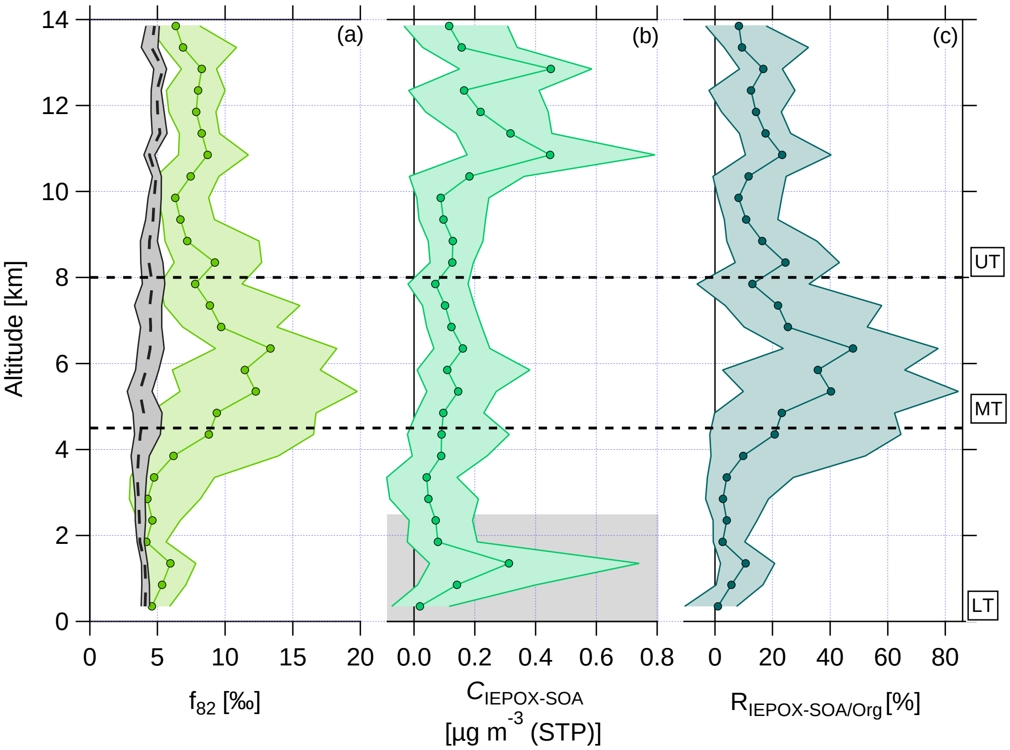

Figure 39: Vertical profiles of median and interquartile ranges of (a) f_{82}, (b) $C_{\text{IEPOX–SOA}}$, and (c) $R_{\text{IEPOX–SOA/Org}}$. The horizontal dashed lines indicate divisions into LT, MT and UT. The vertical dashed line with the grey shaded area in panel (a) presents the calculated median background values f_{82}^{Bg} with interquartile ranges using Eq. (9). This equation is valid for areas with strong monoterpene influence (Hu et al., 2015, Appendix A). The grey shaded area in panel (b) covers data sampled below 2.5 km, which are underestimated due to impaction losses of the CPI in the C-ToF-AMS inlet system (see Sect. 2.1.2). This figure is adapted from Schulz et al. (2018).

in the Amazon atmosphere at altitudes between ground and 14 km.

Figure 39 presents the vertical profile of the IEPOX-SOA tracer f_{82} (panel a) and the calculated median background values f_{82}^{Bg} (see Eq. 9). The median background values are quite constant between 4 and 5 ‰ over the whole altitude range with small interquartile ranges (see Fig. 39, panel a, vertical dashed line with interquartile ranges in grey). This indicates that continuous emissions and processing of isoprene tend to build an ubiquitous background level up to 14 km. In the LT, f_{82} shows constant median values around 5 ‰, slightly increasing in the interquartile ranges in the upper part of the LT. These values are similar to or higher than the calculated median background values f_{82}^{Bg}, suggesting an influence of IEPOX-SOA on the organic aerosol composition (see Sect. 2.2.1.3). In the UT, the values of f_{82} are again quite constant over the altitude range, but with increased median values around 8 ‰. The values in the UT lie above the background values and are even

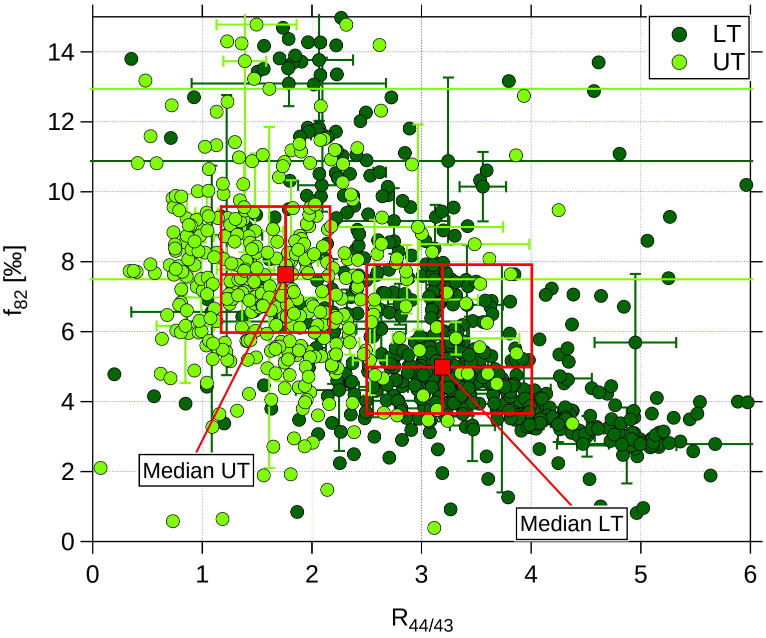

Figure 40: Scatter plot of f_{82} against $R_{44/43}$ for the LT (dark green) and UT (light green). Data are averaged over two minutes. The red markers and boxes show median values and interquartile ranges for the LT and UT, respectively. For clarity reasons only some of the uncertainty bars are shown. This figure is adapted from Schulz et al. (2018).

higher than in the LT. This indicates that IEPOX-SOA can have an important impact on the organic aerosol composition in the UT.

Although the characteristics of the MT are not the focus here due to the overall low organic mass concentrations, it should be mentioned that the highest median values of f_{82} were observed in the MT between 4.5 and 8 km. The interquartile ranges are extended here, but the median values reach up to 12 ‰.

Figure 39, panel (b) depicts the vertical profile of the median IEPOX-SOA mass concentrations, which are calculated using Eq. (8) (see Sect. 2.2.1.3). The lowest values can be found in the LT and MT. However, in the UT, especially at altitudes above 10 km, a strong increase of the IEPOX-SOA mass concentration is observed. Here, IEPOX-SOA contributes up to 20 % to the organic mass concentration (see Fig. 39, panel c). The highest contribution of IEPOX-SOA to the organic aerosol mass is observed in the MT, whereas in the LT up to 10 % can be attributed to IEPOX-SOA. This implies that not only in the LT, but also in the MT as well as in the UT IEPOX-SOA contributes to a significant amount to the organic aerosol composition.

The correlation of f_{82} with $R_{44/43}$ (as a measure of oxidation, see Sect. 4.1.3.1) is presented in Fig. 40 using data averaged over two minutes. Again, the two different green colours refer to the LT (dark green) and the UT (light green).

In the LT, high $R_{44/43}$ but low f_{82} values are observed. The f_{82} values are similar to or slightly below the calculated background value of ~4 ‰. However, lower $R_{44/43}$ values are correlated with higher f_{82} in the LT. For the UT the values of $R_{44/43}$ are generally lower, and correspond to higher f_{82} values. The median values for f_{82} and $R_{44/43}$ illustrate that the differences are also significant. This suggests that less photooxidized organic aerosol is related to IEPOX-SOA.

This leads to the question of the formation of IEPOX-SOA, especially in the UT. In general, SOA formation can occur either through NPF with subsequent growth or by condensation or reactive uptake on pre-existing particles without NPF. However, at the time that NPF occurs, the aerosol particles would be too small to be measurable with the C-ToF-AMS, implying that growth of these newly formed particles is necessary.

The formation pathway of IEPOX-SOA is illustrated in Fig. 4, and depends e.g. on the NO conditions. The observed enhanced NO mixing ratios (see Fig. 42 in Sect. 4.1.3.3) in the UT would likely change the reaction pathway of isoprene to a non-IEPOX route and subsequently no IEPOX-SOA formation would occur. Based on the observed IEPOX-SOA in the UT, the oxidation of isoprene to IEPOX may occur before reaching these high altitudes.

In previous laboratory studies it was found that acidic aerosol is needed for reactive uptake or condensation of gaseous IEPOX onto particles. In the laboratory, the acidic conditions are often realized by using sulfate seed particles (e.g., Surratt et al., 2010; Darer et al., 2011; Lin et al., 2012; Lin et al., 2013). Also in field studies a correlation between IEPOX-SOA and sulfate aerosol was proposed (e.g., Lin et al., 2013; Allan et al., 2014; Hu et al., 2015; Xu et al., 2015b; Marais et al., 2016; de Sá et al., 2017).

Figure 41 shows the scatter plot of IEPOX-SOA against nitrate (panel a) and sulfate (panel b) mass concentrations for LT and UT, respectively. The data are averaged over two minutes. In the LT, no correlation between IEPOX-SOA and nitrate is found. However, in the UT an enhanced correlation between IEPOX-SOA and nitrate can be seen (see Fig. 41, panel a). For sulfate, the correlation is very low both in the LT and UT (see Fig. 41, panel b). This indicates that sulfate might not be necessary for the formation of IEPOX-SOA, but nitrate could be an important, possibly sufficient component in the UT.

Although the correlation between IEPOX-SOA and nitrate is weak, it may indicate that not only sulfate, but also nitrate can provide the acidic conditions for the partitioning of IEPOX to IEPOX-SOA. The acidity calculations in Sect. 4.1.2.3 showed that the aerosol in the LT is mainly neutralized when taking the inorganics (nitrate and sulfate) into account. However, in the UT the aerosol is not fully neutralized considering the inorganics. The presence of organic sulfates and nitrates could also affect the acidity calculations. The out-of-cloud aerosol data are already corrected for the organic nitrates

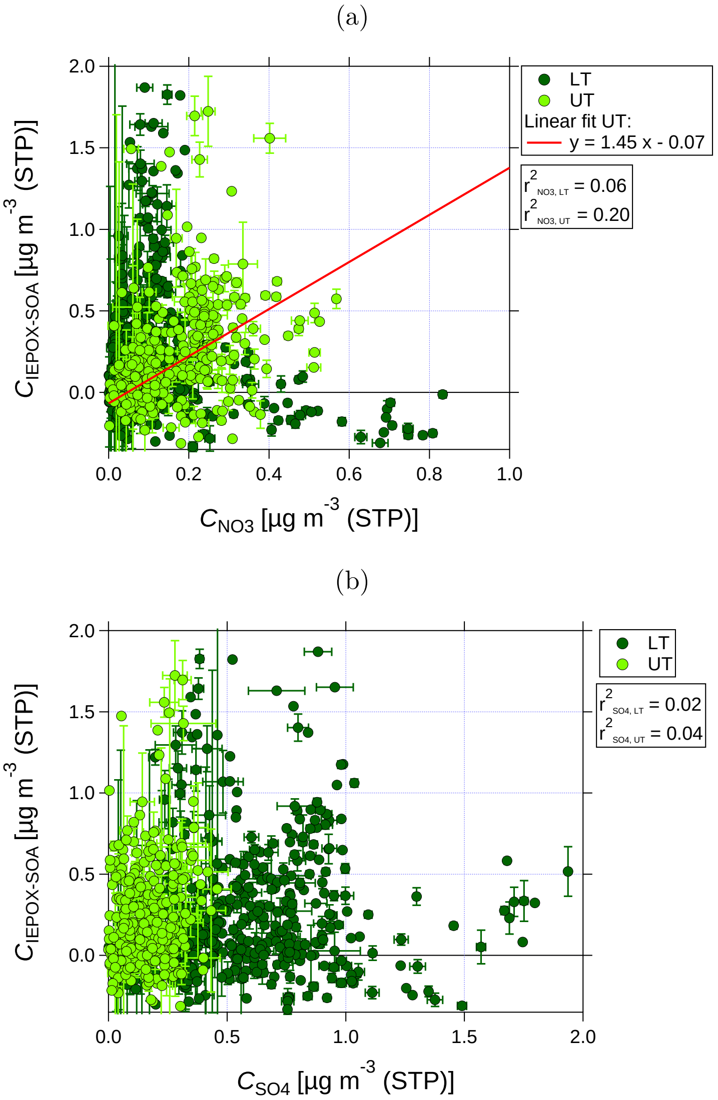

Figure 41: Panel (a): Scatter plot of $C_{\text{IEPOX–SOA}}$ against nitrate mass concentrations for the LT (dark green) and UT (light green). Data are averaged over two minutes and presented together with the values for Pearson's R^2 for the correlation between $C_{\text{IEPOX–SOA}}$ and nitrate mass concentration for the LT and UT, respectively. The linear regression for the correlation between $C_{\text{IEPOX–SOA}}$ and nitrate mass concentration in the UT considers the uncertainties from both parameters and is presented in (a). For clarity reasons only some of the uncertainty bars are shown. Panel (b): Same plot as panel (a), but for sulfate. Both figures are adapted from Schulz et al. (2018).

according to Sect. 2.2.2. However, for organic sulfates such a similar correction is not possible with data from a C-ToF-AMS as there are no different fragmentation patterns between inorganic and organic sulfates (Farmer et al., 2010).

The observed increase of the nitrate mass concentrations in the UT (see Fig. 29, panel b) and the enhanced correlation of nitrate and $C_{\text{IEPOX–SOA}}$

give indications for the formation of organic nitrates with the contribution of IEPOX. This is further investigated in Sect. 4.1.3.3.

Comparison with literature

Up to now f_{82} data from the tropical UT have not yet been reported elsewhere in the literature. Aircraft measurements above the Amazon rainforest were reported by Allan et al. (2014), but these data are restricted to altitudes below 5 km, corresponding to the definition of the LT in this study. In Allan et al. (2014), two cases are presented and show background (4 ‰) and increased values (9 ‰) of f_{82}. The highest values of f_{82} were found on top of the BL, decreasing with increasing altitudes. These values are similar to the data from the LT presented here although f_{82} remains constant above the BL.

During the GoAmazon14/5 campaign ground measurements at two different stations (T3 and T0t) were completed. The recent study by de Sá et al. (2017) reported measurements of IEPOX-SOA. The production of IEPOX-SOA was enhanced with increased sulfate concentration, but decreased with increased NO mixing ratios (de Sá et al., 2017). Thus, a correlation between IEPOX-SOA and sulfate was observed for the ground measurements (de Sá et al., 2017). This is different to the out-of-cloud aerosol data from the LT and UT of the ACRIDICON-CHUVA campaign.

The result of positive matrix factorization (PMF) analysis on the data from the ground station during the wet season show that the majority of the organic matter was SOA with the IEPOX-SOA factor contributing with 17 % (de Sá et al., 2018). This confirms the observations during the ACRIDICON-CHUVA campaign, where up to 10 % in the LT and up to 20 % in the UT of the organics can be explained with IEPOX-SOA.

Summary

IEPOX-SOA was observed in the LT, MT, and UT. There seems to be a ubiquitous background of IEPOX-SOA up to high altitudes. However, a local minimum of IEPOX-SOA was discovered above deforested regions as the source for isoprene is missing. The data from the UT showed that less oxidized organics are correlated with increased values of the IEPOX-SOA marker f_{82}. IEPOX-SOA contributes up to 10 % of the organic aerosol in the LT and up to 20 % in the UT. The formation of IEPOX-SOA can likely occur at all altitudes. Therefore, isoprene needs to be oxidized to IEPOX.

IEPOX can condense on pre-existing aerosol particles as the appropriate conditions are fulfilled, e.g. the acidity of the aerosol. Laboratory and previous field studies from the ground or low altitudes show that sulfate aerosol is often related to IEPOX condensation. This was not observed clearly in the out-of-cloud aerosol data of the ACRIDICON-CHUVA campaign. Instead, a stronger correlation with nitrate was found indicating the formation of organic nitrates.

4.1.3.3 *Particulate organic nitrates* (partly adapted from Schulz et al. (2018))

Organic nitrates form from the oxidation of biogenic VOC by NO_3 descending from reactive nitrogen (e.g., Ng et al., 2017). The vertical profiles of NO and NO_y mixing ratios are shown in Fig. 42, panel (a) and (b). The mixing ratios of both species are highest in the LT and decrease towards the MT before reaching increased values in the UT again. In the LT, increased NO_x mixing ratios arise from anthropogenic emissions coming from Manaus (Kuhn et al., 2010) and other pollution sources. A likely source for NO_x in the UT is the production by lightning (Schumann and Huntrieser, 2007). Due to the relatively low O_3 values in the UT, NO_x exists mainly in form of NO. After conversion to NO_y (mainly HNO_3), NO_x can act here also as a source for (organic) nitrate aerosol and explains the increase in nitrate aerosol mass concentration (see Sect. 4.1.2).

As already mentioned in Sect. 4.1.2, the detected ammonium in the out-of-cloud aerosol data is mainly sufficient enough to neutralize the aerosol in the LT, whereas in the UT the aerosol is not fully neutralized. However, also organics can react with inorganic species forming organic nitrates and sulfates. In the following, the four approaches to estimate the presence of organic nitrates as described in Sect. 2.2.2 are discussed.

A first estimation of the particulate nitrate content from organic nitrates is the ratio of NO^+ to NO_2^+. From calibration measurements with ammonium nitrate during the ACRIDICON-CHUVA campaign this ratio is known and was found to be in the range between 1.49 and 1.56 with a mean and standard deviation value of 1.52 ± 0.03.

Figure 43 shows the scatter plot of the corrected NO^+ and NO_2^+ for the LT (dark blue) and the UT (light blue). The linear fit curves for the LT and UT have an intercept of 0, proving that the applied correction described in Sect. 2.2.2 is essential. Nevertheless, it has to be noted that the correction is based on correlations between different m/z signals derived from measurements at low altitudes (Fry et al., 2018). Thus the application to UT data bears uncertainties, because the conditions (especially temperature) are different. However, data from a HR-ToF-AMS at these altitudes are currently not available.

The linear fit for the LT data shows a higher slope than that derived from calibrations with ammonium nitrate. The linear fit for the UT shows an even higher slope. This can be seen as a first hint that organic nitrates might be observed, especially in the UT.

Vertical profiles of median values of m/z 30 and m/z 46, and of the ratio NO^+ to NO_2^+ are depicted in Fig. 42, panel (c) and (d), respectively. During the whole vertical profile the two lines in panel (c) behave similarly, except

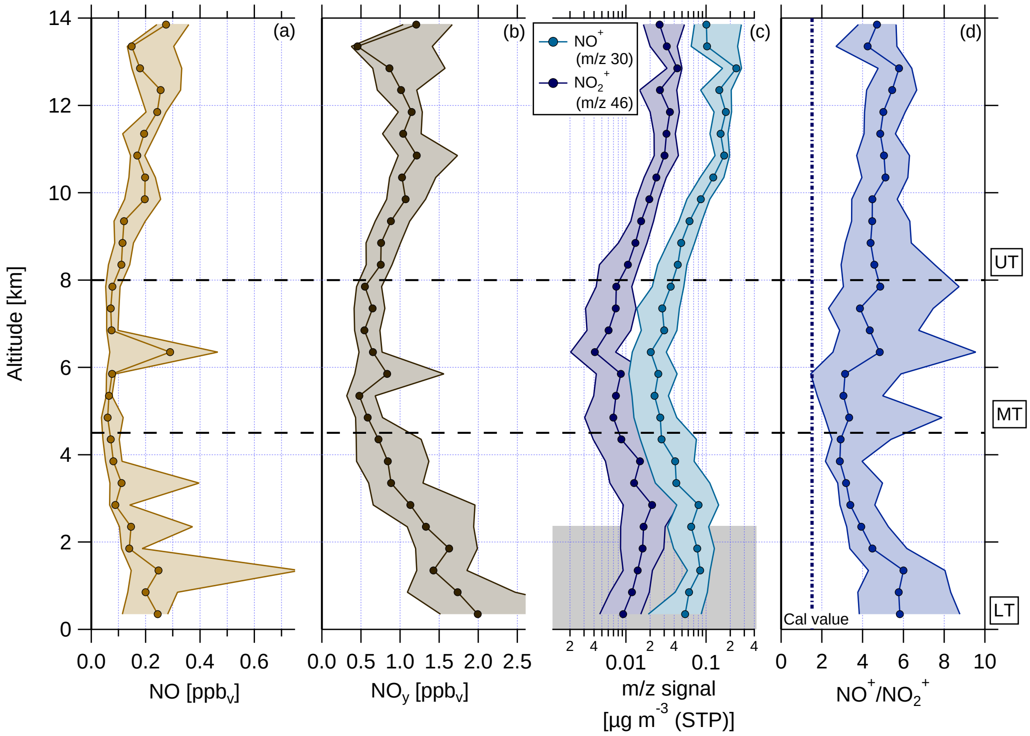

Figure 42: Vertical profiles of (a) NO mixing ratio, (b) reactive nitrogen NO_y mixing ratio, (c) NO^+ (m/z 30, light blue) and NO_2^+ (m/z 46, dark blue) mass signal, and (d) ratio of NO^+ (m/z 30) to NO_2^+ (m/z 46). Horizontal dashed lines indicate divisions into LT, MT and UT. The grey shaded area in panel (c) covers data sampled below 2.5 km, which are underestimated due to impaction losses of the CPI in the C-ToF-AMS inlet system (see Sect. 2.1.2). The vertical dashed line in panel (d) presents the ratio of NO^+ to NO_2^+ derived during calibration measurements. This figure is adapted from Schulz et al. (2018).

for the altitude range between 2 and 6 km, where the distance between them becomes smaller. Compared to the values derived from calibrations with ammonium nitrate, the measured ratios of NO^+ to NO_2^+ during the flights are much higher and the median values range between 2 and 6 (panel d). As described in Sect. 2.2.2, higher NO^+ to NO_2^+ ratios are an indicator for organic nitrates and the observed ratio profile can be seen as a first evidence for the presence of organic nitrates.

The second estimation provides a range with a lower and upper limit of nitrate mass concentration of organic nitrates according to Eq. (12) and (13) (Sect. 2.2.2). Figure 44, panel (a) shows the estimated lower and upper limits as vertical profiles. In the LT and MT the derived values are below or around zero such that a presence of organic nitrates is unlikely. However, with increasing altitude, the lower and upper limits are also increasing. Especially at altitudes higher than 10 km, both parameters are above zero and the presence of organic nitrates becomes likely. The weakness of this method lies in

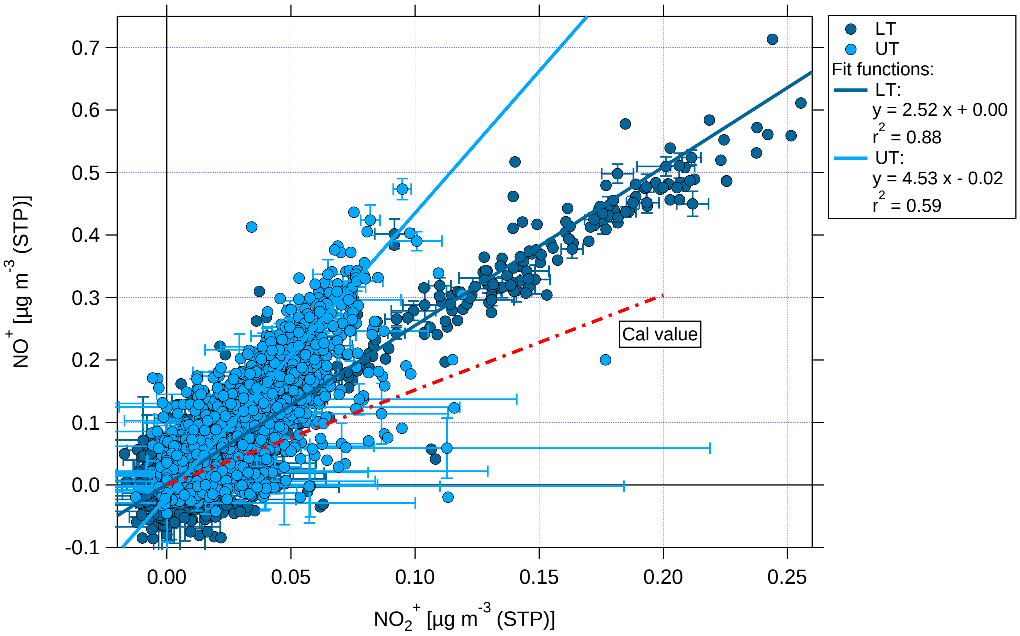

Figure 43: Scatter plot of NO^+ and NO_2^+ for the LT (dark blue) and the UT (light blue). The nitrate signals have been corrected for organic interference according to Fry et al. (2018). The linear fit curves are shown in dark blue for the LT, and in light blue for the UT, respectively. The uncertainties of both parameters are considered for the calculation of the linear fit curve coefficients (see Sect. C.4). For clarity reasons only some of the uncertainty bars are shown. The ratio of NO^+ and NO_2^+ derived from calibrations with ammonium nitrate is presented by the red dashed line. This figure is adapted from Schulz et al. (2018).

its dependence on ammonium measurements (see Eq. 12 and 13). Interferences of water in the fragmentation table can lead to a biased estimation of ammonium concentrations (Allan et al., 2004). Biased ammonium concentrations can be one reason for the derived negative values for upper and lower limits of $pRONO_2$.

The third approach uses Eq. (14) to estimate the amount of nitrate mass concentration of organic nitrates. As described in Kiendler-Scharr et al. (2016), a fixed value of 10 for R_{RONO_2} is used here (see Sect. 2.2.2). In Fig. 44, panel (b) the calculated particulate nitrate mass concentration of organic nitrates ($pRONO_2^{Farmer}$) is presented. The measured nitrate mass concentration is also shown. The detection limit is set to 0.1 µg m^{-3}, which was reported by Bruns et al. (2010) as a conservative approach. Calculated $pRONO_2^{Farmer}$ are quite similar to the measured nitrate in the vertical profile, although they are slightly smaller, especially in the UT. Values for $pRONO_2^{Farmer}$ in the LT and MT are below the detection limit. Interestingly, at altitudes above 10 km the derived values are partly above the detection limit. This points again to the presence of organic nitrates, especially in the UT at altitudes above 10 km, but the presence of organic nitrates at altitudes below 10 km

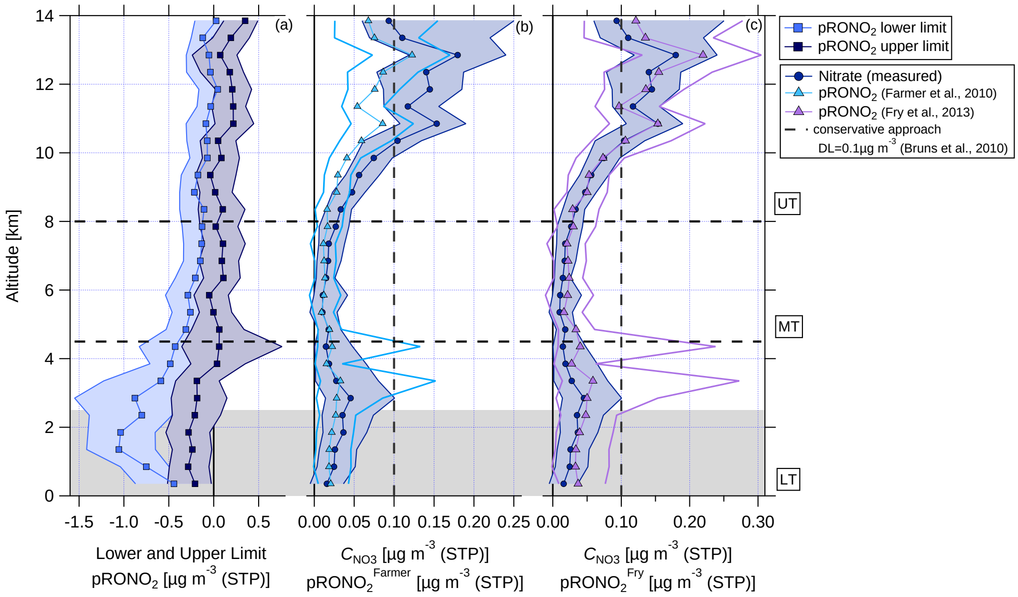

Figure 44: Vertical profiles of (a) calculated lower and upper limits of organic nitrate mass concentration, (b) measured nitrate mass concentration and organic nitrate mass concentration calculated according to Farmer et al. (2010) and Kiendler-Scharr et al. (2016), and (c) measured nitrate mass concentration and organic nitrate mass concentration calculated according to Fry et al. (2013). Horizontal dashed lines gives divisions into LT with BL, MT and UT. The vertical dashed line in (b) shows the conservative detection limit of 0.1 µg m^{-3} after Bruns et al. (2010). The grey shaded area covers data sampled below 2.5 km, which are underestimated due to impaction losses of the CPI in the C-ToF-AMS inlet system (see Sect. 2.1.2). Detailed information on the different approaches can be found in Sect. 2.2.2. This figure is adapted from Schulz et al. (2018).

cannot be excluded.

The fourth approach is based on Eq. (15) and addresses an estimation of the ratio of organic nitrates from the ratio for inorganic nitrates determined from the usual calibration measurements (see Sect. 2.2.2). Using the value of $R_{\mathrm{cal}} = 1.53 \pm 0.03$ from calibrations during the ACRIDICON-CHUVA campaign results in $R_{\mathrm{RONO_2}} = 3.44 \pm 0.05$ (mean and standard deviation). This value is lower than the ratios reported above from standards and also lower than the ratio that is used for the estimation of Farmer et al. (2010) and Kiendler-Scharr et al. (2016). The vertical profile of $\mathrm{pRONO}_2^{\mathrm{Fry}}$ is shown in Fig. 44, panel (c), again with the measured nitrate mass concentration in the background. The vertical profile of $\mathrm{pRONO}_2^{\mathrm{Fry}}$ shows similar values than the measured nitrate. At altitudes above 10 km the highest values are reached, suggesting the likely presence of organic nitrates. Some median values of $\mathrm{pRONO}_2^{\mathrm{Fry}}$ are slightly higher than the measured nitrate concentration, but this lies in the range of uncertainty of the data.

In Fig. 45, a comparison between the measured nitrate mass concentration and the calculated $pRONO_2$ according to Farmer et al. (2010) and Kiendler-Scharr et al. (2016) (panel a) and Fry et al. (2013) (panel b) is presented. The data are divided into LT (dark blue) and UT (light blue), and averaged over two minutes. The 1:1 line implies, that all nitrate is present as organic nitrate with a relative fraction of 100 %. The slope of the linear regression that lies below the 1:1 line describes the relative content of nitrate that is present as organic nitrate less than 100 %.

As a result of the scatter plot shown in Fig. 45, the estimation according to Farmer et al. (2010) and Kiendler-Scharr et al. (2016) could explain around 71 % of the measured nitrate in the UT and 32 % in the LT with organic nitrates (see Fig. 45, panel a). For the comparison with Fry et al. (2013), the whole amount of measured nitrate in the UT and 57 % of the measured nitrate in the LT could be explained by organic nitrates (see Fig. 45, panel b). The slight overestimation for the UT lies in the range of uncertainty of the data. As a qualitative result both comparisons show that in the UT a higher organic nitrate fraction is observed than in the LT.

The quantification of the nitrate content of organic nitrates remains difficult, but a qualitative statement can be made. Methods one, three and four agree with each other that at all altitudes organic nitrates are likely present. In the LT and MT, the calculated values lie below the detection limit introduced by Bruns et al. (2010). However, in the UT above 10 km the presence of organic nitrates is supported by the results of all four methods.

Another possible formation pathway of organic nitrate can occur via the isoprene oxidation in NO dominant conditions (see Fig. 4). As NO is increasing at higher altitudes (see Fig. 42, panel a), ISOPOO can oxidize to e.g. MACR leading to gas phase organic nitrates that can partition into the aerosol phase. Thus, organic nitrates formed from isoprene oxidation via a non-IEPOX pathway could also contribute to the SOA amount as IEPOX-SOA accounts for 20 % of the organic mass in the UT (see Sect. 4.1.3.2).

Organic sulfates can also be formed in the absence of sufficient ammonium. Farmer et al. (2010) reported that organic sulfates cannot be quantified using C-ToF-AMS data due to a missing tracer ion. Organic sulfates would lead to similar fragmentation patterns as inorganic sulfates (Farmer et al., 2010). However, as will be shown in Sect. 4.1.4.2, the ion at m/z 99 ($C_4H_3OS^+$) could be related to volcanically influenced organic sulfate.

Facing the similar mass concentration of nitrate and sulfate, and especially the increase of nitrate in the UT, the presence of organic nitrates likely plays a similar or even larger role than organic sulfates.

The study by Darer et al. (2011) about formation and stability of organic nitrates and sulfates reports that nitrate and sulfates have similar kinetic properties regarding the reaction with tertiary epoxides. According to their study, organic nitrates have shorter lifetimes than organic sulfates and are stable only for short time periods (a few days) before they undergo substi-

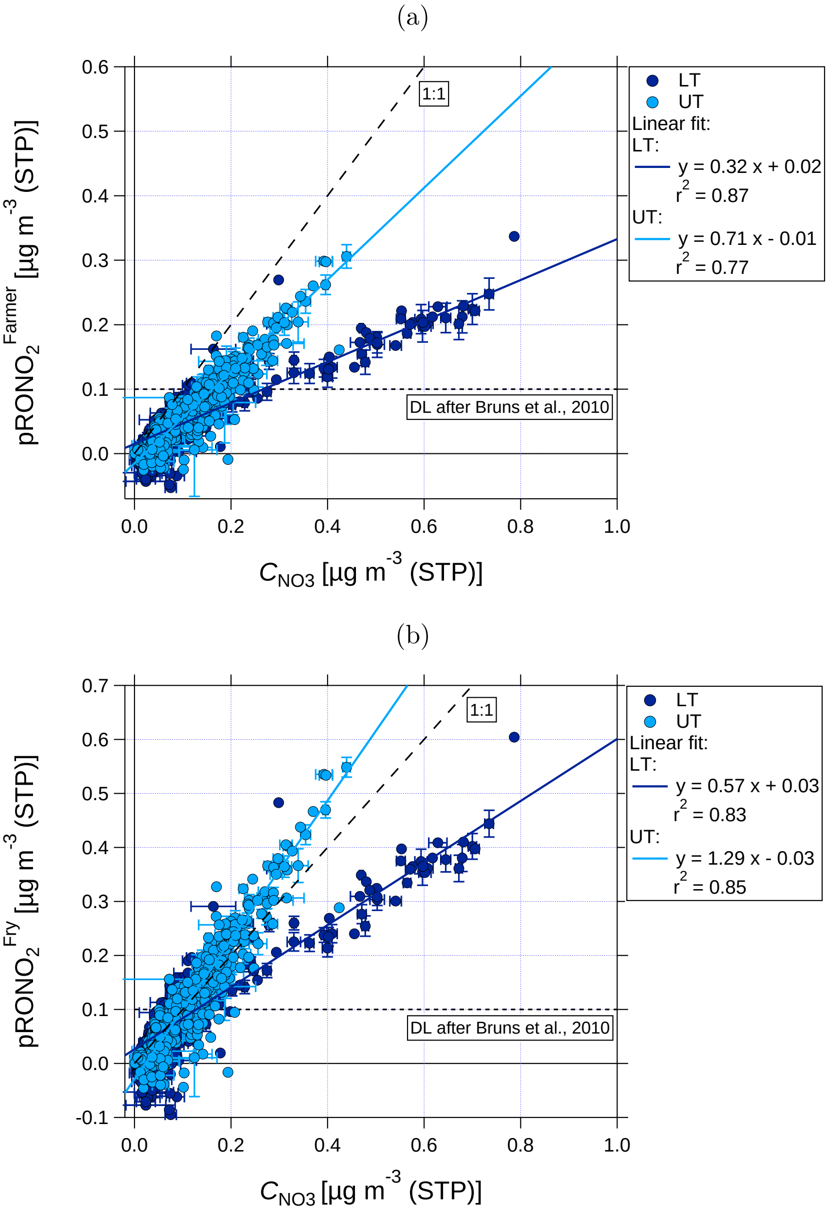

Figure 45: Panel (a): Scatter plot of measured nitrate mass concentration against organic nitrate mass concentration calculated according to Farmer et al. (2010) and Kiendler-Scharr et al. (2016) for the LT (dark blue) and UT (light blue), respectively. Data are averaged over two minutes. The horizontal dashed line shows the conservative detection limit of 0.1 $\mu g\,m^{-3}$ according to Bruns et al. (2010). The 1:1 line indicates that all particulate nitrate is present as organic nitrate. Also shown are the two fit functions for LT (dark blue) and UT (light blue) with correlation coefficients. The uncertainties of both parameters are considered for the calculation of the linear fit curve coefficients (see Sect. C.4). For clarity reasons only some of the uncertainty bars are shown. Panel (b): Same plot as panel (a), but with organic nitrate mass concentration calculated according to Fry et al. (2013). Both figures are adapted from Schulz et al. (2018).

tution reactions of nitrate by sulfate or water. Unfortunately, no statement of the temperature dependency of the reactions is given (Darer et al., 2011). The temperatures measured in the UT are low (210 - 240 K, see Fig. 20) and could slow down chemical reaction processes and possibly shift the reactions in favour of organic nitrates for a longer time period. In field experiments it was shown that low temperatures favour the formation of organic nitrates (Lee et al., 2014). The condensation of organic nitrates may be important for the growth of newly formed particles in the atmosphere (Berkemeier et al., 2016).

Another important factor for condensational growth may be the phase state of SOA particles. Over the Amazon basin, SOA particles are predicted to be liquid in the BL, whereas they are assumed to be mostly in a glassy state (solid) at altitudes above 5 km (Shiraiwa et al., 2017). Due to low temperatures and the phase state, diffusion processes are slowed down and/or limited. Gas-phase partitioning may favour in such conditions NPF with subsequent growth of the particles (Shiraiwa et al., 2017). The formation of organic nitrates with the contribution of IEPOX could serve as an example of such a process.

Comparison with literature

The aerosol particles measured during the SAMBBA aircraft campaign above the Amazon basin was found to be mainly neutralized, but there was evidence that some organic nitrate was present at altitudes up to 5 km (Allan et al., 2014).

Single particle measurements in the free troposphere showed that particles containing oxidized organics often also contain nitrate (Froyd et al., 2009). It is suggested that the gas-phase organic nitrates have lifetimes in the free troposphere that are long enough to enable partitioning of the organic nitrates between particle and gas phase (Froyd et al., 2009). Besides the above mentioned pathways including SOA formation, organic nitrates may also form via the reaction of organics with the nitrate radical (Ng et al., 2008).

Various field measurements in the US and Europe show that organic nitrates are ubiquitous, and that they play an important role in the formation of SOA (Ng et al., 2017). This may also apply to the Amazon basin as NO_x and VOCs are essential for the formation of organic nitrates, and abundant in the Amazon basin as well.

The presence of organic nitrates was observed in the Amazon atmosphere from ground measurements. The estimated amount of organic nitrates was 87 % of the total nitrate according to the ratio of NO_2^+ to NO^+ (de Sá et al., 2018, Supplement).

Single particle measurements in the tropical troposphere show that organic sulfates are abundant in the free troposphere (Froyd et al., 2010b). One of these organic sulfates was identified as an IEPOX sulfate ester and observed in 80 % of the measured particles in the tropical free troposphere. A direct comparison is difficult due to different measurement techniques. However, this supports the finding of IEPOX-SOA in the UT, although a sulfate contribution was not identified in the ACRIDICON-CHUVA data.

Summary

Four different methods to estimate the presence of organic nitrates were presented. Only a qualitative statement can be made. However, organic nitrate are likely present at all altitudes, especially in the UT the existence of organic nitrate is confirmed by all methods.
Nitrate aerosol particles can provide the necessary acidic conditions for the condensation of IEPOX. However, also a non-IEPOX pathway is possible under the enhanced NO conditions observed in the UT. Besides organic nitrates, also organic sulfate can form. However, the low temperatures in the UT would favour the formation of organic nitrates.
The phase state of SOA is supposed to influence condensation processes, and could affect NPF with subsequent growth of the particles in the UT rather than condense on pre-existing solid SOA.

4.1.4 *Case studies*

Some case studies from the ACRIDICON-CHUVA campaign are discussed briefly in this section. Organic mass spectra are shown for different cases. Furthermore, scatter plots of f_{44} and f_{43}, and f_{44} and f_{60} will be presented (see Sect. 2.2.1.1 and 2.2.1.2). The map in Fig. 46 highlights the discussed flights sections. The case studies describes influences of forestation on SOA properties, African volcanic emissions on aerosol composition, and biomass burning influence. All the shown spectra are representative for conditions found in the Amazon rainforest, but do not serve for generalization as statistical analyses are not done for these case studies.

4.1.4.1 *Influence of forestation on SOA properties*

The specific analysis of two flights, AC12 and AC18, highlights the influence of forested and deforested areas with respect to the presence of IEPOX-SOA. Figure 47 shows the normalized averaged organic mass spectra of two flights sections measured in the LT during flight AC12 and AC18. The spectra are normalized to the highest peak of the spectra, m/z 44. Thus, a difference seen in the spectra is a relative difference with respect to m/z 44. The mass spectrum from flight AC12 was averaged over 9.5 min, whereas the mass spectrum of AC18 was averaged over 12.5 min. The different locations of the flight sections are visible in the map shown in Fig. 46 in green and brown, respectively. AC12 was conducted on September 18, 2014 over a deforested

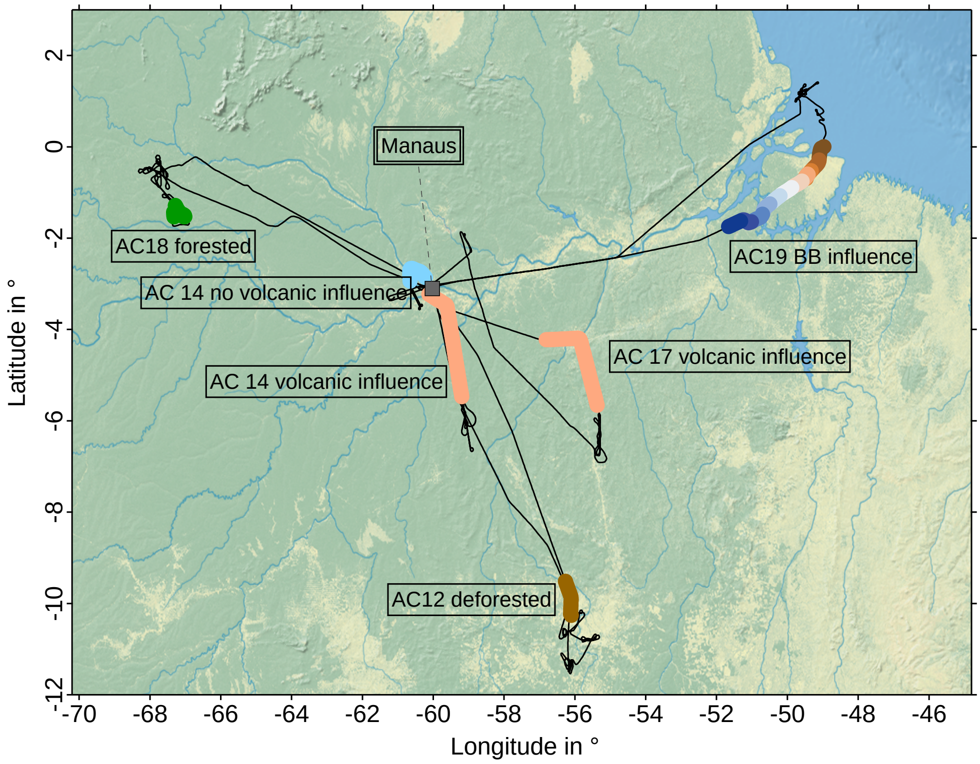

Figure 46: Map of the selected flights sections with the whole flight track in black, respectively. The colours of the sections refer to the colours of corresponding figures shown in the following. The location of Manaus is labelled.

area, whereas AC18 was completed on September 28, 2014 above a remote and forested area.

The organic mass spectrum measured during AC12 is dominated by peaks at m/z 28 and 44. There is almost no contribution from peaks at higher m/z. This spectra is typical for oxidized organics (see Sect. 2.2.1.1 and Zhang et al. (2005a)).

In contrast is the mass spectrum obtained during AC18. It is also dominated by peaks at m/z 28 and 44, but also major contributions from peaks at m/z 29 and 43 are observed. Furthermore, peaks at m/z 53, 55 and 82 are visible. Especially the marker peaks at m/z 29, 43, 53 and 82 are typical for IEPOX-SOA (see Sect. 2.2.1.3 and Robinson et al. (2011)).

Relative to m/z 44 the contributions of m/z 43 vary above forested and deforested areas. Information on the oxidation state can be derived when comparing the signals at m/z 43 and 44 (see Sect. 2.2.1.1). As already investigated in Sect. 4.1.3.1 differences in the oxidation state can be expected for different altitude regions. As this case study compares two flights sections sampled in the LT, the oxidation state differs for aerosol sampled above forested and deforested regions. The scatter plot of f_{44} and f_{43} is shown in Fig. 48, panel a. The data are clearly separated into two spots. Organic aerosol sampled

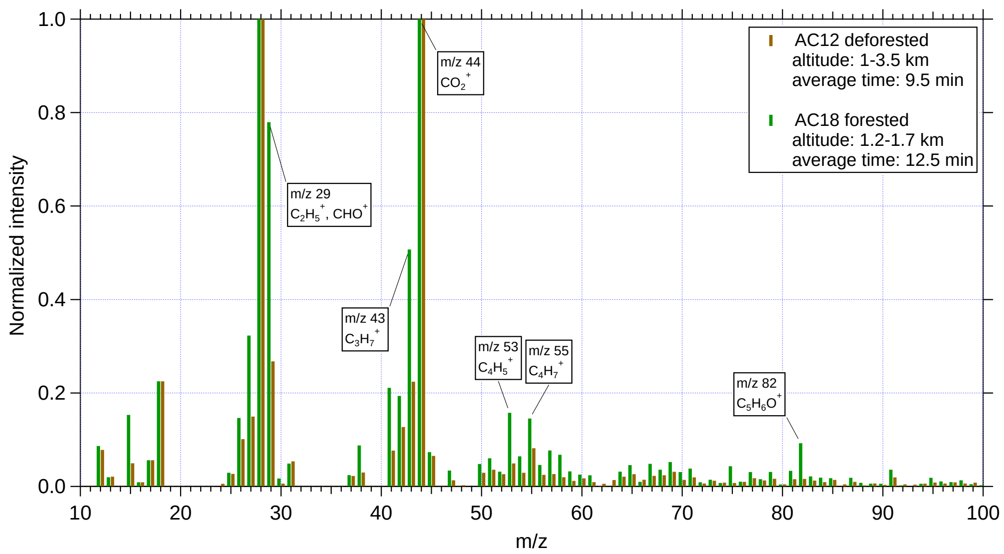

Figure 47: Normalized averaged organic mass spectra during flights sections of the flights AC12 (brown, representing deforested conditions) and AC18 (green, representing forested conditions), conducted on September 18 and 28, 2014, respectively. Specific peaks are labelled.

above deforested area show a higher oxidation state than the organic aerosol sampled above the forested area.

Figure 48, panel (b) depicts the scatter plot of f_{44} against f_{82} for the two flight sections. Data sampled above the deforested area show f_{82} values below 5 ‰ and scatter around the calculated background value (see Eq. 9 in Sect. 2.2.1.3). In contrast, the data sampled above the forested area are strongly enhanced with values between 10 and 20 ‰. The calculated background is slightly larger than for the deforested example. However, the data of the forested area are severely enhanced compared to the background value. Thus, an influence of IEPOX-SOA is observed for forested areas. The aerosol sampled above the deforested area consisted of strongly oxygenated organics. The geographical difference between the flights (see map in Fig. 46) is likely to explain this finding. AC18 was conducted north-west of Manaus above a strongly forested and remote region. The conditions for the formation of IEPOX-SOA are given, as e.g. isoprene is available due to emissions from vegetation, and oxidation can take place leading to IEPOX-SOA. In contrast, flight AC12 was conducted south of Manaus above a deforested region. This region is characterized with pastured areas and some cities. As the remote vegetation is missing in the surrounding of the flight section where the measurements took place, an important factor (isoprene) for IEPOX-SOA formation is not available. This is likely to explain the absence of locally formed IEPOX-SOA observed during AC12.

This example illustrates the different aerosol composition above forested and deforested areas with respect to SOA formation.

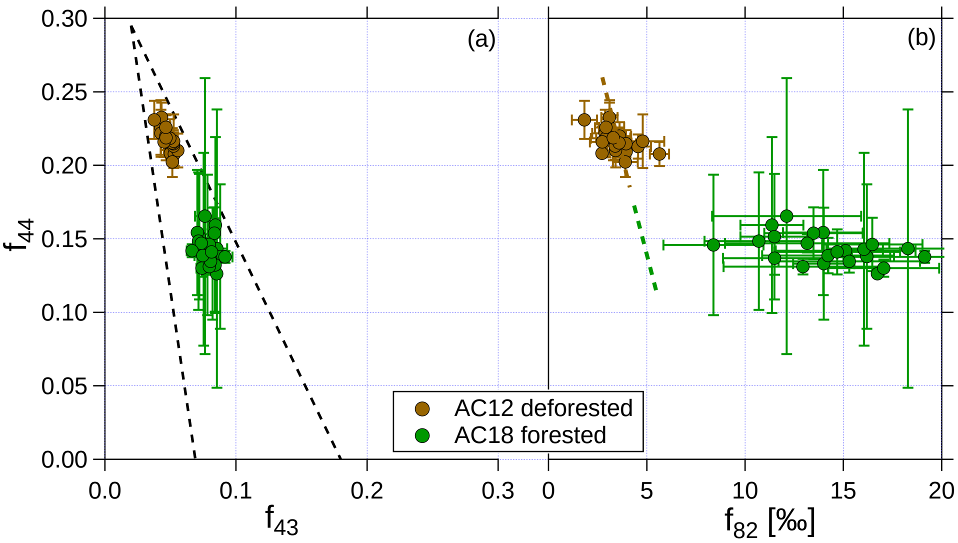

Figure 48: Panel (a): Scatter plot of f_{44} vs. f_{43} for the flights sections during AC12 and AC18 representing deforested and forested conditions. The dashed lines indicate the triangle in where the data are typically located (see Sect. 2.2.1.1 and Ng et al. (2011a)). For clarity reasons only some of the uncertainty bars are shown. Panel (b): Scatter plot of f_{44} vs. f_{82} for the same flights sections. The coloured dashed lines represent the calculated background values of f_{82} (see Sect. 2.2.1.3 and Hu et al. (2015)).

4.1.4.2 *Volcanic influence*

Emissions of African volcanoes can influence the aerosol properties in the Amazon basin (e.g., Andreae and Andreae, 1988; Pöhlker et al., 2018a; Saturno et al., 2018). Occasionally, volcanic emissions from Africa are transported above the Atlantic ocean and can reach the Amazon basin. During this long-range transport the volcanic gaseous sulfur emissions are processed leading to the formation of sulfate aerosol (Salcedo et al., 2006; DeCarlo et al., 2008).

During the flights AC14 and AC17 conducted on September 21 and 27, 2014 these long-range transported air masses were observed. Figure 49 shows the time series of the altitude, the CO mixing ratio, and the organic and sulfate aerosol mass concentrations during AC14 and AC17. The time period with the volcanic influence is highlighted in red (panel a and b), whereas the time period without volcanic influence is highlighted in light blue (panel a). The volcanically influenced air mass was measured at altitudes of 4 - 5 km during both flights. The CO mixing ratio shows constant values around 80 ppb. The organic mass concentrations were low with values below 1 $\mu g\,m^{-3}$. In contrast, the sulfate mass concentrations are strongly enhanced with values between 1 and 2.2 $\mu g\,m^{-3}$, respectively. The aerosol composition in the Amazon basin is usually dominated by organics (see Sect. 4.1.2.2 and e.g. Artaxo

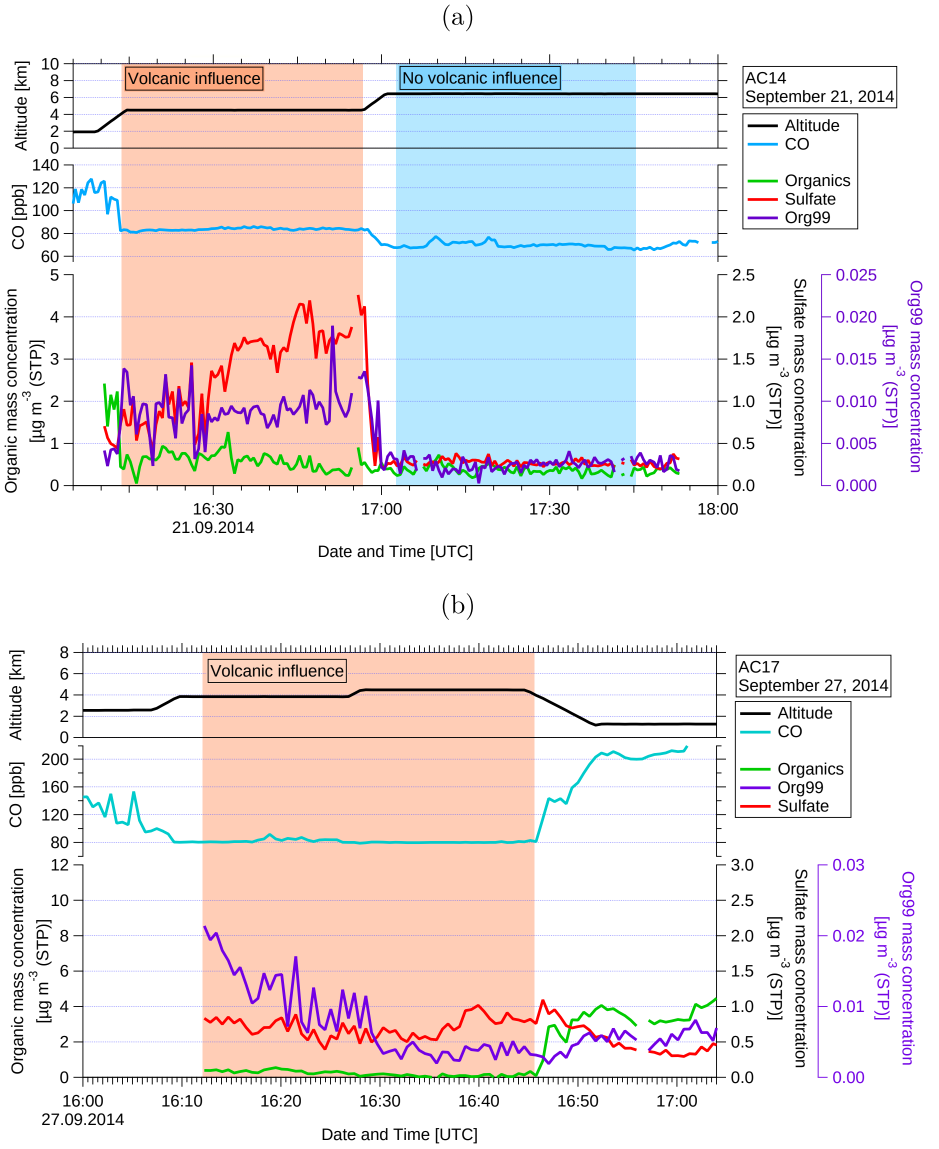

Figure 49: Panel (a): Time series of altitude (upper panel, black), CO mixing ratio (middle panel, light blue), and aerosol mass concentrations (lower panel) for organics (green), sulfate (red), and Org99 (purple) for flight AC14, conducted on September 21, 2014. The period of the measurements of volcanic influenced air is highlighted in red. The period without volcanic influence is highlighted in light blue. Panel (b): Same plot as panel (a) for flight AC17, conducted on September 27, 2014. The period of the measurements of volcanic influenced air is highlighted in red.

et al. (2013), Brito et al. (2014), and Andreae et al. (2015)). Here, the sulfate concentrations are dominating and show high values for the Amazon basin compared to the organics. These increased sulfate mass concentrations are only observed under volcanic influence (Saturno et al., 2018). For a comparison the flight section of AC14 at 6 km altitude is presented (see Fig. 49,

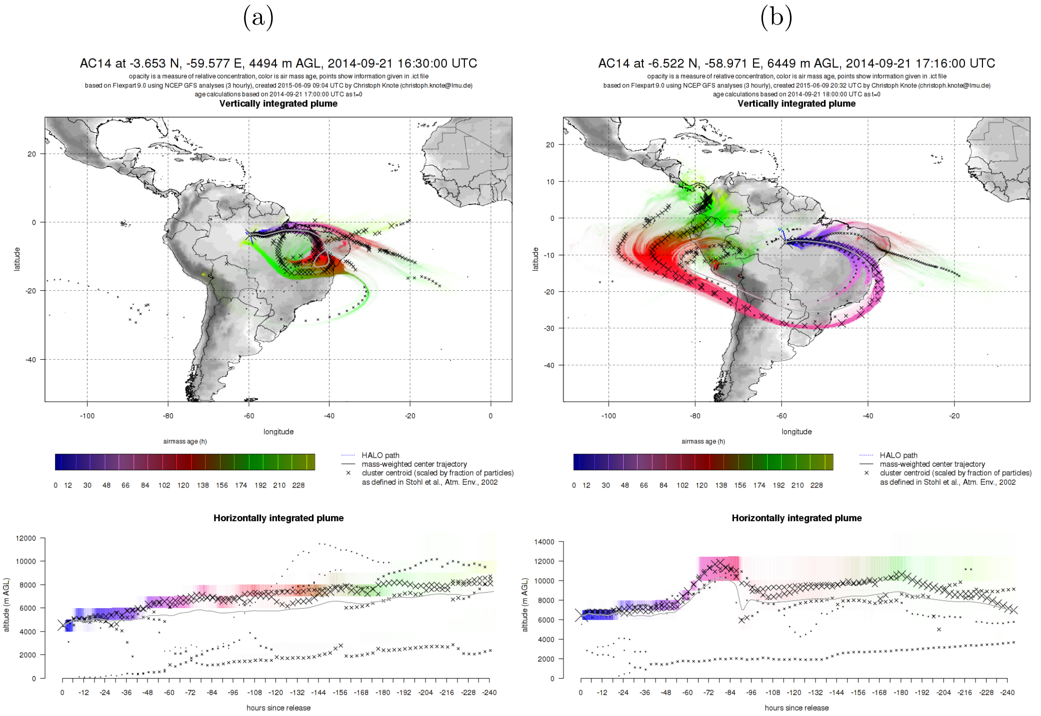

Figure 50: Panel (a): Exemplary FLEXPART trajectories for the time period of volcanic influence during flight AC14. The horizontally and vertically integrated plume was calculated along the flight track. Panel (b): Same plot as panel (a), but valid for the time period without volcanic influence during flight AC14.

panel a, light blue shaded area). The CO values are around 70 ppb and lower than during the time periods of volcanic influence. The organic and sulfate mass concentrations are less than 0.5 µg m^{-3} and show different characteristics than the time period of volcanic influence.
Backward trajectory calculations with FLEXPART were performed along the flight track and show that the air masses sampled for the time period with volcanic influence partly originated from southern Africa (see Fig. 50, panel a). The air mass was transported above the Atlantic ocean and arrived the Amazon basin in a distinct layer between 4 and 5 km (see Fig. 49 and Saturno et al. (2018)). A detailed study on this transport pathway can be found in Saturno et al. (2018). The backward trajectories for the air mass without volcanic influence shows that the origin was mainly above the western coast of South America resulting in different air mass characteristics as described above (see Fig. 50, panel b).
Comparing the different characteristics of the two air masses, the difference should also be visible in the mass spectra. The normalized averaged mass spectra for organics (green) and sulfate (red) are shown in Fig. 51 and taken from the highlighted flights sections of flight AC14 (see Fig. 49, panel a). The lighter colours represent the volcanic influenced time period, whereas

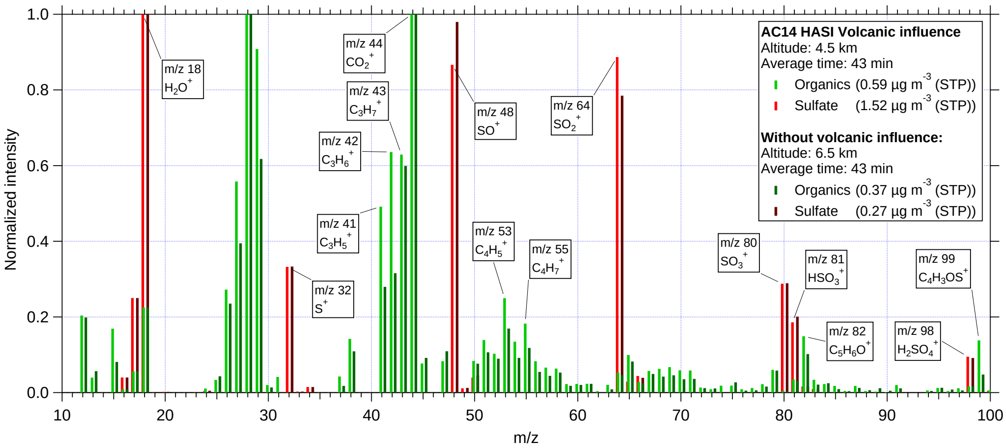

Figure 51: Averaged mass spectra of organics (green) and sulfate (red) for the time period with and without the enhanced sulfate concentrations showing the influence of an African volcano during the flight AC14, completed on September 21, 2014.

the darker colours refer to the non-volcanic influence. Specific ions are labelled, respectively. For sulfate the mass spectra are normalized to the signal intensity of the ion at $m/z\,18$, for organics the signal at $m/z\,44$ was used. The averaging time for both spectra are 43 min. The corresponding mass concentrations are given in the legend, respectively. The sulfate mass spectra show the typical fragmentation of sulfate, which consists of ions at $m/z\,18$, 32, 48, 64, 80, 81 and 98. Interestingly, the signals at $m/z\,48$ and 64 contributes with a different proportion relative to the signal at $m/z\,18$. The volcanic influenced sulfate shows a higher contribution of $m/z\,64$ than the non-volcanic sulfate.

The organic mass spectra are both characterized by marker peaks at $m/z\,29$, 41, 43, 44, and 55 indicating a mixture of oxidized organic aerosol (see Sect. 2.2.1.1). Interestingly, the ratios of $m/z\,41$ and 42 relative to $m/z\,44$ differ between the aerosol measured during volcanic and non-volcanic influence, whereas the relative ratio of $m/z\,43$ is similar, respectively. This indicates different organics, possibly explained by the geographical origin and processes during transport. Marker peaks for IEPOX-SOA are also visible in the spectra for both time periods, albeit the volcanic influenced organic aerosol show a higher signal intensity of $m/z\,82$. As already explained, IEPOX-SOA formation is favoured under acidic conditions (see Sect. 2.2.1.3 and 4.1.3.2). An assumption would be that the processed sulfate aerosol from the long-range transport provide surface for further reactions. As it was already discussed in Sect. 4.1.2.3, the acidity of this aerosol is strongly enhanced. This could favour reactions, e.g. condensation or reactive uptake of VOCs leading to organic sulfates. Combined with the enhanced peak at $m/z\,82$ in the organic mass spectra of volcanic influence, the condensation of IEPOX resulting in organic sulfates is likely observed during this flight section. Interestingly, the peak at m/z 99 is pronounced in the organic mass spectrum with volcanic influence. The enhanced peak at m/z 99 was detected during all flight sections that are related to these long-range transported air masses. This suggests that the peak at m/z 99 could be related to volcanically influenced air masses.

There could be different reasons explaining this distinct peak. One possibility could be that the ion at m/z 99 is $H_3SO_4^+$, as it could be formed in the vaporization and ionization process of sulfate or sulfuric acid. However, it is unlikely that more $H_3SO_4^+$ ions than $H_2SO_4^+$ ions are formed (Hogrefe et al., 2004).

Another possible explanation would be that the source ion of the peak at m/z 99 is related to organic sulfates ($C_4H_3OS^+$). The mass spectra of organic sulfates have the same fragmentation pattern as inorganic sulfates (Farmer et al., 2010), and could be therefore not identified. However, a recent study by Huang et al. (2015) showed that the signal at m/z 99 can partially explained by the organic sulfate ion $C_4H_3OS^+$ although the signal intensity is rather low. There is no standard mass spectra for organic sulfates representing the current conditions in the Amazon basin. Thus, a complete explanation of the source ion of m/z 99 is not available.

The time series of Org99 mass concentration is presented in purple in Fig. 49. During the time period of volcanic influence the mass concentration of Org99 is enhanced, whereas it is much lower during the time period without volcanic influence. Although Org99 and the increased sulfate mass concentration are not identical in their temporal evolution, a correlation of both parameters during the time of the volcanic influence is observed. Further investigation of this feature is needed. However, this example gives indications that an enhanced peak of m/z 99 could be related to organic sulfates.

4.1.4.3 *Biomass burning influence*

The last example presented here is the influence of biomass burning (BB) on the organic aerosol composition. This influence is investigated with the tracer f_{60} (see Sect. 2.2.1.2). Several flights aimed at the chasing of air and clouds above BB regions. However, the measured f_{60} values are almost always close to the threshold value of 3 ‰ during the whole campaign (see Fig. 54, panel a). There seems to be a dependency of the altitude, but this is just visible for the parameter f_{44} and was discussed in Sect. 4.1.3.1. Some of the data points are below zero. This shows the scattering of the signal at m/z 60.

Especially during the dry season emissions of BB influence the aerosol composition in the Amazon rainforest (Darbyshire et al., 2018). Thus, it was expected that the influence of BB is more obvious in the data and the observed low values of f_{60} are not anticipated. Flight AC19 headed to the Atlantic coast. On the way a large fire from BB was spotted by the scien-

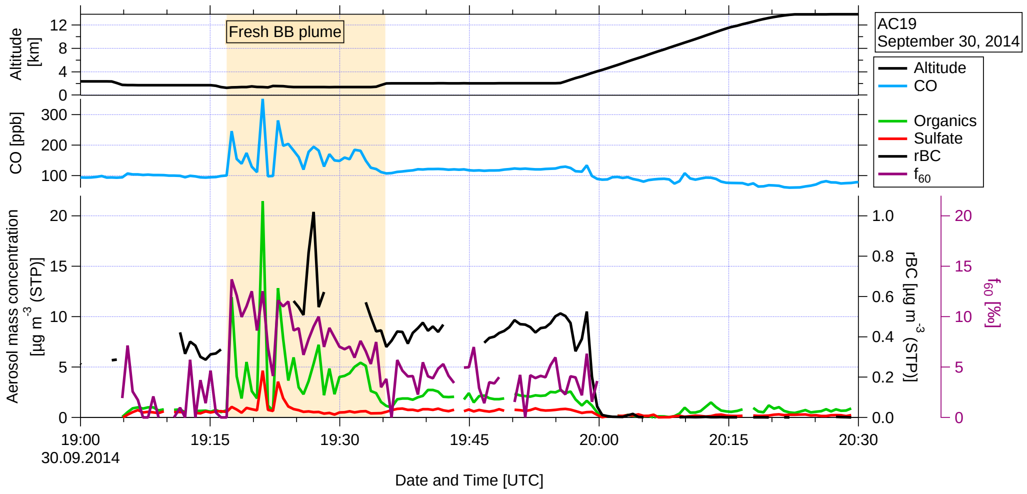

Figure 52: Time series of altitude (upper panel, black), CO mixing ratios (middle panel, blue), and aerosol mass concentrations (lower panel) including organics (green), sulfate (red), rBC (black), and f_{60} (purple) for a flight section of AC19 completed on September 30, 2014 showing the influence of a freshly emitted BB plume.

tists, and the flight pattern was changed to probe the fire emissions. The flight AC19 was conducted on September 30, 2014. The time series show a strong increase for the organics, sulfate, and rBC mass concentrations (see Fig. 52, the appropriate time period is highlighted in light orange). Also the CO mixing ratio was increased significantly in this period. Also depicted in Fig. 52 is the time series of f_{60} with enhanced values during the time period of the fresh BB plume. Despite the probing of the BB plume, f_{60} is decreasing within a few minutes. This indicates that f_{60} is reduced already on a short time scale. The normalized averaged organic mass spectrum for the highlighted time period is shown in Fig. 53. The spectrum was normalized to the signal intensity at m/z 44. The marker peaks for BB at m/z 60 and 73 are visible and labelled. Figure 54, panel (a) shows the scatter plot of f_{44} and f_{60} for the out-of-cloud aerosol measured during all flights of the ACRIDICON-CHUVA campaign. The values are around or below the threshold of 3 ‰ reported by Cubison et al. (2011). Interestingly, the data points from the flight section of the fresh BB plume during AC19 are different (see Fig. 54, panel b). The data sampled before the fresh BB plume show again values around the threshold (dark brown squares). During the plume f_{60} is significantly enhanced with 14 ‰. However, f_{60} is reduced within 20 min to values close to the threshold at 3 ‰. This suggests that the aerosol from the BB source is oxidized strongly by OH, and that the marker f_{60} is reduced to threshold values, with at the same time increasing f_{44} values. The fast oxidation of the marker for BB explains most likely why most of the data are around the threshold value. It further shows that the lifetime of f_{60} is

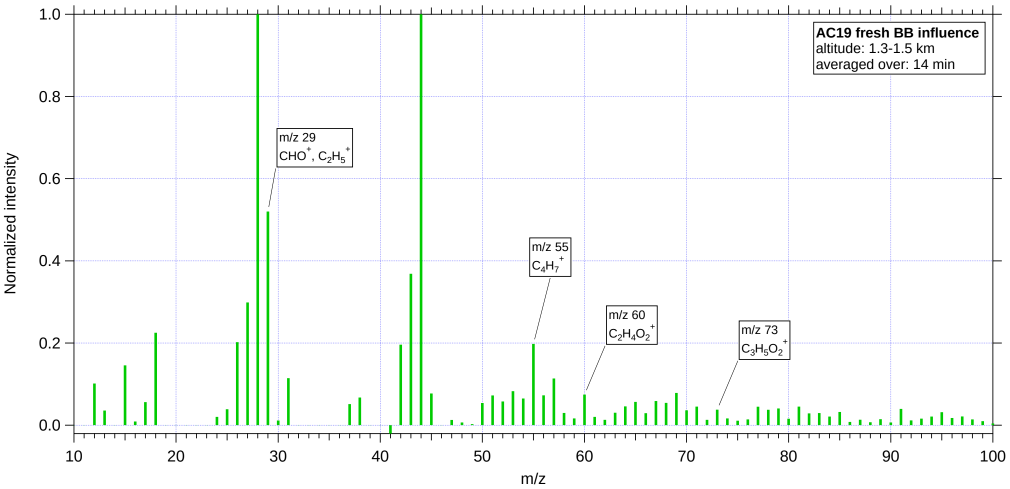

Figure 53: Averaged mass spectrum for the flight section of AC19 with BB influence. The marker peaks of BB are labelled, respectively.

highly dependent on the location the measurements take place as high OH concentrations facilitate the oxidative decay.

4.1.4.4 *Summary*

A general conclusion from these case studies is that the aerosol can differ largely in the LT in terms of composition, oxidation state, and sources.

The influence of forestation on the composition of the local atmosphere was investigated. The organic aerosol shows higher photooxidation states and less IEPOX-SOA contribution above deforested areas. This case study serves as an example of anthropogenic influence in a pristine environment like the Amazon basin.

Long-range transported aerosol from African volcanoes mainly consist of sulfate and affect the aerosol composition in the Amazon basin remarkably such that the dominant contributor is sulfate instead of organics for several days. Additionally, the long-range transported sulfate could support further reactions with e.g. VOCs leading to organic sulfates. The ion at m/z 99 was identified in the mass spectra showing volcanic influence and could serve as an indicative marker for organic sulfates.

The tracer f_{60} is a specific marker for identifying BB influence on organic aerosol (Cubison et al., 2011), but hardly shows a significant effect of BB on the organic aerosol composition during the ACRIDICON-CHUVA campaign. A fresh BB plume was probed and shows strongly enhanced values of f_{60}. Interestingly, this marker was oxidized within a very short time interval of 20 minutes resulting in background values that were observed during the campaign. Thus, the lifetime of the marker is highly dependent on the amount of OH as it facilitates the oxidative decay.

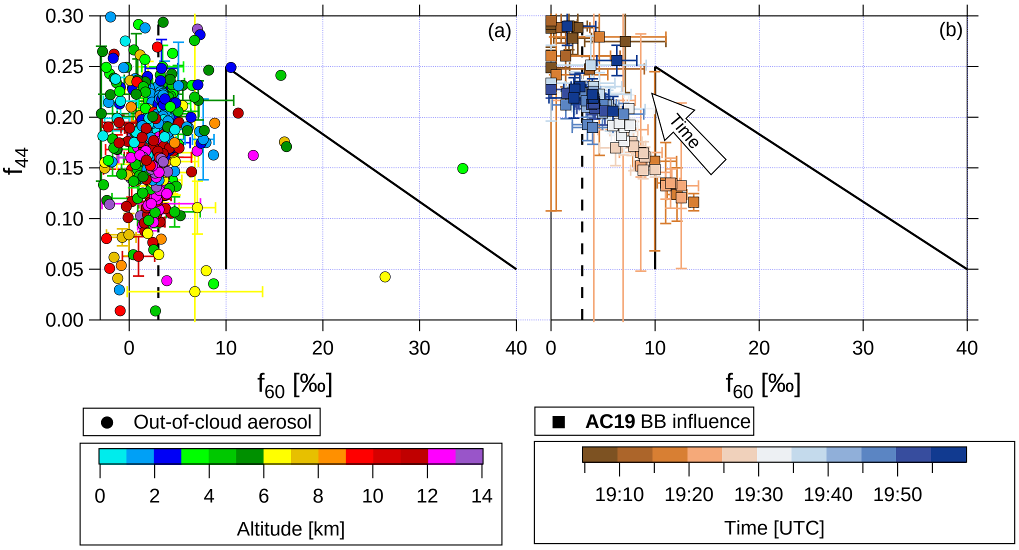

Figure 54: Panel (a): Scatter plot of f_{44} vs. f_{60} coloured with altitude for all flights averaged over five minutes. The vertical dashed line represents the threshold value of 3 ‰ (Cubison et al., 2011). The solid black lines give orientation where BB is strongly influencing the organic aerosol (Cubison et al., 2011). For clarity reasons only some of the uncertainty bars are shown. Panel (b): Same plot as panel (a), but only for the flight section of AC19 showing the influence of BB coloured with time.

4.2 CLOUD PARTICLE RESIDUAL PROPERTIES

Another important aspect of aerosol particles is the availability to act as cloud condensation nuclei (CCN) or ice nucleating particles (INP). The size and composition of the aerosol particles affect whether the particle can act as CCN and how efficient the cloud activation is (Dusek et al., 2006). Measurements with the C-ToF-AMS at the HALO-CVI inlet during the ACRIDICON-CHUVA campaign allow a closer look into the chemical composition of cloud particle residuals (CPR). Although CCN and INP are not necessarily equivalent to CPR, the analysis of CPR helps to understand which particles initiate droplet or ice formation (Cziczo et al., 2017).
A quality check of the data is done in the beginning of this chapter explaining the sorting of the data into data from particle-free air and data from CPR. Number, mass and composition properties are presented allowing a characterization of the measured CPR. One focus of the analysis is then put on the organic fraction of the CPR.

4.2.1 *Data quality check*

Similar to the measurements behind the HASI, data from particle-free air are needed to determine the background conditions. Outside of clouds the HALO-CVI acts like a particle filter due to the provided counterflow and allows such a determination of the background signal in the C-ToF-AMS. The conditions for a data point to be counted as particle-free data are as follows:

- position of switching valve on HALO-CVI
- $N_{residual} = 0\,\mathrm{cm}^{-3}$ (measured with the CPC of the HALO-CVI-Rack)
- no cloud signal at least 20 s before and during measurement time of one C-ToF-AMS data point (cloud mask of NIXE-CAPS data)
- counterflow of the HALO-CVI is on
- no artefact signal from valve switching

A cloud mask was provided by the NIXE-CAPS (see Sect. 2.3.6). This mask allows to distinguish between measurements in ambient air out-of-cloud and in clouds. The artefact signal occurred sometimes during the valve switching processes when changing the inlet line. As it is not a real signal of ambient air, it has to be removed from the analysis.
These conditions allow the sorting of the HALO-CVI data into particle-free data and real CPR data. For almost every flight such particle-free data are available and used to adjust the gas-phase correction in the fragmentation

table (Allan et al., 2004). Especially the entries for carbon dioxide (CO_2) and water need be adjusted differently than for the out-of-cloud aerosol measurements. This is caused by the drying method of the counterflow in the HALO-CVI. A molecular sieve filters water molecules out of the particle free air that provides the counterflow. The size of CO_2 molecules is similar to water molecules and, thus, also CO_2 is filtered. The carrying air (with the dried CPR) that arrives at the C-ToF-AMS has therefore a much lower amount of CO_2 and water than ambient air that needs to be accounted for in the fragmentation table.

The counterflow of the HALO-CVI ensures that only cloud droplets and ice crystals enter the inlet, whereas aerosol particles and ambient air are rejected. This separation is a prerequisite for the analysis of CPR. It also causes an enrichment of the CPR that needs to be accounted for in the data analysis. This enrichment is implemented by dividing the derived mass concentrations by the enrichment factor (EF), ranging between 4 and 187. Time periods when the counterflow was off were excluded from the analysis.

A correction of the nitrate signal due to organic interferences as described in Sect. 2.2.2 is applied to the CPR data, too. This correction is relevant in regions with high organic and little nitrate contribution (Fry et al., 2018, Supplement). Measurements above the Amazon basin fulfil these conditions, and thus, out-of-cloud aerosol as well as CPR data are affected and need to be corrected.

The particle-free data not only allow the adjustment of the fragmentation table, but also the determination of a detection limit (DL). The fragmentation table used for the CPR data has significant differences to the one used for the out-of-cloud data. Thus, the values for the DL of the CPR data need to be calculated separately. Although the cubic spline method was used for the DL determination of the out-of-cloud data (see Sect. 2.2.3.4), the DL for the CPR data was calculated using the filter based method (see Sect. 2.2.3.1). Measurements in a cloud are not continuous like out-of-cloud measurements. The filter method represents the conditions for the CPR measurements in this case better than a time-dependent method. In total, 659 data points are used as particle-free data.

The vertical profile of the particle-free data, already with the EF taken into account, is shown in Fig. 55. The data points for all shown species scatter around 0, as expected. A slight bias was observed for organics (panel a), where the data are scattering between -0.05 and 0. This is only detected at altitudes below 7 km. A similar behaviour, but in this case a slight bias to positive values, was found for nitrate and ammonium (panel b and d). The reason for the opposed behaviour of organics and nitrate could be the correction due to biogenic influence that was applied. This correction is based on ground measurements that were performed with a HR-ToF-AMS (Fry et al., 2018, Supplement). Up to now, there are no appropriate measurements with

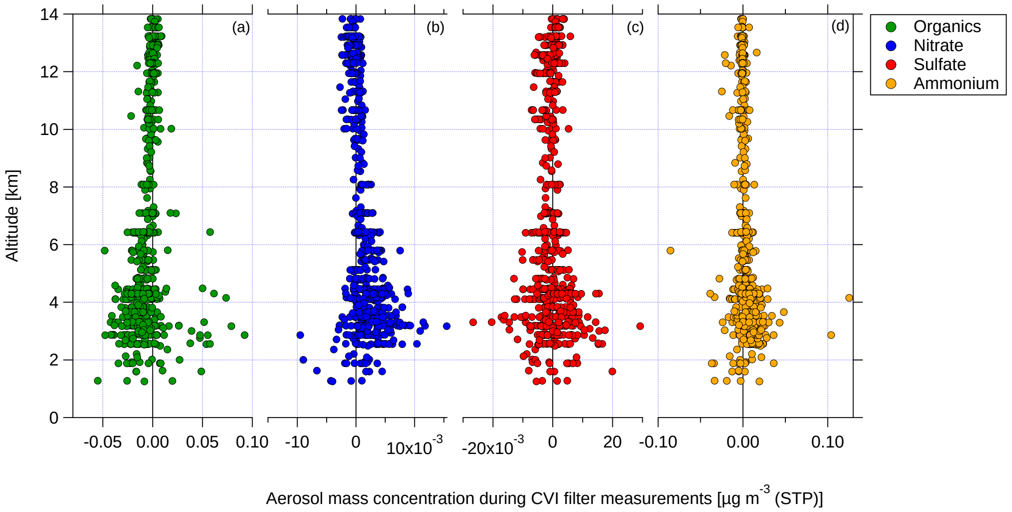

Figure 55: Vertical profile of the particle-free data measured behind the HALO-CVI with the EF taken into account for (a) organics, (b) nitrate, (c) sulfate and (d) ammonium.

Table 5: Derived σ and DL values for the different species. These values are used to determine a total DL

	organics	nitrate	sulfate	ammonium	chloride
σ	0.1809	0.03565	0.07726	0.1619	0.06284
DL ($\mu g\,m^{-3}$ (STP))	0.5427	0.10695	0.23178	0.4857	0.18852

such a high resolution in the tropical UT, and of CPR. The data presented here were obtained using a C-ToF-AMS that does not show such a high resolution. It is possible that the correction of biogenic influence needs to be adjusted for CPR measurements. However, this was not further investigated and the data are taken as such. The ammonium signal can still have interferences from the gas phase water originating from cloud droplet evaporation at low altitudes. In the UT (above 8 km) the particle-free data of all species show a scattering around 0.

The signal of the particle-free data is not divided by the EF for the DL determination due to the fact that it is a real signal in the mass spectrometer and thus, should be treated as such. Table 5 gives the derived σ and DL values for the different species. A total DL is derived from using Eq. 19:

$$\begin{aligned}\mathrm{DL}_{\mathrm{CVI}} &= 3 \cdot \sigma_{\mathrm{total}} \\ &= 3 \cdot \sqrt{\sigma_{\mathrm{Org}}^2 + \sigma_{\mathrm{NO3}}^2 + \sigma_{\mathrm{SO4}}^2 + \sigma_{\mathrm{NH4}}^2} \\ &= 0.77\ \mu\mathrm{g\ m}^{-3}\end{aligned} \tag{19}$$

A data point is counted as CPR data if the sum of all species, not corrected for the EF, is above the DL. Analogue to the out-of-cloud data, chloride is again not considered in the following analysis. The conditions for a data point to be counted as CPR data are:

- position of switching valve on HALO-CVI
- sufficient signal intensity ($\sum_{species} > DL_{CVI}$)
- $N_{residual} > 0$ (i.e. being in a cloud)
- inside of clouds (cloud mask of NIXE-CAPS data)
- counterflow of the HALO-CVI is on
- no artefact signal from valve switching

In total, 246 data points fulfil these conditions and are used as CPR data in the following analysis.

4.2.2 *Cloud particle residual number, mass and composition*

The vertical profiles of the relative contributions, and the total mass and number concentrations of the CPR are given in Fig. 56. The CPR number concentration was measured with the CPC in the HALO-CVI-Rack. The altitude range is divided into the LT up to 4.5 km and the UT with altitudes between 8 and 15 km. The sampling conditions in the MT were too dangerous for the aircraft due to supercooled clouds. Therefore, no measurements in the MT were performed, and consequently, no analysis is done for the MT. The altitude region where the ambient temperature is 0 °C is highlighted in light blue. The observed temperatures in the LT were always above 0 °C, i.e. only liquid phase clouds were sampled. In the LT the highest mass and number concentration of the CPR were measured. The number concentrations range between 10^{-3} and $100\,\mathrm{cm}^{-3}$ and shows a high variability. The total mass concentration is the sum of the mass concentrations of all four species. The values are quite stable over the altitude range of the LT, but vary between 0.1 and $1\,\mu\mathrm{g\,m}^{-3}$. The composition of the CPR is dominated by organics with 70 %. However, sulfate, ammonium, and nitrate show a significant amount with in total 30 %. Sulfate has a decreasing contribution to the composition of the CPR in the LT from 30 % at lowest altitudes down to 10 % in the upper LT. The CPR in the LT consist of roughly 10 % ammonium. This contribution is stable over the altitude range in the LT. Nitrate

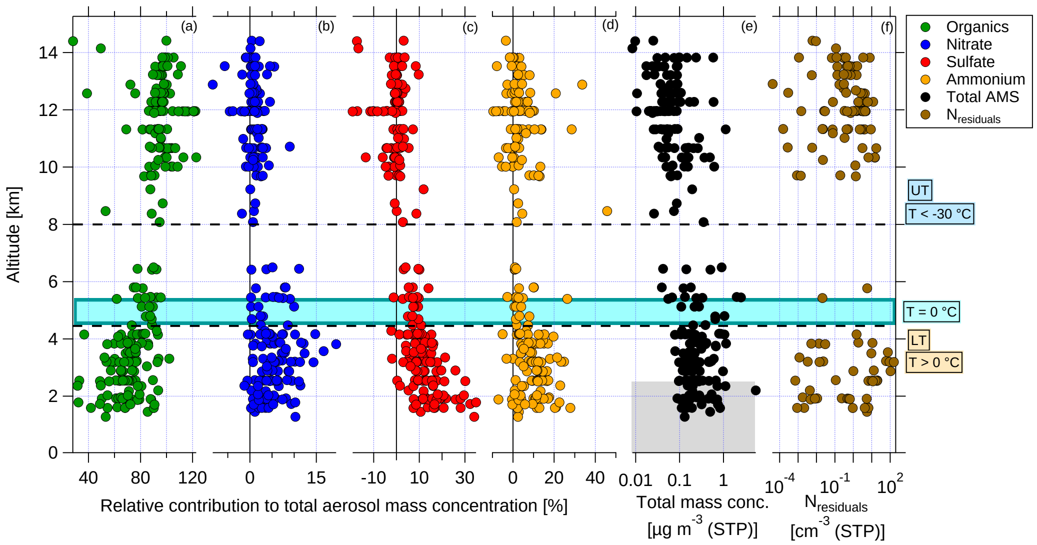

Figure 56: Vertical profile of the relative contributions of (a) organics, (b) nitrate, (c) sulfate, and (d) ammonium. Panel (e) and (f) show the total residual mass and number concentration, respectively. The grey shaded area in panel (e) covers data sampled below 2.5 km, which are underestimated due to impaction losses of the CPI in the C-ToF-AMS inlet system (see Sect. 2.1.2). The number concentration was measured with a CPC in the HALO-CVI-Rack. Note, that the scale in panel (e) and (f) is logarithmic. The altitude region with an ambient temperature of 0 °C is indicated with the light blue shaded area. Dashed horizontal lines indicates the division into LT and UT. The corresponding temperatures for these regions are given on the right.

contributes to roughly 5 % to the composition of the CPR in the LT and shows an increasing trend towards the upper part of the LT.

The altitude region where the temperature ranges around 0 °C is characterized with a shift of the organic contribution towards higher values, whereas nitrate, sulfate and ammonium show lower fractions.

The temperatures measured in the UT are ranging down to less than -60 °C. Supercooled droplets and ice crystals can coexist (mixed-phase clouds) at temperatures between 0 and -38 °C. However, pure ice clouds can also occur. Measurements of the cloud particle shape (whether they are spherical (liquid) or aspherical (ice)) and cloud particle phase gave indications that at temperatures of -20 °C and below most of the cloud particles consists of ice (Costa et al., 2017; Jäkel et al., 2017). Thus, the CPR sampled in the UT are representative for the residuals of ice clouds.

In the UT almost all CPR consist of organics. The relative nitrate contribution is around zero and shows only statistical scattering. The same is valid for sulfate and ammonium. Due to the statistical scatter the relative contributions are sometimes below 0 % (for nitrate, sulfate and ammonium) and above 100 % (for organics).

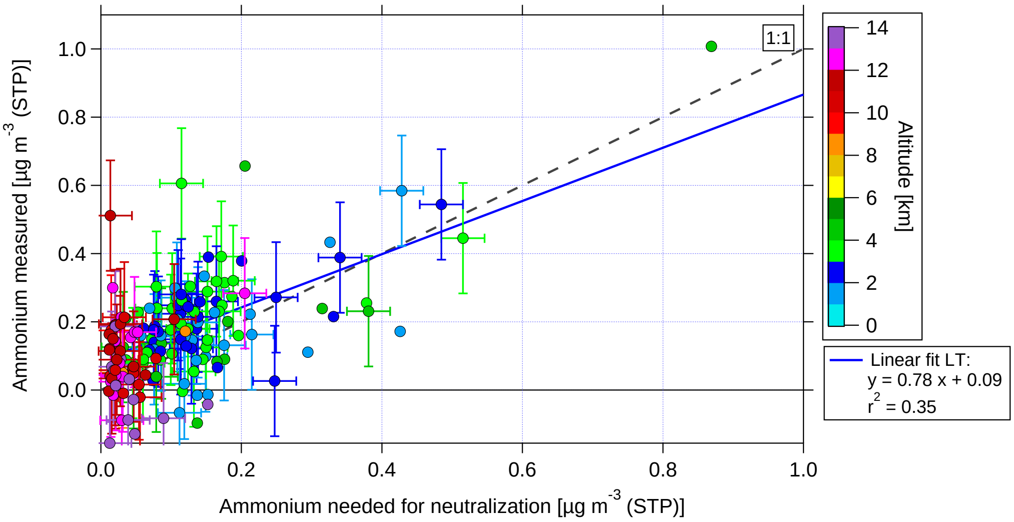

Figure 57: Scatter plot of measured and for neutralization needed ammonium. Data are coloured with altitude. The dashed line shows the 1:1 line. The fit function is only calculated for the LT. The uncertainties of both parameters are considered for the calculation of the linear fit curve coefficients (see Sect. C.4). For clarity reasons only some of the uncertainty bars are shown.

The total mass concentration is decreasing in the UT compared to the LT with values often below 0.1 µg m^{-3}. The number concentration varies strongly between 10^{-4} and 10^2 cm^{-3} in the LT and UT.

As for the out-of-cloud aerosol, ammonium is needed to neutralize sulfate and nitrate in the CPR. Thus, the acidity calculation of the inorganic species give information whether the CPR are acidic or neutralized. It should be noted here again, that only the inorganic species are taken into account and further neutralization processes with organics are not considered within this calculation. Figure 57 shows the scatter plot of measured and for neutralization needed ammonium. As the mass concentrations for nitrate, sulfate and ammonium are small in the UT, the scattering of the data is high. Thus, only the data sampled in the LT are used for a fit function. The slope of the fit function for the LT is close to 1. Thus, the CPR sampled in liquid clouds seem to be neutralized regarding the inorganic species.

4.2.2.1 *Comparison with out-of-cloud aerosol*

It is interesting to compare the composition of out-of-cloud aerosol and cloud particle residuals (CPR) in different altitude regions. For this purpose, a comparison of the different species fractions for the LT and UT is shown in Fig. 58. The composition of the out-of-cloud aerosol included the rBC fraction (see Fig. 30). The rBC data for the CPR were not provided yet in final form and are therefore not used in this analysis. For this reason the contribution of the individual species in the out-of-cloud aerosol is recalculated without rBC. In

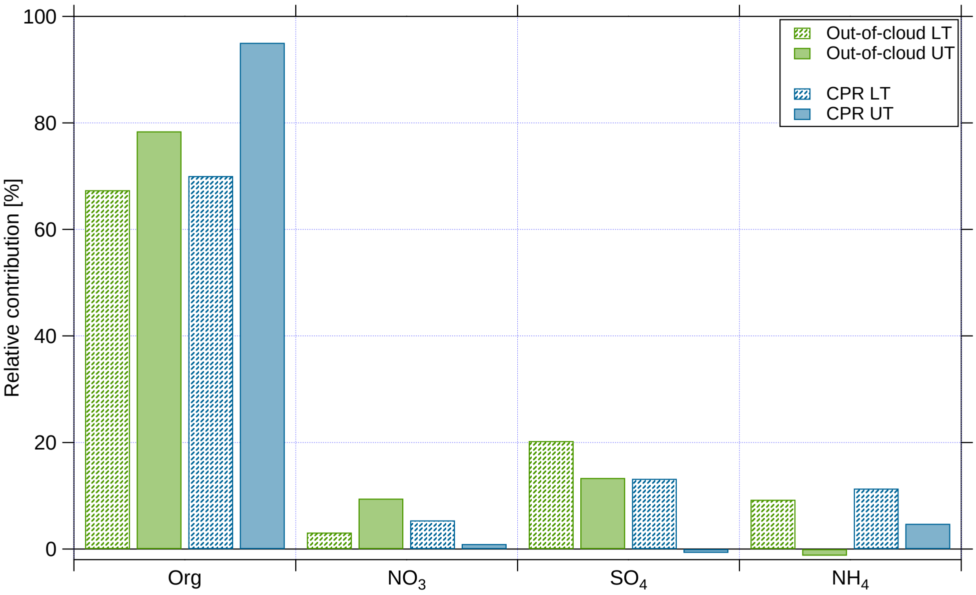

Figure 58: Comparison of out-of-cloud aerosol (green) and CPR (blue) composition divided into the LT (bars with pattern) and UT (solid bars).

Fig. 58 out-of-cloud data are depicted in green, whereas CPR data are shown in blue. The bars with the pattern represent the LT data, and the filled bars illustrates the UT data. The organic fraction is the major contributor of the composition of both out-of-cloud aerosol and CPR in the LT and UT. Similar to the out-of-cloud aerosol, the organic fraction of the CPR increases in the UT compared to the LT. Interestingly, the organic fractions show a similar contribution to the composition of the out-of-cloud aerosol and the CPR in the LT with 67 % and 70 %, respectively. In contrast, the organic fraction of the CPR in the UT is with 95 % higher than the organic fraction of the out-of-cloud aerosol in the UT with 78 %.

Nitrate shows an increasing contribution in the UT for the out-of-cloud data. This was explained with organic nitrates (see Sect. 4.1.3.3). The CPR show a higher contribution of nitrate in the LT and almost no nitrate in the UT.

Sulfate and ammonium show the highest contribution to the composition of the out-of-cloud aerosol and the CPR in the LT with decreasing fractions in the UT. However, sulfate shows almost no contribution to the CPR in the UT. Ammonium is not contributing to the out-of-cloud aerosol in the UT.

One argument in the analysis of the out-of-cloud data was the scavenging of soluble aerosol particles in clouds during vertical transport. The same argument is valid for the CPR as nitrate and sulfate are not detectable in the UT. Both species as well as their precursor gases nitric and sulfuric acid have a high solubility in liquid cloud droplets, and thus, can be removed by e.g. wet deposition during vertical transport inside of a cloud. Additionally, soluble organic material can also be washed out during the vertical transport. In contrast, insoluble organic material can be transported in clouds as interstitial aerosol to higher altitudes and act as CPR.

4.2.2.2 *Comparison with literature*

The current knowledge of ice and cloud residual particles is limited due to only few in-situ field studies (Cziczo and Froyd, 2014). Especially measurements of deep convective clouds in the tropics are rare. Different measurement techniques also impede a general comparison of the results.

A review about the composition of cirrus ice residuals mentioned a large range in the number concentration between 10^{-7} and $0.1\,\mathrm{cm}^{-3}$ (Cziczo and Froyd, 2014). It should be noted here that cirrus clouds show different properties than the outflow region of deep convective clouds due to different formation processes.

Aircraft measurements of ice cloud residuals in the mid-latitudes identified mineral dust (50 %) and biological particles (30 %) as the main contributors of the residuals (Pratt et al., 2009).

Single particle mass spectrometer measurements in the tropical tropopause region showed that cirrus cloud residuals consist of an internal mixture of sulfate and organics. However, the residual particles were chemically identical to unfrozen aerosol particles, and show the typical mass signatures of tropical tropopause aerosol (Froyd et al., 2010a). The sulfate-containing cloud residuals were neutralized and it was concluded that sulfate enriched aerosol do not initiate ice formation. Enhanced organic content did not suppress freezing mechanisms. Furthermore, it was noticed that mineral dust was not comprised, and that biomass burning particles were depleted in the cirrus residuals (Froyd et al., 2010a). The measured ice crystal number concentration ranged between 20 and $50\,\mathrm{L}^{-1}$, corresponding to 0.02 to $0.05\,\mathrm{cm}^{-3}$. The ice residual and out-of-cloud aerosol particles were neither recently transported from the lower troposphere nor was there a strong stratospheric influence.

Cziczo et al. (2013) reported aircraft measurements of cirrus cloud residual particles and also identified mineral dust and metallic particles as the dominant source of residual particles. Sulfate and organic particles were diminished. In contrast to Pratt et al. (2009), biological particles and elemental carbon were not detected in the residual particles.

A measurement campaign on a mountaintop site investigated remote continental warm clouds in northern mid-latitudes (Drewnick et al., 2007). The cloud residuals consisted mainly of organics (53 - 73 %) independent of the origin of air masses. The out-of-cloud aerosol comprised organic nitrates, whereas in the cloud residuals ammonium nitrate was identified. The relative contribution of nitrate to the total mass concentration was similar in the out-of-cloud aerosol and CPR (Drewnick et al., 2007).

Measurement results of warm clouds on another mountaintop site in mid-latitudes presented an organic mass fraction between 20 and 60 %. Contrasting the aforementioned study by Drewnick et al. (2007), the nitrate and ammonium mass fractions were significantly enhanced in the cloud residuals compared to the out-of-cloud aerosol (Schneider et al., 2017).

Regarding the results of the ACRIDICON-CHUVA campaign, the high variability of the CPR number concentration confirms previous studies (Cziczo and Froyd, 2014). The analysis of the CPR presented from the ACRIDICON-CHUVA campaign showed a major contribution of organics. Especially in the UT, where ice crystals were most likely present, almost all CPR consisted of organic material. There seems to be a slight enhancement of nitrate in the CPR in the LT compared to the out-of-cloud aerosol. This would confirm the finding by Schneider et al. (2017). In contrast to Froyd et al. (2010a), sulfate did not contribute to the CPR sampled in the UT. As it was shown in Sect. 4.1.2.2, soluble aerosol was removed during the vertical transport. Thus, only insoluble, organic material can reach the UT and is available for ice formation. Further information on the oxidation state of the organics is discussed in the next section supporting the understanding whether the CPR are transported from the LT or formed in the UT or during transport to the UT.

4.2.2.3 *Summary*

The CPR sampled in the LT were from liquid phase clouds as the temperatures were above 0 °C. In contrast to this, the temperatures in the UT were below -30 °C representing measurements of CPR from mixed-phase and ice clouds. Cloud spectrometer measurements suggest that at temperature of -20 °C and below most of the cloud droplets were frozen and thus, the CPR measured in the UT are sampled in ice cloud conditions (Costa et al., 2017; Jäkel et al., 2017). The number and mass concentrations of the CPR are in total highest in the LT and decreasing in the UT, but both show a high variability. The CPR consist mainly of organics. The organic contribution is 70 % in the LT (liquid clouds) and further increasing up to 95 % in the UT (ice clouds). In the LT the inorganic fractions show a significant contribution of 30 % with sulfate as the major fraction. The CPR sampled in liquid clouds were neutralized regarding the inorganic fraction. A comparison to the out-of-cloud aerosol shows that both the out-of-cloud aerosol and the CPR consist mainly of organics. In the following a deeper look into the organic signals will clarify which organic material is involved in cloud and/or ice formation.

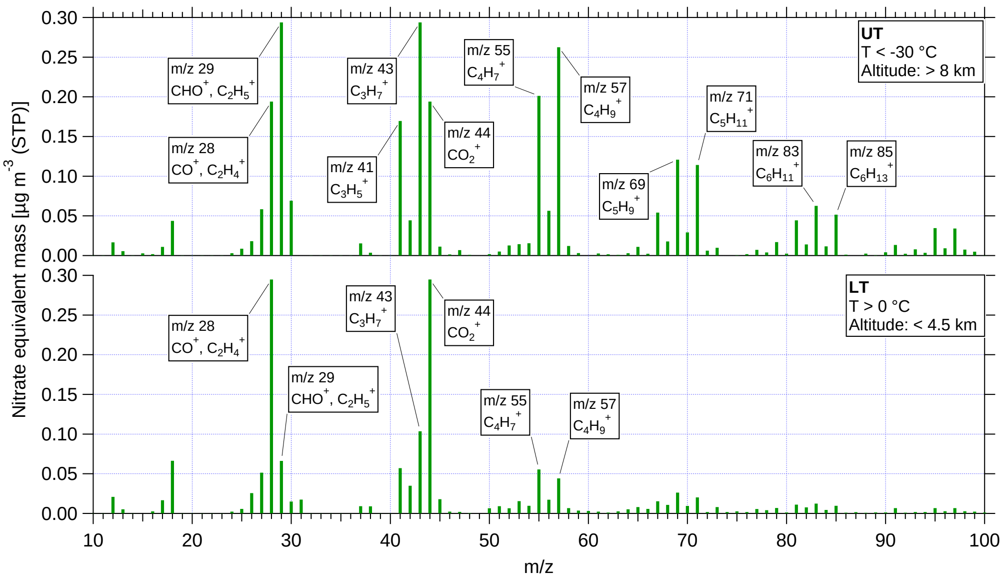

Figure 59: Averaged organic mass spectra of CPR for the LT (lower panel) and UT (upper panel). Specific peaks in the spectra are labelled, respectively.

4.2.3 *Organic cloud particle residual properties*

As mentioned above, the organic fraction is dominating the CPR in the LT and UT. A closer look into the mass spectra for the LT and UT gives information on the similarity and differences of the CPR measured in these regions. Figure 59 depicts the averaged organic mass spectra for the CPR sampled in the LT and UT (lower and upper panel, respectively). The mass spectrum of the LT is representative for measurements at temperatures above 0 °C and therefore for liquid clouds, whereas the temperatures for measurements in the UT are below -30 °C and representative for ice clouds.

The organic mass spectrum of the CPR measured in the LT shows characteristic peaks at m/z 28 and 44, and smaller, but still significant peaks at m/z 29, 43, 55 and 57. This spectrum resembles the mass spectra of OOA (see Sect. 2.2.1.1). Table 6 gives the squares of Pearson's correlation coefficients for the measured organic mass spectra with the averaged standard organic mass spectra for OOA, LV-OOA, SV-OOA, and HOA. The mass spectra representative for the LT does not show a very high r^2 value for either of the standard spectra, but it is highest for the comparison with the OOA and SV-OOA spectra. This could be due to the fact that the mass spectra is dominated by just a few signals that dominate the correlation. In order to minimize this effect, the square root of the spectra was used for the correlation (Rebotier and Prather, 2007).

The dominant peaks in the mass spectrum of the CPR sampled in the UT are observed at m/z 29 and 44, and very distinct "double" peaks at m/z 41 and 43, 55 and 57, 69 and 71, as well as 83 and 85. These double peaks

Table 6: Overview of r^2 values for different correlations of standard spectra and measured spectra in the LT and UT.

	OOA			HOA
		LVOOA	SVOOA	
LT	0.55	0.49	0.54	0.33
UT	0.42	0.31	0.58	0.67

are typical for HOA. The comparison with the standard HOA spectra shows a good correlation (see Tab. 6). The enhanced r^2 value for the comparison with the SV-OOA spectrum is caused by the “double”peaks that are partly present in the SV-OOA spectrum. The finding of HOA-like spectra in the UT is unexpected as HOA signals are caused by fossil fuel combustion (FF) (see Sect. 2.2.1.2). One source of FF emissions in the UT is the exhaust of aircraft. However, the air traffic above the Amazon basin is not very pronounced. HALO flew always close to convective cells where vertically transported air most likely influenced the measured region.

Compared with the mass spectra of the out-of-cloud aerosol, some interesting aspects occur. The organic mass spectrum of the CPR of the LT (Fig. 59, lower panel) is similar to the one of out-of-cloud aerosol sampled in the LT (see Fig. 47). Both spectra show oxidized organics. However, there is a vast difference in the mass spectra representative for the UT. While the CPR (Fig. 59, upper panel) show signals of HOA, these signals are not identified in the out-of-cloud aerosol spectrum at all (see e.g. Fig. 16, 47, and 53). One possibility to detect and classify specific organics is a PMF analysis. This was so far not done for the presented data, but could offer more details of the contribution of e.g. HOA to the organics in the out-of-cloud aerosol and CPR.

Some peaks are of interest when comparing the mass spectra of the CPR from the LT and UT. A deeper analysis of these signals is done in the following.

One of the dominating peaks in the spectrum of the LT is the signal at $m/z\,44$. In the spectrum of the UT this peak is still abundant, but not dominating. In contrast to this, the signal at $m/z\,43$ has only a minor contribution in the spectra of the LT, whereas it is one of the main peaks in the spectra of the UT. The difference between the two spectra regarding f_{43} and f_{44} (see Sect. 2.2.1.1) is seen more clearly in Fig. 60. Panel (a) shows the data colour-coded by altitude, whereas panel (b) depicts the same data colour-coded by temperature.

The data are spread in the triangle shaped area. Data points in blue and green were sampled in the LT, whereas the red and pink data points represent measurements of CPR in the UT. The data points from the LT are found in the upper left corner with high f_{44} and low f_{43} and in the middle range. These areas represent organic compounds that are strongly oxygenated. Interestingly, only data points from the UT are found in the lower right corner of the triangle. This area is defined with lower f_{44} and higher f_{43} values and represents organic compounds that are less oxygenated.
The same plot is depicted in Fig. 60, panel (b), but the data are colour-coded by temperature instead of altitude. All the data that are above 0 °C were sampled in the LT representing liquid clouds. The data points that show the lowest oxygenation of the organic compounds were measured at temperatures below -30 °C representing ice clouds.
Also shown in Fig. 60 are the median and interquartile ranges of the out-of-cloud aerosol. The lower photooxidation state of the CPR sampled in the UT shows a similar trend to that of the out-of-cloud aerosol measured in the UT, although it is more pronounced with even smaller f_{44} values. However, the photooxidation state of the CPR sampled in the LT shows a large scattering, but still are comparable to the photooxidation state of the out-of-cloud aerosol measured in the LT.
The relation between the temperature and f_{44} is shown in Fig. 61 for the CPR and out-of-cloud aerosol. A temperature dependence is not observed for the CPR measured in the LT and UT, although a different behaviour can be seen. The linear fit function for the LT data shows only a low value of r^2. Thus, there seems to be no linear correlation. Similar to this, the out-of-cloud data also do not show a temperature dependence in the LT and UT. At highest temperatures, which correspond to the lowest altitudes, the range of f_{44} shows the different oxidation states of the organics. A broad range of f_{44} is observed for the out-of-cloud aerosol and the CPR. The f_{44} values of the CPR are narrower in the UT with overall lower values than observed for the out-of-cloud aerosol. Again, this confirms the arguments that the organic CPR measured in the LT and UT are different from each other. Furthermore, it shows once more that the CPR measured in the UT have a different organic composition than the out-of-cloud aerosol in the UT.

The temperature dependence of f_{44} was already investigated in Schneider et al. (2017). Measurements from a mountaintop site at mid-latitudes in warm clouds during the Hill Cap Cloud Thuringia 2010 (HCCT) campaign found higher f_{44} values at lower temperatures (temperature ranged between -3 and 16 °C) (Schneider et al., 2017). One factor that determines the cloud droplet composition is the influence of different VOCs emissions as a function of temperature (Schneider et al., 2017). The temperature range during HCCT is comparable to the measurement conditions in the LT during

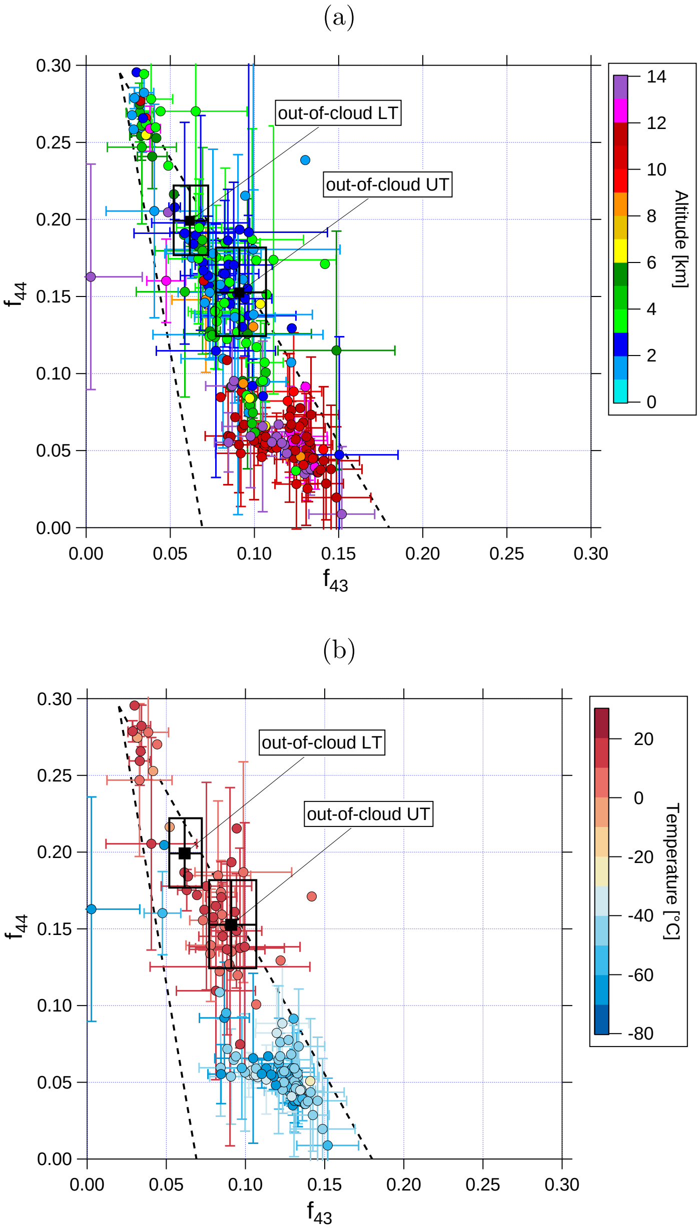

Figure 60: Scatter plot of f_{44} and f_{43} for CPR. The data are coloured with (a) altitude and (b) temperature, respectively. For clarity reasons only some of the uncertainty bars are shown. The black dots indicate median and interquartile ranges of the out-of-cloud data for the LT and UT, respectively.

ACRIDICON-CHUVA. However, a comparison between these two measurement sites is difficult. The source of VOCs is always below the mobile measurement platform at an almost constant temperature for the ACRIDICON-CHUVA campaign. In contrast to this is the static measurement platform during the HCCT campaign, where different temperatures do not correspond to different altitudes, but rather to different day times and air masses. Thus, the different temperature behaviour observed in the two

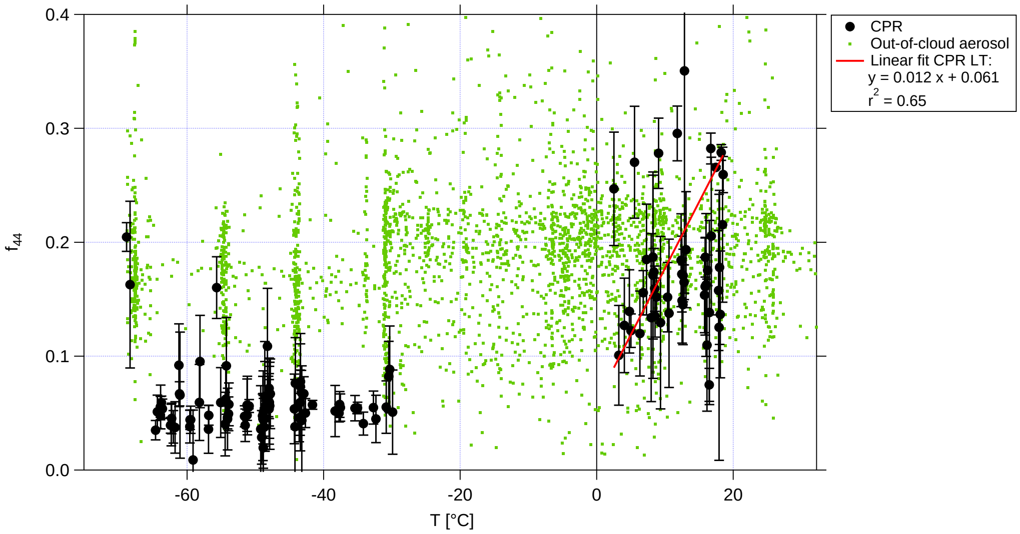

Figure 61: Scatter plot of f_{44} and temperature for CPR (black dots) and for out-of-cloud aerosol (green dots). A linear fit function for f_{44} measured in the LT is shown in red. The uncertainties of f_{44} are considered for the calculation of the linear fit curve coefficients (see Sect. C.4), whereas the uncertainty of the temperature is low and assumed to be negligible.

data sets cannot be compared directly.

Two effects could explain the higher f_{44} values at lower altitudes in the LT. The first effect is that aerosol particles, which are more oxidized, can be activated more efficiently as CCN at lower supersaturations. The other effect is related to aqueous SOA production. This in-cloud SOA formation process was observed in several field and laboratory studies (e.g, Carlton et al., 2007; Sorooshian et al., 2007; Ervens et al., 2011; Sorooshian et al., 2013).

CCN that contain SOA are either formed or further oxidized due to chemical processes in cloud droplets and due to several cloud formation and evaporation cycles. This process could be pronounced at cloud base. Larger rain droplets can experience gravitation and fall, but do not necessarily reach the surface. If the droplets evaporate, further oxidized aerosol particles would be released at lower altitudes. These particles can still act as CCN at sufficient but lower supersaturations than they were activated before. This cloud processing would explain the existence of OOA in out-of-cloud aerosol as well as in liquid CPR in the LT.

In summary, the CPR in the LT, sampled from liquid phase clouds, are more oxidized than the CPR sampled in the UT in ice clouds. As mentioned before, the CPR sampled in the LT seem to be formed secondary and oxidized. In contrast to this is the organic mass spectrum of the UT. There are indications that the CPR mainly consist of HOA. The source of HOA is most likely FF emissions in the BL (e.g., Ng et al., 2011b). This implies a fast transport of the freshly emitted HOA within the clouds up to high altitudes. Scavenging of the HOA-containing particles can be excluded during the vertical lifting if these particles are small enough not to collide with falling droplets during wet deposition processes. As HOA is insoluble in water, no nucleation scavenging and subsequent wet deposition is expected during the vertical lifting. This is confirmed by the finding that HOA was not observed in the CPR of liquid clouds sampled in the LT. The signal of HOA was also not identified in the spectra of the out-of-cloud aerosol in the UT. One reason could be the low number concentration of INP when released of the cloud compared to the number of out-of-cloud aerosol. A PMF analysis would help to identify whether HOA is present in the out-of-cloud aerosol and if so to which extent. Another reason would be the fast oxidation of HOA particles when the cloud is evaporating so that the distinct signature cannot be identified in the out-of-cloud data any more. In contrast to the fast oxidation outside of clouds are photooxidation processes in the cloud. As sunlight won't pass through the cloud, photooxidation processes are impeded. At mid-latitudes the photooxidation of HOA is supposed to happen within roughly one week (Molina et al., 2004; Zhang et al., 2005b). That would scale the vertical transport of the HOA to the UT also to one week. However, photooxidation can be faster in the tropics. Additionally, deep convection occurs on a daily basis in the Amazon region. Thus, the UT is continuously seeded with aerosol that contains HOA and can influence INP characteristics in the UT.

The question remains whether HOA-containing aerosol act as INP at low temperatures (< -30 °C) or if these aerosol particles are deposited on ice crystals. Mineral dust is a good example for an effective INP that could serve as surface when activated as such. Occasionally, mineral dust from the Sahara can be long-range transported and influence the Amazonian aerosol composition. However, this transport is supposed to occur only in the wet season (e.g., Formenti et al., 2001; Wang et al., 2016b; Pöhlker et al., 2018a).

During ACRIDICON-CHUVA ice clouds were observed already at temperatures below -20 °C (Costa et al., 2017; Jäkel et al., 2017). No homogeneous freezing is expected as no supercooled droplets are present. Thus, HOA could serve directly as INP. The ability of predominantly organic anthropogenic particles to act as INP was reported by Knopf et al. (2010). Samples were taken in and around Mexico City and analysed in the laboratory. The anthropogenic organic particles were INP-active at conditions similar to those observed in cirrus formation, i.e. temperatures between -68 and -38 °C and supersaturation with respect to ice (Knopf et al., 2010). It was concluded that anthropogenic organic particles can sufficiently act as INP and influence freezing mechanisms in clouds. Cirrus conditions in the polluted northern hemisphere are suggested to be controlled by homogeneous and heterogeneous freezing, whereas in the cleaner southern hemisphere more homogeneous freezing occurs (Haag et al., 2003). It can be concluded, that there seems to be already a strong anthropogenic influence in the pristine Amazon

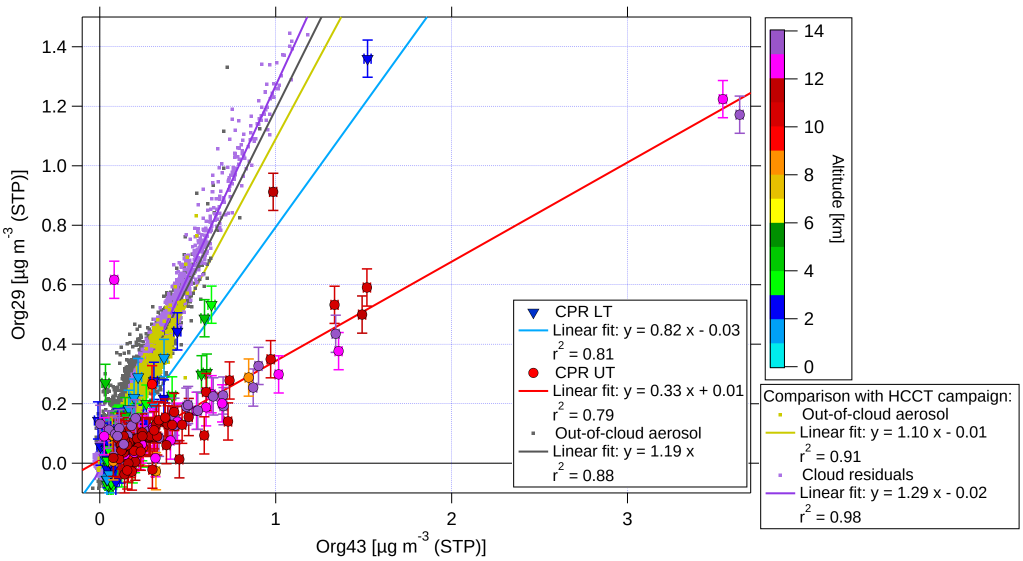

Figure 62: Scatter plot of the organic signal at m/z 29 (Org29) and at m/z 43 (Org43). Data for the LT and UT from this study are coloured with altitude. The two corresponding fit functions are shown in blue and red, respectively. The uncertainties of both parameters are considered for the calculation of the linear fit curve coefficients (see Sect. C.4). The out-of-cloud aerosol data and the appropriate fit function are given in grey. As a comparison data and fit functions from the HCCT campaign are shown in yellow and purple (data are personal communication: J. Schneider, MPIC, 2018).

basin as HOA, emitted on ground, influences the INP and cloud characteristics in the UT.

Another peak of interest is the signal at m/z 29 (CHO^+). The contribution of the signal at m/z 29 differs significantly between the LT and UT. The peak plays only a minor role in the spectrum of the LT, whereas it is one of the dominant one in the spectrum of the UT (see Fig. 59). The ratio of Org29 (organic signal at m/z 29) to Org43 (organic signal at m/z 43) gives further evidence of different chemical characteristics. The signal at m/z 29 is influenced by the air signal (isotope of nitrogen) and corrected in the fragmentation table so that the offset of the scatter plot Org29 to Org43 is zero (see Fig. 62). A different slope of the fit function implies a different chemical signature. The fit function of the CPR sampled in the LT has a much higher slope than the fit function of the CPR sampled in the UT. A higher slope indicates a larger influence of the functional group -CHO (aldehydes). One characteristic especially of short-chained aldehydes is the solubility in water. This supports the aforementioned argument that the organic CPR in the LT are different from those in the UT.
Also depicted in Fig. 62 are the out-of-cloud data, shown in grey. The out-of-cloud data do not show such an altitude-dependent separation compared

to the CPR. The fit function of the out-of-cloud data reveals an even higher slope than that for the CPR of the LT. This suggests that different organic compounds influence whether a particle remains in the interstitial aerosol or is activated as CCN or INP.

Figure 62 also compares the ACRIDICON-CHUVA data with data from the HCCT campaign (see above, data are personal communication: J. Schneider, MPIC, 2018). During the HCCT campaign, warm clouds were measured. Thus, the results should be comparable to the LT measurements of the ACRIDICON-CHUVA campaign. The data of the ACRIDICON-CHUVA campaign are shown in grey (out-of-cloud aerosol), blue (CPR sampled in the LT), and red (CPR sampled in the UT). The data of the HCCT campaign are representative for out-of-cloud aerosol (yellow), and CPR (purple).

The slopes representing ACRIDICON-CHUVA – out-of-cloud, HCCT – out-of-cloud, and HCCT – cloud residuals have the highest values. In contrast to this are the slopes of ACRIDICON-CHUVA – CPR sampled in the LT (intermediate) and UT (lowest). This supports the previous argument that the organic CPR in the UT are different than in the LT.

More marker peaks of interest are the signals at m/z 60 (biomass burning marker) and 82 (IEPOX-SOA marker). The behaviour of both markers in the out-of-cloud aerosol has been discussed in Sect. 4.1.3.2 and 4.1.4. Whereas f_{60}, a marker for BB, showed only background values when looking at the overall campaign, a deeper analysis of one event showed the fast oxidation that leads to a reduction in f_{60}. The marker f_{82} indicated IEPOX-SOA, which was found not only in the LT close to the source of isoprene, but also in the UT within a significant amount of the organic aerosol. Now the question arises how f_{60} and f_{82} behave when the aerosol particles acted as CCN or served as INP.

Figure 63 shows the scatter plots of f_{44} against f_{60} coloured with temperature. The data of f_{60} are spread along different f_{44} values and show overall low f_{60} signals. The CPR sampled in liquid clouds scatter around the background value of 3 ‰. Interestingly, the data from ice clouds with lower f_{44} show also lower f_{60} values. These values are below the background value reported by Cubison et al. (2011) and scatter around 0.

Compared to out-of-cloud aerosol (see Fig. 54, panel a), the distribution looks similar with overall low values that scatter around the background value of 3 ‰. Only the CPR sampled in the UT in ice clouds show lower values.

Figure 64 shows the scatter plot of f_{82} against $R_{44/43}$, also coloured with temperature. The values of f_{82} vary between 0 and 25 ‰ with a major spot around 5 ‰. CPR sampled in liquid clouds show values around the f_{82} background of 3 ‰. These data correspond to very high $R_{44/43}$ values, representing aged organic CPR with low IEPOX-SOA influence. Besides small f_{82} values, also enhanced values around 6 ‰ are observed for the CPR sampled

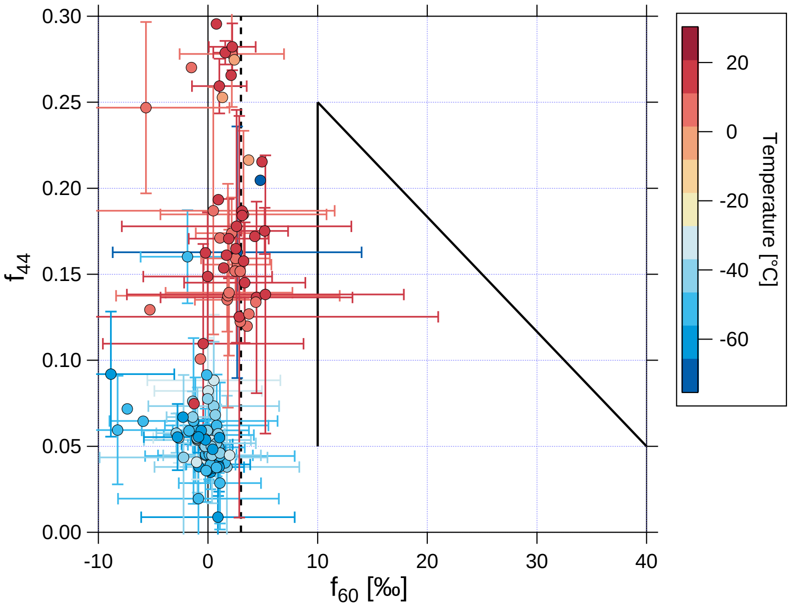

Figure 63: Scatter plot of f_{60} and f_{44} measured in CPR. The data are coloured with temperature. The dashed and solid lines give orientation values for background and BB influence as reported in Cubison et al. (2011), respectively. For clarity reasons only some of the uncertainty bars are shown.

in liquid clouds in the LT. Similar enhanced values of f_{82}, but significantly lower $R_{44/43}$ are observed for CPR sampled in ice clouds in the UT. CPR in liquid as well as in ice clouds contain IEPOX-SOA with different photooxidation states, respectively. The question remains whether isoprene, or more precisely the gaseous oxidation products of isoprene, or the out-of-cloud aerosol that contain IEPOX-SOA condense on or are scavenged by the cloud droplets and/or ice particles.
Also depicted in Fig. 64 are the median and interquartile ranges of the out-of-cloud aerosol sampled in the LT and UT (see Fig. 40). The CPR sampled in the LT are located between the two median values that represent the out-of-cloud aerosol from the LT and UT. In contrast to this, the CPR sampled in ice clouds in the UT are further shifted to lower $R_{44/43}$ values indicating an even lower photooxidation state.

4.2.3.1 *Comparison with literature*

Previous studies pointed out the capability of clouds to redistribute gases, aerosol and moisture during vertical transport or several cloud cycles (e.g., Wonaschuetz et al., 2012; Schneider et al., 2017). Furthermore, in-cloud production of SOA was measured during field and laboratory studies (e.g., Sorooshian et al., 2006; Sorooshian et al., 2007; Sorooshian et al., 2010; Wonaschuetz et al., 2012; Brégonzio-Rozier et al., 2016).

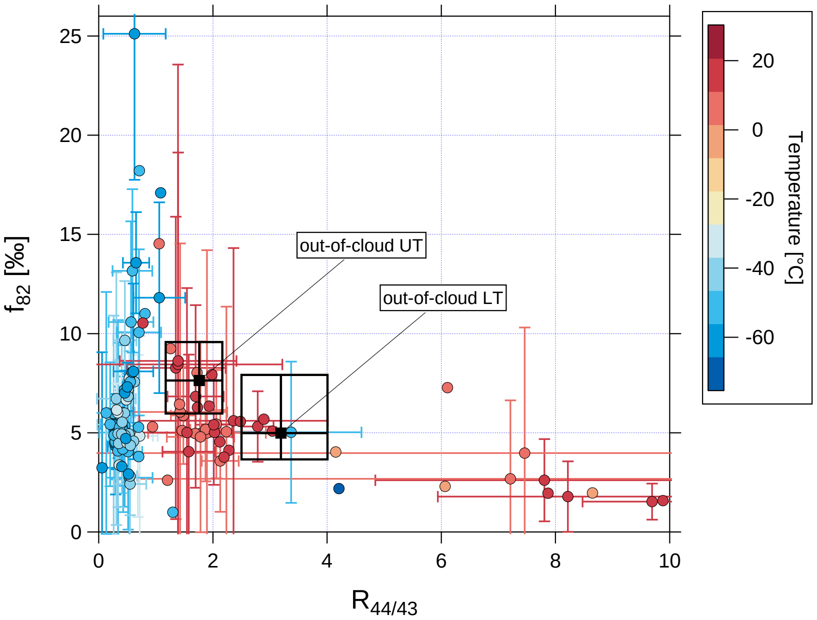

Figure 64: Scatter plot of f_{82} and $R_{44/43}$ measured in CPR. The data are coloured with temperature. For clarity reasons only some of the uncertainty bars are shown. The black dots indicate the median values of the out-of-cloud aerosol data, respectively (see Fig. 40).

As already mentioned before, a temperature dependence of f_{44} was found in cloud droplet residuals measured on a mountaintop site in the mid-latitudes (Schneider et al., 2017). The data presented here show a different behaviour. While Schneider et al. (2017) reported higher f_{44} at lower temperatures, the data presented here indicate the opposite with higher f_{44} values at higher temperatures for the CPR sampled in the LT. However, as the measurement conditions differ from each other, a direct comparison is difficult.

Several studies investigated the influence of clouds on SOA production and found out that in-cloud processes lead to different end-products of organic species and that SOA formation can be enhanced in the presence of liquid water (e.g., Wonaschuetz et al., 2012; Sorooshian et al., 2013; Brégonzio-Rozier et al., 2016). The chemical composition of the CPR in the LT and UT differ in several ways. SOA production is possible in liquid phase clouds in the LT, where the mass spectra show evidence for oxidized organics. There are some indications that IEPOX-SOA is partly present in the CPR sampled in liquid and ice clouds. However, CPR sampled in ice clouds consist most likely of primary organics emitted by fossil fuel combustion in the BL. In previous studies it was already shown that anthropogenic particles that consist mainly of organics act sufficiently as INP (Knopf et al., 2010). The presented data imply that HOA can act as INP and therefore influence the cloud freezing mechanisms, especially in the UT.

Bacer (2019) investigated the contribution of four different aerosol species (dust, BC, glassy organics, and biogenic aerosol) to heterogeneous ice nucleation within the ECHAM5/MESSy Atmospheric Chemistry (EMAC) model. The focus is set on cirrus and mixed-phase clouds. The results show a major contribution of organics in cirrus clouds at pressures lower than 200 hPa, whereas black carbon and dust contribute mainly to newly formed ice crystals in the pressure range between 250 and 500 hPa. The large contribution of organics is highest in the tropics considering the zonal mean (Bacer, 2019). Although, cirrus clouds are different to deep convective clouds, the observations of organic CPR presented here partly agree to the model results. The contribution of rBC cannot be presented here, but is of high interest for further research.

The phase state of SOA is supposed to affect freezing mechanisms, as glassy SOA can persist long enough to reach high altitudes. There, homogeneous freezing can be suppressed and heterogeneous freezing mechanisms would dominate the processes in clouds (Shiraiwa et al., 2017). This is in contrast to the findings described here. The CPR sampled in the iced part of the deep convective clouds do not consist mainly of SOA. However, heterogeneous freezing might occur through HOA containing particles suggesting a suppression of homogeneous freezing mechanism.

An overall comparison remains difficult as no similar field study in the tropical UT at altitudes up to 14 km was reported.

4.2.3.2 *Summary*

The organic properties of the measured CPR were analysed and discussed. The CPR sampled in liquid clouds consisted of organics, sulfate and nitrate, and were activated as CCN leading to wet deposition removal. Thus, insoluble organic material was identified in the CPR sampled in ice clouds. It seems that the CPR sampled in ice clouds acted as INP. The averaged organic mass spectra of the CPR measured in liquid clouds in the LT and in ice clouds in the UT show different signatures. Whereas the CPR sampled in liquid clouds consisted of oxidized, most likely secondary organic matter, the CPR sampled in ice clouds consisted of HOA that is typically representing freshly emitted particles from FF. This finding is unexpected, as the out-of-cloud aerosol mass spectra do not imply the existence of HOA in the UT. Possibly, the CPR are oxidized fast when the cloud is evaporating so that the signature cannot be identified in the out-of-cloud aerosol any more.

There are indications for in-cloud SOA formation in liquid clouds the LT. The CPR sampled in ice clouds the UT are not affected by photooxidation or only to a small amount. The comparison with the out-of-cloud aerosol demonstrated a similar behaviour, i.e. less photooxidized organics in the UT. However, the CPR sampled in ice clouds are less oxidized than out-of-cloud aerosol i the UT.

The comparison of m/z 29 and m/z 43 resulted in different slopes for the

CPR measured in liquid and ice clouds. This shows again the varying chemical composition of the CPR at different altitudes and thereby temperature regions.

The marker for BB was found to scatter around the background value of 3 ‰ for CPR sampled in liquid clouds. However, even lower values scattering around 0 were observed for CPR sampled in ice clouds. Thus, BB emissions do not contribute to the chemical composition of CPR.

Enhanced signals of IEPOX-SOA were identified in the mass spectra of CPR sampled both in the LT and UT. However, it remains unclear whether the oxidation products of isoprene are scavenged by the cloud droplets/ice crystals or if the out-of-cloud aerosol consisting of IEPOX-SOA is acting as CCN and/or INP.

5

CONCLUSIONS AND OUTLOOK

The aim of this thesis was the investigation of secondary organic aerosol (SOA) in the pristine Amazonian atmosphere regarding their chemical properties, formation pathways, and their interactions with clouds.

Data from the ACRIDICON-CHUVA aircraft campaign were analysed and discussed. This campaign was conducted in 2014 during the dry season and the results are representative for this conditions. The data used for this study were obtained using a compact time-of-flight aerosol mass spectrometer (C-ToF-AMS). During the measurement campaign this instrument was connected to two different aircraft inlet systems providing quantitative chemical composition measurements of out-of-cloud aerosol and cloud particle residuals (CPR).

A newly designed C-ToF-AMS inlet system was applied in order to face the changing conditions during measurements at varying altitudes. Laboratory measurements show the occurrence of impaction losses of aerosol particles when measuring at high ambient pressures leading to an underestimation of the aerosol mass. This effect becomes insignificant at altitudes above 2.5 km as comparison measurements with a HR-ToF-AMS on another aircraft showed (Mei et al., 2019).

Regarding the various objectives of the ACRIDICON-CHUVA campaign, different questions were introduced assessing the chemical composition of out-of-cloud aerosol and CPR, formation pathways of SOA, as well as different case studies showing the influence of processes like forestation changes, and volcanic as well as biomass burning (BB) emissions.

The altitude range of the measurements is divided into three regions, the lower troposphere (LT), the middle troposphere (MT), and the upper troposphere (UT) albeit the focus of the results is put on the comparison between the aerosol characteristics in the LT and UT.

The out-of-cloud aerosol consist at all altitudes predominantly of organics with fractions of around 70 %. The highest aerosol mass concentrations were observed in the LT. Although the mass concentrations of all species are decreasing in the MT, organic and nitrate show increased values in the UT suggesting either transport or formation pathways of organic-dominated aerosol. The photooxidation state of the organic aerosol was found to be different in the LT and UT. Whereas the organic aerosol is mostly oxidized in the LT, the organic aerosol particles observed in the UT are less oxidized. This finding and further analyses as backward trajectory analysis suggest that there is no significant contribution of BL aerosol in the UT. The formation of

SOA in the UT is an explanation for the lower oxidation state of the organic aerosol. Another indicator for SOA formation in the UT is the aerosol size distribution. The highest concentrations of the smallest particles in the size range between 90 and 600 nm are found in the UT.

Further investigations of the organic aerosol composition identified IEPOX-SOA as a significant contributor in the LT (10 %) as well as in the UT (20 %). There seems to be a ubiquitous occurrence of IEPOX-SOA up to high altitudes. The precursor gas of IEPOX-SOA is isoprene, an abundant VOC that is emitted by vegetation. However, a local minimum of IEPOX-SOA was discovered above deforested regions as the source for isoprene is missing. Thus, anthropogenically motivated land-use change modifies local atmospheric characteristics as the emissions of biogenic VOC and related SOA formation processes are influenced.

The formation pathway of IEPOX-SOA depends on the aerosol acidity as the condensation of gaseous IEPOX is favoured on acidic surfaces. In general, the aerosol in the LT is neutralized, whereas the aerosol in the UT tend to be acidic. An enhanced correlation between the mass concentrations of IEPOX-SOA and nitrate suggest that not only sulfate (suggested to be crucial for IEPOX-SOA formation according to the literature), but also nitrate can provide the necessary acidic conditions leading to the formation of organic nitrates.

Different approaches were evaluated regarding the existence and amount of organic nitrates. Especially in the UT organic nitrates are present. As nitrate aerosol particles can provide the necessary acidic conditions for the condensation of IEPOX, IEPOX-SOA can occur as organic nitrate. However, also a non-IEPOX pathway to form organic nitrates is possible under the enhanced NO conditions observed in the UT.

Taken together, the formation of SOA is an important process in the Amazonian atmosphere affecting the aerosol properties either at lower altitudes when subsidence occurs and/or at higher altitudes when entrainment of upper tropospheric aerosol into the tropical tropopause layer takes place.

Three different case studies were discussed in order to show the effects of different processes. The deforestation of the Amazon rainforest has several effects (e.g., Davidson et al., 2012). Regarding the aerosol properties an enhanced photooxidation state and less IEPOX-SOA contribution to the organic aerosol was identified. Thus, the anthropogenic induced deforestation has a measurable influence on aerosol properties and thereby on the local atmosphere, presumably also on clouds.

Long-range transported aerosol from African volcanoes mainly consist of sulfate and affect the aerosol composition in the Amazon basin remarkably. For several days during the ACRIDICON-CHUVA campaign, sulfate had a major impact on the aerosol composition albeit this air mass was observed in a distinct layer between 4 and 5 km altitude. However, the long-range transported sulfate could support further reactions with e.g. biogenic VOCs leading to organic sulfates.

The measurements of a fresh BB plume allowed the investigation of the specific BB marker f_{60} as it was oxidized within a short time interval and consequently cannot serve as a unique and persistent marker in the tropical conditions of the Amazon atmosphere.

The CPR were sampled in liquid and ice clouds and consist mainly of organics with values of ~ 70 % and up to 95 %, respectively. The inorganic fraction in the CPR sampled in liquid clouds was dominated by sulfate. The organic mass spectra of the CPR from liquid and ice clouds differ significantly. Whereas the CPR of the liquid clouds consist of oxidized, most likely secondary organic matter, the ice residuals consist of primarily emitted HOA. There are indications for in-cloud SOA formation in liquid clouds. The ice residuals are not affected by photooxidation or only to a small amount. The comparison with the out-of-cloud aerosol showed a similar behaviour, i.e. less photooxidized organics in the UT. However, the ice residuals consist of different organics than the out-of-cloud aerosol in the UT.

BB emissions do not seem to contribute to the chemical composition of CPR. However, enhanced signals of IEPOX-SOA were identified in the mass spectra of CPR sampled both in liquid and ice clouds. The formation process of IEPOX-SOA-containing CPR remains complex and need further investigation.

It seems that the HOA-containing CPR in the UT acted as INP, as in the LT the CPR consisting of OOA, sulfate and nitrate are activated as CCN and removed by wet deposition. The freezing process in the observed ice clouds appears to be dominated by heterogeneous freezing induced by vertically transported HOA-containing particles. These are the first results of C-ToF-AMS measurements coupled with the HALO-CVI at altitudes up to 14 km in the tropical troposphere.

Taken together, the freezing mechanisms in clouds are affected by anthropogenically emitted aerosol particles that can act as INP and likely shifts the freezing from homogeneous to dominantly heterogeneous processes in the UT. Another effect is the transport of pollutants that are transported from the BL up to high altitudes. Both effects influence the properties of clouds and lead to changing impacts of aerosol-cloud-interactions. An overview of the different findings of this study is depicted in Fig. 65.

Despite the various findings of this study, it shows limitations as the investigation of the chemical composition is only valid for particles in the accumulation mode. SOA formation is not only occurring in this size range, but rather an important growing process of Aitken mode particles. Thus, data from different instruments should accompany the analysis of e.g. IEPOX-SOA containing particles in order to comprehend formation processes. Further, gas-phase measurements of isoprene oxidation products or OH together with particle

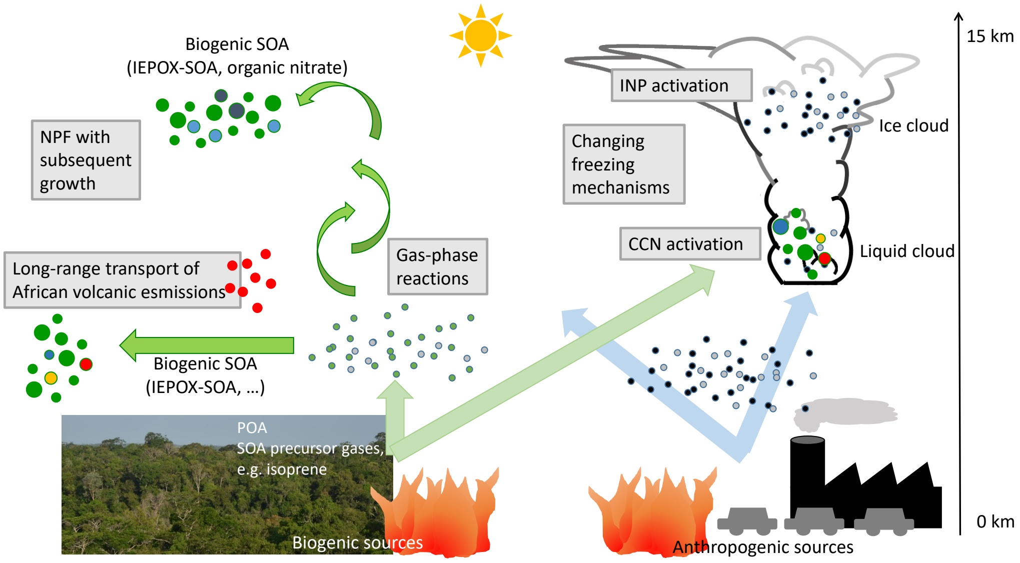

Figure 65: Scheme of the different findings presented in this studies. Processes are shown in grey boxes.

chemical composition measurements would complete the understanding of biogenic driven SOA formation above the Amazon basin.

The analysis of CPR offers new insights of compounds that are relevant for cloud processes. However, as the first measurements of CPR in the tropical UT are presented here, the amount of reliable data is sparse. Furthermore, the investigation of the chemical composition of CPR in mixed-phase clouds should be targeted albeit in-situ measurements entails dangerous conditions. In terms of technical improvements the O-ring of the CPI should be reduced to smaller diameters. Thus, the O-ring will be less squeezed at higher pressures and impaction losses of incoming aerosol particles would be reduced. The data analysis presented here focused among other things on specific marker ions in the organic mass spectra. Further investigation should target on the ion at m/z 99 whether it can serve as a useful criteria for identifying organic sulfates. Additionally, a PMF analysis would help to classify the specific organics offering more details of the contribution of e.g. HOA to the organics in the out-of-cloud aerosol and CPR.

Despite of its limitations, this study offers valuable insights into formation processes of SOA in the pristine Amazonian atmosphere regarding IEPOX-SOA and organic nitrates, as well as provides new findings of the composition of CPR in the tropical upper troposphere.

BIBLIOGRAPHY

Afchine, A., C. Rolf, A. Costa, N. Spelten, M. Riese, B. Buchholz, V. Ebert, R. Heller, S. Kaufmann, A. Minikin, C. Voigt, M. Zöger, J. Smith, P. Lawson, A. Lykov, S. Khaykin, and M. Krämer (2018). „Ice particle sampling from aircraft – influence of the probing position on the ice water content“. *Atmos. Meas. Tech.* 11.7, pp. 4015–4031. DOI: 10.5194/amt-11-4015-2018.

Aiken, A. C., D. Salcedo, M. J. Cubison, J. A. Huffman, P. F. DeCarlo, I. M. Ulbrich, K. S. Docherty, D. Sueper, J. R. Kimmel, D. R. Worsnop, A. Trimborn, M. Northway, E. A. Stone, J. J. Schauer, R. M. Volkamer, E. Fortner, B. de Foy, J. Wang, A. Laskin, V. Shutthanandan, J. Zheng, R. Zhang, J. Gaffney, N. A. Marley, G. Paredes-Miranda, W. P. Arnott, L. T. Molina, G. Sosa, and J. L. Jimenez (2009). „Mexico City aerosol analysis during MILAGRO using high resolution aerosol mass spectrometry at the urban supersite (T0) – Part 1: Fine particle composition and organic source apportionment“. *Atmos. Chem. Phys.* 9.17, pp. 6633–6653. DOI: 10.5194/acp-9-6633-2009.

Alfarra, M. R., H. Coe, J. D. Allan, K. N. Bower, H. Boudries, M. R. Canagaratna, J. L. Jimenez, J. T. Jayne, A. A. Garforth, S. M. Li, and D. R. Worsnop (2004). „Characterization of urban and rural organic particulate in the lower Fraser valley using two Aerodyne Aerosol Mass Spectrometers“. *Atmos. Environ.* 38.34, pp. 5745–5758. ISSN: 1352-2310. DOI: 10.1016/j.atmosenv.2004.01.054.

Alfarra, M. R., A. S. Prevot, S. Szidat, J. Sandradewi, S. Weimer, V. A. Lanz, D. Schreiber, M. Mohr, and U. Baltensperger (2007). „Identification of the mass spectral signature of organic aerosols from wood burning emissions“. *Environ. Sci. Technol.* 41.16, pp. 5770–7. URL: https://www.ncbi.nlm.nih.gov/pubmed/17874785.

Allan, J. D., A. E. Delia, H. Coe, K. N. Bower, M. R. Alfarra, J. L. Jimenez, A. M. Middlebrook, F. Drewnick, T. B. Onasch, M. R. Canagaratna, J. T. Jayne, and D. R. Worsnop (2004). „A generalised method for the extraction of chemically resolved mass spectra from Aerodyne Aerosol Mass Spectrometer data“. *Journal of Aerosol Science* 35.7, pp. 909–922. ISSN: 0021-8502. DOI: 10.1016/j.jaerosci.2004.02.007.

Allan, J. D., W. T. Morgan, E. Darbyshire, M. J. Flynn, P. I. Williams, D. E. Oram, P. Artaxo, J. Brito, J. D. Lee, and H. Coe (2014). „Airborne observations of IEPOX-derived isoprene SOA in the Amazon during SAMBBA“. *Atmos. Chem. Phys.* 14.20, pp. 11393–11407. ISSN: 1680-7316. DOI: 10.5194/acp-14-11393-2014.

Allan, J. D., J. L. Jimenez, P. I. Williams, M. R. Alfarra, K. N. Bower, J. T. Jayne, H. Coe, and D. R. Worsnop (2003). „Quantitative sampling using an Aerodyne aerosol mass spectrometer 1. Techniques of data interpretation and error analysis“. *J. Geophys. Res.-Atmos.* 108.D3. ISSN: 01480227. DOI: 10.1029/2002jd002358.

Andreae, M. O. and T. W. Andreae (1988). „The cycle of biogenic sulfur compounds over the Amazon Basin: 1. Dry season“. *J. Geophys. Res.-Atmos.* 93.D2, pp. 1487–1497.

Andreae, M. O. and P. Crutzen (1997). „Atmospheric Aerosols: Biogeochemical Sources and“. *Science.*

Andreae, M. O., O. C. Acevedo, A. Araujo, P. Artaxo, C. G. G. Barbosa, H. M. J. Barbosa, J. Brito, S. Carbone, X. Chi, B. B. L. Cintra, N. F. da Silva, N. L. Dias, C. Q. Dias, F. Ditas, R. Ditz, A. F. L. Godoi, R. H. M. Godoi, M. Heimann, T. Hoffmann, J. Kesselmeier, T. Konemann, M. L. Kruger, J. V. Lavric, A. O. Manzi, A. P. Lopes, D. L. Martins, E. F. Mikhailov, D. Moran-Zuloaga, B. W. Nelson, A. C. Nolscher, D. S. Nogueira, M. T. F. Piedade, C. Pohlker, U. Poschl, C. A. Quesada, L. V. Rizzo, C. U. Ro, N. Ruckteschler, L. D. A. Sa, M. D. Sa, C. B. Sales, R. M. N. dos Santos, J. Saturno, J. Schongart, M. Sorgel, C. M. de Souza, R. A. F. de Souza, H. Su, N. Targhetta, J. Tota, I. Trebs, S. Trumbore, A. van Eijck, D. Walter, Z. Wang, B. Weber, J. Williams, J. Winderlich, F. Wittmann, S. Wolff, and A. M. Yanez-Serrano (2015). „The Amazon Tall Tower Observatory (ATTO): overview of pilot measurements on ecosystem ecology, meteorology, trace gases, and aerosols“. *Atmos. Chem. Phys.* 15.18, pp. 10723–10776. ISSN: 1680-7316. DOI: 10.5194/acp-15-10723-2015.

Andreae, M. O., A. Afchine, R. Albrecht, B. A. Holanda, P. Artaxo, H. M. J. Barbosa, S. Borrmann, M. A. Cecchini, A. Costa, M. Dollner, D. Fütterer, E. Järvinen, T. Jurkat, T. Klimach, T. Konemann, C. Knote, M. Krämer, T. Krisna, L. A. T. Machado, S. Mertes, A. Minikin, C. Pöhlker, M. L. Pöhlker, U. Pöschl, D. Rosenfeld, D. Sauer, H. Schlager, M. Schnaiter, J. Schneider, C. Schulz, A. Spanu, V. B. Sperling, C. Voigt, A. Walser, J. Wang, B. Weinzierl, M. Wendisch, and H. Ziereis (2018). „Aerosol characteristics and particle production in the upper troposphere over the Amazon Basin“. *Atmos. Chem. Phys.* 18.2, pp. 921–961. DOI: 10.5194/acp-18-921-2018.

Andreae, M., P Artaxo, V Beck, M Bela, S Freitas, C Gerbig, K Longo, J. Munger, K. T. Wiedemann, and S. Wofsy (2012). „Carbon monoxide and related trace gases and aerosols over the Amazon Basin during the wet and dry seasons“. *Atmos. Chem. Phys.* 12.13, pp. 6041–6065.

Artaxo, P., W. Maenhaut, H. Storms, and R. Vangrieken (1990). „Aerosol Characteristics and Sources for the Amazon Basin during the Wet Season“. *J. Geo-*

phys. Res.-Atmos. 95.D10, pp. 16971–16985. ISSN: 2169-897X. DOI: 10.1029/JD095iD10p16971.

Artaxo, P., L. V. Rizzo, J. F. Brito, H. M. J. Barbosa, A. Arana, E. T. Sena, G. G. Cirino, W. Bastos, S. T. Martin, and M. O. Andreae (2013). „Atmospheric aerosols in Amazonia and land use change: from natural biogenic to biomass burning conditions“. *Faraday Discuss.* 165, pp. 203–235. ISSN: 1359-6640. DOI: 10.1039/c3fd00052d.

Asa-Awuku, A., A. Sorooshian, R. C. Flagan, J. H. Seinfeld, and A. Nenes (2015). „CCN properties of organic aerosol collected below and within marine stratocumulus clouds near Monterey, California“. *Atmosphere* 6.11, pp. 1590–1607.

Atkins, P., J. De Paula, and J. Keeler (2018). *Atkins' physical chemistry.* Oxford university press. ISBN: 9780198769866.

Ayres, B. R., H. M. Allen, D. C. Draper, S. S. Brown, R. J. Wild, J. L. Jimenez, D. A. Day, P. Campuzano-Jost, W. Hu, J. de Gouw, A. Koss, R. C. Cohen, K. C. Duffey, P. Romer, K. Baumann, E. Edgerton, S. Takahama, J. A. Thornton, B. H. Lee, F. D. Lopez-Hilfiker, C. Mohr, P. O. Wennberg, T. B. Nguyen, A. Teng, A. H. Goldstein, K. Olson, and J. L. Fry (2015). „Organic nitrate aerosol formation via NO_3 and biogenic volatile organic compounds in the southeastern United States“. *Atmos. Chem. Phys.* 15.23, pp. 13377–13392. ISSN: 1680-7324. DOI: 10.5194/acp-15-13377-2015.

Bacer, S. (2019). „Global numerical simulations of atmospheric ice crystals“. PhD Thesis. Gutenberg University Mainz, Max Planck Graduate Center.

Baehr, J., H. Schlager, H. Ziereis, P. Stock, P. van Velthoven, R. Busen, J. Ström, and U. Schumann (2003). „Aircraft observations of NO, NO_y, CO, and O_3 in the upper troposphere from 60° N to 60° S-Interhemispheric differences at mitlatitudes“. *Geophys. Res. Lett.* 30.11.

Bahreini, R., E. J. Dunlea, B. M. Matthew, C. Simons, K. S. Docherty, P. F. DeCarlo, J. L. Jimenez, C. A. Brock, and A. M. Middlebrook (2008). „Design and operation of a pressure-controlled inlet for airborne sampling with an aerodynamic aerosol lens“. *Aerosol. Sci. Technol.* 42.6, pp. 465–471. ISSN: 0278-6826. DOI: 10.1080/02786820802178514.

Bahreini, R., J. L. Jimenez, J. Wang, R. C. Flagan, J. H. Seinfeld, J. T. Jayne, and D. R. Worsnop (2003). „Aircraft-based aerosol size and composition measurements during ACE-Asia using an Aerodyne aerosol mass spectrometer“. *J. Geophys. Res.-Atmos.* 108.D23. ISSN: 2156-2202. DOI: 10.1029/2002JD003226.

Baumgardner, D., R. Newton, M. Krämer, J. Meyer, A. Beyer, M. Wendisch, and P. Vochezer (2014). „The Cloud Particle Spectrometer with Polarization Detection (CPSPD): A next generation open-path cloud probe for distinguishing liquid cloud droplets from ice crystals“. *Atmospheric research* 142, pp. 2–14.

Berkemeier, T., M. Shiraiwa, U. Pöschl, and T. Koop (2014). „Competition between water uptake and ice nucleation by glassy organic aerosol particles“. *Atmos. Chem. Phys.* 14.22, pp. 12513–12531. DOI: 10.5194/acp-14-12513-2014.

Berkemeier, T., M. Ammann, T. F. Mentel, U. Poschl, and M. Shiraiwa (2016). „Organic Nitrate Contribution to New Particle Formation and Growth in Secondary Organic Aerosols from alpha-Pinene Ozonolysis“. *Environ. Sci. Technol.* 50.12, pp. 6334–42. DOI: 10.1021/acs.est.6b00961.

Borrmann, S., D. Kunkel, R. Weigel, A. Minikin, T. Deshler, J. C. Wilson, J. Curtius, C. M. Volk, C. D. Homan, A. Ulanovsky, F. Ravegnani, S. Viciani, G. N. Shur, G. V. Belyaev, K. S. Law, and F. Cairo (2010). „Aerosols in the tropical and subtropical UT/LS: in-situ measurements of submicron particle abundance and volatility“. *Atmos. Chem. Phys.* 10.12, pp. 5573–5592. ISSN: 1680-7316. DOI: 10.5194/acp-10-5573-2010.

Boucher, O., D. Randall, P. Artaxo, C. Bretherton, G. Feingold, P. Forster, V.-M. Kerminen, Y. Kondo, H. Liao, U. Lohmann, S. K. Rasch P. andSatheesh, S. Sherwood, B. Stevens, and X. Y. Zhang (2013a). *Climate change 2013: The Physical Science Basis. Contribution of Working Group I to the Fifth Assessment Report of the Intergovernmental Panel on climate Change.* Ed. by T. F. Stocker, D. Qin, P. G.-K., T. M., S. K. Allen, J. Boschung, A. Nauels, Y. Xia, V. Bex, and P. M. Midgley. Cambridge University Press, Cambridge, UK and New York, NY, USA.

Boucher, O., D. Randall, P. Artaxo, C. Bretherton, G. Feingold, P. Forster, V.-M. Kerminen, Y. Kondo, H. Liao, U. Lohmann, S. K. Rasch P. andSatheesh, S. Sherwood, B. Stevens, and X. Y. Zhang (2013b). *Climate change 2013: The Physical Science Basis. Contribution of Working Group I to the Fifth Assessment Report of the Intergovernmental Panel on climate Change.* Ed. by T. F. Stocker, D. Qin, P. G.-K., T. M., S. K. Allen, J. Boschung, A. Nauels, Y. Xia, V. Bex, and P. M. Midgley. Fig. 7.13, Chapter 7, p. 598. Cambridge University Press, Cambridge, UK and New York, NY, USA.

Boyd, C. M., J. Sanchez, L. Xu, A. J. Eugene, T. Nah, W. Y. Tuet, M. I. Guzman, and N. L. Ng (2015). „Secondary organic aerosol formation from the β-pinene+NO_3 system: effect of humidity and peroxy radical fate“. *Atmos. Chem. Phys.* 15.13, pp. 7497–7522. DOI: 10.5194/acp-15-7497-2015.

Brégonzio-Rozier, L., C. Giorio, F. Siekmann, E. Pangui, S. B. Morales, B. Temime-Roussel, A. Gratien, V. Michoud, M. Cazaunau, H. L. DeWitt, A. Tapparo, A. Monod, and J.-F. Doussin (2016). „Secondary organic aerosol formation from isoprene photooxidation during cloud condensation-evaporation cycles". *Atmos. Chem. Phys.* 16.3, pp. 1747–1760. DOI: 10.5194/acp-16-1747-2016.

Brito, J., L. V. Rizzo, W. T. Morgan, H. Coe, B. Johnson, J. Haywood, K. Longo, S. Freitas, M. O. Andreae, and P. Artaxo (2014). „Ground-based aerosol characterization during the South American Biomass Burning Analysis (SAMBBA) field experiment". *Atmos. Chem. Phys.* 14.22, pp. 12069–12083. ISSN: 1680-7316. DOI: 10.5194/acp-14-12069-2014.

Brito, J., E. Freney, P. Dominutti, A. Borbon, S. L. Haslett, A. M. Batenburg, A. Colomb, R. Dupuy, C. Denjean, F. Burnet, T. Bourriane, A. Deroubaix, K. Sellegri, S. Borrmann, H. Coe, C. Flamant, P. Knippertz, and A. Schwarzenboeck (2018). „Assessing the role of anthropogenic and biogenic sources on PM_1 over southern West Africa using aircraft measurements". *Atmos. Chem. Phys.* 18.2, pp. 757–772. DOI: 10.5194/acp-18-757-2018.

Bruno, D. R., J Lide-Thomas, et al. (2014). *CRC Handbook of Chemistry and Physics, CRC Press, 2014: CRC Handbook of Chemistry and Physics*. Vol. 1. Bukupedia.

Bruns, E. A., V. Perraud, A. Zelenyuk, M. J. Ezell, S. N. Johnson, Y. Yu, D. Imre, B. J. Finlayson-Pitts, and M. L. Alexander (2010). „Comparison of FTIR and particle mass spectrometry for the measurement of particulate organic nitrates". *Environ. Sci. Technol.* 44.3, pp. 1056–61. DOI: 10.1021/es9029864.

Budisulistiorini, S. H., M. R. Canagaratna, P. L. Croteau, W. J. Marth, K. Baumann, E. S. Edgerton, S. L. Shaw, E. M. Knipping, D. R. Worsnop, J. T. Jayne, A. Gold, and J. D. Surratt (2013). „Real-time continuous characterization of secondary organic aerosol derived from isoprene epoxydiols in downtown Atlanta, Georgia, using the Aerodyne Aerosol Chemical Speciation Monitor". *Environ. Sci. Technol.* 47.11, pp. 5686–94. DOI: 10.1021/es400023n.

Canagaratna, M. R., J. T. Jayne, J. L. Jimenez, J. D. Allan, M. R. Alfarra, Q. Zhang, T. B. Onasch, F. Drewnick, H. Coe, A. Middlebrook, A. Delia, L. R. Williams, A. M. Trimborn, M. J. Northway, P. F. DeCarlo, C. E. Kolb, P. Davidovits, and D. R. Worsnop (2007). „Chemical and microphysical characterization of ambient aerosols with the Aerodyne Aerosol Mass Spectrometer". *Mass Spectrom Rev* 26.2, pp. 185–222. DOI: 10.1002/mas.20115.

Canagaratna, M. R., J. T. Jayne, D. A. Ghertner, S. Herndon, Q. Shi, J. L. Jimenez, P. J. Silva, P. Williams, T. Lanni, F. Drewnick, et al. (2004). „Chase studies of particulate emissions from in-use New York City vehicles". *Aeros. Sci. Techn.* 38.6, pp. 555–573.

Capes, G., B. Johnson, G. McFiggans, P. I. Williams, J. Haywood, and H. Coe (2008). „Aging of biomass burning aerosols over West Africa: Aircraft measurements of chemical composition, microphysical properties, and emission ratios“. *J. Geophys. Res.-Atmos.* 113.D23.

Carlton, A. G., C. Wiedinmyer, and J. H. Kroll (2009). „A review of Secondary Organic Aerosol (SOA) formation from isoprene“. *Atmos. Chem. Phys.* 9.14, pp. 4987–5005. ISSN: 1680-7316.

Carlton, A. G., B. J. Turpin, K. E. Altieri, S. Seitzinger, A. Reff, H.-J. Lim, and B. Ervens (2007). „Atmospheric oxalic acid and SOA production from glyoxal: Results of aqueous photooxidation experiments“. *Atmospheric Environment* 41.35, pp. 7588–7602.

Chen, Q., D. K. Farmer, J. Schneider, S. R. Zorn, C. L. Heald, T. G. Karl, A. Guenther, J. D. Allan, N. Robinson, H. Coe, J. R. Kimmel, T. Pauliquevis, S. Borrmann, U. Poschl, M. O. Andreae, P. Artaxo, J. L. Jimenez, and S. T. Martin (2009). „Mass spectral characterization of submicron biogenic organic particles in the Amazon Basin“. *Geophys. Res. Lett.* 36.20. ISSN: 0094-8276. DOI: 10.1029/2009gl039880.

Chen, Q., D. K. Farmer, L. V. Rizzo, T. Pauliquevis, M. Kuwata, T. G. Karl, A. Guenther, J. D. Allan, H. Coe, M. O. Andreae, U. Poschl, J. L. Jimenez, P. Artaxo, and S. T. Martin (2015). „Submicron particle mass concentrations and sources in the Amazonian wet season (AMAZE-08)“. *Atmos. Chem. Phys.* 15.7, pp. 3687–3701. ISSN: 1680-7316. DOI: 10.5194/acp-15-3687-2015.

Claeys, M., B. Graham, G. Vas, W. Wang, R. Vermeylen, V. Pashynska, J. Cafmeyer, P. Guyon, M. O. Andreae, P. Artaxo, and W. Maenhaut (2004). „Formation of secondary organic aerosols through photooxidation of isoprene“. *Science* 303.5661, pp. 1173–1176. ISSN: 0036-8075. DOI: 10.1126/science.1092805.

Collow, A. B. M., M. A. Miller, and L. C. Trabachino (July 2016). „Cloudiness over the Amazon rainforest: Meteorology and thermodynamics“. *J. Geophys. Res.-Atmos.* 121.13, pp. 7990–8005. ISSN: 2169-8996. DOI: 10.1002/2016JD024848.

Costa, A., J. Meyer, A. Afchine, A. Luebke, G. Günther, J. R. Dorsey, M. W. Gallagher, A. Ehrlich, M. Wendisch, D. Baumgardner, H. Wex, and M. Krämer (2017). „Classification of Arctic, midlatitude and tropical clouds in the mixed-phase temperature regime“. *Atmos. Chem. Phys.* 17.19, pp. 12219–12238. DOI: 10.5194/acp-17-12219-2017.

Crenn, V., J. Sciare, P. L. Croteau, S. Verlhac, R. Fröhlich, C. A. Belis, W. Aas, M. Äijälä, A. Alastuey, B. Artiñano, D. Baisnée, N. Bonnaire, M. Bressi, M. Canagaratna, F. Canonaco, C. Carbone, F. Cavalli, E. Coz, M. J. Cubison, J. K. Esser-Gietl, D. C. Green, V. Gros, L. Heikkinen, H. Herrmann, C. Lunder, M. C. Minguillón, G. Močnik, C. D. O’Dowd, J. Ovadnevaite, J.-E. Petit, E.

Petralia, L. Poulain, M. Priestman, V. Riffault, A. Ripoll, R. Sarda-Estève, J. G. Slowik, A. Setyan, A. Wiedensohler, U. Baltensperger, A. S. H. Prévôt, J. T. Jayne, and O. Favez (2015). „ACTRIS ACSM intercomparison – Part 1: Reproducibility of concentration and fragment results from 13 individual Quadrupole Aerosol Chemical Speciation Monitors (Q-ACSM) and consistency with co-located instruments“. *Atmos. Meas. Tech.* 8.12, pp. 5063–5087. DOI: 10.5194/amt-8-5063-2015.

Crippa, M., P. F. DeCarlo, J. G. Slowik, C. Mohr, M. F. Heringa, R. Chirico, L. Poulain, F. Freutel, J. Sciare, J. Cozic, C. F. Di Marco, M. Elsasser, J. B. Nicolas, N. Marchand, E. Abidi, A. Wiedensohler, F. Drewnick, J. Schneider, S. Borrmann, E. Nemitz, R. Zimmermann, J. L. Jaffrezo, A. S. H. Prevot, and U. Baltensperger (2013). „Wintertime aerosol chemical composition and source apportionment of the organic fraction in the metropolitan area of Paris“. *Atmos. Chem. Phys.* 13.2, pp. 961–981. ISSN: 1680-7316. DOI: 10.5194/acp-13-961-2013.

Crippa, M., F. Canonaco, V. A. Lanz, M. Aijala, J. D. Allan, S. Carbone, G. Capes, D. Ceburnis, M. Dall’Osto, D. A. Day, P. F. DeCarlo, M. Ehn, A. Eriksson, E. Freney, L. Hildebrandt Ruiz, R. Hillamo, J. L. Jimenez, H. Junninen, A. Kiendler-Scharr, A. M. Kortelainen, M. Kulmala, A. Laaksonen, A. Mensah, C. Mohr, E. Nemitz, C. O’Dowd, J. Ovadnevaite, S. N. Pandis, T. Petaja, L. Poulain, S. Saarikoski, K. Sellegri, E. Swietlicki, P. Tiitta, D. R. Worsnop, U. Baltensperger, and A. S. H. Prevot (2014). „Organic aerosol components derived from 25 AMS data sets across Europe using a consistent ME-2 based source apportionment approach“. *Atmos. Chem. Phys.* 14.12, pp. 6159–6176. ISSN: 1680-7316. DOI: 10.5194/acp-14-6159-2014.

Cubison, M. J., A. M. Ortega, P. L. Hayes, D. K. Farmer, D. Day, M. J. Lechner, W. H. Brune, E. Apel, G. S. Diskin, J. A. Fisher, H. E. Fuelberg, A. Hecobian, D. J. Knapp, T. Mikoviny, D. Riemer, G. W. Sachse, W. Sessions, R. J. Weber, A. J. Weinheimer, A. Wisthaler, and J. L. Jimenez (2011). „Effects of aging on organic aerosol from open biomass burning smoke in aircraft and laboratory studies“. *Atmos. Chem. Phys.* 11.23, pp. 12049–12064. ISSN: 1680-7316. DOI: 10.5194/acp-11-12049-2011.

Cziczo, D. J. and K. D. Froyd (2014). „Sampling the composition of cirrus ice residuals“. *Atmospheric Research* Volume 142. DOI: 10.1016/j.atmosres.2013.06.012.

Cziczo, D. J., K. D. Froyd, C. Hoose, E. J. Jensen, M. Diao, M. A. Zondlo, J. B. Smith, C. H. Twohy, and D. M. Murphy (2013). „Clarifying the Dominant Sources and Mechanisms of Cirrus Cloud Formation“. *Science* 340.6138, pp. 1320–1324. DOI: 10.1126/science.1234145.

Cziczo, D. J., L. Ladino, Y. Boose, Z. A. Kanji, P. Kupiszewski, S. Lance, S. Mertes, and H. Wex (2017). „Measurements of Ice Nucleating Particles and Ice Residuals“. *Meteorological Monographs* 58, pp. 8.1–8.13. DOI: 10.1175/AMSMONOGRAPHS-D-16-0008.1.

Dahlkötter, F., M. Gysel, D. Sauer, A. Minikin, R. Baumann, P. Seifert, A. Ansmann, M. Fromm, C. Voigt, and B. Weinzierl (2014). „The Pagami Creek smoke plume after long-range transport to the upper troposphere over Europe - aerosol properties and black carbon mixing state“. *Atmos. Chem. Phys.* 14.12, pp. 6111–6137. ISSN: 1680-7324. DOI: 10.5194/acp-14-6111-2014.

Darbyshire, E., W. T. Morgan, J. D. Allan, D. Liu, M. J. Flynn, J. R. Dorsey, S. J. O’Shea, D. Lowe, K. Szpek, F. Marenco, B. T. Johnson, S. Bauguitte, J. M. Haywood, J. F. Brito, P. Artaxo, K. M. Longo, and H. Coe (2018). „The vertical distribution of biomass burning pollution over tropical South America from aircraft in situ measurements during SAMBBA“. *Atmos. Chem. Phys. Discuss.* 2018, pp. 1–26. DOI: 10.5194/acp-2018-921.

Darer, A. I., N. C. Cole-Filipiak, A. E. O’Connor, and M. J. Elrod (2011). „Formation and Stability of Atmospherically Relevant Isoprene-Derived Organosulfates and Organonitrates“. *Environ. Sci. Technol.* 45.5, pp. 1895–1902. DOI: 10.1021/es103797z.

Daumit, K. E., A. J. Carrasquillo, J. F. Hunter, and J. H. Kroll (2014). „Laboratory studies of the aqueous-phase oxidation of polyols: submicron particles vs. bulk aqueous solution“. *Atmos. Chem. Phys.* 14.19, pp. 10773–10784. DOI: 10.5194/acp-14-10773-2014.

Davidson, E. A., A. C. de Araújo, P. Artaxo, J. K. Balch, I. F. Brown, M. M. Bustamante, M. T. Coe, R. S. DeFries, M. Keller, M. Longo, et al. (2012). „The Amazon basin in transition“. *Nature* 481.7381, p. 321.

De Sá, S. S., B. B. Palm, P. Campuzano-Jost, D. A. Day, W. Hu, G. Isaacman-VanWertz, L. D. Yee, J. Brito, S. Carbone, I. O. Ribeiro, G. G. Cirino, Y. Liu, R. Thalman, A. Sedlacek, A. Funk, C. Schumacher, J. E. Shilling, J. Schneider, P. Artaxo, A. H. Goldstein, R. A. F. Souza, J. Wang, K. A. McKinney, H. Barbosa, M. L. Alexander, J. L. Jimenez, and S. T. Martin (2018). „Urban influence on the concentration and composition of submicron particulate matter in central Amazonia“. *Atmos. Chem. Phys.* 18.16, pp. 12185–12206. DOI: 10.5194/acp-18-12185-2018.

De Sá, S. S., B. B. Palm, P. Campuzano-Jost, D. A. Day, M. K. Newburn, W. Hu, G. Isaacman-VanWertz, L. D. Yee, R. Thalman, J. Brito, S. Carbone, P. Artaxo, A. H. Goldstein, A. O. Manzi, R. A. F. Souza, F. Mei, J. E. Shilling, S. R. Springston, J. Wang, J. D. Surratt, M. L. Alexander, J. L. Jimenez, and S. T. Martin (2017). „Influence of urban pollution on the production of organic particulate matter from isoprene epoxydiols in central Amazonia“. *Atmos. Chem. Phys.* 17.11, pp. 6611–6629. ISSN: 1680-7324. DOI: 10.5194/acp-17-6611-2017.

DeCarlo, P. F., J. G. Slowik, D. R. Worsnop, P. Davidovits, and J. L. Jimenez (2004). „Particle morphology and density characterization by combined mobility and aerodynamic diameter measurements. Part 1: Theory“. *Aerosol. Sci. Technol.* 38.12, pp. 1185–1205. ISSN: 0278-6826. DOI: 10.1080/027868290903907.

DeCarlo, P. F., J. R. Kimmel, A. Trimborn, M. J. Northway, J. T. Jayne, A. C. Aiken, M. Gonin, K. Fuhrer, T. Horvath, K. S. Docherty, D. R. Worsnop, and J. L. Jimenez (2006). „Field-deployable, high-resolution, time-of-flight aerosol mass spectrometer“. *Anal. Chem.* 78.24, pp. 8281–9. DOI: 10.1021/ac061249n.

DeCarlo, P. F., E. J. Dunlea, J. R. Kimmel, A. C. Aiken, D. Sueper, J. Crounse, P. O. Wennberg, L. Emmons, Y. Shinozuka, A. Clarke, J. Zhou, J. Tomlinson, D. R. Collins, D. Knapp, A. J. Weinheimer, D. D. Montzka, T. Campos, and J. L. Jimenez (2008). „Fast airborne aerosol size and chemistry measurements above Mexico City and Central Mexico during the MILAGRO campaign“. *Atmos. Chem. Phys.* 8.14, pp. 4027–4048. DOI: 10.5194/acp-8-4027-2008.

Decesari, S, S Fuzzi, M. Facchini, M Mircea, L Emblico, F Cavalli, W. Maenhaut, X. Chi, G Schkolnik, A Falkovich, et al. (2006). „Characterization of the organic composition of aerosols from Rondônia, Brazil, during the LBA-SMOCC 2002 experiment and its representation through model compounds“. *Atmos. Chem. Phys.* 6.2, pp. 375–402. DOI: 10.5194/acp-6-375-2006.

DLR (2018a). *HALO Specifications.* last access: 17.09.2018. URL: https://www.halo.dlr.de/aircraft/specifications.html.

DLR (2018b). *The Basis HALO Measurement and Sensor System (BAHAMAS).* last access: 17.09.2018. URL: https://www.halo.dlr.de/instrumentation/basis.html.

Docherty, K. S., E. A. Stone, I. M. Ulbrich, P. F. DeCarlo, D. C. Snyder, J. J. Schauer, R. E. Peltier, R. J. Weber, S. M. Murphy, J. H. Seinfeld, B. D. Grover, D. J. Eatough, and J. L. Jimenez (2008). „Apportionment of Primary and Secondary Organic Aerosols in Southern California during the 2005 Study of Organic Aerosols in Riverside (SOAR-1)“. *Environ. Sci. Tech.* 42.20, pp. 7655–7662. DOI: 10.1021/es8008166.

Drewnick, F. (2012). „Speciation analysis in on-line aerosol mass spectrometry“. *Anal Bioanal Chem* 404.8, pp. 2127–31. DOI: 10.1007/s00216-012-6295-x.

Drewnick, F., S. S. Hings, P. DeCarlo, J. T. Jayne, M. Gonin, K. Fuhrer, S. Weimer, J. L. Jimenez, K. L. Demerjian, S. Borrmann, and D. R. Worsnop (2005). „A new time-of-flight aerosol mass spectrometer (TOF-AMS) - Instrument description and first field deployment“. *Aerosol. Sci. Technol.* 39.7, pp. 637–658. ISSN: 0278-6826. DOI: 10.1080/02786820500182040.

Drewnick, F., S. S. Hings, M. R. Alfarra, A. S. H. Prevot, and S. Borrmann (2009). „Aerosol quantification with the Aerodyne Aerosol Mass Spectrometer: detection limits and ionizer background effects“. *Atmos. Meas. Tech.* 2.1, pp. 33–46. ISSN: 1867-1381. DOI: 10.5194/amt-2-33-2009.

Drewnick, F., J. Schneider, S. S. Hings, N. Hock, K. Noone, A. Targino, S. Weimer, and S. Borrmann (2007). „Measurement of Ambient, Interstitial, and Residual Aerosol Particles on a Mountaintop Site in Central Sweden using an Aerosol Mass Spectrometer and a CVI“. *Journal of Atmospheric Chemistry* 56.1, pp. 1–20. ISSN: 1573-0662. DOI: 10.1007/s10874-006-9036-8.

Dusek, U., G. P. Frank, L. Hildebrandt, J. Curtius, J. Schneider, S. Walter, D. Chand, F. Drewnick, S. Hings, D. Jung, S. Borrmann, and M. O. Andreae (2006). „Size Matters More Than Chemistry for Cloud-Nucleating Ability of Aerosol Particles“. *Science* 312.5778, pp. 1375–1378. DOI: 10.1126/science.1125261.

ERIKS GmbH (2015). *o-ring.info*. last access: 06.04.2018. ERIKS GmbH, Dichtomatik Vertriebsgesell. für Technische Dichtungen mbH. URL: http://de.dichtomatik.com/en/produktkatalog/o_ringe/030_or_fkm_80.html.

Ervens, B., B. Turpin, and R. Weber (2011). „Secondary organic aerosol formation in cloud droplets and aqueous particles (aqSOA): a review of laboratory, field and model studies“. *Atmos. Chem. Phys.* 11.21, pp. 11069–11102.

Farmer, D. K., A. Matsunaga, K. S. Docherty, J. D. Surratt, J. H. Seinfeld, P. J. Ziemann, and J. L. Jimenez (2010). „Response of an aerosol mass spectrometer to organonitrates and organosulfates and implications for atmospheric chemistry“. *Proc Natl Acad Sci USA* 107.15, pp. 6670–6675. DOI: 10.1073/pnas.0912340107.

Farmer, D. K., C. D. Cappa, and S. M. Kreidenweis (2015). „Atmospheric Processes and Their Controlling Influence on Cloud Condensation Nuclei Activity“. *Chemical Reviews* 115.10, pp. 4199–4217. DOI: 10.1021/cr5006292.

Fisch, G, J. Tota, L. Machado, M. S. Dias, R. d. F. Lyra, C. Nobre, A. Dolman, and J. Gash (2004). „The convective boundary layer over pasture and forest in Amazonia“. *Theoretical and Applied Climatology* 78.1-3, pp. 47–59.

Formenti, P., M. O. Andreae, L. Lange, G. Roberts, J. Cafmeyer, I. Rajta, W. Maenhaut, B. N. Holben, P. Artaxo, and J. Lelieveld (2001). „Saharan dust in Brazil and Suriname during the Large-Scale Biosphere-Atmosphere Experiment in Amazonia (LBA) - Cooperative LBA Regional Experiment (CLAIRE) in March 1998“. *J. Geophys. Res.-Atmos.* 106.D14, pp. 14919–14934. DOI: 10.1029/2000JD900827.

Fröhlich, R., V. Crenn, A. Setyan, C. A. Belis, F. Canonaco, O. Favez, V. Riffault, J. G. Slowik, W. Aas, M. Aijälä, A. Alastuey, B. Artiñano, N. Bonnaire, C. Bozzetti, M. Bressi, C. Carbone, E. Coz, P. L. Croteau, M. J. Cubison, J. K. Esser-Gietl, D. C. Green, V. Gros, L. Heikkinen, H. Herrmann, J. T. Jayne, C. R. Lunder, M. C. Minguillón, G. Močnik, C. D. O'Dowd, J. Ovadnevaite, E. Petralia, L. Poulain, M. Priestman, A. Ripoll, R. Sarda-Estève, A. Wiedensohler, U. Baltensperger, J. Sciare, and A. S. H. Prévôt (2015). „ACTRIS ACSM intercomparison – Part 2: Intercomparison of ME-2 organic source apportionment results from 15 individual, co-located aerosol mass spectrometers“. *Atmos. Meas. Tech.* 8.6, pp. 2555–2576. DOI: 10.5194/amt-8-2555-2015.

Froyd, K. D., D. M. Murphy, T. J. Sanford, D. S. Thomson, J. C. Wilson, L. Pfister, and L. Lait (2009). „Aerosol composition of the tropical upper troposphere“. *Atmos. Chem. Phys.* 9.13, pp. 4363–4385. ISSN: 1680-7316.

Froyd, K. D., D. M. Murphy, P. Lawson, D. Baumgardner, and R. L. Herman (2010a). „Aerosols that form subvisible cirrus at the tropical tropopause“. *Atmos. Chem. Phys.* 10.1, pp. 209–218. DOI: 10.5194/acp-10-209-2010.

Froyd, K. D., S. M. Murphy, D. M. Murphy, J. A. de Gouw, N. C. Eddingsaas, and P. O. Wennberg (2010b). „Contribution of isoprene-derived organosulfates to free tropospheric aerosol mass“. *Proc Natl Acad Sci USA* 107.50, pp. 21360–21365. DOI: 10.1073/pnas.1012561107.

Fry, J. L., A. Kiendler-Scharr, A. W. Rollins, P. J. Wooldridge, S. S. Brown, H. Fuchs, W. Dubé, A. Mensah, M. dal Maso, R. Tillmann, H.-P. Dorn, T. Brauers, and R. C. Cohen (2009). „Organic nitrate and secondary organic aerosol yield from NO_3 oxidation of β-pinene evaluated using a gas-phase kinetics/aerosol partitioning model“. *Atmos. Chem. Phys.* 9.4, pp. 1431–1449. DOI: 10.5194/acp-9-1431-2009.

Fry, J. L., A. Kiendler-Scharr, A. W. Rollins, T. Brauers, S. S. Brown, H.-P. Dorn, W. P. Dubé, H. Fuchs, A. Mensah, F. Rohrer, R. Tillmann, A. Wahner, P. J. Wooldridge, and R. C. Cohen (2011). „SOA from limonene: role of NO_3 in its generation and degradation“. *Atmos. Chem. Phys.* 11.8, pp. 3879–3894. DOI: 10.5194/acp-11-3879-2011.

Fry, J. L., D. C. Draper, K. J. Zarzana, P. Campuzano-Jost, D. A. Day, J. L. Jimenez, S. S. Brown, R. C. Cohen, L. Kaser, A. Hansel, L. Cappellin, T. Karl, A. H. Roux, A. Turnipseed, C. Cantrell, B. L. Lefer, and N. Grossberg (2013). „Observations of gas- and aerosol-phase organic nitrates at BEACHON-RoMBAS 2011“. *Atmos. Chem. Phys.* 13.17, pp. 8585–8605. ISSN: 1680-7316. DOI: 10.5194/acp-13-8585-2013.

Fry, J. L., S. S. Brown, A. M. Middlebrook, P. M. Edwards, P. Campuzano-Jost, D. A. Day, J. L. Jimenez, H. M. Allen, T. B. Ryerson, I. Pollack, M. Graus, C. Warneke, J. A. de Gouw, C. A. Brock, J. Gilman, B. M. Lerner, W. P. Dubé, J. Liao, and A. Welti (2018). „Secondary organic aerosol (SOA) yields from NO3 radical + isoprene based on nighttime aircraft power plant plume transects“. *Atmos. Chem. Phys.* 18.16, pp. 11663–11682. DOI: 10.5194/acp-18-11663-2018.

Fueglistaler, S., A. E. Dessler, T. J. Dunkerton, I. Folkins, Q. Fu, and P. W. Mote (2009). „Tropical Tropopause Layer“. *Reviews of Geophysics* 47.1. ISSN: 8755-1209. DOI: 10.1029/2008rg000267.

Gerbig, C., S. Schmitgen, D. Kley, A. Volz-Thomas, K. Dewey, and D. Haaks (1999). „An improved fast-response vacuum-UV resonance fluorescence CO instrument“. *J. Geophys. Res.-Atmos.* 104.D1, pp. 1699–1704.

Giangrande, S. E., Z. Feng, M. P. Jensen, J. M. Comstock, K. L. Johnson, T. Toto, M. Wang, C. Burleyson, N. Bharadwaj, F. Mei, L. A. T. Machado, A. O. Manzi, S. Xie, S. Tang, M. A. F. Silva Dias, R. A. F. de Souza, C. Schumacher, and S. T. Martin (2017). „Cloud characteristics, thermodynamic controls and radiative impacts during the Observations and Modeling of the Green Ocean Amazon (GoAmazon2014/5) experiment“. *Atmos. Chem. Phys.* 17.23, pp. 14519–14541. DOI: 10.5194/acp-17-14519-2017.

Grimm Aerosol Technik (2008). *Aerosol spectrometer Series 1.129 “SKY-OPC“*. Manual.

Guenther, A. B., X. Jiang, C. L. Heald, T. Sakulyanontvittaya, T. Duhl, L. K. Emmons, and X. Wang (2012). „The Model of Emissions of Gases and Aerosols from Nature version 2.1 (MEGAN2.1): an extended and updated framework for modeling biogenic emissions“. *Geoscientific Model Development* 5.6, pp. 1471–1492. ISSN: 1991-959x. DOI: 10.5194/gmd-5-1471-2012.

Haag, W., B. Kärcher, J. Ström, A. Minikin, U. Lohmann, J. Ovarlez, and A. Stohl (2003). „Freezing thresholds and cirrus cloud formation mechanisms inferred from in situ measurements of relative humidity“. *Atmos. Chem. Phys.* 3.5, pp. 1791–1806. DOI: 10.5194/acp-3-1791-2003.

Hallquist, M., J. C. Wenger, U. Baltensperger, Y. Rudich, D. Simpson, M. Claeys, J. Dommen, N. M. Donahue, C. George, A. H. Goldstein, J. F. Hamilton, H. Herrmann, T. Hoffmann, Y. Iinuma, M. Jang, M. E. Jenkin, J. L. Jimenez, A. Kiendler-Scharr, W. Maenhaut, G. McFiggans, T. F. Mentel, A. Monod, A. S. H. Prévôt, J. H. Seinfeld, J. D. Surratt, R. Szmigielski, and J. Wildt (2009). „The formation, properties and impact of secondary organic aerosol: current and emerging issues". *Atmos. Chem. Phys.* 9.14, pp. 5155–5236. DOI: 10.5194/acp-9-5155-2009.

Hennigan, C. J., A. P. Sullivan, J. L. Collett, and A. L. Robinson (2010). „Levoglucosan stability in biomass burning particles exposed to hydroxyl radicals". *Geophys. Res. Lett.* 37.9. ISSN: 0094-8276. DOI: 10.1029/2010GL043088.

Henning, S., K. Dieckmann, K. Ignatius, M. Schäfer, P. Zedler, E. Harris, B. Sinha, D. van Pinxteren, S. Mertes, W. Birmili, M. Merkel, Z. Wu, A. Wiedensohler, H. Wex, H. Herrmann, and F. Stratmann (2014). „Influence of cloud processing on CCN activation behaviour in the Thuringian Forest, Germany during HCCT-2010". *Atmos. Chem. Phys.* 14.15, pp. 7859–7868. DOI: 10.5194/acp-14-7859-2014.

Hinds, W. C. (1999). *Aerosol technology: properties, behavior, and measurement of airborne particles.* Wiley-Interscience. Wiley. ISBN: 9780471194101.

Hings, S. S. (2006). „Characterisation and Field Deployment of a Novel Quantitative Time-of-Flight Aerosol Mass Spectrometer (ToF-AMS)". PhD Thesis. Gutenberg University, Mainz.

Hogrefe, O., F. Drewnick, G. G. Lala, J. J. Schwab, and K. L. Demerjian (2004). „Development, Operation and Applications of an Aerosol Generation, Calibration and Research Facility Special Issue of Aerosol Science and Technology on Findings from the Fine Particulate Matter Supersites Program". *Aerosol Science and Technology* 38.sup1, pp. 196–214. DOI: 10.1080/02786820390229516.

Holton, J. R. (2004). *An Introduction to Dynamic Meteorology.* Elsevier Academic Press.

Hu, W. W., P. Campuzano-Jost, B. B. Palm, D. A. Day, A. M. Ortega, P. L. Hayes, J. E. Krechmer, Q. Chen, M. Kuwata, Y. J. Liu, S. S. de Sa, K. McKinney, S. T. Martin, M. Hu, S. H. Budisulistiorini, M. Riva, J. D. Surratt, J. M. St Clair, G. Isaacman-Van Wertz, L. D. Yee, A. H. Goldstein, S. Carbone, J. Brito, P. Artaxo, J. A. de Gouw, A. Koss, A. Wisthaler, T. Mikoviny, T. Karl, L. Kaser, W. Jud, A. Hansel, K. S. Docherty, M. L. Alexander, N. H. Robinson, H. Coe, J. D. Allan, M. R. Canagaratna, F. Paulot, and J. L. Jimenez (2015). „Characterization of a real-time tracer for isoprene epoxydiols-derived secondary organic aerosol (IEPOX-SOA) from aerosol mass spectrometer measurements“. *Atmos. Chem. Phys.* 15.20, pp. 11807–11833. ISSN: 1680-7316. DOI: 10.5194/acp-15-11807-2015.

Huang, D. D., Y. J. Li, B. P. Lee, and C. K. Chan (2015). „Analysis of Organic Sulfur Compounds in Atmospheric Aerosols at the HKUST Supersite in Hong Kong Using HR-ToF-AMS“. *Environ. Sci. Technol.* 49.6, pp. 3672–3679. DOI: 10.1021/es5056269.

Huffman, J. A., K. S. Docherty, C. Mohr, M. J. Cubison, I. M. Ulbrich, P. J. Ziemann, T. B. Onasch, and J. L. Jimenez (2009). „Chemically-Resolved Volatility Measurements of Organic Aerosol from Different Sources“. *Environ. Sci. Tech.* 43.14, pp. 5351–5357. DOI: 10.1021/es803539d.

Huffman, J., J. T. Jayne, F. Drewnick, A. Aiken, T. Onasch, D. Worsnop, and J. L. Jimenez (Dec. 2005). „Design, Modeling, Optimization, and Experimental Tests of a Particle Beam Width Probe for the Aerodyne Aerosol Mass Spectrometer“. *Aerosol. Sci. Technol.* 39.

Jäkel, E., M. Wendisch, T. C. Krisna, F. Ewald, T. Kölling, T. Jurkat, C. Voigt, M. A. Cecchini, L. A. T. Machado, A. Afchine, A. Costa, M. Krämer, M. O. Andreae, U. Pöschl, D. Rosenfeld, and T. Yuan (2017). „Vertical distribution of the particle phase in tropical deep convective clouds as derived from cloud-side reflected solar radiation measurements“. *Atmos. Chem. Phys.* 17.14, pp. 9049–9066. DOI: 10.5194/acp-17-9049-2017.

Jayne, J. T., D. C. Leard, X. F. Zhang, P. Davidovits, K. A. Smith, C. E. Kolb, and D. R. Worsnop (2000). „Development of an aerosol mass spectrometer for size and composition analysis of submicron particles“. *Aerosol. Sci. Technol.* 33.1-2, pp. 49–70. ISSN: 0278-6826. DOI: 10.1080/027868200410840.

Jimenez, J. L., J. T. Jayne, Q. Shi, C. E. Kolb, D. R. Worsnop, I. Yourshaw, J. H. Seinfeld, R. C. Flagan, X. F. Zhang, K. A. Smith, J. W. Morris, and P. Davidovits (2003). „Ambient aerosol sampling using the Aerodyne Aerosol Mass Spectrometer“. *J. Geophys. Res.-Atmos.* 108.D7. ISSN: 2169-897X. DOI: 10.1029/2001jd001213.

Jimenez, J. L., M. R. Canagaratna, N. M. Donahue, A. S. Prevot, Q. Zhang, J. H. Kroll, P. F. DeCarlo, J. D. Allan, H. Coe, N. L. Ng, A. C. Aiken, K. S. Docherty, I. M. Ulbrich, A. P. Grieshop, A. L. Robinson, J. Duplissy, J. D. Smith, K. R. Wilson, V. A. Lanz, C. Hueglin, Y. L. Sun, J. Tian, A. Laaksonen, T. Raatikainen, J. Rautiainen, P. Vaattovaara, M. Ehn, M. Kulmala, J. M. Tomlinson, D. R. Collins, M. J. Cubison, E. J. Dunlea, J. A. Huffman, T. B. Onasch, M. R. Alfarra, P. I. Williams, K. Bower, Y. Kondo, J. Schneider, F. Drewnick, S. Borrmann, S. Weimer, K. Demerjian, D. Salcedo, L. Cottrell, R. Griffin, A. Takami, T. Miyoshi, S. Hatakeyama, A. Shimono, J. Y. Sun, Y. M. Zhang, K. Dzepina, J. R. Kimmel, D. Sueper, J. T. Jayne, S. C. Herndon,

A. M. Trimborn, L. R. Williams, E. C. Wood, A. M. Middlebrook, C. E. Kolb, U. Baltensperger, and D. R. Worsnop (2009). „Evolution of organic aerosols in the atmosphere". *Science* 326.5959, pp. 1525–9. ISSN: 1095-9203 (Electronic) 0036-8075 (Linking). DOI: 10.1126/science.1180353.

Kanakidou, M., J. H. Seinfeld, S. N. Pandis, I. Barnes, F. J. Dentener, M. C. Facchini, R. Van Dingenen, B. Ervens, A. Nenes, C. J. Nielsen, E. Swietlicki, J. P. Putaud, Y. Balkanski, S. Fuzzi, J. Horth, G. K. Moortgat, R. Winterhalter, C. E. L. Myhre, K. Tsigaridis, E. Vignati, E. G. Stephanou, and J. Wilson (2005). „Organic aerosol and global climate modelling: a review". *Atmos. Chem. Phys.* 5.4, pp. 1053–1123. DOI: 10.5194/acp-5-1053-2005.

Kiendler-Scharr, A., A. A. Mensah, E. Friese, D. Topping, E. Nemitz, A. S. H. Prevot, M. Aijala, J. Allan, F. Canonaco, M. Canagaratna, S. Carbone, M. Crippa, M. Dall Osto, D. A. Day, P. De Carlo, C. F. Di Marco, H. Elbern, A. Eriksson, E. Freney, L. Hao, H. Herrmann, L. Hildebrandt, R. Hillamo, J. L. Jimenez, A. Laaksonen, G. McFiggans, C. Mohr, C. O'Dowd, R. Otjes, J. Ovadnevaite, S. N. Pandis, L. Poulain, P. Schlag, K. Sellegri, E. Swietlicki, P. Tiitta, A. Vermeulen, A. Wahner, D. Worsnop, and H. C. Wu (2016). „Ubiquity of organic nitrates from nighttime chemistry in the European submicron aerosol". *Geophys. Res. Lett.* 43.14, pp. 7735–7744. ISSN: 0094-8276. DOI: 10.1002/2016gl069239.

Kimmel, J. (2011). *Aerodyne ToF-AMS DAQ Users Manual v4.0.0.* Ed. by P. De-Carlo, J. Kimmel, J. Jimenez, M.Canagaratna, J.Jayne, and D. Worsnop.

Knollenberg, R. G. (1970). „The Optical Array: An Alternative to Scattering or Extinction for Airborne Particle Size Determination". *Journal of Applied Meteorology* 9.1, pp. 86–103. DOI: 10.1175/1520-0450(1970)009<0086:TOAAAT>2.0.CO;2.

Knopf, D. A., B. Wang, A. Laskin, R. C. Moffet, and M. K. Gilles (2010). „Heterogeneous nucleation of ice on anthropogenic organic particles collected in Mexico City". *Geophys. Res. Lett.* 37.11. DOI: 10.1029/2010GL043362.

Köhler, H. (1936). „The nucleus in and the growth of hygroscopic droplets". *Trans. Faraday Soc.* 32 (0), pp. 1152–1161. DOI: 10.1039/TF9363201152.

Köllner, F. (2019). „Aerosol in the summertime Arctic lower troposphere: Composition, sources and formation". PhD Thesis. Gutenberg University, Mainz.

Krechmer, J. E., M. M. Coggon, P. Massoli, T. B. Nguyen, J. D. Crounse, W. Hu, D. A. Day, G. S. Tyndall, D. K. Henze, J. C. Rivera-Rios, J. B. Nowak, J. R. Kimmel, R. L. Mauldin, H. Stark, J. T. Jayne, M. Sipilä, H. Junninen, J. M. S. Clair, X. Zhang, P. A. Feiner, L. Zhang, D. O. Miller, W. H. Brune, F. N. Keutsch, P. O. Wennberg, J. H. Seinfeld, D. R. Worsnop, J. L. Jimenez, and

M. R. Canagaratna (2015). „Formation of Low Volatility Organic Compounds and Secondary Organic Aerosol from Isoprene Hydroxyhydroperoxide Low-NO Oxidation“. *Environ. Sci. Technol.* 49.17, pp. 10330–10339. DOI: 10.1021/acs.est.5b02031.

Kroll, J. H. and J. H. Seinfeld (2008). „Chemistry of secondary organic aerosol: Formation and evolution of low-volatility organics in the atmosphere“. *Atmos. Environ.* 42.16, pp. 3593 –3624. ISSN: 1352-2310. DOI: https://doi.org/10.1016/j.atmosenv.2008.01.003.

Kuhn, U., L. Ganzeveld, A. Thielmann, T. Dindorf, G. Schebeske, M. Welling, J. Sciare, G. Roberts, F. X. Meixner, J. Kesselmeier, J. Lelieveld, O. Kolle, P. Ciccioli, J. Lloyd, J. Trentmann, P. Artaxo, and M. O. Andreae (2010). „Impact of Manaus City on the Amazon Green Ocean atmosphere: ozone production, precursor sensitivity and aerosol load“. *Atmos. Chem. Phys.* 10.19, pp. 9251–9282. ISSN: 1680-7316. DOI: 10.5194/acp-10-9251-2010.

Kulkarni, P., P. A. Baron, and K. Willeke (2011). *Aerosol measurement: principles, techniques, and applications.* John Wiley & Sons. DOI: 10.1002/9781118001684.

Laborde, M., M. Schnaiter, C. Linke, H. Saathoff, K. H. Naumann, O. Möhler, S. Berlenz, U. Wagner, J. W. Taylor, D. Liu, M. Flynn, J. D. Allan, H. Coe, K. Heimerl, F. Dahlkötter, B. Weinzierl, A. G. Wollny, M. Zanatta, J. Cozic, P. Laj, R. Hitzenberger, J. P. Schwarz, and M. Gysel (2012). „Single Particle Soot Photometer intercomparison at the AIDA chamber“. *Atmospheric Measurement Techniques* 5, pp. 3077–3097. DOI: 10.5194/amt-5-3077-2012.

Lee, L., P. J. Wooldridge, J. B. Gilman, C. Warneke, J. de Gouw, and R. C. Cohen (2014). „Low temperatures enhance organic nitrate formation: evidence from observations in the 2012 Uintah Basin Winter Ozone Study“. *Atmos. Chem. Phys.* 14.22, pp. 12441–12454. ISSN: 1680-7316. DOI: 10.5194/acp-14-12441-2014.

Lee, T., A. P. Sullivan, L. Mack, J. L. Jimenez, S. M. Kreidenweis, T. B. Onasch, D. R. Worsnop, W. Malm, C. E. Wold, W. M. Hao, and J. L. C. Jr. (2010). „Chemical Smoke Marker Emissions During Flaming and Smoldering Phases of Laboratory Open Burning of Wildland Fuels“. *Aerosol Science and Technology* 44.9, pp. i–v. DOI: 10.1080/02786826.2010.499884.

Levin, E. J. T., A. J. Prenni, B. B. Palm, D. A. Day, P. Campuzano-Jost, P. M. Winkler, S. M. Kreidenweis, P. J. DeMott, J. L. Jimenez, and J. N. Smith (2014). „Size-resolved aerosol composition and its link to hygroscopicity at a forested site in Colorado“. *Atmos. Chem. Phys.* 14.5, pp. 2657–2667. DOI: 10.5194/acp-14-2657-2014.

Lim, Y. B., Y. Tan, M. J. Perri, S. P. Seitzinger, and B. J. Turpin (2010). „Aqueous chemistry and its role in secondary organic aerosol (SOA) formation“. *Atmos. Chem. Phys.* 10.21, pp. 10521–10539. DOI: 10.5194/acp-10-10521-2010.

Lin, Y.-H., E. M. Knipping, E. S. Edgerton, S. L. Shaw, and J. D. Surratt (2013). „Investigating the influences of SO_2 and NH_3 levels on isoprene-derived secondary organic aerosol formation using conditional sampling approaches“. *Atmos. Chem. Phys.* 13.16, pp. 8457–8470. DOI: 10.5194/acp-13-8457-2013.

Lin, Y.-H., Z. Zhang, K. S. Docherty, H. Zhang, S. H. Budisulistiorini, C. L. Rubitschun, S. L. Shaw, E. M. Knipping, E. S. Edgerton, T. E. Kleindienst, A. Gold, and J. D. Surratt (2012). „Isoprene Epoxydiols as Precursors to Secondary Organic Aerosol Formation: Acid-Catalyzed Reactive Uptake Studies with Authentic Compounds“. *Environ. Sci. Technol.* 46.1, pp. 250–258. DOI: 10.1021/es202554c.

Liu, J., L. M. Russell, A. K. Y. Lee, K. A. McKinney, J. D. Surratt, and P. J. Ziemann (2017). „Observational evidence for pollution-influenced selective uptake contributing to biogenic secondary organic aerosols in the southeastern U.S.“ *Geophys. Res. Lett.* ISSN: 1944-8007. DOI: 10.1002/2017GL074665.

Liu, J., E. L. D'Ambro, B. H. Lee, F. D. Lopez-Hilfiker, R. A. Zaveri, J. C. Rivera-Rios, F. N. Keutsch, S. Iyer, T. Kurten, Z. Zhang, A. Gold, J. D. Surratt, J. E. Shilling, and J. A. Thornton (2016a). „Efficient Isoprene Secondary Organic Aerosol Formation from a Non-IEPOX Pathway“. *Environ. Sci. Technol.* 50.18, pp. 9872–9880. DOI: 10.1021/acs.est.6b01872.

Liu, P. S. K., R. Deng, K. A. Smith, L. R. Williams, J. T. Jayne, M. R. Canagaratna, K. Moore, T. B. Onasch, D. R. Worsnop, and T. Deshler (2007). „Transmission efficiency of an aerodynamic focusing lens system: Comparison of model calculations and laboratory measurements for the Aerodyne Aerosol Mass Spectrometer“. *Aerosol. Sci. Technol.* 41.8, pp. 721–733. ISSN: 0278-6826. DOI: 10.1080/02786820701422278.

Liu, P., P. J. Ziemann, D. B. Kittelson, and P. H. McMurry (1995a). „Generating Particle Beams of Controlled Dimensions and Divergence: I. Theory of Particle Motion in Aerodynamic Lenses and Nozzle Expansions“. *Aerosol Science and Technology* 22.3, pp. 293–313. DOI: 10.1080/02786829408959748.

Liu, P., P. J. Ziemann, D. B. Kittelson, and P. H. McMurry (1995b). „Generating Particle Beams of Controlled Dimensions and Divergence: II. Experimental Evaluation of Particle Motion in Aerodynamic Lenses and Nozzle Expansions“. *Aerosol Science and Technology* 22.3, pp. 314–324. DOI: 10.1080/02786829408959749.

Liu, Y., J. Brito, M. R. Dorris, J. C. Rivera-Rios, R. Seco, K. H. Bates, P. Artaxo, J. Duvoisin S., F. N. Keutsch, S. Kim, A. H. Goldstein, A. B. Guenther, A. O. Manzi, R. A. Souza, S. R. Springston, T. B. Watson, K. A. McKinney, and S. T. Martin (2016b). „Isoprene photochemistry over the Amazon rainforest“. *Proc Natl Acad Sci USA* 113.22, pp. 6125–30. DOI: 10.1073/pnas.1524136113.

Liu, Y., F. Siekmann, P. Renard, A. El Zein, G. Salque, I. El Haddad, B. Temime-Roussel, D. Voisin, R. Thissen, and A. Monod (2012). „Oligomer and SOA formation through aqueous phase photooxidation of methacrolein and methyl vinyl ketone“. *Atmospheric Environment* 49, pp. 123–129.

Liu, Y., M. Kuwata, B. F. Strick, F. M. Geiger, R. J. Thomson, K. A. McKinney, and S. T. Martin (2015). „Uptake of Epoxydiol Isomers Accounts for Half of the Particle-Phase Material Produced from Isoprene Photooxidation via the HO2 Pathway“. *Environ. Sci. Technol.* 49.1, pp. 250–258. DOI: 10.1021/es5034298.

Machado, L. A. T., A. J. P. Calheiros, T. Biscaro, S. Giangrande, M. A. F. Silva Dias, M. A. Cecchini, R. Albrecht, M. O. Andreae, W. F. Araujo, P. Artaxo, S. Borrmann, R. Braga, C. Burleyson, C. W. Eichholz, J. Fan, Z. Feng, G. F. Fisch, M. P. Jensen, S. T. Martin, U. Pöschl, C. Pöhlker, M. L. Pöhlker, J.-F. Ribaud, D. Rosenfeld, J. M. B. Saraiva, C. Schumacher, R. Thalman, D. Walter, and M. Wendisch (2018). „Overview: Precipitation characteristics and sensitivities to environmental conditions during GoAmazon2014/5 and ACRIDICON-CHUVA“. *Atmos. Chem. Phys.* 18.9, pp. 6461–6482. DOI: 10.5194/acp-18-6461-2018.

Machado, L., H Laurent, N Dessay, and I Miranda (2004). „Seasonal and diurnal variability of convection over the Amazonia: a comparison of different vegetation types and large scale forcing“. *Theoretical and Applied Climatology* 78.1-3, pp. 61–77.

Mahnke, C. O. (2018). „Untersuchungen zu Wolkenbildung und Aerosolmikrophysik in der tropischen Toposphäre und UT/LS: Messtechnik und flugzeuggetragene In-situ-Beobachtungen“. PhD Thesis. Gutenberg University Mainz.

Malavelle, F. F., J. M. Haywood, L. M. Mercado, G. A. Folberth, N. Bellouin, S. Sitch, and P. Artaxo (2019). „Studying the impact of biomass burning aerosol radiative and climate effects on the Amazon rainforest productivity with an Earth system model“. *Atmos. Chem. Phys.* 19.2, pp. 1301–1326. DOI: 10.5194/acp-19-1301-2019.

Marais, E. A., D. J. Jacob, J. L. Jimenez, P. Campuzano-Jost, D. A. Day, W. Hu, J. Krechmer, L. Zhu, P. S. Kim, C. C. Miller, J. A. Fisher, K. Travis, K. Yu, T. F. Hanisco, G. M. Wolfe, H. L. Arkinson, H. O. T. Pye, K. D. Froyd, J. Liao, and V. F. McNeill (2016). „Aqueous-phase mechanism for secondary organic aerosol formation from isoprene: application to the southeast United States and co-benefit of SO_2 emission controls“. *Atmos. Chem. Phys.* 16.3, pp. 1603–1618. ISSN: 1680-7324. DOI: 10.5194/acp-16-1603-2016.

Marenco, F., B. Johnson, J. M. Langridge, J. Mulcahy, A. Benedetti, S. Remy, L. Jones, K. Szpek, J. Haywood, K. Longo, and P. Artaxo (2016). „On the vertical distribution of smoke in the Amazonian atmosphere during the dry season“. *Atmos. Chem. Phys.* 16.4, pp. 2155–2174. DOI: 10.5194/acp-16-2155-2016.

Martin, S. T., M. O. Andreae, D. Althausen, P. Artaxo, H. Baars, S. Borrmann, Q. Chen, D. K. Farmer, A. Guenther, S. S. Gunthe, J. L. Jimenez, T. Karl, K. Longo, A. Manzi, T. Müller, T. Pauliquevis, M. D. Petters, A. J. Prenni, U. Pöschl, L. V. Rizzo, J. Schneider, J. N. Smith, E. Swietlicki, J. Tota, J. Wang, A. Wiedensohler, and S. R. Zorn (2010). „An overview of the Amazonian Aerosol Characterization Experiment 2008 (AMAZE-08)“. *Atmos. Chem. Phys.* 10.23, pp. 11415–11438. ISSN: 1680-7324. DOI: 10.5194/acp-10-11415-2010.

Martin, S. T., P. Artaxo, L. A. T. Machado, A. O. Manzi, R. A. F. Souza, C. Schumacher, J. Wang, M. O. Andreae, H. M. J. Barbosa, J. Fan, G. Fisch, A. H. Goldstein, A. Guenther, J. L. Jimenez, U. Pöschl, M. A. Silva Dias, J. N. Smith, and M. Wendisch (2016). „Introduction: Observations and Modeling of the Green Ocean Amazon (GoAmazon2014/5)“. *Atmos. Chem. Phys.* 16.8, pp. 4785–4797. DOI: 10.5194/acp-16-4785-2016.

Matthew, B. M., A. M. Middlebrook, and T. B. Onasch (2008). „Collection Efficiencies in an Aerodyne Aerosol Mass Spectrometer as a Function of Particle Phase for Laboratory Generated Aerosols“. *Aerosol. Sci. Technol.* 42.11, pp. 884–898. DOI: 10.1080/02786820802356797.

Mei, F., A. Setyan, Q. Zhang, and J. Wang (2013). „CCN activity of organic aerosols observed downwind of urban emissions during CARES“. *Atmos. Chem. Phys.* 13.24, pp. 12155–12169. DOI: 10.5194/acp-13-12155-2013.

Mei, F., J. M. Comstock, J. Wang, M. Pekour, J. Shilling, C. Long, J. Tomlinson, B. Schmid, J. Hubbe, T. Krisna, A. Giez, M. Wendisch, B. Weinzierl, M. Zoeger, C. Schulz, H. Schlager, J. Schneider, S. S. de Sa, S. Springston, M. A. Cecchini, L. A. T. Machado, and S. Martin (2019). „Comparison of Aircraft Measurements during GoAmazon2014/5 and ACRIDICON-CHUVA“. *submitted to Atmos. Meas. Tech.*

Meyer, J. (2013). „Ice crystal measurements with the new particle spectrometer NIXE-CAPS“. PhD Thesis. Forschungszentrum Jülich.

Middlebrook, A. M., R. Bahreini, J. L. Jimenez, and M. R. Canagaratna (2012). „Evaluation of Composition-Dependent Collection Efficiencies for the Aerodyne Aerosol Mass Spectrometer using Field Data“. *Aerosol. Sci. Technol.* 46.3, pp. 258–271. ISSN: 0278-6826. DOI: 10.1080/02786826.2011.620041.

Minikin, A., D. Sauer, A. Ibrahim, H. Franke, T. Röschenthaler, D. A. Fütterer, and A. Petzold (2017). „The HALO Submicrometer Aerosol Inlet (HASI): Design concept and first characterization“. URL: http://elib.dlr.de/116282/.

Möhler, O, S Benz, H Saathoff, M Schnaiter, R Wagner, J Schneider, S Walter, V Ebert, and S Wagner (2008). „The effect of organic coating on the heterogeneous ice nucleation efficiency of mineral dust aerosols“. *Environmental Research Letters* 3.2, p. 025007.

Molina, M. J., A. V. Ivanov, S. Trakhtenberg, and L. T. Molina (2004). „Atmospheric evolution of organic aerosol“. *Geophys. Res. Lett.* 31.22. DOI: 10.1029/2004GL020910.

Molleker, S., F. Helleis, T. Klimach, C. Gurk, O. Appel, A. Huenig, A. Dragoneas, F. Rubach, C. Schulz, F. Köllner, H.-C. Clemen, and S. Borrmann (2019). „Application of an O-ring pinch device as a constant pressure inlet for airborne sampling“. *in prep. for Atmos. Meas. Tech.*

Murphy, D. M., D. J. Cziczo, K. D. Froyd, P. K. Hudson, B. M. Matthew, A. M. Middlebrook, R. E. Peltier, A. Sullivan, D. S. Thomson, and R. J. Weber (2006). „Single-particle mass spectrometry of tropospheric aerosol particles“. *J. Geophys. Res.-Atmos.* 111.D23.

Ng, N. L., A. J. Kwan, J. D. Surratt, A. W. H. Chan, P. S. Chhabra, A. Sorooshian, H. O. T. Pye, J. D. Crounse, P. O. Wennberg, R. C. Flagan, and J. H. Seinfeld (2008). „Secondary organic aerosol (SOA) formation from reaction of isoprene with nitrate radicals (NO_3)“. *Atmos. Chem. Phys.* 8.14, pp. 4117–4140. DOI: 10.5194/acp-8-4117-2008.

Ng, N. L., M. R. Canagaratna, Q. Zhang, J. L. Jimenez, J. Tian, I. M. Ulbrich, J. H. Kroll, K. S. Docherty, P. S. Chhabra, R. Bahreini, S. M. Murphy, J. H. Seinfeld, L. Hildebrandt, N. M. Donahue, P. F. DeCarlo, V. A. Lanz, A. S. H. Prevot, E. Dinar, Y. Rudich, and D. R. Worsnop (2010). „Organic aerosol components observed in Northern Hemispheric datasets from Aerosol Mass Spectrometry“. *Atmos. Chem. Phys.* 10.10, pp. 4625–4641. ISSN: 1680-7316. DOI: 10.5194/acp-10-4625-2010.

Ng, N. L., M. R. Canagaratna, J. L. Jimenez, P. S. Chhabra, J. H. Seinfeld, and D. R. Worsnop (2011a). „Changes in organic aerosol composition with aging inferred from aerosol mass spectra“. *Atmos. Chem. Phys.* 11.13, pp. 6465–6474. ISSN: 1680-7316. DOI: 10.5194/acp-11-6465-2011.

Ng, N. L., M. R. Canagaratna, J. L. Jimenez, Q. Zhang, I. M. Ulbrich, and D. R. Worsnop (2011b). „Real-time methods for estimating organic component mass concentrations from aerosol mass spectrometer data“. *Environ. Sci. Technol.* 45.3, pp. 910–6. DOI: 10.1021/es102951k.

Ng, N. L., S. S. Brown, A. T. Archibald, E. Atlas, R. C. Cohen, J. N. Crowley, D. A. Day, N. M. Donahue, J. L. Fry, H. Fuchs, R. J. Griffin, M. I. Guzman, H. Herrmann, A. Hodzic, Y. Iinuma, J. L. Jimenez, A. Kiendler-Scharr, B. H. Lee, D. J. Luecken, J. Q. Mao, R. McLaren, A. Mutzel, H. D. Osthoff, B. Ouyang, B. Picquet-Varrault, U. Platt, H. O. T. Pye, Y. Rudich, R. H. Schwantes, M. Shiraiwa, J. Stutz, J. A. Thornton, A. Tilgner, B. J. Williams, and R. A. Zaveri (2017). „Nitrate radicals and biogenic volatile organic compounds: oxidation, mechanisms, and organic aerosol“. *Atmos. Chem. Phys.* 17.3, pp. 2103–2162. ISSN: 1680-7316. DOI: 10.5194/acp-17-2103-2017.

Ogren, J. A., J. Heintzenberg, and R. J. Charlson (1985). „In-situ sampling of clouds with a droplet to aerosol converter“. *Geophys. Res. Lett.* 12.3, pp. 121–124. ISSN: 1944-8007. DOI: 10.1029/GL012i003p00121.

Ortega, A. M., P. L. Hayes, Z. Peng, B. B. Palm, W. Hu, D. A. Day, R. Li, M. J. Cubison, W. H. Brune, M. Graus, C. Warneke, J. B. Gilman, W. C. Kuster, J. de Gouw, C. Gutiérrez-Montes, and J. L. Jimenez (2016). „Real-time measurements of secondary organic aerosol formation and aging from ambient air in an oxidation flow reactor in the Los Angeles area“. *Atmos. Chem. Phys.* 16.11, pp. 7411–7433. DOI: 10.5194/acp-16-7411-2016.

Pandis, S. N., N. M. Donahue, B. N. Murphy, I. Riipinen, C. Fountoukis, E. Karnezi, D. Patoulias, and K. Skyllakou (2013). „Introductory lecture: Atmospheric organic aerosols: insights from the combination of measurements and chemical transport models“. *Faraday discussions* 165, pp. 9–24.

Park, K., D. B. Kittelson, M. R. Zachariah, and P. H. McMurry (2004). „Measurement of inherent material density of nanoparticle agglomerates“. *Journal of Nanoparticle Research* 6.2, pp. 267–272. DOI: 10.1023/B:NANO.0000034657.71309.e6.

Paulot, F., J. D. Crounse, H. G. Kjaergaard, A. Kürten, J. M. St. Clair, J. H. Seinfeld, and P. O. Wennberg (2009). „Unexpected Epoxide Formation in the Gas-Phase Photooxidation of Isoprene“. *Science* 325.5941, pp. 730–733. DOI: 10.1126/science.1172910.

Pieber, S. M., I. El Haddad, J. G. Slowik, M. R. Canagaratna, J. T. Jayne, S. M. Platt, C. Bozzetti, K. R. Daellenbach, R. Fröhlich, A. Vlachou, F. Klein, J. Dommen, B. Miljevic, J. L. Jiménez, D. R. Worsnop, U. Baltensperger, and A. S. H. Prévôt (2016). „Inorganic Salt Interference on CO2+ in Aerodyne

AMS and ACSM Organic Aerosol Composition Studies“. *Environ. Sci. Technol.* 50.19, pp. 10494–10503. DOI: 10.1021/acs.est.6b01035.

Pöhlker, C., D. Walter, H. Paulsen, T. Könemann, E. Rodríguez-Caballero, D. Moran-Zuloaga, J. Brito, S. Carbone, C. Degrendele, V. R. Després, F. Ditas, B. A. Holanda, J. W. Kaiser, G. Lammel, J. V. Lavrič, J. Ming, D. Pickersgill, M. L. Pöhlker, M. Praß, N. Ruckteschler, J. Saturno, M. Sörgel, Q. Wang, B. Weber, S. Wolff, P. Artaxo, U. Pöschl, and M. O. Andreae (2018a). „Land cover and its transformation in the backward trajectory footprint region of the Amazon Tall Tower Observatory“. *Atmos. Chem. Phys. Discuss.* 2018, pp. 1–69. DOI: 10.5194/acp-2018-323.

Pöhlker, M. L., F. Ditas, J. Saturno, T. Klimach, I. Hrabě de Angelis, A. C. Araùjo, J. Brito, S. Carbone, Y. Cheng, X. Chi, R. Ditz, S. S. Gunthe, B. A. Holanda, K. Kandler, J. Kesselmeier, T. Könemann, O. O. Krüger, J. V. Lavrič, S. T. Martin, E. Mikhailov, D. Moran-Zuloaga, L. V. Rizzo, D. Rose, H. Su, R. Thalman, D. Walter, J. Wang, S. Wolff, H. M. J. Barbosa, P. Artaxo, M. O. Andreae, U. Pöschl, and C. Pöhlker (2018b). „Long-term observations of cloud condensation nuclei over the Amazon rain forest – Part 2: Variability and characteristics of biomass burning, long-range transport, and pristine rain forest aerosols“. *Atmos. Chem. Phys.* 18.14, pp. 10289–10331. DOI: 10.5194/acp-18-10289-2018.

Pratt, K. A., P. J. DeMott, J. R. French, Z. Wang, D. L. Westphal, A. J. Heymsfield, C. H. Twohy, A. J. Prenni, and K. A. Prather (2009). „In situ detection of biological particles in cloud ice-crystals“. *Nature Geoscience* 2.6, p. 398.

Rebotier, T. P. and K. A. Prather (2007). „Aerosol time-of-flight mass spectrometry data analysis: A benchmark of clustering algorithms“. *Analytica Chimica Acta* 585.1, pp. 38 –54. ISSN: 0003-2670. DOI: https://doi.org/10.1016/j.aca.2006.12.009.

Reitz, P. (2011). „Chemical composition measurements of cloud condensation nuclei and ice nuclei by aerosol mass spectrometry“. PhD Thesis. Gutenberg University, Mainz. URL: http://nbn-resolving.org/urn:nbn:de:hebis:77-28691.

Riemann-Campe, K., K. Fraedrich, and F. Lunkeit (2009). „Global climatology of convective available potential energy (CAPE) and convective inhibition (CIN) in ERA-40 reanalysis“. *Atmospheric Research* 93.1-3, pp. 534–545.

Riipinen, I., T. Yli-Juuti, J. R. Pierce, T. Petäjä, D. R. Worsnop, M. Kulmala, and N. M. Donahue (2012). „The contribution of organics to atmospheric nanoparticle growth“. *Nature Geoscience* 5. DOI: 10.1038/ngeo1499.

Riva, M., S. H. Budisulistiorini, Y. Chen, Z. Zhang, E. L. D’Ambro, X. Zhang, A. Gold, B. J. Turpin, J. A. Thornton, M. R. Canagaratna, and J. D. Surratt (2016). „Chemical Characterization of Secondary Organic Aerosol from Oxidation of Isoprene Hydroxyhydroperoxides“. *Environ. Sci. Technol.* 50.18, pp. 9889–9899. ISSN: 0013-936X. DOI: 10.1021/acs.est.6b02511.

Robinson, N. H., J. F. Hamilton, J. D. Allan, B. Langford, D. E. Oram, Q. Chen, K. Docherty, D. K. Farmer, J. L. Jimenez, M. W. Ward, C. N. Hewitt, M. H. Barley, M. E. Jenkin, A. R. Rickard, S. T. Martin, G. McFiggans, and H. Coe (2011). „Evidence for a significant proportion of Secondary Organic Aerosol from isoprene above a maritime tropical forest“. *Atmos. Chem. Phys.* 11.3, pp. 1039–1050. ISSN: 1680-7316. DOI: 10.5194/acp-11-1039-2011.

Rogge, W. F., L. M. Hildemann, M. A. Mazurek, and G. R. a. Cass (1998). „Sources of Fine Organic Aerosol. 9. Pine, Oak, and Synthetic Log Combustion in Residential Fireplaces“. *Environ. Sci. Technol.* 32.1, pp. 13–22. DOI: 10.1021/es960930b.

Rollins, A. W., A. Kiendler-Scharr, J. L. Fry, T. Brauers, S. S. Brown, H.-P. Dorn, W. P. Dubé, H. Fuchs, A. Mensah, T. F. Mentel, F. Rohrer, R. Tillmann, R. Wegener, P. J. Wooldridge, and R. C. Cohen (2009). „Isoprene oxidation by nitrate radical: alkyl nitrate and secondary organic aerosol yields“. *Atmos. Chem. Phys.* 9.18, pp. 6685–6703. DOI: 10.5194/acp-9-6685-2009.

Rosenfeld, D., U. Lohmann, G. B. Raga, C. D. O’Dowd, M. Kulmala, S. Fuzzi, A. Reissell, and M. O. Andreae (2008). „Flood or drought: how do aerosols affect precipitation?“ *Science* 321.5894, pp. 1309–13. DOI: 10.1126/science.1160606.

Rosenfeld, D., M. O. Andreae, A. Asmi, M. Chin, G. de Leeuw, D. P. Donovan, R. Kahn, S. Kinne, N. Kivekäs, M. Kulmala, et al. (2014). „Global observations of aerosol-cloud-precipitation-climate interactions“. *Reviews of Geophysics* 52.4, pp. 750–808.

Saha, S., S. Moorthi, X. Wu, J. Wang, S. Nadiga, P. Tripp, D. Behringer, Y.-T. Hou, H. ya Chuang, M. Iredell, M. Ek, J. Meng, R. Yang, M. P. Mendez, H. van den Dool, Q. Zhang, W. Wang, M. Chen, and E. Becker (2014). „The NCEP Climate Forecast System Version 2“. *Journal of Climate* 27.6, pp. 2185–2208. DOI: 10.1175/JCLI-D-12-00823.1.

Salcedo, D., T. B. Onasch, K. Dzepina, M. R. Canagaratna, Q. Zhang, J. A. Huffman, P. F. DeCarlo, J. T. Jayne, P. Mortimer, D. R. Worsnop, C. E. Kolb, K. S. Johnson, B. Zuberi, L. C. Marr, R. Volkamer, L. T. Molina, M. J. Molina, B. Cardenas, R. M. Bernabé, C. Márquez, J. S. Gaffney, N. A. Marley, A. Laskin, V. Shutthanandan, Y. Xie, W. Brune, R. Lesher, T. Shirley, and J. L. Jimenez (2006). „Characterization of ambient aerosols in Mexico City during the MCMA-2003 campaign with Aerosol Mass Spectrometry: results from the CENICA Supersite“. *Atmos. Chem. Phys.* 6.4, pp. 925–946. DOI: 10.5194/acp-6-925-2006.

Saturno, J., F. Ditas, M. Penning de Vries, B. A. Holanda, M. L. Pöhlker, S. Carbone, D. Walter, N. Bobrowski, J. Brito, X. Chi, A. Gutmann, I. Hrabe de Angelis, L. A. T. Machado, D. Moran-Zuloaga, J. Rüdiger, J. Schneider, C. Schulz, Q. Wang, M. Wendisch, P. Artaxo, T. Wagner, U. Pöschl, M. O. Andreae, and C. Pöhlker (2018). „African volcanic emissions influencing atmospheric aerosols over the Amazon rain forest“. *Atmos. Chem. Phys.* 18.14, pp. 10391–10405. DOI: 10.5194/acp-18-10391-2018.

Schauer, J. J., M. J. Kleeman, G. R. Cass, and B. R. T. Simoneit (2001). „Measurement of Emissions from Air Pollution Sources. 3. C1-C29 Organic Compounds from Fireplace Combustion of Wood“. *Environ. Sci. Technol.* 35.9, pp. 1716–1728. DOI: 10.1021/es001331e.

Schmale, J., J. Schneider, T. Jurkat, C. Voigt, H. Kalesse, M. Rautenhaus, M. Lichtenstern, H. Schlager, G. Ancellet, F. Arnold, M. Gerding, I. Mattis, M. Wendisch, and S. Borrmann (2010). „Aerosol layers from the 2008 eruptions of Mount Okmok and Mount Kasatochi: In situ upper troposphere and lower stratosphere measurements of sulfate and organics over Europe“. *J. Geophys. Res.-Atmos.* 115. ISSN: 2169-897X. DOI: 10.1029/2009jd013628.

Schmale, J., J. Schneider, G. Ancellet, B. Quennehen, A. Stohl, H. Sodemann, J. F. Burkhart, T. Hamburger, S. R. Arnold, A. Schwarzenboeck, S. Borrmann, and K. S. Law (2011). „Source identification and airborne chemical characterisation of aerosol pollution from long-range transport over Greenland during POLARCAT summer campaign 2008“. *Atmos. Chem. Phys.* 11.19, pp. 10097–10123. ISSN: 1680-7316. DOI: 10.5194/acp-11-10097-2011.

Schneider, J., N. Hock, S. Weimer, S. Borrmann, U. Kirchner, R. Vogt, and V. Scheer (2005). „Nucleation particles in diesel exhaust: composition inferred from in situ mass spectrometric analysis“. *Environ. Sci. Technol.* 39.16, pp. 6153–61. URL: https://www.ncbi.nlm.nih.gov/pubmed/16173576.

Schneider, J., S. Weimer, F. Drewnick, S. Borrmann, G. Helas, P. Gwaze, O. Schmid, M. O. Andreae, and U. Kirchner (2006). „Mass spectrometric analysis and aerodynamic properties of various types of combustion-related aerosol particles“. *International Journal of Mass Spectrometry* 258.1-3, pp. 37–49. ISSN: 1387-3806. DOI: 10.1016/j.ijms.2006.07.008.

Schneider, J., F. Freutel, S. R. Zorn, Q. Chen, D. K. Farmer, J. L. Jimenez, S. T. Martin, P. Artaxo, A. Wiedensohler, and S. Borrmann (2011). „Mass- spectrometric identification of primary biological particle markers and application to pristine submicron aerosol measurements in Amazonia“. *Atmos. Chem. Phys.* 11.22, pp. 11415–11429. ISSN: 1680-7316. DOI: 10.5194/acp-11-11415-2011.

Schneider, J., S. Mertes, D. van Pinxteren, H. Herrmann, and S. Borrmann (2017). „Uptake of nitric acid, ammonia, and organics in orographic clouds: mass spectrometric analyses of droplet residual and interstitial aerosol particles“. *Atmos. Chem. Phys.* 17.2, pp. 1571–1593. ISSN: 1680-7316. DOI: 10.5194/acp-17-1571-2017.

Schulz, C., J. Schneider, B. Amorim Holanda, O. Appel, A. Costa, S. S. de Sá, V. Dreiling, D. Fütterer, T. Jurkat-Witschas, T. Klimach, C. Knote, M. Krämer, S. T. Martin, S. Mertes, M. L. Pöhlker, D. Sauer, C. Voigt, A. Walser, B. Weinzierl, H. Ziereis, M. Zöger, M. O. Andreae, P. Artaxo, L. A. T. Machado, U. Pöschl, M. Wendisch, and S. Borrmann (2018). „Aircraft-based observations of isoprene-epoxydiol-derived secondary organic aerosol (IEPOX-SOA) in the tropical upper troposphere over the Amazon region“. *Atmos. Chem. Phys.* 18.20, pp. 14979–15001. DOI: 10.5194/acp-18-14979-2018.

Schumann, U. and H. Huntrieser (2007). „The global lightning-induced nitrogen oxides source“. *Atmos. Chem. Phys.* 7.14, pp. 3823–3907. DOI: 10.5194/acp-7-3823-2007.

Schwarz, J. P., R. S. Gao, D. W. Fahey, D. S. Thomson, L. A. Watts, J. C. Wilson, J. M. Reeves, M. Darbeheshti, D. G. Baumgardner, G. L. Kok, S. H. Chung, M. Schulz, J. Hendricks, A. Lauer, B. Kärcher, J. G. Slowik, K. H. Rosenlof, T. L. Thompson, A. O. Langford, M. Loewenstein, and K. C. Aikin (2006). „Single-particle measurements of midlatitude black carbon and light-scattering aerosols from the boundary layer to the lower stratosphere“. *J. Geophys. Res.-Atmos.* 111.D16. DOI: 10.1029/2006JD007076.

Seinfeld, J. and S. Pandis (2006). *Atmos. Chem. Phys.: From Air Pollution to Climate Change.* Wiley. ISBN: 9780471720188.

Shilling, J. E., R. A. Zaveri, J. D. Fast, L. Kleinman, M. L. Alexander, M. R. Canagaratna, E. Fortner, J. M. Hubbe, J. T. Jayne, A. Sedlacek, A. Setyan, S. Springston, D. R. Worsnop, and Q. Zhang (2013). „Enhanced SOA formation from mixed anthropogenic and biogenic emissions during the CARES campaign“. *Atmos. Chem. Phys.* 13.4, pp. 2091–2113. DOI: 10.5194/acp-13-2091-2013.

Shilling, J. E., M. S. Pekour, E. C. Fortner, P. Artaxo, S. de Sá, J. M. Hubbe, K. M. Longo, L. A. T. Machado, S. T. Martin, S. R. Springston, J. Tomlinson, and J. Wang (2018). „Aircraft observations of the chemical composition and aging of aerosol in the Manaus urban plume during GoAmazon 2014/5“. *Atmos. Chem. Phys.* 18.14, pp. 10773–10797. DOI: 10.5194/acp-18-10773-2018.

Shiraiwa, M., Y. Li, A. P. Tsimpidi, V. A. Karydis, T. Berkemeier, S. N. Pandis, J. Lelieveld, T. Koop, and U. Pöschl (2017). „Global distribution of particle phase state in atmospheric secondary organic aerosols“. *Nature Communications* 8, p. 15002. DOI: 10.1038/ncomms15002.

Shrivastava, M., L. K. Berg, J. D. Fast, R. C. Easter, A. Laskin, E. G. Chapman, W. I. Gustafson, Y. Liu, and C. M. Berkowitz (2013). „Modeling aerosols and their interactions with shallow cumuli during the 2007 CHAPS field study“. *J. Geophys. Res.-Atmos.* 118.3, pp. 1343–1360.

Shrivastava, M., C. D. Cappa, J. Fan, A. H. Goldstein, A. B. Guenther, J. L. Jimenez, C. Kuang, A. Laskin, S. T. Martin, N. L. Ng, T. Petaja, J. R. Pierce, P. J. Rasch, P. Roldin, J. H. Seinfeld, J. Shilling, J. N. Smith, J. A. Thornton, R. Volkamer, J. Wang, D. R. Worsnop, R. A. Zaveri, A. Zelenyuk, and Q. Zhang (2017). „Recent advances in understanding secondary organic aerosol: Implications for global climate forcing“. *Reviews of Geophysics* 55.2, pp. 509–559. ISSN: 1944-9208. DOI: 10.1002/2016RG000540.

Simoneit, B. R. T., J. J. Schauer, C. G. Nolte, D. R. Oros, V. O. Elias, M. P. Fraser, W. F. Rogge, and G. R. Cass (1999). „Levoglucosan, a tracer for cellulose in biomass burning and atmospheric particles“. *Atmos. Environ.* 33.2, pp. 173–182.

Sorooshian, A., N. L. Ng, A. W. H. Chan, G. Feingold, R. C. Flagan, and J. H. Seinfeld (2007). „Particulate organic acids and overall water-soluble aerosol composition measurements from the 2006 Gulf of Mexico Atmospheric Composition and Climate Study (GoMACCS)“. *J. Geophys. Res.-Atmos.* 112.D13. ISSN: 2169-897x. DOI: 10.1029/2007jd008537.

Sorooshian, A., V. Varutbangkul, F. J. Brechtel, B. Ervens, G. Feingold, R. Bahreini, S. M. Murphy, J. S. Holloway, E. L. Atlas, G. Buzorius, et al. (2006). „Oxalic acid in clear and cloudy atmospheres: Analysis of data from International Consortium for Atmospheric Research on Transport and Transformation 2004“. *J. Geophys. Res.-Atmos.* 111.D23.

Sorooshian, A., S. M. Murphy, S. Hersey, R. Bahreini, H. Jonsson, R. C. Flagan, and J. H. Seinfeld (2010). „Constraining the contribution of organic acids and AMS m/z 44 to the organic aerosol budget: On the importance of meteorology, aerosol hygroscopicity, and region“. *Geophys. Res. Lett.* 37.21.

Sorooshian, A., Z. Wang, M. M. Coggon, H. H. Jonsson, and B. Ervens (2013). „Observations of sharp oxalate reductions in stratocumulus clouds at variable altitudes: Organic acid and metal measurements during the 2011 E-PEACE campaign“. *Environ. Sci. Technol.* 47.14, pp. 7747–7756.

St. Clair, J. M., J. C. Rivera-Rios, J. D. Crounse, H. C. Knap, K. H. Bates, A. P. Teng, S. Jørgensen, H. G. Kjaergaard, F. N. Keutsch, and P. O. Wennberg (2016). „Kinetics and Products of the Reaction of the First-Generation Isoprene Hydroxy Hydroperoxide (ISOPOOH) with OH“. *J. Phys. Chem. A* 120.9, pp. 1441–1451. DOI: 10.1021/acs.jpca.5b06532.

Stephens, M., N. Turner, and J. Sandberg (2003). „Particle identification by laser-induced incandescence in a solid-state laser cavity“. *Appl. Opt.* 42.19, pp. 3726–3736. DOI: 10.1364/AO.42.003726.

Stohl, A., S. Eckhardt, C. Forster, P. James, N. Spichtinger, and P. Seibert (2002). „A replacement for simple back trajectory calculations in the interpretation of atmospheric trace substance measurements“. *Atmos. Environ.* 36.29, pp. 4635–4648. ISSN: 1352-2310. DOI: 10.1016/S1352-2310(02)00416-8.

Stohl, A., C. Forster, A. Frank, P. Seibert, and G. Wotawa (2005). „Technical note: The Lagrangian particle dispersion model FLEXPART version 6.2“. *Atmos. Chem. Phys.* 5.9, pp. 2461–2474. DOI: 10.5194/acp-5-2461-2005. URL: https://www.atmos-chem-phys.net/5/2461/2005/.

Sueper and collaborators (2018). *ToF-AMS Data Analysis Software Webpage.* last access: 10.12.2018. URL: http://cires1.colorado.edu/jimenez-group/wiki/index.php/ToF-AMS_Analysis_Software.

Sullivan, A. P., N. Hodas, B. J. Turpin, K. Skog, F. N. Keutsch, S. Gilardoni, M. Paglione, M. Rinaldi, S. Decesari, M. C. Facchini, L. Poulain, H. Herrmann, A. Wiedensohler, E. Nemitz, M. M. Twigg, and J. L. Collett Jr. (2016). „Evidence for ambient dark aqueous SOA formation in the Po Valley, Italy“. *Atmos. Chem. Phys.* 16.13, pp. 8095–8108. DOI: 10.5194/acp-16-8095-2016.

Surratt, J. D., S. M. Murphy, J. H. Kroll, N. L. Ng, L. Hildebrandt, A. Sorooshian, R. Szmigielski, R. Vermeylen, W. Maenhaut, M. Claeys, R. C. Flagan, and J. H. Seinfeld (2006). „Chemical composition of secondary organic aerosol formed from the photooxidation of isoprene“. *Journal of Physical Chemistry A* 110.31, pp. 9665–90. DOI: 10.1021/jp061734m.

Surratt, J. D., A. W. Chan, N. C. Eddingsaas, M. Chan, C. L. Loza, A. J. Kwan, S. P. Hersey, R. C. Flagan, P. O. Wennberg, and J. H. Seinfeld (2010). „Reactive intermediates revealed in secondary organic aerosol formation from isoprene“. *Proc Natl Acad Sci USA USA* 107.15, pp. 6640–5. DOI: 10.1073/pnas.0911114107.

Surratt, J. D., J. H. Kroll, T. E. Kleindienst, E. O. Edney, M. Claeys, A. Sorooshian, N. L. Ng, J. H. Offenberg, M. Lewandowski, M. Jaoui, R. C. Flagan, and J. H. Seinfeld (2007). „Evidence for Organosulfates in Secondary Organic Aerosol“. *Environ. Sci. Technol.* 41.2, pp. 517–527. DOI: 10.1021/es062081q.

TSI Inc. (2000). *Model 3010 Condensation Particle Counter.* Manual.

Tsigaridis, K. and M. Kanakidou (2003). „Global modelling of secondary organic aerosol in the troposphere: a sensitivity analysis“. *Atmos. Chem. Phys.* 3.5, pp. 1849–1869. DOI: 10.5194/acp-3-1849-2003.

Turpin, B. J. and H.-J. Lim (2001). „Species contributions to PM2. 5 mass concentrations: Revisiting common assumptions for estimating organic mass". *Aerosol Science & Technology* 35.1, pp. 602–610. DOI: 10.1080/02786820119445.

Ulbrich, I. M., M. R. Canagaratna, Q. Zhang, D. R. Worsnop, and J. L. Jimenez (2009). „Interpretation of organic components from Positive Matrix Factorization of aerosol mass spectrometric data". *Atmos. Chem. Phys.* 9.9, pp. 2891–2918. ISSN: 1680-7316. DOI: 10.5194/acp-9-2891-2009.

Von der Weiden, S.-L., F. Drewnick, and S. Borrmann (2009). „Particle Loss Calculator – a new software tool for the assessment of the performance of aerosol inlet systems". *Atmos. Meas. Techn.* 2.2, pp. 479–494. DOI: 10.5194/amt-2-479-2009.

Wang, J., R. Krejci, S. Giangrande, C. Kuang, H. M. J. Barbosa, J. Brito, S. Carbone, X. Chi, J. Comstock, F. Ditas, J. Lavric, H. E. Manninen, F. Mei, D. Moran-Zuloaga, C. Pöhlker, M. L. Pöhlker, J. Saturno, B. Schmid, R. A. F. Souza, S. R. Springston, J. M. Tomlinson, T. Toto, D. Walter, D. Wimmer, J. N. Smith, M. Kulmala, L. A. T. Machado, P. Artaxo, M. O. Andreae, T. Petäjä, and S. T. Martin (2016a). „Amazon boundary layer aerosol concentration sustained by vertical transport during rainfall". *Nature* 539, p. 416. DOI: 10.1038/nature19819.

Wang, Q., J. Saturno, X. Chi, D. Walter, J. V. Lavric, D. Moran-Zuloaga, F. Ditas, C. Pöhlker, J. Brito, S. Carbone, P. Artaxo, and M. O. Andreae (2016b). „Modeling investigation of light-absorbing aerosols in the Amazon Basin during the wet season". *Atmos. Chem. Phys.* 16.22, pp. 14775–14794. DOI: 10.5194/acp-16-14775-2016.

Weigel, R., S. Borrmann, J. Kazil, A. Minikin, A. Stohl, J. C. Wilson, J. M. Reeves, D. Kunkel, M. de Reus, W. Frey, E. R. Lovejoy, C. M. Volk, S. Viciani, F. D'Amato, C. Schiller, T. Peter, H. Schlager, F. Cairo, K. S. Law, G. N. Shur, G. V. Belyaev, and J. Curtius (2011). „In situ observations of new particle formation in the tropical upper troposphere: the role of clouds and the nucleation mechanism". *Atmos. Chem. Phys.* 11.18, pp. 9983–10010. ISSN: 1680-7316. DOI: 10.5194/acp-11-9983-2011.

Weigel, R., P. Spichtinger, C. Mahnke, M. Klingebiel, A. Afchine, A. Petzold, M. Krämer, A. Costa, S. Molleker, P. Reutter, M. Szakáll, M. Port, L. Grulich, T. Jurkat, A. Minikin, and S. Borrmann (2016). „Thermodynamic correction of particle concentrations measured by underwing probes on fast-flying aircraft". *Atmos. Meas. Techn.* 9.10, pp. 5135–5162. DOI: 10.5194/amt-9-5135-2016.

Wendisch, M., U. Poschl, M. O. Andreae, L. A. T. Machado, R. Albrecht, H. Schlager, D. Rosenfeld, S. T. Martin, A. Abdelmomonem, A. Afchine, A. C.

Araujo, P. Artaxo, H. Aufmhoff, H. M. J. Barbosa, S. Borrmann, R. Braga, B. Buchholz, M. A. Cecchini, A. Costa, J. Curtius, M. Dollner, M. Dorf, V. Dreiling, V. Ebert, A. Ehrlich, F. Ewald, G. Fisch, A. Fix, F. Frank, D. Futterer, C. Heckl, F. Heidelberg, T. Huneke, E. Jakel, E. Jarvinen, T. Jurkat, S. Kanter, U. Kastner, M. Kenntner, J. Kesselmeier, T. Klimach, M. Knecht, R. Kohl, T. Kolling, M. Kramer, M. Kruger, T. C. Krisna, J. V. Lavric, K. Longo, C. Mahnke, A. O. Manzi, B. Mayer, S. Mertes, A. Minikin, S. Molleker, S. Munch, B. Nillius, K. Pfeilsticker, C. Pohlker, A. Roiger, D. Rose, D. Rosenowow, D. Sauer, M. Schnaiter, J. Schneider, C. Schulz, R. A. F. de Souza, A. Spanu, P. Stock, D. Vila, C. Voigt, A. Walser, D. Walter, R. Weigel, B. Weinzierl, F. Werner, M. A. Yamasoe, H. Ziereis, T. Zinner, and M. Zoger (2016). „ACRIDICON-CHUVA CAMPAIGN Studying Tropical Deep Convective Clouds and Precipitation over Amazonia Using the New German Research Aircraft HALO“. *B. Am. Meteorol. Soc.* 97.10, pp. 1885–1908. ISSN: 0003-0007. DOI: 10.1175/Bams-D-14-00255.1.

Wennberg, P. (2013). „Let’s abandon the "high NO_x" and "low NO_x" terminology“. *IGAC News* 50, pp. 3–4.

Wonaschuetz, A., A. Sorooshian, B. Ervens, P. Y. Chuang, G. Feingold, S. M. Murphy, J. Gouw, C. Warneke, and H. H. Jonsson (2012). „Aerosol and gas re-distribution by shallow cumulus clouds: An investigation using airborne measurements“. *J. Geophys. Res.-Atmos.* 117.D17.

Worton, D. R., J. D. Surratt, B. W. Lafranchi, A. W. Chan, Y. Zhao, R. J. Weber, J. H. Park, J. B. Gilman, J. de Gouw, C. Park, G. Schade, M. Beaver, J. M. Clair, J. Crounse, P. Wennberg, G. M. Wolfe, S. Harrold, J. A. Thornton, D. K. Farmer, K. S. Docherty, M. J. Cubison, J. L. Jimenez, A. A. Frossard, L. M. Russell, K. Kristensen, M. Glasius, J. Mao, X. Ren, W. Brune, E. C. Browne, S. E. Pusede, R. C. Cohen, J. H. Seinfeld, and A. H. Goldstein (2013). „Observational insights into aerosol formation from isoprene“. *Environ. Sci. Technol.* 47.20, pp. 11403–13. DOI: 10.1021/es4011064.

Xu, L., S. Suresh, H. Guo, R. J. Weber, and N. L. Ng (2015a). „Aerosol characterization over the southeastern United States using high-resolution aerosol mass spectrometry: spatial and seasonal variation of aerosol composition and sources with a focus on organic nitrates“. *Atmos. Chem. Phys.* 15.13, pp. 7307–7336. DOI: 10.5194/acp-15-7307-2015.

Xu, L., H. Guo, C. M. Boyd, M. Klein, A. Bougiatioti, K. M. Cerully, J. R. Hite, G. Isaacman-VanWertz, N. M. Kreisberg, C. Knote, K. Olson, A. Koss, A. H. Goldstein, S. V. Hering, J. de Gouw, K. Baumann, S. H. Lee, A. Nenes, R. J. Weber, and N. L. Ng (2015b). „Effects of anthropogenic emissions on aerosol formation from isoprene and monoterpenes in the southeastern United States“. *Proc Natl Acad Sci USA* 112.1, pp. 37–42. DOI: 10.1073/pnas.1417609112.

Zhang, Q., M. R. Alfarra, D. R. Worsnop, J. D. Allan, H. Coe, M. R. Canagaratna, and J. L. Jimenez (2005a). „Deconvolution and quantification of hydrocarbon-like and oxygenated organic aerosols based on aerosol mass spectrometry“. *Environ. Sci. Technol.* 39.13, pp. 4938–52. DOI: 10.1021/es048568l.

Zhang, Q., D. R. Worsnop, M. R. Canagaratna, and J. L. Jimenez (2005b). „Hydrocarbon-like and oxygenated organic aerosols in Pittsburgh: insights into sources and processes of organic aerosols“. *Atmos. Chem. Phys.* 5.12, pp. 3289–3311. DOI: 10.5194/acp-5-3289-2005.

Zhang, Q., M. R. Canagaratna, J. T. Jayne, D. R. Worsnop, and J. L. Jimenez (2005c). „Time- and size-resolved chemical composition of submicron particles in Pittsburgh: Implications for aerosol sources and processes“. *J. Geophys. Res.-Atmos.* 110.D7. ISSN: 2169-897x. DOI: ArtnD07s0910.1029/2004jd004649.

Zhang, Q., J. L. Jimenez, D. R. Worsnop, and M. Canagaratna (2007a). „A case study of urban particle acidity and its influence on secondary organic aerosol“. *Environ. Sci. Technol.* 41.9, pp. 3213–9. URL: https://www.ncbi.nlm.nih.gov/pubmed/17539528.

Zhang, Q., J. L. Jimenez, M. R. Canagaratna, J. D. Allan, H. Coe, I. Ulbrich, M. R. Alfarra, A. Takami, A. M. Middlebrook, Y. L. Sun, K. Dzepina, E. Dunlea, K. Docherty, P. F. DeCarlo, D. Salcedo, T. Onasch, J. T. Jayne, T. Miyoshi, A. Shimono, S. Hatakeyama, N. Takegawa, Y. Kondo, J. Schneider, F. Drewnick, S. Borrmann, S. Weimer, K. Demerjian, P. Williams, K. Bower, R. Bahreini, L. Cottrell, R. J. Griffin, J. Rautiainen, J. Y. Sun, Y. M. Zhang, and D. R. Worsnop (2007b). „Ubiquity and dominance of oxygenated species in organic aerosols in anthropogenically-influenced Northern Hemisphere midlatitudes“. *Geophys. Res. Lett.* 34.13, p. L13801. ISSN: 0094-8276. DOI: 10.1029/2007gl029979.

Zhang, Q., J. L. Jimenez, M. R. Canagaratna, I. M. Ulbrich, N. L. Ng, D. R. Worsnop, and Y. Sun (2011). „Understanding atmospheric organic aerosols via factor analysis of aerosol mass spectrometry: a review“. *Anal. Bioanal. Chem.* 401.10, pp. 3045–67. DOI: 10.1007/s00216-011-5355-y.

Zhang, R., I. Suh, J. Zhao, D. Zhang, E. C. Fortner, X. Tie, L. T. Molina, and M. J. Molina (2004). „Atmospheric New Particle Formation Enhanced by Organic Acids“. *Science* 304.5676, pp. 1487–1490. ISSN: 0036-8075. DOI: 10.1126/science.1095139.

Ziereis, H., H. Schlager, P. Schulte, P. F. J. van Velthoven, and F. Slemr (2000). „Distributions of NO, NO_x , and NO_y in the upper troposphere and lower stratosphere between 28° and 61°N during POLINAT 2“. *Journal of Geophysical Research* 105.D3, pp. 3653–3664. ISSN: 2156-2202. DOI: 10.1029/1999JD900870.

Part II

APPENDIX

A

APPENDIX - METHODS

A.1 CONSTANT PRESSURE INLET

For the TE_L of the C-ToF-AMS with respect to the CPC, the following steps had been made during the data analysis. The C-ToF-AMS data were corrected with IE and RIE values derived from calibrations. A flow calibration was done before and applied. The mass concentrations used here are only the nitrate mass concentrations from ammonium nitrate measurements. The CPC and OPC data were pressure corrected and the number concentrations of the used reference instrument (CPC or OPC) were calculated to mass concentrations using the density of ammonium nitrate (1.72 g cm^{-3}), the nitrate proportion of ammonium nitrate (62/80) and the Jayne shape factor (0.8 for ammonium nitrate) (Jayne et al., 2000) (see Eq. 20).

$$C_{mass}^{ref} = C_{num}^{ref} \cdot 10^6 \cdot \frac{\pi}{6} \cdot \left(d_p \cdot 10^{-9}\right)^3 \cdot J_s \cdot \rho \cdot \frac{62}{80} \cdot 10^{12} \cdot \frac{p_0}{p_{amb}} \tag{20}$$

Errors for the TE_L were calculated with counting statistics and a value for the reproducibility (rep_i) of each instrument. The counting statistics describe the sum of the counts during the measured time and are multiplied with the flow into the instrument. For the C-ToF-AMS a factor of 0.5 needs to be considered due to the open/closed measurement mode. The values for the reproducibility are 2 % for the CPC (TSI Inc., 2000), 3 % for the OPC (Grimm Aerosol Technik, 2008) and 12 % for the C-ToF-AMS (more precisely: for the CPI) (Köllner, 2019).

$$\begin{aligned} \Delta TE &= TE \cdot \left[(\Delta AMS)^2 + (rep_{AMS})^2 + (\Delta ref)^2 + (rep_{ref})^2\right]^{\frac{1}{2}} \\ &= TE \cdot \left[\left(\frac{1}{\sum_{i=1}^{C} C_i^{ref} \cdot f_{AMS} \cdot 0.5}\right)^2 + (rep_{AMS})^2 \right. \\ &\qquad \left. + \left(\frac{1}{\sum_{i=1}^{C} C_i^{ref} \cdot f_{ref}}\right)^2 + (rep_{ref})^2\right]^{\frac{1}{2}} \end{aligned} \tag{21}$$

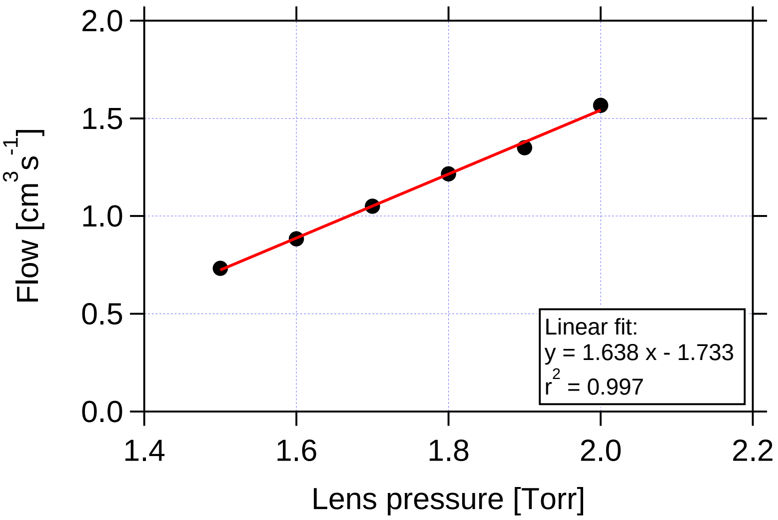

Figure 66: Flow calibration before the ACRIDICON-CHUVA campaign. The linear fit coefficients are given.

A.2 DETERMINATION OF THE VACUUM AERODYNAMIC DIAMETER

To determine the vacuum aerodynamic diameter d_{va} from the mobility diameter d_{mob}, the density ρ and the Jayne shape factor J_s need to be considered. For ammonium nitrate particles, the density is equal to 1.72 $\mathrm{g\,cm^{-3}}$ and the Jayne shape factor is 0.8 (Jayne et al., 2000). This value is a simplification. The complete calculation of J_s can be found in DeCarlo et al. (2004).

$$\mathrm{d_{va}} = \mathrm{d_{mob}} \cdot \rho \cdot J_s \tag{22}$$

A.3 C-TOF-AMS CALIBRATIONS DURING ACRIDICON-CHUVA

A.3.1 *Flow calibrations*

A flow calibration was conducted before the ACRIDICON-CHUVA campaign. The flow calibration is necessary to calibrate the flow that goes into the instrument to the pressure in the aerodynamic lens (see Fig. 66). The flow is also a factor in the quantification of the mass concentration (see Eq. 1).

A.3.2 *IE Calibration values*

The C-ToF-AMS was calibrated with monodisperse ammonium nitrate and sulfate before, during and after the campaigns in order to estimate relative ionisation efficiencies for nitrate and sulfate. Determined values can be found in Tab. 7 for the ACRIDICON-CHUVA campaign.

Table 7: Relative ionisation efficiencies (RIE) used for data analysis for the ACRIDICON-CHUVA campaign. $\mathrm{RIE}_{\mathrm{NH4}}$ and $\mathrm{RIE}_{\mathrm{SO4}}$ are determined from calibrations with ammonium nitrate and sulfate before, during and after the campaign. $\mathrm{RIE}_{\mathrm{NO3}}$ and $\mathrm{RIE}_{\mathrm{Org}}$ are literature values (Alfarra et al., 2004; Canagaratna et al., 2007).

$\mathrm{RIE}_{\mathrm{NO3}}$	$\mathrm{RIE}_{\mathrm{NH4}}$	$\mathrm{RIE}_{\mathrm{SO4}}$	$\mathrm{RIE}_{\mathrm{Org}}$
1.1	3.77	0.89	1.4

B

APPENDIX - CAMPAIGNS

B.1 PARTICLE LOSS CALCULATION

The particle loss calculator (PLC) determines the transmission efficiency for different particle sizes (von der Weiden et al., 2009) through the tubing of the inlets to the C-ToF-AMS. The used parameters can be found in Tab. 8 for the HASI and in Tab. 9 for the HALO-CVI. For the calculation for the HASI the shrouded section of the HASI was ignored due to non-applicability of the PLC for these types of inlets (von der Weiden et al., 2009). The same applies for the HALO-CVI, so that only the tubing between the HASI or HALO-CVI and the C-ToF-AMS is considered, respectively.

Table 8: Parameters used for calculating the transmission efficiency of the tubing between the HASI inlet and the C-ToF-AMS for different particle sizes. The PLC was developed at the MPIC (von der Weiden et al., 2009).

Section	Flow [l min^{-1}]	Tube length [m]	First inner diameter [mm]	Second inner diameter [mm]	Inclination angel [°]	Bend angle [°]
1 (Tubing AMS, SP2, Bypass)	2.6	0.14	5	5	0	90
2 (Tubing AMS, SP2, Bypass)	2.6	0.18	5	5	40	0
3 (Tubing AMS, SP2, Bypass)	2.6	0.61	5	5	10	90
4 (Tubing AMS)	0.1	0.64	5	5	90	90
5 (Tubing AMS)	0.1	0.25	5	5	0	90
6 (Tubing AMS)	0.1	0.05	5	5	90	0
7 (Tubing AMS)	0.1	0.24	5	5	0	90
8 (Tubing AMS)	0.1	0.5	5	5	90	0
9 (Tubing AMS)	0.1	0.1	5	5	80	90
10 (Tubing AMS)	0.1	0.2	5	5	90	0
11 (Tubing AMS)	0.1	0.15	5	5	0	90

Table 9: Parameters used for calculating the transmission efficiency of the tubing from the HALO-CVI to the C-ToF-AMS for different particle sizes. The PLC was developed at the MPIC (von der Weiden et al., 2009).

Section	Flow [l min^{-1}]	Tube length [m]	First inner diameter [mm]	Second inner diameter [mm]	Inclination angel [°]	Bend angle [°]
1 (Tubing AMS)	0.1	2.2	5	5	90	90
2 (Tubing AMS)	0.1	0.2	5	5	0	90
3 (Tubing AMS)	0.1	0.04	5	5	90	90
4 (Tubing AMS)	0.1	0.18	5	5	50	90
5 (Tubing AMS)	0.1	0.12	5	5	0	90
6 (Tubing AMS)	0.1	0.19	5	5	90	0
7 (Tubing AMS)	0.1	0.1	5	5	80	90
8 (Tubing AMS)	0.1	0.2	5	5	90	0
9 (Tubing AMS)	0.1	0.15	5	5	0	90

C

APPENDIX - RESULTS

C.1 MASS CALCULATIONS FROM UHSAS-A NUMBER CONCENTRATIONS

A comparison between the total mass concentration (C_{AMS}+C_{rBC}) and the mass concentration derived from UHSAS-A size-resolved number concentrations is possible. The number concentration of the UHSAS-A is size-resolved meaning that this data set is a matrix. A volume concentration is calculated from the number concentration using Eq. (23). The matrix format remains unchanged. After summing up over all size bins the volume concentration can be converted into a mass concentration using the fractional composition derived by the C-ToF-AMS and the individual densities (see Eq. 24 and Tab. 10).

$$C_{volume}^{\mathrm{UHSAS}} = C_{number}^{\mathrm{UHSAS}} \cdot \frac{4}{3}\pi \cdot \left(\frac{d_p}{2}\right)^3 \tag{23}$$

$$\begin{aligned} C_{mass}^{\mathrm{UHSAS}} = & \sum_{sizebins} C_{volume}^{\mathrm{UHSAS}} \cdot [rel_{Org} \cdot \rho_{Org} \\ & + (rel_{NO3} + rel_{SO4} + rel_{NH4}) \cdot \rho_{Inorg} \\ & + rel_{rBC} \cdot \rho_{rBC}] \end{aligned} \tag{24}$$

Table 10: Densities used for the calculation of the mass concentrations derived from UHSAS-A number concentrations.

	Organics	Inorganics (NH_4NO_3 and $(NH_4)_2SO_4$)	Black carbon
Density [g cm^{-3}]	1.2 [1]	1.75 [2]	1.8 [3]

[1] Turpin and Lim (2001)
[2] Bruno and Lide-Thomas (2014)
[3] Park et al. (2004)

C.2 DIAMETERS FROM SIZE DISTRIBUTIONS

From a log-normal size distribution different characteristic diameters can be derived. The only parameter which needs to be known is σ, the geometric standard deviation of the log-normal distribution, and d_p^0 (mode diameter), the diameter where the maximum of the distribution lies. The count median diameter (CMD) is the median diameter of the size distribution. The mass median diameter (MMD) is the diameter at which 50 % of the mass lies below and 50 % of the mass above it. In contrast to this, is the diameter of average mass ($d_{\overline{m}}$) defined as the diameter at which its mass multiplied with the total number accounts for the total mass. All the definitions and Eq. (25), (26), and (27) can be found in Hinds (1999).

$$CMD = \frac{d_p^0}{\exp\left[-1 \cdot (\ln(\sigma))^2\right]} \tag{25}$$

$$MMD = CMD \cdot \exp\left[3 \cdot (\ln\sigma)^2\right] \tag{26}$$

$$d_{\overline{m}} = CMD \cdot \exp\left[1.5 \cdot (\ln\sigma)^2\right] \tag{27}$$

C.3 ACIDITY CALCULATIONS

The acidity calculations take the inorganic mass concentrations into account. Chloride is not considered her as it always lies below the DL. The amount of measured ammonium is compared with the amount of needed ammonium that would be necessary to neutralize the measured nitrate and sulfate. More information on this calculation can be found in Zhang et al. (2007a).

$$C_{\mathrm{NH4}}^{\mathrm{needed}} = \frac{18}{62} \cdot C_{\mathrm{NO3}} + \frac{2 \cdot 18}{96} \cdot C_{\mathrm{SO4}} \tag{28}$$

C.4 UNCERTAINTY CALCULATIONS AND FITTING

The uncertainties for the different species are calculated from a continuous σ derived from DL calculations according to Sect. 2.2.3.4 for the out-of-cloud aerosol. For CPR a constant σ for each species is derived from filter measurements (see Sect. 4.2.1). Thus, uncertainties for organics, nitrate, sulfate, ammonium, Org29, Org43, Org44, Org60, Org82, NO^+, NO_2^2 and m/z 82 are determined. Uncertainty propagation occurs when calculating ratios e.g. f_{43}, f_{44}, or calculating mass concentrations of e.g. IEPOX-SOA using Eq. (8) or organic nitrate using Eq. (14). Therefore, the Gaussian uncertainty propagation is used, where the parameter's uncertainties need to be independent from each other. Although Org43 is contributing to the total signal of the organics (Org), ΔOrg is not dominated by ΔOrg43, ΔOrg44, ΔOrg60, or ΔOrg82, respectively. Overall, the independence of ΔOrg and Δ of the specific organic signal needs to be assumed when the Gaussian uncertainty propagation is applied. The following equations are used for the uncertainty propagation calculations:

$$\Delta f_{43} = \left[\left(\frac{1}{\mathrm{Org}} \cdot \Delta\mathrm{Org43}\right)^2 + \left(\frac{\mathrm{Org43}}{\mathrm{Org}^2} \cdot \Delta\mathrm{Org}\right)^2\right]^{\frac{1}{2}} \tag{29}$$

$$\Delta f_{44} = \left[\left(\frac{1}{\mathrm{Org}} \cdot \Delta\mathrm{Org44}\right)^2 + \left(\frac{\mathrm{Org44}}{\mathrm{Org}^2} \cdot \Delta\mathrm{Org}\right)^2\right]^{\frac{1}{2}} \tag{30}$$

$$\Delta f_{60} = \left[\left(\frac{1}{\mathrm{Org}} \cdot \Delta\mathrm{Org60}\right)^2 + \left(\frac{\mathrm{Org60}}{\mathrm{Org}^2} \cdot \Delta\mathrm{Org}\right)^2\right]^{\frac{1}{2}} \tag{31}$$

$$\Delta f_{82} = \left[\left(\frac{1}{\mathrm{Org}} \cdot \Delta\mathrm{Org82}\right)^2 + \left(\frac{\mathrm{Org82}}{\mathrm{Org}^2} \cdot \Delta\mathrm{Org}\right)^2\right]^{\frac{1}{2}} \tag{32}$$

$$\Delta R_{44/43} = \left[\left(\frac{1}{\mathrm{Org43}} \cdot \Delta\mathrm{Org44}\right)^2 + \left(\frac{\mathrm{Org44}}{\mathrm{Org43}^2} \cdot \Delta\mathrm{Org43}\right)^2\right]^{\frac{1}{2}} \tag{33}$$

$$\Delta C_{mass}^{\mathrm{UHSAS}} = \left[(V \cdot \Delta\rho)^2 + (\rho \cdot \Delta V)^2\right]^{\frac{1}{2}} \tag{34}$$

$$\text{with } \Delta\rho = (\rho_{Inorg} - \rho_{Org}) \cdot \Delta rel_{species} \tag{35}$$

$$\text{and } \Delta V = \frac{1}{6} \cdot \pi \cdot 3 \cdot d^2 \cdot \Delta d \tag{36}$$

$$\Delta C_{\mathrm{NH4}}^{\mathrm{needed}} = \left[\left(\frac{18}{62} \cdot \Delta C_{\mathrm{NO3}}\right)^2 + \left(\frac{2 \cdot 18}{96} \cdot \Delta C_{\mathrm{SO4}}^2\right)\right]^{\frac{1}{2}} \tag{37}$$

$$\begin{aligned}\Delta C(\mathrm{IEPOX{-}SOA}) = \Bigg[&\left(\frac{1}{f_{82}^{IEPOXSOA} - f_{82}^{Bg}} \cdot \Delta C(m/z\,82) \right)^2 \\ &+ \left(\frac{-f_{82}^{Bg}}{f_{82}^{IEPOXSOA} - f_{82}^{Bg}} \cdot \Delta C(Org) \right)^2 \\ &+ \left(\frac{C(m/z\,82) - C(Org) \cdot f_{82}^{IEPOXSOA}}{(f_{82}^{IEPOXSOA} - f_{82}^{Bg})^2} \cdot \Delta f_{82}^{Bg} \right)^2 \Bigg]^{\frac{1}{2}}\end{aligned} \tag{38}$$

$$\begin{aligned}\Delta \mathrm{pRONO}_2^{Farmer} = \Bigg[&\left(\frac{(1 + R_{\mathrm{RONO}}) \cdot (R_{\mathrm{amb}} - R_{\mathrm{cal}})}{(1 + R_{\mathrm{amb}}) \cdot (R_{\mathrm{RONO}} - R_{\mathrm{cal}})} \cdot \Delta C_{\mathrm{NO3}} \right)^2 \\ &+ \left(C_{\mathrm{NO3}} \cdot \frac{(1 + R_{\mathrm{RONO}}) \cdot (R_{\mathrm{cal}} + 1)}{(1 + R_{\mathrm{amb}})^2 \cdot (R_{\mathrm{RONO}} - R_{\mathrm{cal}})} \cdot \Delta R_{\mathrm{amb}} \right)^2 \\ &+ \left(-C_{\mathrm{NO3}} \cdot \frac{(1 + R_{\mathrm{RONO}}) \cdot (R_{\mathrm{RONO}} - R_{\mathrm{amb}})}{(1 + R_{\mathrm{amb}}) \cdot (R_{\mathrm{RONO}} - R_{\mathrm{cal}})^2} \cdot \Delta R_{\mathrm{cal}} \right)^2 \Bigg]^{\frac{1}{2}}\end{aligned} \tag{39}$$

$$\begin{aligned}\Delta \mathrm{pRONO}_2^{Fry} = \Bigg[&\left(\frac{(1 + R_{\mathrm{RONO}}) \cdot (R_{\mathrm{amb}} - R_{\mathrm{cal}})}{(1 + R_{\mathrm{amb}}) \cdot (R_{\mathrm{RONO}} - R_{\mathrm{cal}})} \cdot \Delta C_{\mathrm{NO3}} \right)^2 \\ &+ \left(C_{\mathrm{NO3}} \cdot \frac{(1 + R_{\mathrm{RONO}}) \cdot (R_{\mathrm{cal}} + 1)}{(1 + R_{\mathrm{amb}})^2 \cdot (R_{\mathrm{RONO}} - R_{\mathrm{cal}})} \cdot \Delta R_{\mathrm{amb}} \right)^2 \\ &+ \left(-C_{\mathrm{NO3}} \cdot \frac{(1 + R_{\mathrm{RONO}}) \cdot (R_{\mathrm{RONO}} - R_{\mathrm{amb}})}{(1 + R_{\mathrm{amb}}) \cdot (R_{\mathrm{RONO}} - R_{\mathrm{cal}})^2} \cdot \Delta R_{\mathrm{cal}} \right)^2 \\ &+ \left(-C_{\mathrm{NO3}} \cdot \frac{(1 + R_{\mathrm{cal}}) \cdot (R_{\mathrm{amb}} - R_{\mathrm{cal}})}{(1 + R_{\mathrm{amb}}) \cdot (R_{\mathrm{RONO}} - R_{\mathrm{cal}})^2} \cdot \Delta R_{\mathrm{RONO}} \right)^2 \Bigg]^{\frac{1}{2}}\end{aligned} \tag{40}$$

For the conversion from UHSAS-A volume to mass concentrations the density is derived from the relative contributions of the species ($rel_{species}$) measured by the C-ToF-AMS. Thus, $\Delta rel_{species}$ describes the total C-ToF-AMS uncertainty of 30 % of each data point for the relative contribution of the appropriate species to the total mass in Eq. (35). In Eq. (36) Δd describes the statistical uncertainty of 11 % of the size determination of the UHSAS-A (Mahnke, 2018).

The fitting of different parameters is performed with the total least squares method. Here, the uncertainties of both parameters (in x and y direction) are considered for the calculation of the linear fit curve coefficients. In the analysis software IGOR Pro 6.37 (Wave Metrics) this fitting method is called orthogonal distance regression, and used for all linear fit curves shown in this study.

ACRONYMS

GENERAL ACRONYMS

ACP	*Atmospheric Chemistry and Physics*
ACRIDICON-CHUVA	Aerosol, Cloud, Precipitation, and Radiation Interactions and Dynamics of Convective Cloud Systems - Cloud Processes of the Main Precipitation Systems in Brazil: A Contribution to Cloud Resolving Modeling and to the GPM (Global Precipitation Measurement)
AMT	*Atmospheric Measurement Techniques*
AENEAS	atmospheric nitrogen oxides measuring system
AMETYST	aerosol measurement system
AMTEX	atmospheric tracer experiment
ATTO	Amazon tall tower observatory
BAHAMAS	BAsic HALO Measurement And Sensor system
BB	biomass burning
BC	black carbon
BFSP	brute-force single particle
BL	(planetary) boundary layer
CCN	cloud condensation nuclei
CPC	condensation particle counter
CPI	constant pressure inlet
CPR	cloud particle residuals
C-ToF-AMS	compact time-of-flight aerosol mass spectrometer
DL	detection limit
DLR	Deutsches Zentrum für Luft- und Raumfahrt

DLR-FX	DLR Flight Experiments
DLR-IPA	DLR Institute of Atmospheric Physics
EF	enrichment factor
EMAC	ECHAM5/MESSy Atmospheric Chemistry
FF	fossil fuel combustion
FZ Jülich	Forschungszentrum Jülich
GFS	Global Forecast System
GoAmazon14/5	Green Ocean Amazon Experiment
HALO	High Altitude and LOng range research aircraft
HALO-CVI	HALO counterflow virtual impactor
HASI	HALO aerosol submicrometer inlet
HCCT	Hill Cap Cloud Thuringia 2010
HOA	hydrocarbon-like organic aerosol
HR-ToF-AMS	high resolution time-of-flight aerosol mass spectrometer
IEPOX	isoprene epoxydiols
IEPOX-SOA	isoprene-epoxydiol secondary organic aerosol
INP	ice nucleating particles
ISOPOO	isoprene peroxide radicals
ISOPOOH	isoprene hydroxy hydroperoxides
ITCZ	intertropical convergence zone
LFC	level of free convection
LO-OOA	less oxidized OOA
LT	lower troposphere
LV-OOA	low-volatile OOA
MACR	methacrolein
MCP	micro-channel plate

MPC	Multiphase Chemistry Department
MPIC	Max Planck Institute for Chemistry
MO-OOA	more oxidized OOA
MT	middle troposphere
MVK	methyl vinyl ketone
NIXE-CAPS	Novel Ice eXpEriment - Cloud, Aerosol and Precipitation Spectrometer
NPF	new particle formation
OA	organic aerosol
OPC	Sky optical particle counter
OOA	oxygenated organic aerosol
PAH	polycyclic aromatic hydrocarbons
PLC	particle loss calculator
PMF	positive matrix factorization
POA	primary organic aerosol
Q-AMS	quadrupole aerosol mass spectrometer
rBC	refractory black carbon
RH	relative humidity
RH_w	relative humidity with respect to water
SAMBBA	South American Biomass Burning Analysis
SOA	secondary organic aerosol
SP2	single particle soot photometer
STP	standard pressure and temperature
SV-OOA	semi-volatile OOA
TROPOS	Leibniz Institute for Tropospheric Research
TTL	tropical transition layer
UHSAS-A	ultra-high sensitivity aerosol spectrometer airborne
UT	upper troposphere
VOC	volatile organic compound

PHYSICAL SYMBOLS

AB	Hz	air beam signal
$CAPE$	J kg^{-1}	convective available potential energy
CE		collection efficiency
CIN	J kg^{-1}	convective inhibition
CMD	m	count median diameter
$d_{\overline{m}}$	m	diameter of average mass
d_p	m	particle diameter
d_{va}	m	particle vacuum aerodynamic diameter
d_{50}	m	cutoff diameter at 50 % efficiency
IE		ionization efficiency
m/z	m	mass to charge ratio
MMD	m	mass median diameter
RIE		relative ionization efficiency
Stk		Stokes number
TE_L		aerodynamic lens transmission efficiency

CHEMICAL SYMBOLS

CO	carbon monoxide
CO_2	carbon dioxide
HO_x	hydrogen oxide radicals
HO_2	hydroperoxyl radicals
NO	nitric oxide
NO_x	nitrogen oxide radicals
NO_y	total reactive nitrogen
NO_3	nitrate radicals
O_3	ozone
OH	hydroxide
$RONO_2$	nitrate content of organic nitrates

LIST OF FIGURES

LIST OF TABLES

PUBLICATIONS

Parts of this work were already published as a paper or presented as a talk or poster on conferences. This list provides an overview of publications related to this work.

PEER REVIEWED PUBLICATIONS

- Wendisch, M., Poschl, U., Andreae, M. O., Machado, L. A. T., Albrecht, R., Schlager, H., Rosenfeld, D., Martin, S. T., Abdelmomonem, A., Afchine, A., Araujo, A. C., Artaxo, P., Aufmhoff, H., Barbosa, H. M. J., Borrmann, S., Braga, R., Buchholz, B., Cecchini, M. A., Costa, A., Curtius, J., Dollner, M., Dorf, M., Dreiling, V., Ebert, V., Ehrlich, A., Ewald, F., Fisch, G., Fix, A., Frank, F., Futterer, D., Heckl, C., Heidelberg, F., Huneke, T., Jakel, E., Jarvinen, E., Jurkat, T., Kanter, S., Kastner, U., Kenntner, M., Kesselmeier, J., Klimach, T., Knecht, M., Kohl, R., Kolling, T., Kramer, M., Kruger, M., Krisna, T. C., Lavric, J. V., Longo, K., Mahnke, C., Manzi, A. O., Mayer, B., Mertes, S., Minikin, A., Molleker, S., Munch, S., Nillius, B., Pfeilsticker, K., Pohlker, C., Roiger, A., Rose, D., Rosenowow, D., Sauer, D., Schnaiter, M., Schneider, J., Schulz, C., de Souza, R. A. F., Spanu, A., Stock, P., Vila, D., Voigt, C., Walser, A., Walter, D., Weigel, R., Weinzierl, B., Werner, F., Yamasoe, M. A., Ziereis, H., Zinner, T., Zoger, M. (2016). „ACRIDICON-CHUVA CAMPAIGN Studying Tropical Deep Convective Clouds, Precipitation over Amazonia Using the New German Research Aircraft HALO“. *B. Am. Meteorol. Soc.*. DOI:10.1175/Bams-D-14-00255.1
- Andreae, M. O., Afchine, A., Albrecht, R., Holanda, B. A., Artaxo, P., Barbosa, H. M. J., Borrmann, S., Cecchini, M. A., Costa, A., Dollner, M., Fütterer, D., Järvinen, E., Jurkat, T., Klimach, T., Konemann, T., Knote, C., Krämer, M., Krisna, T., Machado, L. A. T., Mertes, S., Minikin, A., Pöhlker, C., Pöhlker, M. L., Pöschl, U., Rosenfeld, D., Sauer, D., Schlager, H., Schnaiter, M., Schneider, J., Schulz, C., Spanu, A., Sperling, V. B., Voigt, C., Walser, A., Wang, J., Weinzierl, B., Wendisch, M., and Ziereis, H.: Aerosol characteristics and particle production in the upper troposphere over the Amazon Basin, *Atmos. Chem. Phys.*, 18, 921-961, https://doi.org/10.5194/acp-18-921-2018, 2018.
- Saturno, J., Ditas, F., Penning de Vries, M., Holanda, B. A., Pöhlker, M. L., Carbone, S., Walter, D., Bobrowski, N., Brito, J., Chi, X., Gutmann, A., Hrabe de Angelis, I., Machado, L. A. T., Moran-Zuloaga, D., Rüdiger, J., Schneider, J., Schulz, C., Wang, Q., Wendisch, M., Artaxo, P., Wagner, T., Pöschl, U., Andreae, M. O., and Pöhlker, C.: African volcanic emissions influencing atmospheric aerosols over the Amazon rain forest, *Atmos. Chem. Phys.*, 18, 10391-10405, https://doi.org/10.5194/acp-18-10391-2018, 2018.

- Schulz, C., Schneider, J., Amorim Holanda, B., Appel, O., Costa, A., de Sá, S. S., Dreiling, V., Fütterer, D., Jurkat-Witschas, T., Klimach, T., Knote, C., Krämer, M., Martin, S. T., Mertes, S., Pöhlker, M. L., Sauer, D., Voigt, C., Walser, A., Weinzierl, B., Ziereis, H., Zöger, M., Andreae, M. O., Artaxo, P., Machado, L. A. T., Pöschl, U., Wendisch, M., and Borrmann, S.: Aircraft-based observations of isoprene-epoxydiol-derived secondary organic aerosol (IEPOX-SOA) in the tropical upper troposphere over the Amazon region, *Atmos. Chem. Phys.*, 18, 14979-15001, https://doi.org/10.5194/acp-18-14979-2018, 2018.

- Mei, F., Comstock, J., Wang, J., Pekour, M., Shilling, J., Schneider, J., Wendisch, M., Long, C., Hubbe, J., Schmid, B., Machado, L., Krisna, T., Giez, A., Weinzierl, B., Zoeger, M., Schulz, C., Mahnke, C., Weigl, R., Pöhlker, M. L., Schlager, H., Cecchini, M., Andreae, M. O., Martin, S., de Sá, S., Fan, J., Tomlinson, J., Springston, S., Poschl, U., Artaxo, P., Pohlker, C., Klimach, T. and Minikin, A.: Comparison of Aircraft Measurements during GoAmazon2014/5 and ACRIDICON-CHUVA, submitted to *Atmos. Meas. Tech.*, 2019

- Haslett, S., Taylor, J., Evans, M., Morris, E., Vogel, B., Dajuma, A., Brito, J., Batenburg, A., Borrmann, S., Schneider, J., Schulz, C., Denjean, C., Bourrianne T., Knippertz, P., Dupuy, R., Schwarzenböck, A., Sauer, D., Flamant, C., Dorsey, J., Crawford, I., and Coe, H.: Remote biomass burning dominates southern West African air pollution during the monsoon, submitted to *Atmos. Chem. Phys.*, 2019

- Holanda, B. A., Pohlker, M. L., Klimach, T., Saturno, J., Ditas, J., Ditas, F., Wang, Q., Schulz, C., Barbosa, H. M. J., Brito, J., Borrmann, S., Cheng, Y., Dollner, M., Förster, J.D., Kaiser, J., Kilcoyne, A. L. D., Knote, C., Kremper, L. A., Krüger, O. O., Fütterer, D., Ma, N., Machado, L. A. T., Ming, J., Moran-Zuloaga, D., Sauer, D., Schlager, H., Schneider, J., Sörgel, M., Su, H., Weinzierl, B., Walser, A., Walter, D., Wendisch, M., Ziereis, H., Artaxo, P., Poschl, U., Andreae, M. O., and Pöhlker, C.: Characterization of transatlantic pollution transport from Africa into the Amazon Basin, in prep. for *Atmos. Chem. Phys.*, 2019

- Molleker, S., Helleis, F., Klimach, T., Gurk, C., Appel, O., Huenig, A., Dragoneas, A., Rubach, F., Schulz, C., Köllner, F., Clemen, H.-C., Borrmann, S.: Application of an O-ring pinch device as a constant pressure inlet for airborne sampling, in prep. for *Atmos. Meas. Tech.*, 2019

CONTRIBUTIONS TO CONFERENCES

- 2014 PhD Conference on Earth System Science, Jena

  Poster: Airborne Aerosol Measurements in Arctic and Tropic Air with an aerosol mass spectrometer (C-ToF-AMS)

- 2015 European Geoscience Union, Vienna

  Poster: Mass spectrometric measurements of submicron aerosol and cloud residual composition in tropic deep convection during ACRIDICON-CHUVA

- 2015 European Aerosol Conference, Milan

  Talk: Airborne submicron aerosol composition measurements in the Arctic in Spring 2014 during RACEPAC

- 2016 International Conference on Clouds & Precipitation, Manchester

  Talk: Cloud residual particle measurements in convective clouds over the Amazon during ACRIDICON-CHUVA

CONTRIBUTIONS TO THIS THESIS

This study was made possible by the valuable contributions of colleagues that are acknowledged here.
Funding of this work was realized by the projects DFG HALO-SPP 1294 and SCHN1138/1-2, and by the project BMBF, grant No. 01LG1205E (ROMIC-SPITFIRE) as well as by internal resources of the Particle Chemistry Department at the Max Planck Institute for Chemistry.
Parts of this study has already been published in peer reviewed journals and when used here referred to appropriately.

In Chapter 2, the experimental work regarding the characterization of the C-ToF-AMS inlet system was conducted by Franziska Köllner, Hans-Christian Clemen and myself. The different approaches for organic nitrates calculations and the analysis of the detection limits were critically discussed with Oliver Appel and Johannes Schneider. Further contributions were made by Frank Drewnick and Anneke Batenburg.

In Chapter 3, the basic meteorological data were provided by Volker Dreiling and Martin Zöger. The measurements for the particle losses in the inlet line were carried out by myself.

Chapter 4 presents the results of the ACRIDICON-CHUVA campaign. This intensive field campaign consumed a lot of work for many people. All participants of the ACRIDICON-CHUVA campaign took their effort for a successful campaign. Meinrat O. Andreae, Ulrich Pöschl, Manfred Wendisch, Paulo Artaxo, and Luiz A. Machado designed the research project. General logistics were handled by DLR-FX, the pilots realized the specific flight patterns. The preparation and certification of the C-ToF-AMS was done by myself with the help of Johannes Schneider, Florian Rubach, Christian Gurk, Thomas Klimach, Frank Helleis, Thomas Böttger, the mechanical and electronical workshop of the MPIC as well as enviscope GmbH. The operation of the instrument during the measurement flights were conducted by Johannes Schneider, myself, Adrian Walser, Daniel Fütterer, Maximilian Dollner, and Mira L. Pöhlker.
Bernadett Weinzierl, Daniel Sauer, Daniel Fütterer, and Adrian Walser performed aerosol number concentration measurements and provided AMETYST and UHSAS-A data. Bruna A. Holanda and Mira L. Pöhlker provided rBC data. Helmut Ziereis provided NO and NO_y data. Christoph Knote provided FLEXPART data. The cloud data were provided by Anja Costa, Martina

Krämer, Tina Jurkat-Witschas and Christiane Voigt.
I analysed the data with the help of Johannes Schneider. During the analysis data were discussed with Oliver Appel. Further helpful contributions were made by Suzane de Sá, Scot T. Martin, and Stephan Borrmann. Data from measurements at the HALO-CVI were discussed with Stephan Mertes. The manuscript of the published paper that is part of this chapter was written by myself with comments from all co-authors.

DECLARATION

I hereby declare that I wrote the dissertation submitted without any unauthorized external assistance and used only sources acknowledged in the work. All textual passages, which are appropriated verbatim or paraphrased from published and unpublished texts as well as all information obtained from oral sources are duly indicated and listed in accordance with bibliographical rules. In carrying out this research, I complied with the rules of standard scientific practice as formulated in the statutes of Johannes Gutenberg University Mainz to insure standard scientific practice. External contributions to data and analyses presented in this study are specified in detail on p. 193.

Mainz, February 11, 2019

Christiane Schulz